2001

# Aspects of the mineralogy of the Murun alkaline complex, Yakutia, Russia

Reguir, Ekaterina

# INFORMATION TO USERS

This manuscript has been reproduced from the microfilm master. UMI films the text directly from the original or copy submitted. Thus, some thesis and dissertation copies are in typewriter face, while others may be from any type of computer printer.

**The quality of this reproduction is dependent upon the quality of the copy submitted.** Broken or indistinct print, colored or poor quality illustrations and photographs, print bleedthrough, substandard margins, and improper alignment can adversely affect reproduction.

In the unlikely event that the author did not send UMI a complete manuscript and there are missing pages, these will be noted. Also, if unauthorized copyright material had to be removed, a note will indicate the deletion.

Oversize materials (e.g., maps, drawings, charts) are reproduced by sectioning the original, beginning at the upper left-hand corner and continuing from left to right in equal sections with small overlaps.

Photographs included in the original manuscript have been reproduced xerographically in this copy. Higher quality 6" x 9" black and white photographic prints are available for any photographs or illustrations appearing in this copy for an additional charge. Contact UMI directly to order.

# Aspects of the mineralogy of the Murun alkaline complex, Yakutia, Russia.

by

**Ekaterina Reguir** ©

Submitted in the partial fulfilment of
the requirements for the degree of

Master of Science

Supervisor: Dr. Roger. H. Mitchell

Department of Geology
Lakehead University
Thunder Bay, Ontario
Canada
April 2001

*Your file   Votre référence*

*Our file   Notre référence*

0-612-60867-0

Canadä

# ABSTRACT

The Murun complex contains a number of unusual and mineralogically unique rocks. Many of them are problematic in terms of their genesis and petrographic interpretation. These enigmatic rocks include charoite assemblages, as well as unique Ba-Sr-rich carbonatites and alkaline ultramafic dykes referred to as lamproites or lamprophyres.

Charoitites occur in about 25 localities along the southern margin of the Little Murun intrusion. Obtained compositional data for charoite suggests, in general, the empirical formula: $(K,Na)_3(Ca,Sr,Ba,Mn)_5Si_{12}O_{30}(OH,F) \cdot 3H_2O$. X-ray diffraction patterns of mosaic-fibrous and schistose charoite are indexed using a primitive monoclinic cell with the following parameters: $a$ =19.86(1) Å, $b$=32.13(2) Å, $c$=7.952(9) Å, $\beta$=97.24° (mosaic-fibrous) and $a$ =32.13(2) Å, $b$=19.64(2) Å, $c$=8.509(6) Å, $\beta$=95.23° (schistose). Some of the patterns of mosaic-fibrous charoite can also be refined on a triclinic cell ($a$ =19.96(1) Å, $b$ = 32.17(2) Å, $c$ =7.258(4) Å, $\alpha$=93.51°, $\beta$=99.45°, $\gamma$=89.50°). Comparison of the compositional and structural data of charoite and "tube"-chain silicates of similar composition (canasite and miserite) suggests that charoite has a significantly higher relative proportion of $SiO_4$ tetrahedra to octahedrally-coordinated cations than two other minerals. Possible similarities between the structural motifs of charoite and phyllosilicates are demonstrated.

The carbonatite bodies are confined to the aegirine-microcline fenite aureole in the southern contact zone of the Little Murun massif with the Precambrian crystalline basement. Three mineralogical types of the studied carbonatites are distinguished: calcite carbonatite (i), Ba-Sr-Ca carbonatite (ii), and phlogopite-calcite carbonatite (iii). In addition, the quartz-feldspar-carbonate rock is classified as a distinct lithological type. Carbonatites of types (i) and (ii) noticeably differ in terms of the composition of rock-forming silicates (potassium feldspar and clinopyroxene) and primary carbonates (Sr-rich calcite or barytocalcite, respectively). In both cases, the primary carbonates underwent complex exsolution processes. Typical exsolution textures are represented by primary carbonates in a core, and the subsolvus mineral assemblage confined to marginal parts of the crystal. The composition of the primary carbonates becomes progressively depleted in Ba + Sr (calcite) or Sr (barytocalcite) towards the margin, suggesting that interstitial fluids played an important role in the onset of exsolution processes promoting an outward diffusion of components in the peripheral zones of carbonate

crystals. In contrast to the calcite-carbonatite, the phlogopite-calcite carbonatite [type (iii)] is devoid of clinopyroxene and Ba-Sr-Ca carbonates, and rarely exhibits exsolution textures. Potassium feldspar and phlogopite from the carbonatite of type (iii) are Ba-rich, and show core-to-rim zonation pattern of decreasing Ba content. The mineralogical differences between the carbonatites of types (i) and (iii) clearly indicate that the latter crystallised from a volatile-rich magma depleted in Na, under more reducing conditions, and upon crystallisation, underwent a rapid loss of residual volatiles. Textural and mineralogical features of the quartz-feldspar-carbonate rock suggest that the rock is transitional from carbonatites to quartz-calcite rocks locally known as "torgolites".

The youngest igneous suite at Murun is represented mostly by dykes and sills. Studied hypabyssal and volcanic rocks are divided into eight petrographic groups: lamprophyre, pseudoleucite syenite, pseudoleucite italite, kalsilite melasyenite, eudialyte-bearing syenite, "potassium-batisite" syenite, lamprophyllite- and barytolamprophyllite-bearing syenite, and aegirinite. The compositional trends of mafic minerals from different groups clearly indicate that their parental magmas could not be derived from the same source, and that the magma mixing cannot account for the diversity of the hypabyssal rocks found at Murun. The compositional data of mafic minerals are in agreement with the previous findings, supporting the consanguineous nature of lamprophyres, phlogopite clinopyroxenites and shonkinites (including melasyenites). The syenitic rocks containing major proportions of such "agpaitic" minerals as eudialyte, "potassium batisite" and lamprophyllite-group minerals clearly represent the most evolved magmas. Compositions of their characteristic accessory minerals crystallised early in the evolutionary history suggest enrichment of parental magmas in Sr, Ba and Zr. The compositions of mafic minerals from pseudoleucite syenites fall off major evolutionary trends, therefore the source of these rocks is uncertain.

Clearly, further studies of the geochemistry and mineralogy of the alkaline ultramafic rocks, unique Ba-Sr-rich carbonatites and charoitites of the Murun complex are required.

# ACKNOWLEDGEMENTS

iii

# TABLE OF CONTENTS

iv

# LIST OF FIGURES

# LIST OF TABLES

# Chapter 1. Introduction

## 1.1. Geological setting

The Murun potassic alkaline complex is one of the largest in the Aldan Shield of eastern Siberia. The complex is a part of the Atbastakh-Murun region of the north-western Aldan Shield. The Murun complex and its fenite aureole occupy a total area of approximately 150-180 sq. km at the current level of erosion. The complex incorporates four distinct intrusive bodies, including Bol'shoi (Great) Murun, Malyi (Little) Murun, Dagaldyn and Kedrovyi (Cedar) (Borisov & Evdokimov 1984; Konev *et al.* 1996). The Little Murun is the largest (*ca.* 48 sq. km) and the best studied of these intrusions.

The Cretaceous alkaline magmatism at Murun is generally confined to the contact between the Archean crystalline basement of the Aldan Shield and the upper Proterozoic - Cambrian sedimentary basin (Fig. 1.1.1). Most authors recognise the following major intrusive phases within the Murun pluton: clinopyroxenite, melasyenites and shonkinites, syenite-porphyries, alkaline syenites, kalsilite and pseudoleucite syenites, nepheline syenites, phonolites and trachytes, dikes of agpaitic rocks and minettes, and carbonatites (Borisov & Evdokimov 1994; Ivanyuk & Evdokimov 1991, Mitchell & Vladykin 1996, Konev *et al.* 1996; Figs. 1.1.1, 2.1.1). The individual multiphase intrusions show little or no evidence of *in situ* magmatic differentiation.

With a few exceptions, the Murun rocks are distinctly potassic in character, with the K to Na atomic ratio reaching 14 in some petrographic units. Some varieties of kalsilite-bearing rocks show unusual textural features, and bear local names unfamiliar to most of western petrologists. These include kalsilite analogues of urtite-melteigites and juvites (yakutites and feldspar yakutites, respectively), and also massive pseudoleucite rocks in which leucite has been replaced by an aggregate of kalsilite plus potassium feldspar (synnyrites and melasynnyrites). It is noteworthy that a few rock types from Murun have been described under different names by different authors (for example, see Chapter 4.1). In some studies, petrographic characterisation and interpretation of certain rock types ("lamproites", yakutites, phlogopite clinopyroxenites, among others) has clearly been made on the basis of premature deductions about their genesis.

1

Fig. 1.1. Schematic Geological Map of the Murun Complex

(after Evdokimov, 1984)

Great Muru

Little Murun

Dagaldyn

Cedar

2.5 km

*Cretaceous Alkaline Igneous Rocks:*

Phonolites, trachytes

Nepheline syenites

Pseudoleucite syenites, fergusites, synnyrites

Alkali syenites

Syenite-porphyries

Melasyenites, shonkinites

Clinopyroxenites

*Proterozoic Metasedimentary Rocks*

*Archean Metamorphic Rocks*

## 1.2    Background information

The complex was discovered in the late 1930-s - early 1940-s by the V.G.Ditmar expedition. Since then, dozens of scientists from different research and prospecting institutions have been involved in the geological exploration of Murun. As this exploration progressed, the complexity of the geological and tectonic situation at Murun became increasingly evident. The Murun complex is, perhaps, best known for a suite of Ca-rich fenitic rocks developed from the Proterozoic carbonaceous sandstones. Beginning in the 1960-s, a number of new minerals of unusual composition and structure have been discovered in the fenites. Many of these, including frankamenite and the new gemstone charoite, are quite common in the Murun rocks, but have not been encountered anywhere else in the world.

There is no agreement between geologists as to what the composition of the parental magma was, or how the intrusions developed in time, or regarding genetic relationships between the individual petrographic series. At present, there are two major views on the evolution of the Murun complex. Orlova *et al.* (1987, 1988) suggest that the complex developed as a layered lopolith by magmatic differentiation. The alternative concept supported by Ivanyuk & Evdokimov (1991), Mitchell & Vladykin (1996), Konev *et al.* (1996) and others suggests that the individual intrusive phases were emplaced independently as a series of plutonic and hypabyssal bodies.

3

# Chapter 2.  Charoite.

## 2.1.  Occurrence, petrographic and mineralogical features of charoite-bearing rocks (charoitites)

Charoitite is the name used locally to refer to a rock consisting of more than 50 vol.% of charoite. Charoitites occur in about 25 localities along the southern margin of the Little Murun pluton. These are collectively known as the "Lilac Rock" charoite deposit (Fig. 2.1.1).

Depending on the geological setting, four types of charoite-bearing rocks have been distinguished by Borisov (1985). The charoitites of *type 1* occur as thin (2-3 cm) veins of fine-grained massive charoite in aegirine fenites developed in the country sedimentary rocks: sandstones, shales and gneisses. The *second* and *third types* occur in breccia zones, and are represented by nests and veins of texturally diverse charoite (type two) and blocks of charoitite (type three). The charoitites of *type four* are found at the contact with carbonatites. The charoitites of types two and three are mined commercially.

A typical sample of charoitite consists of rounded grains of quartz and microcline, as well as euhedral crystals and stellate aggregates of greenish black aegirine, honey-yellow tinaksite and greenish grey frankamenite set in a mesostasis of charoite demonstrating a diversity of colours and textures (Figs. 2.1.2-2.1.5). Charoitites from some localities within the Lilac Rock deposit also contain large subhedral crystals of pearly-white platy fedorite and pale bluish green pectolite (Fig. 2.1.6), sprays of colourless strontian fluorapatite (Fig. 2.1.7) and brownish red miserite, as well as platy crystals of tokkoite, commonly in intergrowths with tinaksite. Associated minerals also include agrellite, hydroxyapophyllite (Fig. 2.1.8), titanite, turkestanite (Fig. 2.1.9), barite, sulphides and carbonates. The latter comprise calcite, strontianite, barytocalcite, witherite, burbankite and ancylite-(Ce), and commonly occur as segregations and microlayers conformable with layers of charoite (Fig. 2.1.10). In BSE images, carbonates commonly appear as exsolution aggregates similar to those found in calcite carbonatite and Ba-Sr-Ca carbonatite (see Chapter 3), but containing generally greater proportions of strontianite and burbankite. Formulae and representative compositions of some of the rock-forming and accessory minerals of charoitites obtained in this work are summarised in Tables 2.1.1-2.1.5.

4
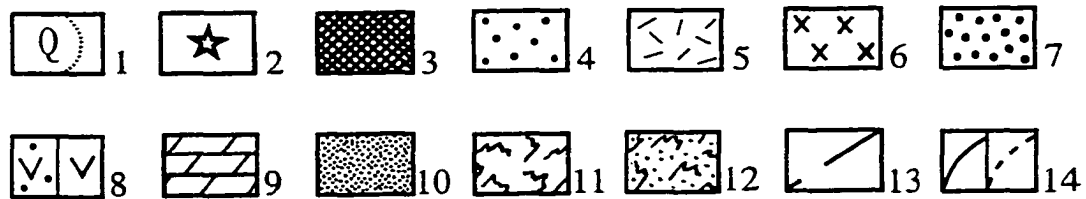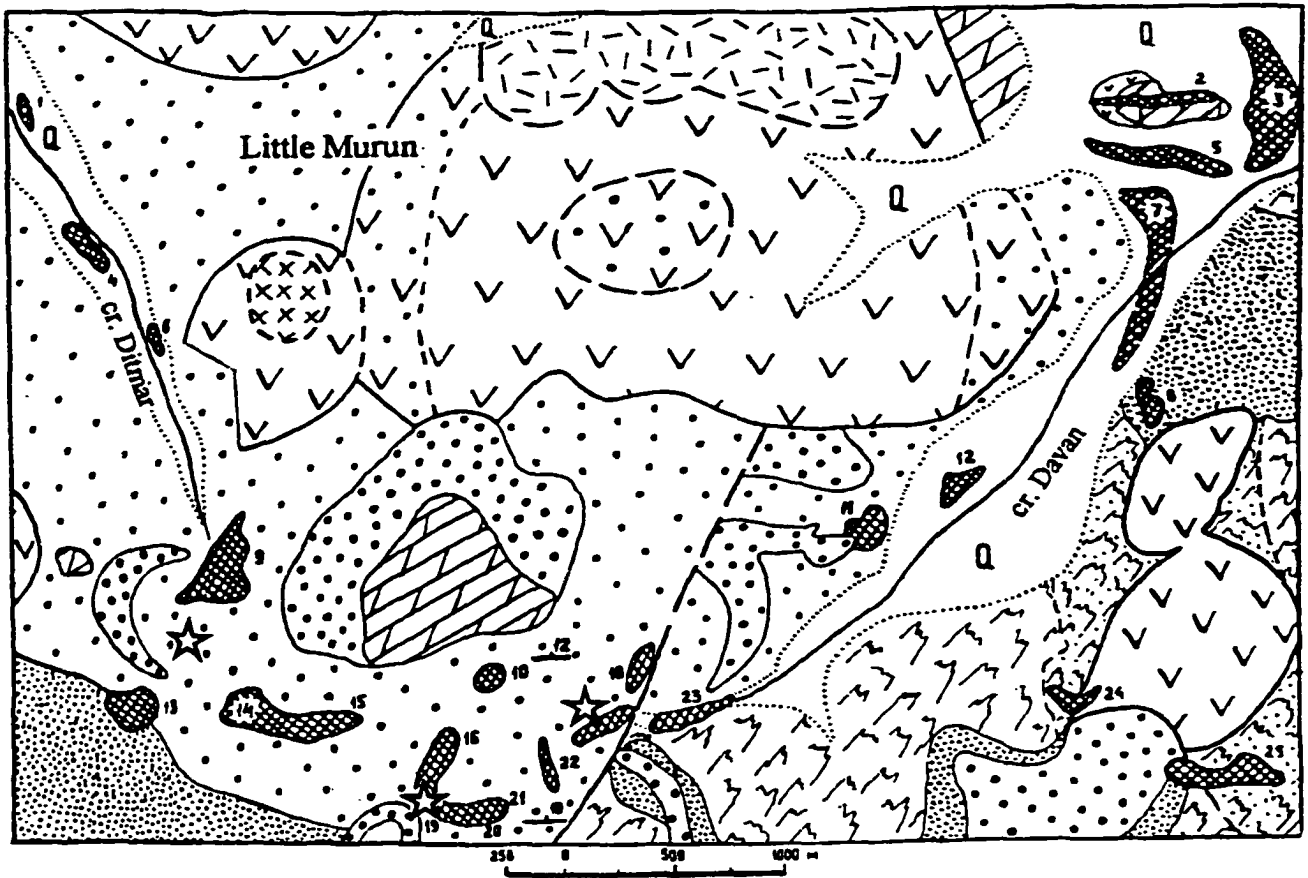
Fig. 2.1.1. Schematic geological map of the "Lilac Rock" deposit (after M.D. Evdokimov & Reguir 1994). 1: Quaternary rocks; 2 – 8: Cretaceous alkaline and carbonatitic rocks (2 – carbonatites and related rocks; 3 – charoitites, 4 – fenites, 5 – nepheline syenites, 6 – pseudoleucite syenites, 7 – porphyritic syenites, 8 – alkaline syenites); 9 – 12: Precambrian metamorphic and sedimentary rocks (9 – sedimentary carbonate rocks, 10 – sandstones and quartzites, 11 – granite gneisses; 12 – fenitized granite gneisses); 13: fault zones; 14: geological contacts (a – observed, b – inferred). Individual charoitite localities are numbered 1-25.

5
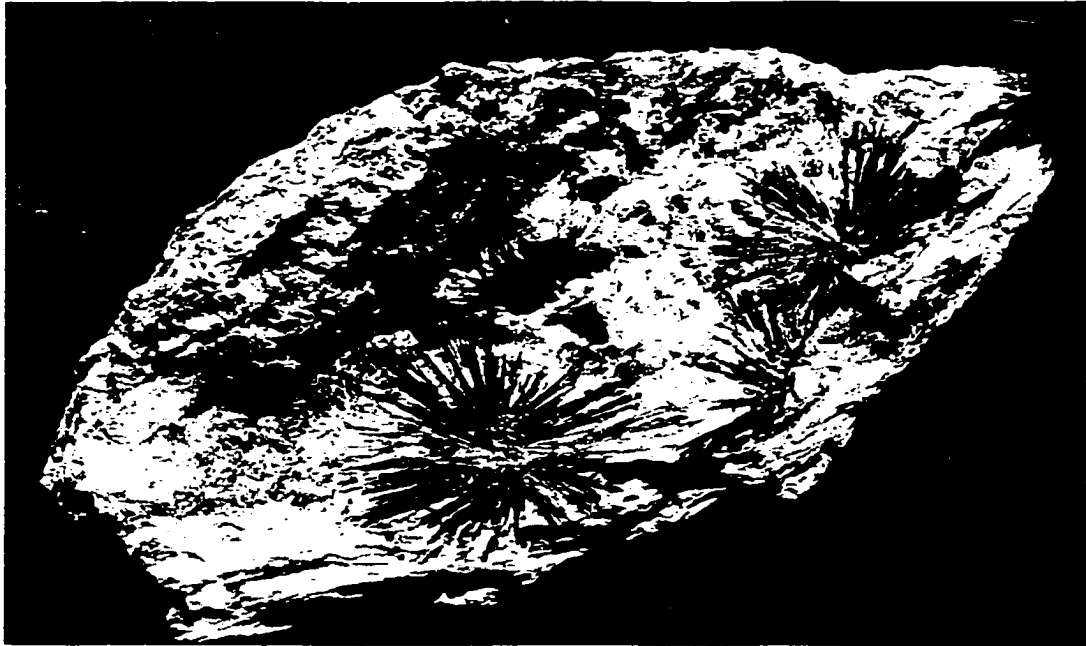
Fig. 2.1.2. Radial aggregates of aegirine (dark green) in schistose charoite (lilac). Yellow — tinaksite. Actual size.
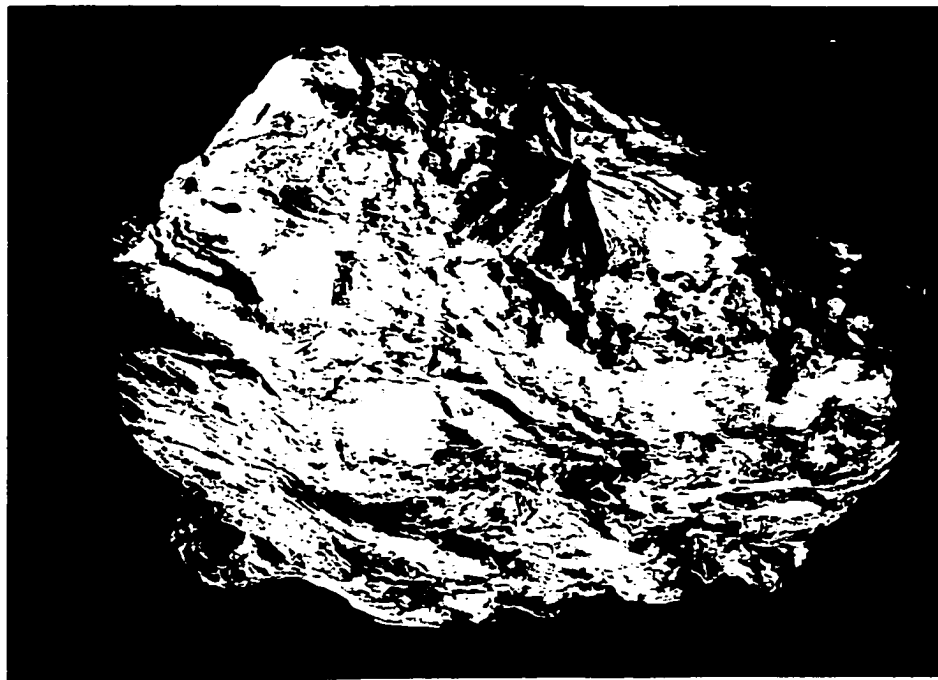


Fig. 2.1.3. Radial aggregate of tinaksite crystals (brownish yellow, top) in schistose charoite. White — quartz. Actual size.

6

Fig. 2.1.4. Frankamenite (grey, greenish grey) in undulatory-fibrous charoite (lilac). White roundish grains are quartz. Actual size.
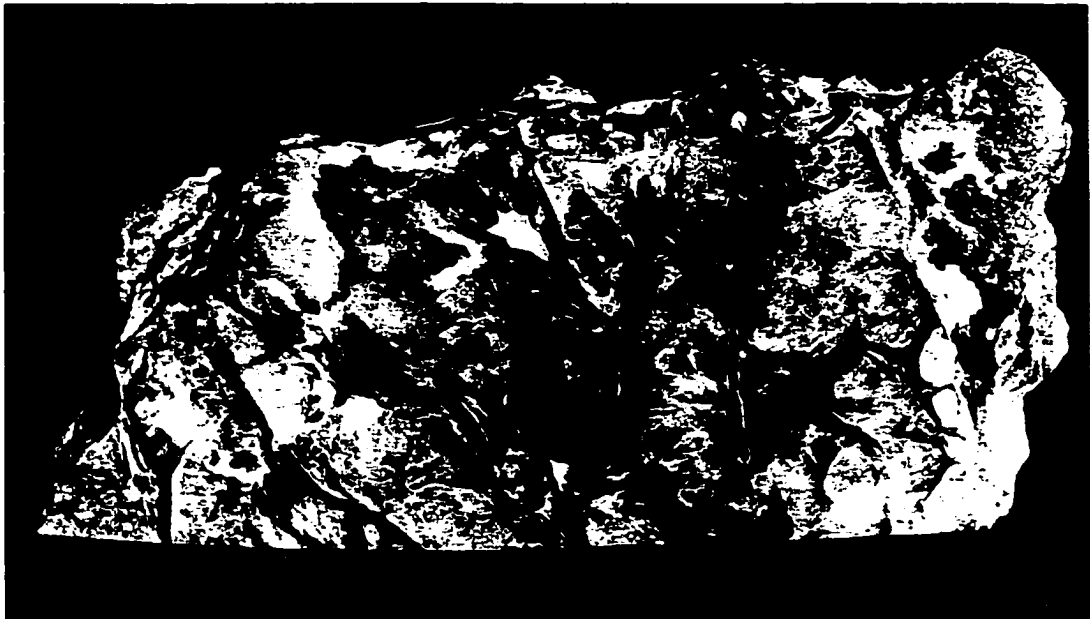


Fig. 2.1.5. Charoite (violet) developed interstitially between the grains of quartz and microcline. Yellow – tinaksite. Note oblique character of charoite with respect to quartz and microcline. Actual size.

7
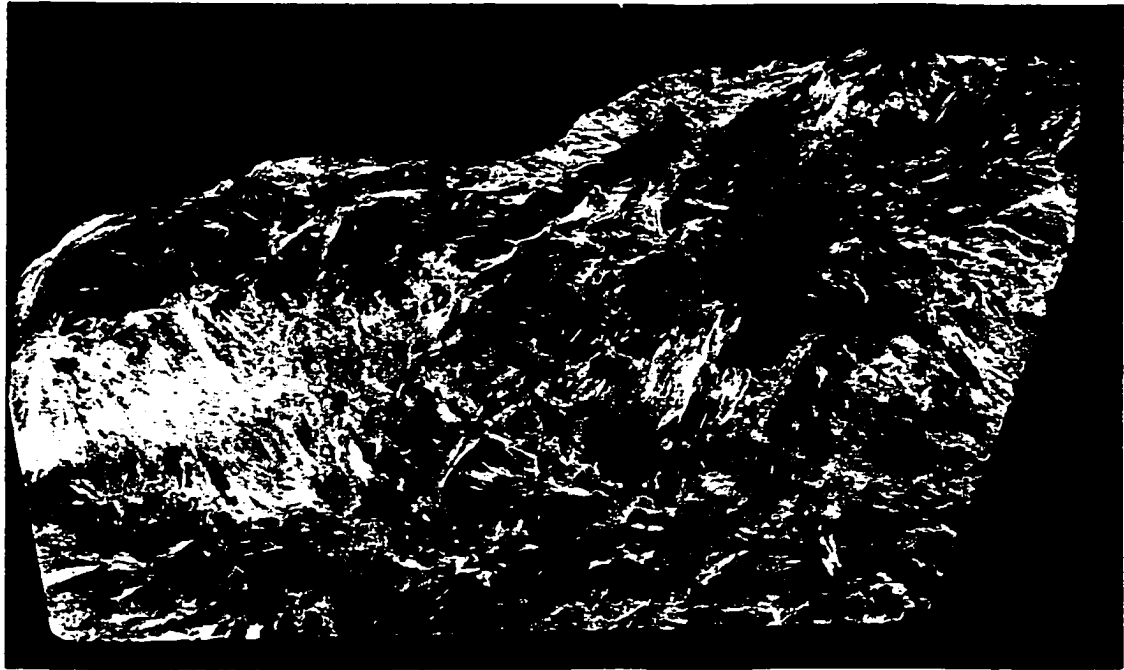
Fig. 2.1.6. Charoite (lilac, violet) in association with pectolite (green), tinaksite (yellow), aegirine (black), quartz and microcline. Actual size.
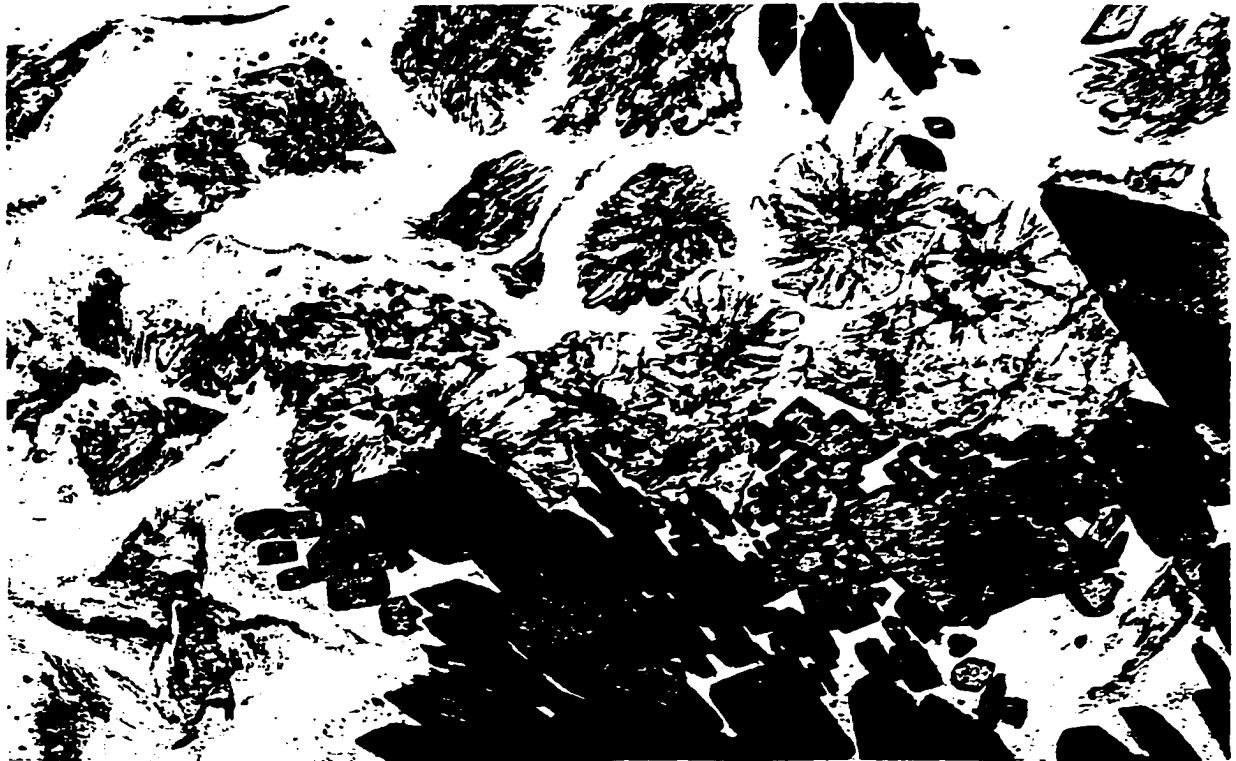


Fig. 2.1.7. Strontian fluorapatite (radial aggregates, grey) and aegirine (brownish green) in charoite (crème). Parallel polars. F.O.V. 3.5 mm

8
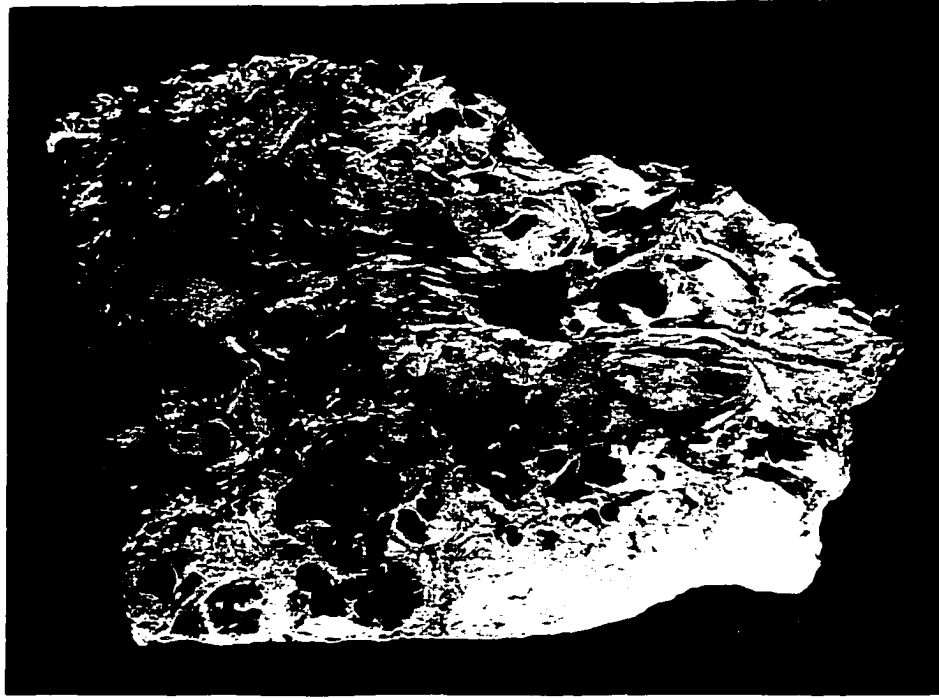
Fig. 2.1.8.  Hydroxyapophyllite (dark brown) in a charoite-quartz-fedorite matrix with aegirine (black). Actual size.
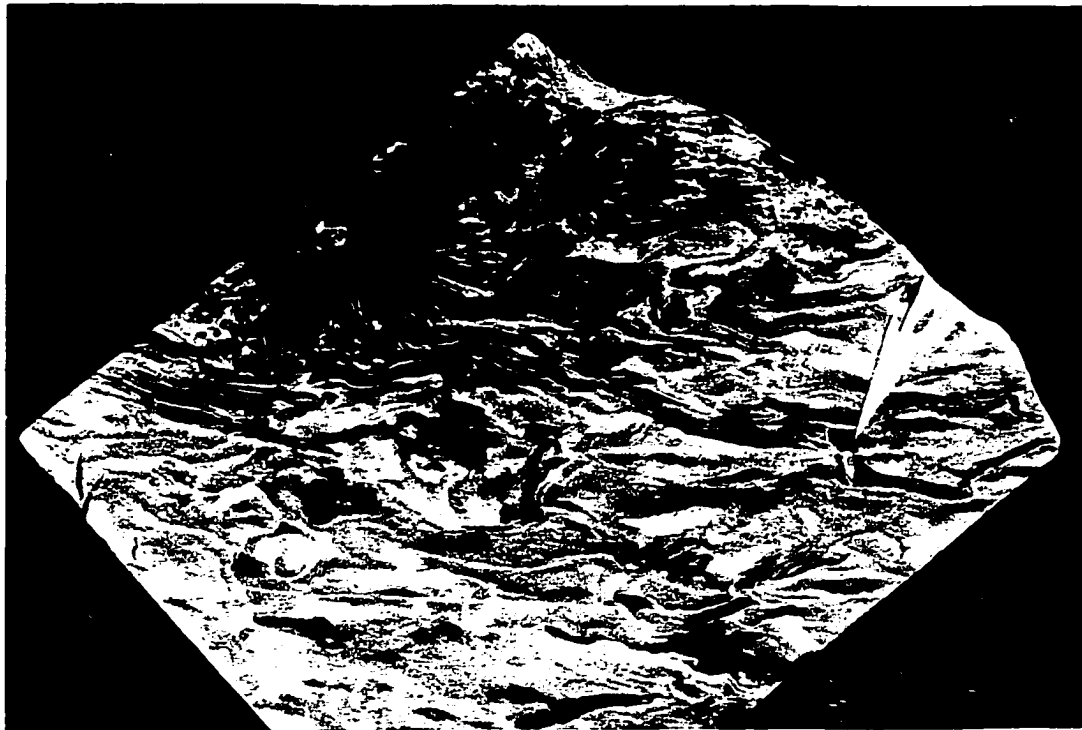


Fig. 2.1.9.  Turkestanite (indicated by an arrow) in schistose charoite. Black – aegirine. Actual size.

9

Table 2.1.1. Characteristic minor and accessory minerals of charoitites.

| MINERAL | FORMULA |
| --- | --- |
| **Silicates:** | |
| MISERITE | $KCa_5 (Si_2O_7)(Si_6O_{15})(OH,F)_2$ |
| FEDORITE | $KNa_4Ca_4(Si,Al)_{16}O_{36}(OH)_4 \cdot 6H_2O$ |
| TOKKOITE | $K_2Ca_4Si_7O_{17}(O,OH,F)_4$ |
| FRANKAMENITE | $Ca_5Na_3K_3(Si_{12}O_{30})F_3(OH) \cdot nH_2O$ |
| PECTOLITE | $NaCa_2Si_3O_8(OH)$ |
| AGRELLITE | $NaCa_2Si_4O_{10}F$ |
| TINAKSITE | $NaK_2Ca_2TiSi_7O_{19}(OH)$ |
| DALYITE | $K_2ZrSi_6O_{15}$ |
| HYDROXYAPOPHYLLITE | $KCa_4Si_8O_{20}(OH,F) \cdot 8H_2O$ |
| TURKESTANITE | $(Ca,Na)_2(K, \ )ThSi_8O_{20} \cdot nH_2O$ |
| **Sulphides:** | |
| MURUNSKITE | $K_2Cu_3FeS_4$ |
| DJERFISHERITE | $K_6(Fe,Cu,Ni)_{25}S_{26}Cl$ |
| IDAITE | $CuFeS_6$ |
| THALCUSITE | $Tl_2Cu_3FeS_4$ |
| **Carbonates:** | |
| PARALSTONITE | $Ba(Ca,Sr)(CO_3)_2$ |
| OLEKMINSKITE | $Sr(Sr,Ca,Ba)(CO_3)_2$ |
| BURBANKITE | $(Na,Ca)_3(Sr,Ba,Ce)_3(CO_3)_5$ |
| ANCYLITE-(CE) | $SrCe(CO_3)_2(OH) \cdot H_2O$ |

: vacant site.

10

Table 2.1.2. Representative compositions of exotic silicates from charoitites.

| Wt.% | 1 | 2 | 3 | 4 | 5 | 6 | 7 | 8 | 9 | 10 | □ |
|---|---|---|---|---|---|---|---|---|---|---|---|
| $SiO_2$ | 56.60 | 57.06 | 56.66 | 55.61 | 57.29 | 55.45 | 65.46 | 65.72 | 55.17 | 54.55 | |
| $TiO_2$ | 9.42 | 8.32 | 10.26 | n.d | 0.05 | n.d | n.d | n.d | n.d | n.d | |
| $Al_2O_3$ | n.d | n.d | n.d | n.d | 0.47 | n.d | n.d | n.d | n.d | n.d | |
| $Fe_2O_3$ | 1.32 | 1.56 | 0.37 | n.d | 0.29 | n.d | 0.18 | n.d | n.d | n.d | |
| $Nb_2O_5$ | 0.50 | 0.29 | n.d | n.d | n.d | n.d | n.d | n.d | n.d | n.d | |
| MnO | 1.03 | 0.80 | 0.42 | 0.30 | 0.07 | 0.53 | 0.13 | 0.33 | 0.63 | 0.65 | |
| MgO | n.d | 0.48 | 0.35 | n.d | n.d | 0.12 | n.d | 0.24 | n.d | n.d | |
| CaO | 14.06 | 14.81 | 14.96 | 22.85 | 21.07 | 21.21 | 17.75 | 17.70 | 34.01 | 33.78 | |
| $Na_2O$ | 3.89 | 3.50 | 4.08 | 6.30 | 7.86 | 6.96 | 7.16 | 7.06 | 9.48 | 9.26 | |
| $K_2O$ | 12.33 | 12.42 | 12.11 | 9.96 | 9.78 | 10.55 | 4.61 | 4.93 | n.d | n.d | |
| F | n.d | n.d | n.d | n.d | n.d | 4.10 | n.d | 2.20 | n.d | n.d | |
| $-O=F_2$ | - | - | - | - | - | 1.72 | - | 0.92 | - | - | |
| $H_2O$ | n.d | n.d | n.d | n.d | n.d | 2.00 | n.d | 2.24 | n.d | n.d | |
| Total | 99.15 | 99.24 | 99.22 | 95.02 | 96.88 | 99.32* | 95.27 | 99.50 | 99.29 | 98.24 | |

| Wt.% | 11 | 12 | 13 | 14 | 15 | 16 | 17 | 18 | 19 | □ |
|---|---|---|---|---|---|---|---|---|---|---|
| $SiO_2$ | 50.90 | 52.60 | 55.07 | 55.65 | 61.83 | 62.25 | 63.44 | 52.33 | 51.89 | |
| $TiO_2$ | 0.36 | 0.64 | 0.57 | 1.42 | 0.69 | 1.56 | 2.92 | n.d | n.d | |
| $Al_2O_3$ | n.d | n.d | n.d | n.d | n.d | n.d | n.d | 0.38 | n.d | |
| $Fe_2O_3$ | n.d | 0.80 | 1.40 | n.d | n.d | n.d | n.d | n.d | n.d | |
| FeO | 0.82 | n.d | n.d | 1.58 | n.d | n.d | 0.01 | n.d | n.d | |
| $ZrO_2$ | n.d | n.d | n.d | n.d | 20.60 | 19.13 | 16.68 | n.d | n.d | |
| $Nb_2O_5$ | n.d | n.d | n.d | n.d | n.d | 0.60 | n.d | n.d | n.d | |
| MnO | 0.17 | 0.21 | 0.80 | 0.70 | n.d | n.d | n.d | n.d | n.d | |
| MgO | n.d | n.d | 1.71 | 0.30 | n.d | n.d | n.d | n.d | n.d | |
| CaO | 33.80 | 34.06 | 24.24 | 25.10 | n.d | n.d | n.d | 23.54 | 24.26 | |
| $Na_2O$ | n.d | 0.10 | 0.33 | 0.60 | n.d | n.d | n.d | n.d | n.d | |
| $K_2O$ | 7.93 | 8.38 | 11.32 | 11.33 | 15.15 | 15.65 | 16.75 | 5.54 | 5.25 | |
| F | n.d | 2.60 | n.d | 1.50 | n.d | n.d | n.d | n.d | n.d | |
| $-O=F_2$ | - | 1.09 | - | 0.63 | - | - | - | - | - | |
| $H_2O$ | n.d | 1.01 | n.d | 2.40 | n.d | n.d | n.d | n.d | n.d | |
| Total | 96.99** | 100.75[#] | 95.44 | 99.95 | 98.27 | 99.19 | 99.80 | 81.79 | 81.40 | |

n.d = not detected. * Total also includes FeO 0.12 wt.%; ** Total also includes (wt.%): BaO 0.47, $La_2O_3$ 0.94 and $Ce_2O_3$ 1.51; [#] Total also includes (wt.%): $REE_2O_3$ 0.62 and $CO_2$ 0.82. All analyses obtained in this work (unless references are given). Analyses 1-3: *tinaksite* (1 − Mu-13; 2 − Mu-10; 3 − Mu-112); 4-6: *frankamenite* (4 − Mu-13; 5 − Evdokimov & Reguir 1994; 6 − Lasebnik & Lasebnik 1981); 7-8: *fedorite* (7 − Mu-11; 8 − Lasebnik & Lasebnik 1981); 9-10: *pectolite* (9 − Mu-117; 10 − Mu-11); 11-12: *miserite* (11 − Mu-2; 12 − Lasebnik & Lasebnik 1981); 13-14: *tokkoite* (13 − Mu-2; 14 − Konev et al. 1996); 15-17: *dalyite* (15 − Mu-11; 16 − Mu-119/7; 17 - Konev et al. 1996); 18-19: *hydroxyapophillite* (Mu-13).

11

## Table 2.1.3. Representative compositions of clinopyroxene, potassium feldspar and titanite from charoitites (this work).

| Wt. % | 1 | 2 | 3 | 4 | 5 | 6 | 7 | 8 | 9 |
|---|---|---|---|---|---|---|---|---|---|
| $SiO_2$ | 51.89 | 53.06 | 52.27 | 53.65 | 64.35 | 64.20 | 64.28 | 30.97 | 30.61 |
| $TiO_2$ | 1.07 | 1.09 | 0.92 | 2.31 | n.d | n.d | n.d | 39.23 | 39.18 |
| $Al_2O_3$ | n.d | n.d | n.d | n.d | 17.46 | 16.69 | 15.67 | n.d | n.d |
| $Fe_2O_3$ | 20.91* | 20.40* | 24.36* | 23.72* | 0.95 | 2.66 | 3.90 | 0.57 | 0.64 |
| FeO | 5.88* | n.d | n.d | n.d | n.d | n.d | n.d | n.d | n.d |
| $V_2O_3$ | 0.59 | 1.59 | n.d | n.d | n.d | n.d | n.d | n.d | n.d |
| $Nb_2O_5$ | n.d | n.d | n.d | n.d | n.d | n.d | n.d | 0.29 | 0.41 |
| MnO | 0.40 | n.d | n.d | n.d | n.d | n.d | n.d | n.d | n.d |
| MgO | 2.68 | 5.54 | 3.50 | 3.40 | n.d | n.d | n.d | n.d | n.d |
| CaO | 9.09 | 8.86 | 4.86 | 3.62 | n.d | n.d | n.d | 27.87 | 27.95 |
| $Na_2O$ | 8.69 | 9.64 | 11.41 | 12.57 | 0.52 | n.d | 0.24 | 0.43 | 0.49 |
| $K_2O$ | n.d | n.d | n.d | n.d | 15.98 | 16.34 | 16.42 | n.d | n.d |
| Total | 101.20 | 100.18 | 97.32 | 99.27 | 99.26 | 98.89 | 100.50 | 99.36 | 99.28 |

### Formulae calculated on the basis of:

| | 6 atoms of oxygen | | | | 8 atoms of oxygen | | | $\Sigma$cations=3 | |
|---|---|---|---|---|---|---|---|---|---|
| Si | 1.981 | 1.979 | 2.069 | 2.063 | 3.005 | 2.998 | 3.001 | 1.013 | 1.002 |
| Ti | 0.031 | 0.031 | 0.027 | 0.067 | - | - | - | 0.965 | 0.965 |
| Al | - | - | - | - | 0.961 | 0.919 | 0.862 | - | - |
| $Fe^{3+}$ | 0.601 | 0.600 | 0.637 | 0.619 | 0.033 | 0.093 | 0.137 | 0.014 | 0.016 |
| $Fe^{2+}$ | 0.188 | - | - | - | - | - | - | - | - |
| V | 0.018 | 0.048 | - | - | - | - | - | - | - |
| Nb | - | - | - | - | - | - | - | 0.004 | 0.006 |
| Mn | 0.013 | - | - | - | - | - | - | - | - |
| Mg | 0.153 | 0.308 | 0.207 | 0.195 | - | - | - | - | - |
| Ca | 0.372 | 0.354 | 0.206 | 0.149 | - | - | - | 0.977 | 0.980 |
| Na | 0.643 | 0.697 | 0.876 | 0.937 | 0.047 | - | 0.022 | 0.027 | 0.031 |
| K | - | - | - | - | 0.952 | 0.973 | 0.978 | - | - |

n.d = not detected; * $Fe^{2+}/Fe^{3+}$ ratio calculated from stoichiometry. Analyses 1-4: clinopyroxene (*Mu-13*: 1-2 − core, 3-4 − rim); 5-7: *potassium feldspar* (5 − *Mu-11*; 6 − *Mu-13*; 7 − *Mu-119/7*); 8-9: titanite (*Mu-117*).

12

Table 2.1.4. Representative compositions of strontian fluorapatite from charoitites (this work).

| Wt. % | 1 low-AZ | 2 high-AZ | 3 low-AZ | 4 high-AZ | 5 low-AZ | 6 high-AZ | 7 |
|---|---|---|---|---|---|---|---|
| $P_2O_5$ | 43.22 | 41.91 | 40.91 | 40.70 | 41.89 | 40.99 | 40.19 |
| CaO | 54.56 | 52.93 | 50.69 | 50.08 | 51.67 | 47.07 | 44.90 |
| SrO | 2.66 | 4.24 | 6.03 | 8.33 | 6.30 | 11.76 | 14.23 |
| $Ce_2O_3$ | n.d | n.d | n.d | n.d | n.d | n.d | 0.64 |
| F | 2.02 | 2.75 | 1.95 | 2.42 | 2.37 | 2.71 | 1.61 |
| $-O=F_2$ | 0.85 | 1.16 | 0.82 | 1.02 | 1.00 | 1.14 | 0.68 |
| | | | | | | | |
| Total | 101.61 | 100.67 | 98.76 | 99.11 | 101.23 | 101.39 | 100.89 |

Formulae calculated on the basis of 8 cations

| | 1 | 2 | 3 | 4 | 5 | 6 | 7 |
|---|---|---|---|---|---|---|---|
| P | 3.030 | 2.999 | 2.997 | 2.966 | 3.003 | 3.019 | 3.004 |
| | | | | | | | |
| Ca | 4.842 | 4.793 | 4.700 | 4.618 | 4.688 | 4.388 | 4.247 |
| Sr | 0.128 | 0.208 | 0.303 | 0.416 | 0.309 | 0.593 | 0.728 |
| Ce | - | - | - | - | - | - | 0.021 |
| $\Sigma$ | 4.970 | 5.001 | 5.003 | 5.034 | 4.997 | 4.981 | 4.996 |
| | | | | | | | |
| F | 0.529 | 0.735 | 0.534 | 0.659 | 0.635 | 0.746 | 0.449 |

n.d = not detected. $AZ$ - average atomic number. Analyses 1-2 – *Mu-139/14*; 3-4 – *Mu-13*; 5-7 – *Mu-121*.

Table 2.1.5. Representative compositions of burbankite from charoitites (this work).

| Wt.% | 1 | 2 | 3 | 4 | 5 | 6 | 7 | 8 | 9 |
|---|---|---|---|---|---|---|---|---|---|
| Na$_2$O | 8.07 | 8.06 | 7.09 | 8.63 | 8.79 | 8.10 | 7.30 | 8.83 | 7.18 |
| CaO | 10.36 | 10.12 | 11.85 | 11.03 | 10.91 | 11.35 | 11.44 | 11.05 | 12.01 |
| SrO | 42.86 | 44.97 | 35.93 | 38.71 | 39.24 | 34.35 | 34.39 | 42.82 | 43.56 |
| BaO | 1.54 | 1.27 | 4.40 | 2.68 | 3.16 | 10.97 | 11.44 | 1.52 | 1.83 |
| La$_2$O$_3$ | 1.80 | 0.35 | 1.97 | 1.94 | 2.26 | n.d | n.d | 0.41 | n.d |
| Ce$_2$O$_3$ | 1.78 | 0.56 | 2.87 | 2.83 | 2.82 | n.d | n.d | 1.01 | n.d |
| CO$_2$* | 33.95 | 33.50 | 33.03 | 33.92 | 34.43 | 32.40 | 32.05 | 34.14 | 33.55 |
| | | | | | | | | | |
| Total* | 100.36 | 98.83 | 97.70$^{#}$ | 99.74 | 101.61 | 97.17 | 96.62 | 99.78 | 98.13 |

Formulae calculated basing on 15 atoms of oxygen:

| | 1 | 2 | 3 | 4 | 5 | 6 | 7 | 8 | 9 |
|---|---|---|---|---|---|---|---|---|---|
| Na | 1.688 | 1.709 | 1.524 | 1.807 | 1.813 | 1.775 | 1.617 | 1.837 | 1.520 |
| Ca | 1.085 | 1.126 | 1.408 | 1.002 | 0.994 | 1.112 | 1.192 | 1.054 | 1.240 |
| $\sum A$ cations | 2.773 | 2.835 | 2.652 | 2.809 | 2.807 | 2.887 | 2.809 | 2.891 | 2.760 |
| | | | | | | | | | |
| Ca | 0.112 | 0.059 | 0.279 | 0.274 | 0.249 | 0.262 | 0.209 | 0.216 | 0.165 |
| Sr | 2.681 | 2.851 | 2.310 | 2.424 | 2.421 | 2.252 | 2.279 | 2.664 | 2.757 |
| Ba | 0.065 | 0.054 | 0.191 | 0.113 | 0.131 | 0.486 | 0.512 | 0.064 | 0.078 |
| La | 0.072 | 0.014 | 0.081 | 0.077 | 0.089 | - | - | 0.016 | - |
| Ce | 0.070 | 0.022 | 0.116 | 0.112 | 0.110 | - | - | 0.040 | - |
| $\sum B$ cations | 3.000 | 3.000 | 3.000$^{##}$ | 3.000 | 3.000 | 3.000 | 3.000 | 3.000 | 3.000 |
| | | | | | | | | | |
| $\sum (A+B)$ cat. | 5.773 | 5.835 | 5.652 | 5.809 | 5.807 | 5.887 | 5.809 | 5.891 | 5.760 |
| | | | | | | | | | |
| CO$_3$ | 5.000 | 5.000 | 5.000 | 5.000 | 5.000 | 5.000 | 5.000 | 5.000 | 5.000 |

n.d = not detected ; * calculated on the basis of stoichiometry. $^{#}$ Total also includes 0.14 wt.% Pr$_2$O$_3$ and 0.42 wt.% Nd$_2$O$_3$; $^{##}$ sum also includes 0.006 apfu Pr$^{3+}$ and 0.017 apfu Nd$^{3+}$. Analyses 1-2: *Mu-11*; 3 − *Mu-13*; 4-5: *Mu-121*; 6-7: *Mu-194/33*; 8-9: *Mu-139/14*.

14
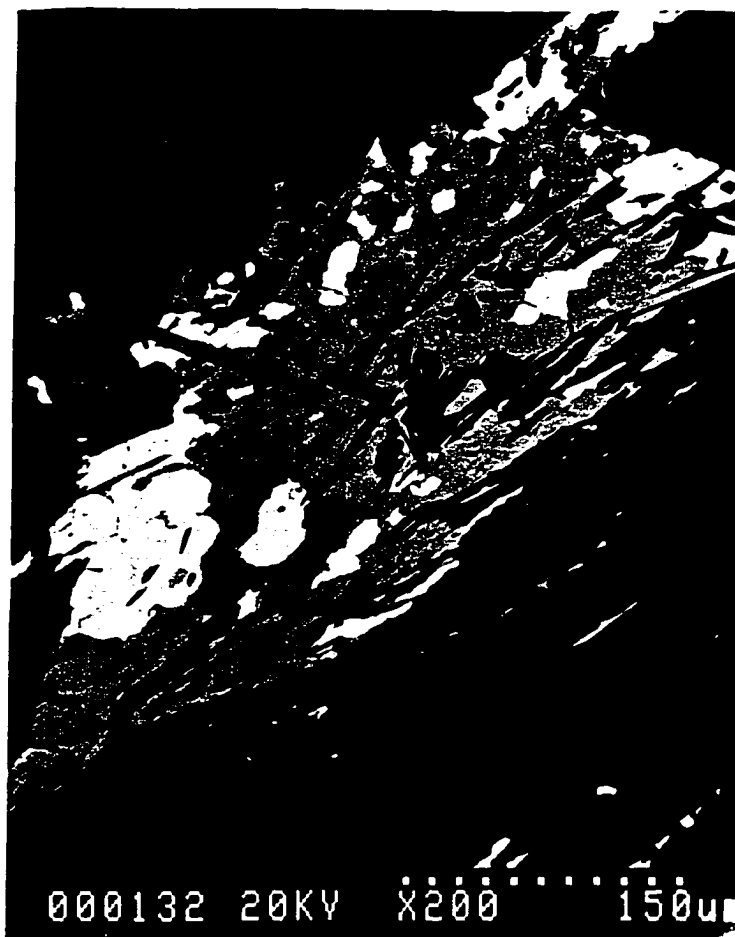
Fig. 2.1.10.  Burbankite (grey) and Sr-rich barytocalcite (white)
interlayered with charoite (black). BSE image.

## 2.2.  Background information on charoite

### 2.2.1  *Name, morphology, physical and optical properties*

Charoite was discovered in 1949 and confirmed as a new mineral species in 1977 (Rogova *et al.* 1978). According to the discoverers of the mineral, the name originates from the Chara River, situated close to the southern border of the Murun complex (Rogova *et al.* 1978). An "unofficial" hypothesis suggests the Russian word "charovat' " (to charm) as a possible origin for the name (Evdokimov 1995).

Eight texturally different varieties of charoite have been previously distinguished (Borisov 1985; Evdokimov 1995). According to these authors, this textural diversity results from different crystallisation conditions as well as tectonic settings in which charoite was

15

Fig. 2.2.1.1. Massive charoite (lilac) with tinaksite (yellow) cut by a veinlet of aegirine. Actual size.



Fig. 2.2.1.2. Mosaic-fibrous charoite (violet) bordered by a quartz-aegirine aggregate. Actual size.

16

formed. The earliest variety to crystallise is massive, very fine-grained charoite (Fig. 2.2.1.1). It was followed by parallel fibrous, undulatory-fibrous (Fig. 2.1.4), felted, radial aggregates, mosaic-fibrous (Fig. 2.2.1.2) and schistose varieties (Figs. 2.1.2, 2.1.3 and 2.1.9). In addition to the textural diversity, charoite shows a broad spectrum of colours from lilac to brown and grey, often within the same hand-specimen. As has been previously indicated by several studies (Nikol'skaya et al. 1976; Yarovoi & Rokshaev 1992; Dutrow & Henry 1996), $Mn^{2+}$ and $Mn^{3+}$ ions are responsible for the colour and cathodoluminescence of charoite. Study of the light dispersion characteristics of charoite (Bukhtiyarova et al. 1996) showed substantial differences in terms of transparency and dispersion indexes between different varieties of the mineral. These authors suggested that strong anisotropism in the light-dispersion properties is responsible for silky iridescence of charoite, whereas the pearly iridescence occurs as a result of isotropic and smooth light dispersion.

Macroscopically, charoite is characterised by vitreous or silky lustre. Measured density of the mineral is 2.54 $g/cm^3$, hardness corresponds to 412±6 $kg/mm^2$ (Mohs 5). In thin section, charoite is colourless. Thick fragments of the mineral can be slightly pleochroic from colourless to pink. Optically, the mineral is biaxial positive, with 2V in the range of 28-30° and the following refraction indices: $\alpha$ = 1.550(2); $\beta$ = 1.553(2); $\gamma$ = 1.559(2) (Rogova et al. 1978).


### 2.2.2. Crystal chemistry of charoite

Since 1976, a number of studies on the composition of charoite have been published. At least, nine different versions of the empirical formula have been proposed (Table 2.2.2.1). The analytical data available show noticeable variations in the proportions of the major elements, i.e. Na, K, Ca, Si and $H_2O$, as well as the minor elements Sr, Ba and Mn (Table 2.2.2.2). In some cases, minute amounts of Fe, Al, Mg, Ti, Zr and Th are also present in charoite.

17

Table 2.2.2.1. Diverse formulae of charoite.

| Formula | Reference |
|---|---|
| $(K_{2.4}Na_{0.6})_3(Ca, Ba, Sr, Mn)_5Si_{12}O_{30}(OH, F)_2 \cdot 3H_2O$ | this work |
| $(K_{3.69}Na_{1.46})(Ca_{6.87}Ba_{0.33}Sr_{0.08}Mn_{0.07})(Si_{18.2}O_{46})(OH_{0.6}F_{0.4}) \cdot H_2O$ | Dutrow et al. (1994) |
| $K_5 Ca_8 (Si_6O_{15})_2(Si_2O_7)(Si_4O_9)(OH) \cdot 3H_2O$ | Vasil'ev (1990) |
| $(K,Na)_5 (Ca,Ba,Sr)_8(Si_6O_{15})_2(Si_2O_7)(Si_4O_9)(OH,F) \cdot nH_2O$ | Nikishova et al. (1985) |
| $(Ca_{1.6}Na_{0.4})_2[K_{0.8} (Sr, Ba)_{0.2}]_{1.0}(Si_{3.9}Al_{0.1})(O_{9.7}OH_{0.3})_{10} \cdot nH_2O$ | Borneman-Starinkevich (1982) |
| $(K,Na)_{3-4}(Ca,Ba,Sr)_5Si_{12}O_{30}(OH,F)_{2-1} \cdot nH_2O$ | Chukhrov (1981) |
| $(Ca,Na)_4(K,Sr,Ba)_2Si_9O_{22}(OH,F)_2 \cdot H_2O$ | Kraeff et al. (1980) |
| $(Ca_{1.57}Na_{0.51}K_{0.93}Ba_{0.07})_{3.11}Si_4O_{10}(OH_{0.58}F_{0.2})_{0.78} \cdot 0.72H_2O$ | Rogova et al. (1978) |
| $(K,Na)_3(Ca,Ba,Mn)_4Si_{10}O_{25}(OH,F) \cdot nH_2O$ | Lasebnik et al. (1977) |
| $(Ca,K,Na) Si_4O_{10}(OH,F) \cdot H_2O$ | Nikol'skaya et al. (1976) |

$H_2O$ is one of the most variable components of the mineral. In most studies, the water content was determined by thermogravimetric analysis. Rogova et al. (1978) and Kraeff (1980) observed continuous loss of hygroscopic $H_2O$ (ca. 2.4-3.2 wt.%) between 30°C and 300°C, with a maximum at about 290-300°C. According to Kraeff (1980), the remainder of the $H_2O$ (ca. 1.5 wt.%) is released from charoite between 300°C and 490°C (maximum at about 430°C). Rogova et al. (1978) reported a loss of ca. 1.3 wt.% $H_2O$ in the temperature range 300-600°C (maximum at 330°C), followed by gradual release of ca. 2.0 wt.% $H_2O$ from 350°C to 1000°C, with minor maxima at 440°C, 760°C and 970°C. Charoite is prone to deuteric/secondary alteration and commonly shows evidence of dehydration, cation leaching, and release of Mn plus Fe in the form of hydroxides.

2.2.3. Structural studies

The crystal structure of charoite has not been thus far determined because none of the textural types yields crystals large enough for single-crystal X-ray studies. Even thin optically uniform fibers appear to be multi-domain intergrowths when examined with a CCD X-ray

18

Table 2.2.2.2. Representative compositions of charoite from the previously published data.

| Wt.% | 1 | 2 | 3 | 4 | 5 | 6 | 7 | 8 |
|---|---|---|---|---|---|---|---|---|
| $SiO_2$ | 56.30 | 56.88 | 58.50 | 57.49 | 57.72 | 57.70 | 58.53 | 58.29 |
| $Al_2O_3$ | 1.85 | n.d | 0.07 | n.d | n.d | n.d | n.d | n.d |
| $Fe_2O_3$ | n.d | n.d | n.d | n.d | n.d | 0.80 | 0.16 | 0.17 |
| FeO | n.d | n.d | 0.01* | n.d | n.d | n.d | n.d | 0.07 |
| MnO | n.d | n.d | 0.07 | n.d | n.d | 0.10 | 0.20 | 0.10 |
| MgO | n.d | n.d | n.d | n.d | n.d | n.d | n.d | 0.33 |
| CaO | 20.44 | 20.95 | 20.50 | 22.00 | 21.30 | 23.24 | 20.54 | 22.98 |
| SrO | 0.90 | 0.90 | 0.50 | 1.04 | 0.56 | 0.80 | n.d | n.d |
| BaO | 3.30 | 2.52 | 2.90 | 0.95 | 2.47 | 2.03 | 2.40 | 1.77 |
| $Na_2O$ | 2.45 | 3.77 | 1.80 | 2.28 | 2.68 | 2.38 | 2.60 | 2.88 |
| $K_2O$ | 10.50 | 10.36 | 8.90 | 8.65 | 9.03 | 7.87 | 7.97 | 8.37 |
| $H_2O^+$ | 3.80 | 4.40 | 4.70 | 5.12 | 4.83 | 4.20 | 7.07 | 4.38 |
| F | n.a | 0.92 | 0.70 | 0.42 | 0.54 | 0.25 | 0.66 | 0.38 |
| $-O=F_2$ | - | 0.39 | 0.30 | 0.18 | 0.23 | 0.11 | 0.28 | 0.16 |
| Total | 99.54 | 100.43 | 98.95 | 97.77 | 98.90 | 99.26 | 99.93 | 99.63** |

n.d = not detected; n.a = not analysed. Analyses 1-2: Rogova *et al.* 1978; 3: Kraeff *et al.* 1980; 4-5: Nikishova *et al.* 1985 (4 – representative analisis; 5 – average of 7 analyses); 7-9: Konev *et al.* 1996 (4 – massive charoite, 5 – radial agregates of charoite, 6 – undulatory-fibrous charoite). * Total Fe is given as FeO; ** Total also includes 0.07 wt.% $TiO_2$.

detector (R.H.Mitchell and P.Burns, personal communication). IR spectra of charoite were found to be reminiscent of layer silicates of apophyllite type (Nikol'skaya *et al.* 1976). A number of X-ray powder diffraction studies conducted on charoite (Rogova *et al.* 1978, Nikishova & Lazebnik 1982, Nikishova *et al.* 1985) showed that most of the XRD patterns measured could be indexed on a monoclinic cell. However, there is a substantial disagreement among the researchers with regard to the unit-cell parameter values (Table 2.2.3.1).

Taking into account compositional similarities between charoite and monoclinic canasite [$K_3Na_3Ca_5(Si_{12}O_{30})(OH,F)_4$], Rogova *et al.* (1978) suggested that these two minerals had some structural affinities. The crystal structure of canasite was determined by Chiragov *et al.* (1969, 1972) and Rozhdestvenskaya *et al.* (1988). It consists of $(Si_{12}O_{30})_\infty$ "tubes" (tunnels) comprising four wollastonite-like "dreier" chains aligned parallel to [010]. The "tubes" are connected by octahedrally-coordinated Na and Ca comprising zigzag walls subparallel to (001). K atoms are accommodated within the "tubes", and are coordinated by nine or twelve oxygens (marginal and central sites, respectively) (Fig. 2.2.3.1).

Nikishova *et al.* (1985) proposed that the textural features, optical properties, Debaye patterns and unit-cell parameters of charoite are more consistent with those of miserite [$KCa_5 (Si_2O_7)(Si_6O_{15})(OH,F)_2$], than canasite. These authors suggest that in spite of the significant compositional differences between these two minerals, charoite and miserite are likely to exhibit similar structural features. The crystal structure of triclinic miserite was described by Scott (1976) as quadruple ($Si_{12}O_{30}$) "tubes" parallel to [001] formed by three-membered sub-chains of silica tetrahedra. The "tubes" are connected along [010] by double walls of $CaO_6$ polyhedra. Independent $Si_2O_7$ groups are "sandwiched" between the two units of the double wall. In common with canasite, K atoms are accommodated within the ($Si_{12}O_{30}$) "tubes" (Fig. 2.2.3.2). The structure of miserite has three independent vacant sites. One is octahedrally-coordinated, and can be occupied by Y, *REE*, *etc.* The other two sites are confined to ($Si_{12}O_{30}$) tunnels and can incorporate large cations, as well as zeolitic $H_2O$ and F (Fig. 2.2.3.2).

20

Table 2.2.3.1. Comparison of the unit-cell parameters of charoite, canasite and miserite.

| $a$ (Å) | $b$ (Å) | $c$ (Å) | $\alpha$, ° | $\beta$, ° | $\gamma$, ° | $V$(Å)$^3$ | REFERENCES |
|---|---|---|---|---|---|---|---|
| **CHAROITE:** | | | | | | | |
| *mosaic-fibrous* | | | | | | | |
| 19.86 | 32.13 | 7.95 | 90 | 97.24 | 90 | 5038.13 | |
| 19.96 | 32.17 | 7.26 | 93.51 | 99.45 | 89.50 | 4589.85 | *THIS WORK* |
| *schistose* | | | | | | | |
| 32.13 | 19.64 | 8.51 | 90 | 95.23 | 90 | 5346.07 | |
| | | | | | | | |
| 31.82 | 7.13 | 22.10 | 90 | 94.25 | 90 | 5000.19 | Rogova *et al.* (1978)* |
| 19.60 | 32.02 | 7.25 | 90 | 94.33 | 90 | 4537.06 | Nikishova & Lasebnik (1982)* |
| 10.70 | 32.00 | 7.25 | 90 | 113.0 | 90 | 2285.06 | Nikishova *et al.* (1985)* |
| 19.61 | 32.12 | 7.20 | 90 | 93.76 | 90 | 4525.32 | ASTM 42-1402 (Vasil'ev, 1990, private communication.)* |
| **CANASITE:** | | | | | | | |
| 18.84 | 7.24 | 12.64 | 90 | 111.76 | 90 | 1601.26 | Rozhdestvenskaya (1988) |
| 18.87 | 7.24 | 12.60 | 90 | 112.00 | 90 | 1596.05 | Dorfman *et al.* (1959) |
| **MISERITE:** | | | | | | | |
| 10.10 | 16.01 | 7.38 | 96.42 | 111.15 | 76.57 | 1081.85 | Scott (1976) |

* Textural type of studied charoite is not given by the authors.

21
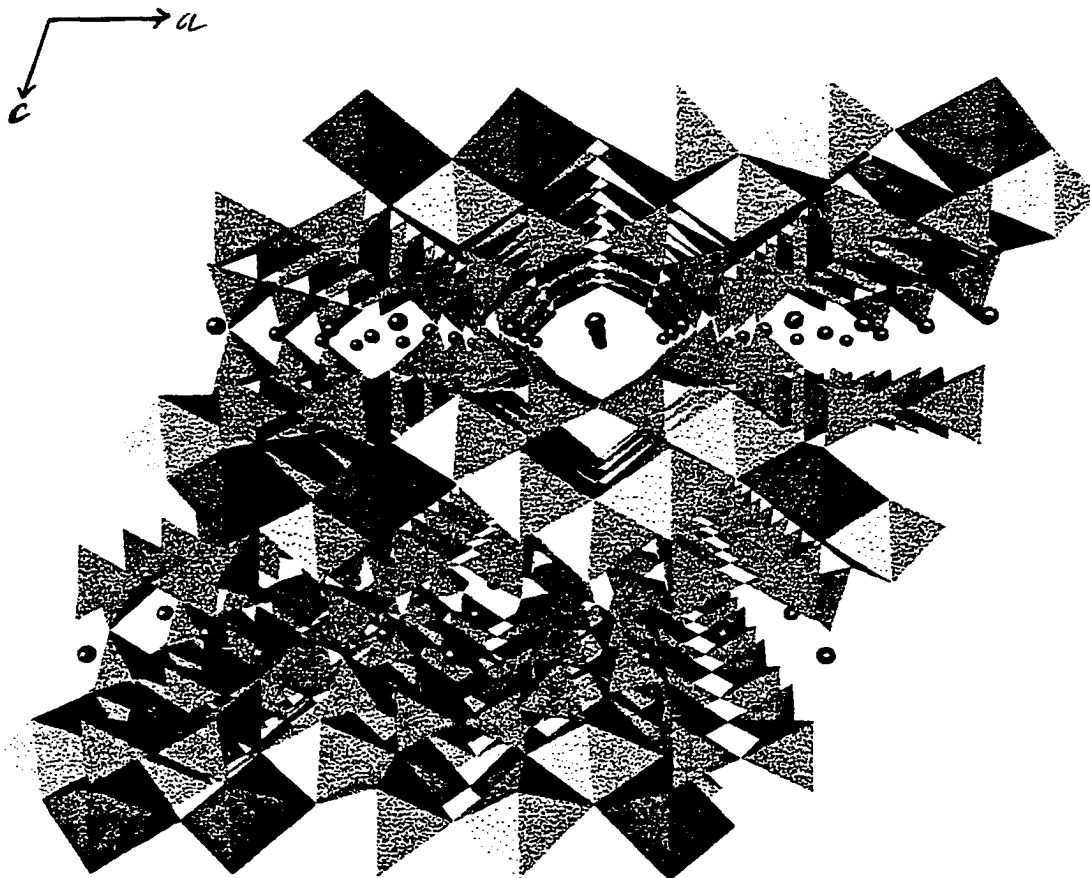
Fig. 2.2.3.1. Polyhedral representation of the crystal structure of canasite viewed
approximately down [010] (Rozhdestvenskaya *et al.*, 1988). The
$(Si_{12}O_{30})_\infty$ "tubes" (green) accommodate K atoms (purple), and are
"interlayered" with zigzag walls of Na- and Ca-centered octahedra (red
and yellow, respectively).

22
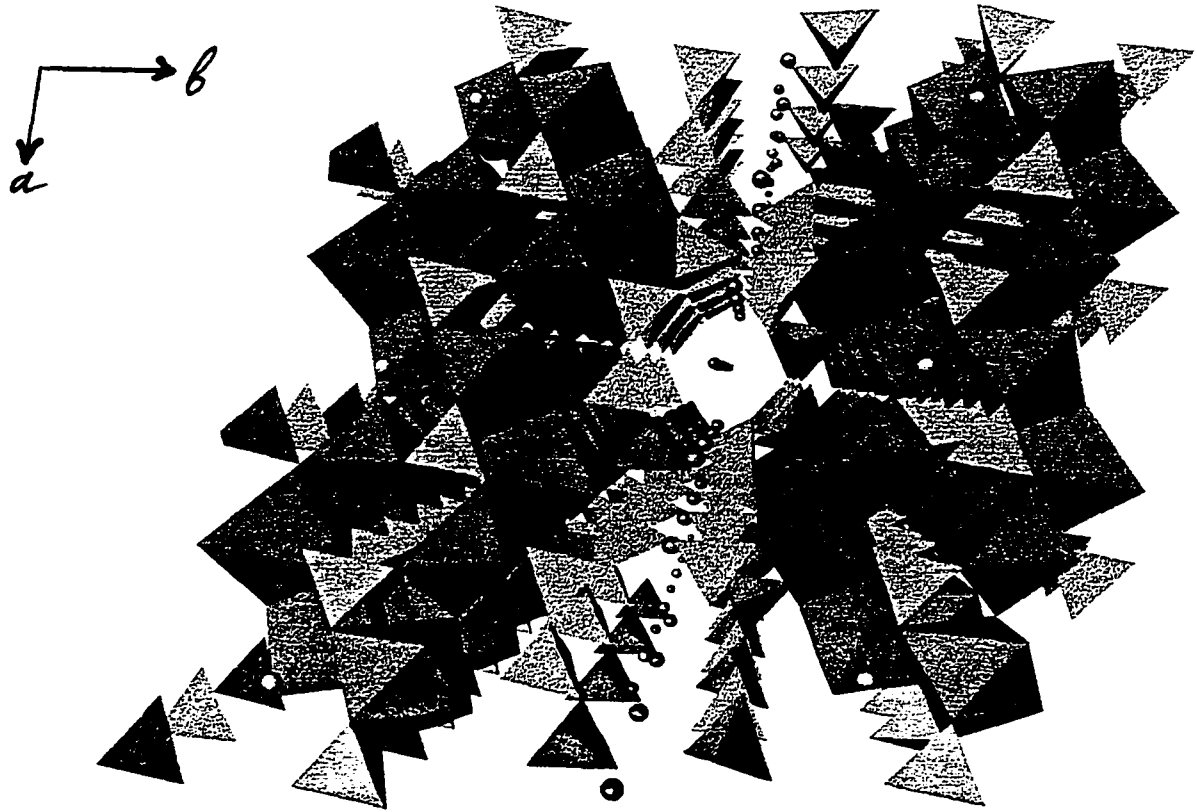
Fig. 2.2.3.2. Perspective view of the miserite structure down [001] (Scott, 1976). Double walls of $CaO_6$ octahedra (red) incorporate $Si_2O_7$ groups (blue) and separate the $(Si_{12}O_{30})_\infty$ tunnels (green). Atoms of K (purple), and two vacant sites (grey and orange) are accommodated within the tunnels. The remaining vacant site (yellow) can be occupied by Y, *REE*, *etc.*

23

### 2.2.4 Genesis of charoitites

The nature of charoitites-forming processes has been a subject of scientific debate. Until now, two major hypotheses have been proposed. Vorob'ev *et al.* (1983) suggest a magmatic origin for the charoite-bearing rocks. According to Vladykin *et al.* (1994), the composition of microinclusions in the minerals of charoitites supports the "magmatic" hypothesis and shows that the charoite rocks crystallised from a fluid-saturated melt corresponding to differentiates of ultrapotassic magmas. However, the majority of researchers interpret charoitites as a typical example of metasomatic rocks (Borisov 1985; Evdokimov & Reguir 1994; Konev *et al.* 1996). According to these authors, the remarkable diversity in texture, colour and chemistry of charoite-bearing rocks, as well as their paragenetic characteristics support this point of view.

## 2.3 Results of the present work

### 2.3.1 Samples description

In this work, we examined a series of fresh samples representing various textural types of charoite. The samples were examined using optical and scanning electron microscopy, back-scattered electron (BSE) imagery, X-ray powder diffraction (XRD), X-ray energy-dispersion spectrometry and transmission electron microscopy (TEM) (see Appendix A).

### 2.3.2 Back-scattered electron imagery

For BSE imagery, we used small (*ca.* 2×0.5 mm) elongate fragments of mosaic-fibrous charoite placed on a carbon tape and coated with gold. In BSE, the mineral appears as thin, acicular fragments and laths with a distinct fibrous texture (Figs. 2.3.2.1, 2.3.2.2a,b). The images were obtained parallel and perpendicular to the direction of charoite fibres. Parallel to the elongation, the fibrous texture persists to at least fractions of a micron (Figs. 2.3.2.3a,b). BSE images across the elongation of the fibres and laths show a conspicuous "basal" cleavage but no other characteristic textural features (Fig. 2.3.2.4a,b).

24

Fig. 2.3.2.1.   BSE image of elongated fragments and fibres of charoite.
F.O.V. 12 μm

25
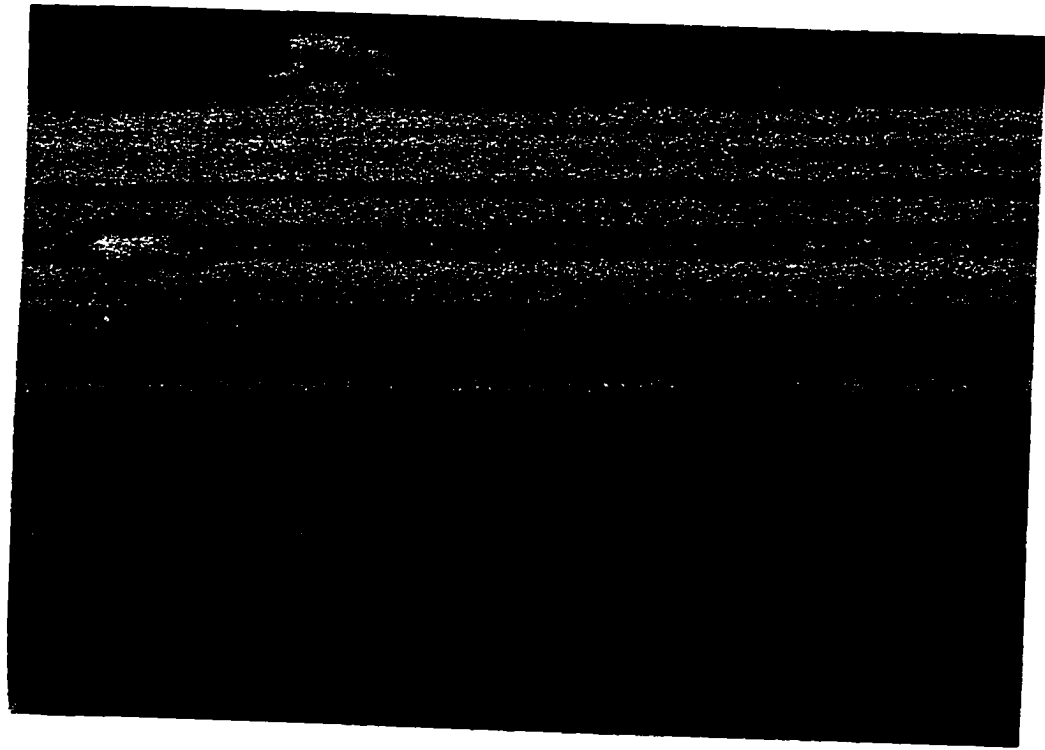
a
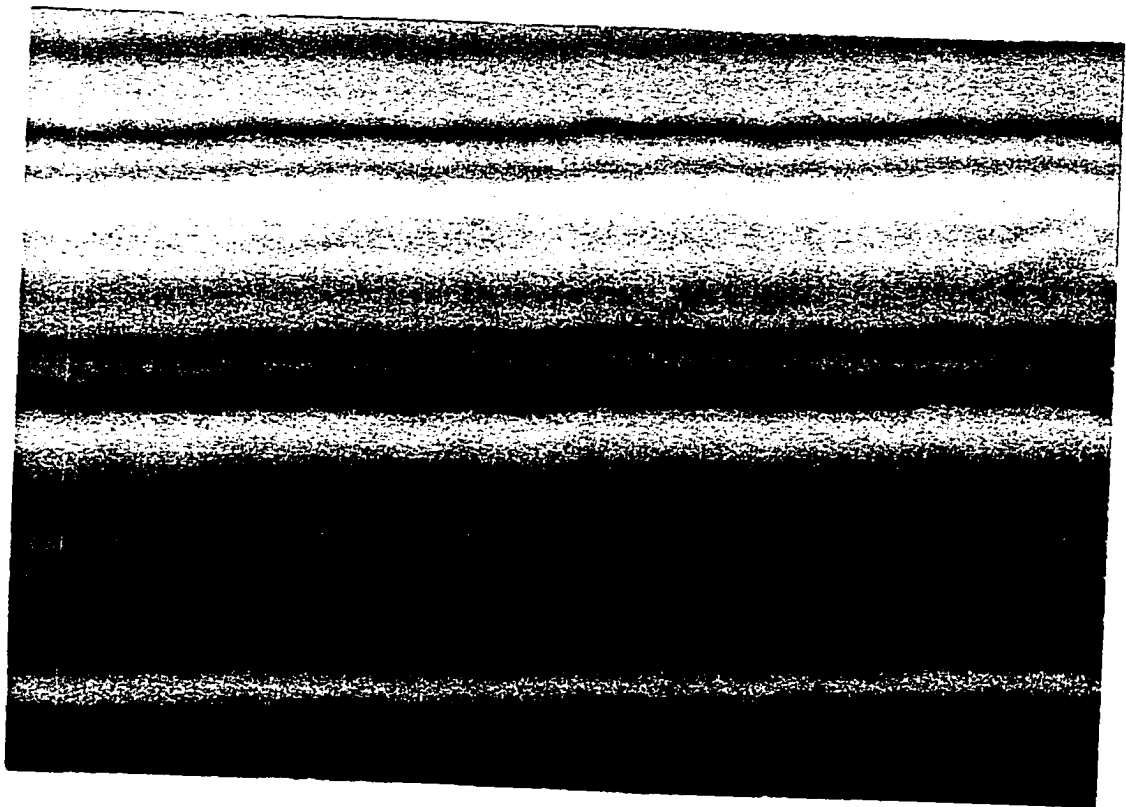


b

Fig. 2.3.2.2.    BSE images of elongated fragments and laths of charoite.
F.O.V. a – 140 μm; b – 40 μm.

26
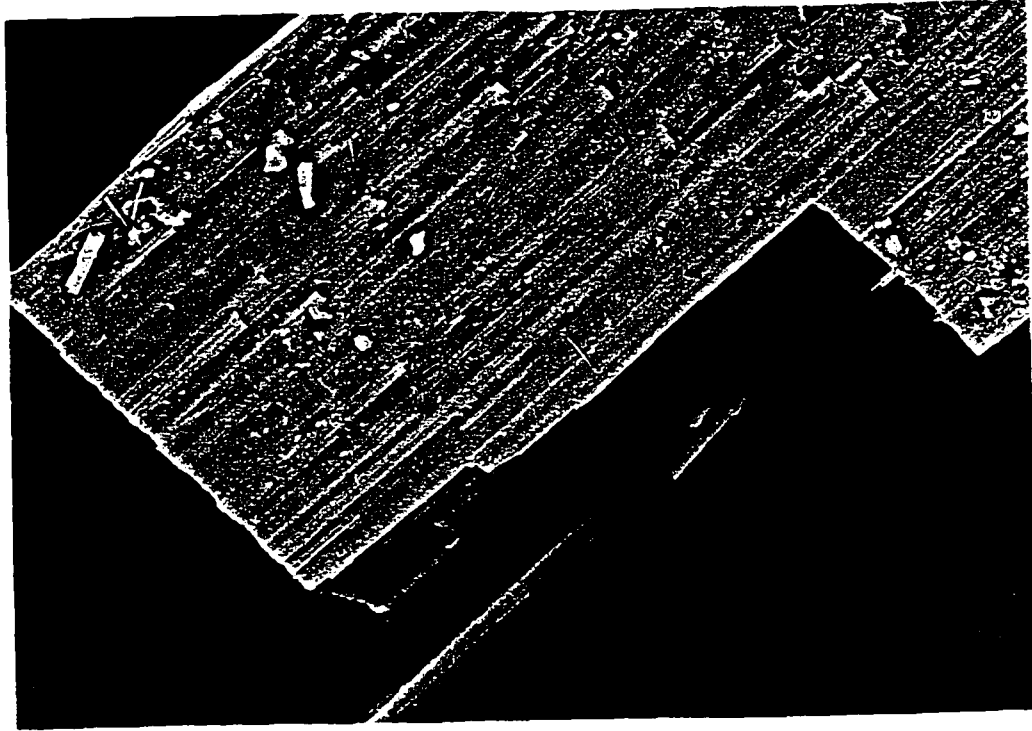
a
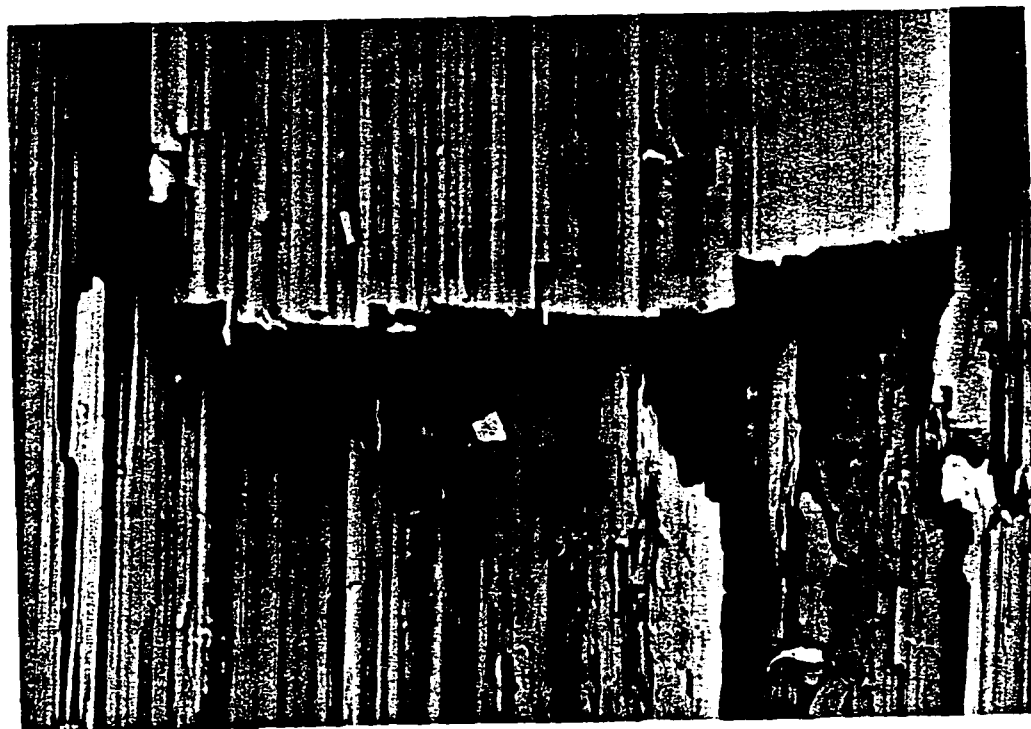


b

Fig. 2.3.2.3. BSE images of charoite fibre along elongation.

F.O.V. a – 6 μm; b – 3 μm.
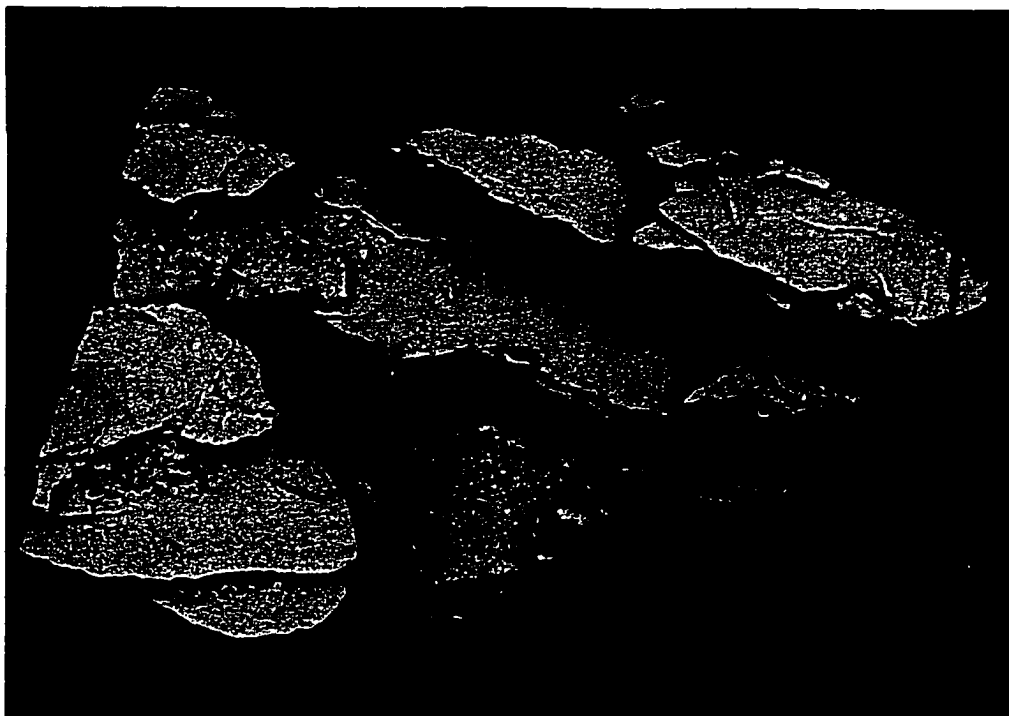
a



b

Fig. 2.3.2.4. BSE images of terminations of charoite fragments.

F.O.V. a – 400 μm; b – 11 μm.

28

### 2.3.3. Composition

In this work, I determined the composition of the massive, parallel-fibrous, undulatory-fibrous, radial, mosaic-fibrous and schistose varieties of charoite. The analytical data show noticeable compositional variations among the different textural types of the mineral, as well as among the grains corresponding to the same type. Concentrations of the major and minor elements in charoite vary as follows (wt.%): $Na_2O$ 1.0-2.0, $K_2O$ 7.6-9.5, $CaO$ 19.6-23.4, $SrO$ 0.4-1.9, $BaO$ 0.7-3.7, $MnO$ 0-0.5, $SiO_2$ 56.0-60.0 (Table 2.3.3.1). In a few cases, minor amounts ($< 0.2$ wt.%) of $TiO_2$ and $MgO$ were detected in the mineral. The $H_2O$ content in charoite was determined by CHN analysis using a SCP SCIENCE analyser. The amount of $H_2O$ in schistose charoite corresponds to 5.3 wt.%. Taking into account the analytical data published previously, and the proposed empirical formulae for charoite (see Chapter 2.2.2; Tables 2.2.2.1, 2.2.2.2), I attempted to calculate the formula on basis of 31 cations, 93 negative charges, 18 and 12 atoms of Si. Calculations to 12 atoms of Si gave the best results (*i.e.* gave cationic sums closest to integers), suggesting, in general, the empirical formula: $(K,Na)_3(Ca,Sr,Ba,Mn)_5Si_{12}O_{30}(OH,F)\cdot 3H_2O$. This formula is close to that given for charoite by Chukhrov (1980) (Table 2.2.2.1). Compositional variations in the samples studied correspond to the generalised empirical formula $(K_{2.03-2.50}Na_{0.42-0.82})_{\Sigma2.46-3.20}(Ca_{4.50-5.23},Sr_{0.05-0.22},Ba_{0.05-0.30},Mn_{0-0.11})_{\Sigma4.84-5.47}Si_{12}O_{30}(OH,F)\cdot 3H_2O$.

### 2.3.4. X-ray diffraction studies

Samples of mosaic-fibrous and schistose charoite were examined by powder X-ray diffraction. Unfortunatelly, data obtained using a STOE Stadi diffractometer were found to be unsatisfactory due to the low peak-to-background ratio. In order to reduce preferred-orientation effects, powder samples studied using a Philips 3710 diffractometer were prepared with hairspray, whose contribution to the XRD patterns relative to other fillers (silicone, vaseline, *etc.*) is minimal.

29

Table 2.2.2.1. Representative compositions of different varieties of charoite (our data).

| Wt.% | 1 | 2 | 3 | 4 | 5 | 6 | 7 | 8 | 9 | 10 | 11 | 12 | 13 |
|---|---|---|---|---|---|---|---|---|---|---|---|---|---|
| $SiO_2$ | 58.25 | 58.93 | 58.90 | 59.58 | 59.45 | 58.32 | 58.58 | 57.54 | 58.03 | 56.91 | 57.89 | 58.99 | 58.71 |
| MnO | 0.20 | 0.14 | n.d | 0.25 | 0.25 | n.d | 0.08 | n.d | n.d | 0.06 | 0.02 | n.d | 0.14 |
| CaO | 21.78 | 21.38 | 21.36 | 22.27 | 22.08 | 21.05 | 21.38 | 21.08 | 20.97 | 20.48 | 21.31 | 22.57 | 23.2 |
| SrO | 0.86 | 1.65 | 1.6 | 0.50 | 1.12 | 21.25 | 1.68 | 1.85 | 1.87 | 1.22 | 1.11 | 0.93 | 0.94 |
| BaO | 1.84 | 0.98 | 1.14 | 1.74 | 1.91 | 1.27 | 0.99 | 0.90 | 0.87 | 1.21 | 0.96 | 0.86 | 0.67 |
| $Na_2O$ | 2.04 | 1.53 | 1.45 | 1.79 | 1.60 | 1.52 | 1.44 | 1.25 | 1.47 | 1.43 | 1.51 | 1.65 | 1.38 |
| $K_2O$ | 8.59 | 9.10 | 8.90 | 9.23 | 9.39 | 8.95 | 9.32 | 8.93 | 9.13 | 9.29 | 8.72 | 9.49 | 8.89 |
| Total | 93.56 | 93.71 | 93.37 | 95.96[#] | 93.86 | 92.36 | 93.47 | 91.55 | 92.34 | 90.60 | 91.59* | 94.49 | 93.95 |

Formulae calculated on the basis of 12 atoms of Si:

| | 1 | 2 | 3 | 4 | 5 | 6 | 7 | 8 | 9 | 10 | 11 | 12 | 13 |
|---|---|---|---|---|---|---|---|---|---|---|---|---|---|
| Si | 12.000 | 12.000 | 12.000 | 12.000 | 12.000[##] | 112.000 | 12.000 | 12.000 | 12.000 | 12.000 | 12.000 | 12.000 | 12.000 |
| Mn | 0.035 | 0.024 | - | 0.043 | 0.043 | 0.014 | 0.014 | - | - | 0.110 | 0.004 | - | 0.024 |
| Ca | 4.808 | 4.665 | 4.663 | 4.806 | 4.766 | 4.641 | 4.693 | 4.711 | 4.646 | 4.627 | 4.733 | 4.920 | 5.085 |
| Sr | 0.103 | 0.195 | 0.191 | 0.058 | 0.131 | 0.149 | 0.200 | 0.224 | 0.224 | 0.149 | 0.133 | 0.110 | 0.111 |
| Ba | 0.149 | 0.078 | 0.091 | 0.137 | 0.151 | 0.102 | 0.079 | 0.074 | 0.071 | 0.100 | 0.078 | 0.069 | 0.054 |
| Na | 0.815 | 0.604 | 0.573 | 0.699 | 0.625 | 0.606 | 0.572 | 0.505 | 0.589 | 0.585 | 0.607 | 0.651 | 0.547 |
| K | 2.258 | 2.364 | 2.313 | 2.372 | 2.413 | 2.349 | 2.436 | 2.376 | 2.409 | 2.499 | 2.306 | 2.463 | 2.318 |
| Σ | 8.168 | 7.920 | 7.831 | 8.115 | 8.129 | 7.861 | 7.984 | 7.890 | 7.939 | 7.960 | 7.883** | 8.213 | 8.139 |

Table 2.3.3.1. (Continues).

| Wt.% | 14 | 15 | 16 | 17 | 18 | 19 | 20 | 21 | 22 | 23 | 24 | 25 |
|---|---|---|---|---|---|---|---|---|---|---|---|---|
| $SiO_2$ | 59.47 | 59.30 | 60.06 | 55.97 | 58.53 | 58.60 | 56.49 | 56.14 | 58.63 | 58.62 | 59.00 | 58.83 |
| MnO | 0.19 | 0.26 | 0.18 | 0.31 | 0.09 | n.d | n.d | 0.02 | 0.52 | 0.43 | 0.25 | 0.18 |
| CaO | 22.48 | 23.12 | 22.98 | 19.63 | 22.97 | 23.07 | 21.66 | 21.89 | 21.66 | 21.45 | 21.04 | 21.35 |
| SrO | 0.76 | 0.48 | 0.75 | n.d | 0.68 | 0.94 | 0.48 | 0.38 | 0.82 | 1.13 | 0.47 | 0.68 |
| BaO | 2.33 | 2.52 | 2.65 | 3.32 | 3.52 | 3.71 | 2.60 | 2.50 | 1.93 | 2.18 | 3.35 | 3.59 |
| $Na_2O$ | 1.56 | 1.68 | 1.71 | 1.54 | 1.34 | 1.05 | 1.53 | 1.29 | 1.72 | 2.05 | 1.80 | 1.51 |
| $K_2O$ | 8.38 | 8.42 | 8.47 | 9.38 | 7.90 | 7.88 | 7.65 | 7.58 | 8.58 | 8.73 | 9.53 | 9.51 |
| Total | 95.17 | 95.78 | 96.80 | 90.20[t] | 95.03 | 95.25 | 90.41 | 89.80 | 95.36 | 94.59 | 95.44 | 95.65 |

Formulae calculated on the basis of 12 atoms of Si:

| | 14 | 15 | 16 | 17 | 18 | 19 | 20 | 21 | 22 | 23 | 24 | 25 |
|---|---|---|---|---|---|---|---|---|---|---|---|---|
| Si | 12.000 | 12.000 | 12.000 | 12.000 | 12.000 | 12.000 | 12.000 | 12.000 | 12.000 | 12.000 | 12.000 | 12.000 |
| Mn | 0.032 | 0.045 | 0.030 | 0.056 | 0.016 | - | - | 0.004 | 0.090 | 0.075 | 0.043 | 0.031 |
| Ca | 4.860 | 5.013 | 4.920 | 4.509 | 5.046 | 5.062 | 4.930 | 5.014 | 4.750 | 4.705 | 4.585 | 4.666 |
| Sr | 0.089 | 0.056 | 0.087 | - | 0.081 | 0.112 | 0.059 | 0.047 | 0.097 | 0.134 | 0.055 | 0.080 |
| Ba | 0.184 | 0.200 | 0.207 | 0.279 | 0.283 | 0.298 | 0.216 | 0.209 | 0.155 | 0.175 | 0.267 | 0.287 |
| Na | 0.610 | 0.659 | 0.622 | 0.640 | 0.553 | 0.417 | 0.630 | 0.535 | 0.683 | 0.814 | 0.710 | 0.597 |
| K | 2.157 | 2.174 | 2.159 | 2.565 | 2.066 | 2.059 | 2.073 | 2.067 | 2.240 | 2.280 | 2.473 | 2.475 |
| Σ | 7.932 | 8.147 | 8.065 | 8.064[t] | 8.025 | 7.948 | 7.908 | 7.876 | 8.015 | 8.183 | 8.133 | 8.136 |

n.d = not detected. * Total also includes 0.07 wt. % MgO; ** includes 0.022 apfu Mg. # Total also includes 0.16 wt.% $TiO_2$; ## includes 0.024 apfu Ti. [t] Total also includes 0.04 wt.% MgO and 0.01 wt.% $TiO_2$; [t] includes 0.013 apfu Mg and 0.002 apfu Ti. Analyses 1-3: massive charoite (Mu-119/7); 4-5: parallel-fibrous charoite (Ch-10); 6-13: undulatory-fibrous charoite (6-11: Ch-11, 12-13: Ch-2); 14-17: radial charoite (Ch-13); 18-21: mosaic-fibrous charoite (18-19: Mu-112, 20-21: Ch-16); 22-25: schistose charoite (22-23: Mu-121, 24-25: Mu-117).

CHARGR.TIF (2994x2434x256 tiff)
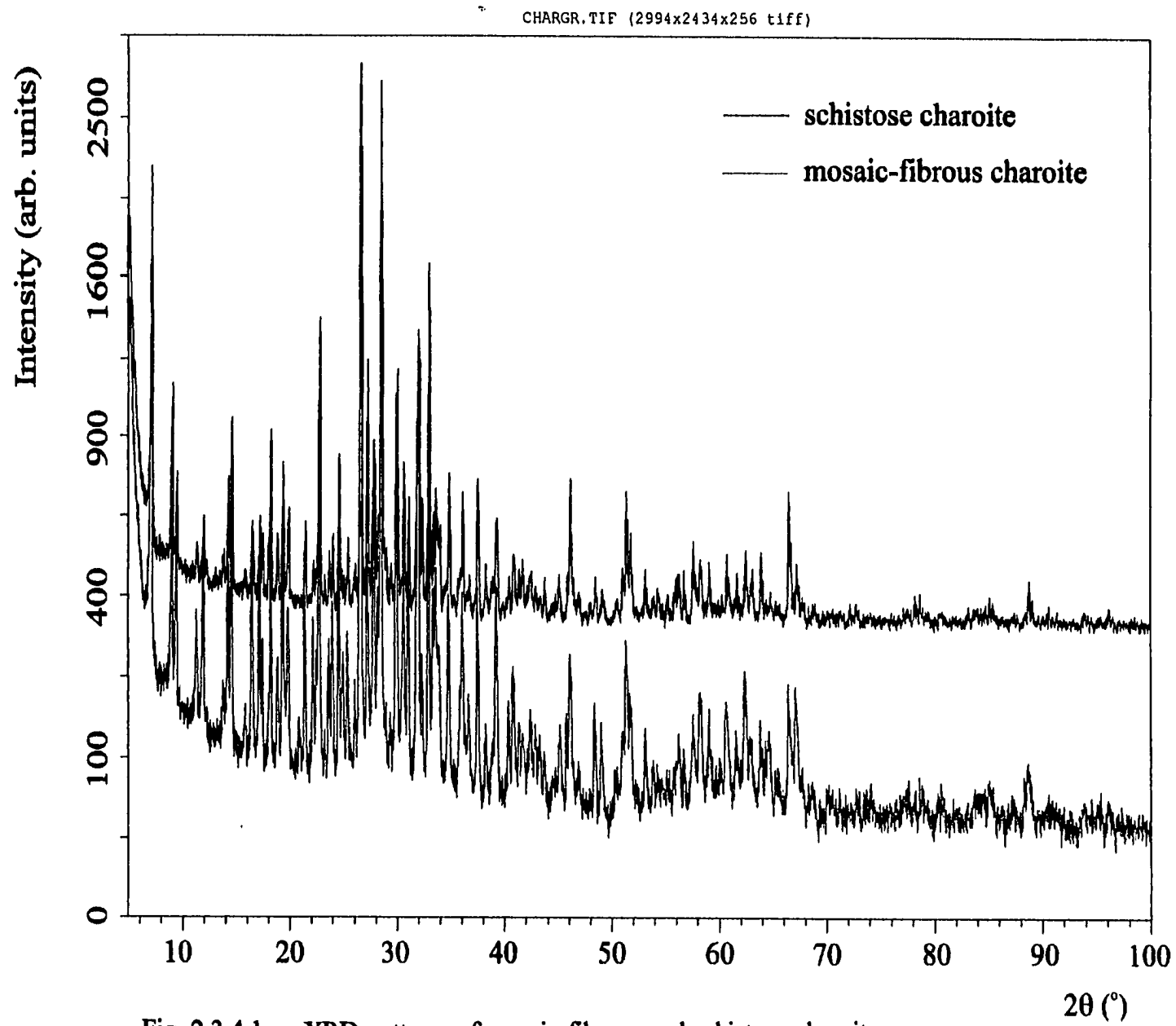


Fig. 2.3.4.1. XRD-patterns of mosaic-fibrous and schistose charoite.

Table 2.3.4.1. Representative X-ray diffraction pattern of mosaic-fibrous charoite with two types of refinement (first 70 reflections).

| | | MONOCLINIC CELL: $a$ =19.86 Å, $b$=32.13 Å, $c$=7.95 Å, $\beta$=97.24° | | | | TRICLINIC CELL: $a$ =19.96 Å, $b$ = 32.17 Å, $c$ =7.26 Å, $\alpha$=93.51°, $\beta$=99.45°, $\gamma$=89.50° | | | |
|---|---|---|---|---|---|---|---|---|---|
| $d_{obs.}$(Å) | $I$ | $d_{calc.}$(Å) | $h$ | $k$ | $l$ | $d_{calc.}$(Å) | $h$ | $k$ | $l$ |
| 32.07 | 80 | 32.13 | 0 | 1 | 0 | 32.07 | 0 | 1 | 0 |
| 12.46 | 90 | 12.45 | 1 | 2 | 0 | 12.45 | -1 | 2 | 0 |
| 9.85 | 30 | 9.85 | 2 | 0 | 0 | 9.85 | 2 | 0 | 0 |
| 9.43 | 30 | 9.42 | 2 | 1 | 0 | 9.42 | -2 | 1 | 0 |
| 7.85 | 15 | 7.89 | 0 | 0 | 1 | - | | | |
| 7.44 | 30 | 7.44 | 1 | 4 | 0 | 7.44 | -1 | 4 | 0 |
| 7.24 | 10 | 7.25 | 2 | 3 | 0 | 7.24 | 2 | 3 | 0 |
| 7.08 | 15 | 7.08 | 0 | 2 | 1 | 7.07 | 0 | 1 | -1 |
| 6.43 | 15 | 6.43 | 0 | 5 | 0 | 6.43 | 3 | 1 | 0 |
| 6.36 | 05 | 6.35 | 0 | 3 | 1 | 6.36 | -1 | 2 | 1 |
| 6.23 | 30 | 6.23 | 2 | 4 | 0 | 6.23 | -2 | 4 | 0 |
| 6.09 | 35 | 6.09 | -2 | 2 | 1 | 6.09 | 1 | 3 | -1 |
| 5.60 | 05 | 5.60 | -2 | 3 | 1 | 5.60 | -3 | 3 | 0 |
| 5.39 | 35 | 5.38 | 2 | 5 | 0 | 5.38 | -2 | 5 | 0 |
| 5.16 | 35 | 5.17 | 1 | 6 | 0 | 5.17 | -1 | 6 | 0 |
| 5.09 | 20 | 5.09 | -2 | 4 | 1 | 5.09 | 3 | 2 | -1 |
| 4.92 | 10 | 4.92 | -1 | 5 | 1 | 4.92 | 4 | 0 | 0 |
| 4.87 | 35 | 4.87 | 4 | 1 | 0 | 4.87 | -4 | 1 | 0 |
| 4.71 | 20 | 4.71 | 2 | 4 | 1 | 4.71 | -4 | 2 | 0 |
| 4.59 | 45 | 4.59 | 0 | 7 | 0 | 4.59 | -3 | 5 | 0 |
| 4.48 | 30 | 4.48 | -3 | 4 | 1 | 4.48 | 3 | 0 | 1 |
| 4.26 | 10 | 4.26 | 1 | 6 | 1 | 4.27 | 3 | 2 | 1 |
| 4.16 | 30 | 4.15 | -2 | 6 | 1 | 4.16 | 2 | 7 | 0 |
| 4.01 | 25 | 4.02 | 0 | 8 | 0 | 4.01 | 0 | 8 | 0 |
| 3.958 | 20 | 3.960 | 4 | 0 | 1 | 3.963 | 1 | 7 | -1 |
| 3.912 | 50 | 3.912 | 5 | 1 | 0 | 3.910 | -4 | 5 | 0 |
| 3.827 | 10 | 3.828 | 5 | 2 | 0 | 3.827 | -1 | 7 | -1 |
| 3.763 | 20 | 3.763 | 3 | 7 | 0 | 3.763 | -3 | 7 | 0 |
| 3.715 | 30 | 3.715 | 4 | 3 | 1 | 3.715 | 2 | 8 | 0 |
| 3.624 | 35 | 3.622 | -5 | 2 | 1 | 3.624 | 1 | 1 | -2 |
| 3.570 | 15 | 3.570 | 0 | 9 | 0 | 3.568 | 0 | 9 | 0 |
| 3.510 | 15 | 3.512 | 2 | 0 | 2 | 3.510 | 1 | 9 | 0 |
| 3.422 | 10 | 3.418 | 1 | 4 | 2 | 3.422 | 3 | 8 | 0 |
| 3.357 | 100 | 3.357 | 2 | 9 | 0 | 3.356 | -2 | 9 | 0 |
| 3.281 | 35 | 3.284 | 6 | 0 | 0 | 3.282 | 6 | 0 | 0 |

Table 2.3.4.1. (Continues).

| | | | | | | | | | |
|---|---|---|---|---|---|---|---|---|---|
| **3.211** | **45** | **3.213** | **0** | **10** | **0** | **3.211** | **0** | **10** | **0** |
| 3.169 | 30 | 3.171 | 1 | 10 | 1 | 3.169 | 1 | 10 | 0 |
| **3.137** | **80** | **3.137** | **3** | **9** | **0** | **3.137** | **-3** | **9** | **0** |
| 3.086 | 10 | 3.087 | 1 | 6 | 2 | 3.089 | 1 | 6 | -2 |
| 3.047 | 10 | 3.046 | -6 | 3 | 1 | 3.045 | 1 | 9 | 1 |
| **2.987** | **50** | **2.990** | **5** | **7** | **0** | **2.986** | **5** | **7** | **0** |
| 2.940 | 15 | 2.942 | -2 | 7 | 2 | 2.942 | 3 | 0 | 2 |
| 2.922 | 25 | 2.922 | 1 | 10 | 1 | 2.921 | -5 | 5 | -1 |
| 2.884 | 35 | 2.886 | 3 | 10 | 0 | 2.885 | 6 | 5 | -1 |
| **2.801** | **50** | **2.801** | **2** | **11** | **0** | **2.801** | **3** | **3** | **2** |
| 2.771 | 15 | 2.773 | -2 | 8 | 2 | 2.772 | -7 | 2 | 0 |
| **2.719** | **50** | **2.723** | **7** | **3** | **0** | **2.719** | **3** | **4** | **2** |
| 2.688 | 30 | 2.687 | -6 | 1 | 2 | 2.688 | 4 | 10 | 0 |
| 2.669 | 35 | 2.669 | 3 | 11 | 0 | 2.669 | -3 | 11 | 0 |
| 2.647 | 25 | 2.647 | 0 | 9 | 2 | 2.647 | 0 | 11 | 1 |
| 2.578 | 30 | 2.577 | 5 | 8 | 1 | 2.578 | -7 | 5 | 0 |
| 2.541 | 05 | 2.543 | 6 | 8 | 0 | 2.540 | -6 | 3 | 2 |
| 2.502 | 15 | 2.502 | 1 | 12 | 1 | 2.502 | 5 | 7 | -2 |
| 2.488 | 30 | 2.487 | -6 | 5 | 2 | 2.488 | 7 | 6 | -1 |
| 2.450 | 15 | 2.450 | -1 | 5 | 3 | 2.450 | -4 | 6 | -2 |
| 2.397 | 30 | 2.397 | 2 | 13 | 0 | 2.397 | -7 | 1 | 2 |
| 2.353 | 10 | 2.353 | 4 | 12 | 0 | 2.353 | -7 | 7 | 1 |
| 2.347 | 05 | 2.347 | 5 | 11 | 0 | 2.347 | -5 | 11 | 0 |
| 2.312 | 10 | 2.313 | 1 | 6 | 3 | 2.312 | -5 | 10 | -1 |
| 2.295 | 30 | 2.295 | 0 | 14 | 0 | 2.295 | -5 | 8 | 2 |
| 2.231 | 15 | 2.230 | 7 | 7 | 1 | 2.232 | -5 | 10 | -1 |
| 2.209 | 20 | 2.209 | 4 | 13 | 0 | 2.209 | -4 | 13 | 0 |
| 2.182 | 15 | 2.182 | -9 | 0 | 1 | 2.182 | 8 | 7 | -1 |
| 2.166 | 15 | 2.166 | 7 | 0 | 2 | 2.166 | -7 | 6 | 2 |
| 2.158 | 15 | 2.159 | -4 | 13 | 1 | 2.158 | 9 | 3 | -1 |
| 2.143 | 10 | 2.142 | 0 | 15 | 0 | 2.143 | 9 | 3 | 0 |
| 2.131 | 15 | 2.130 | 1 | 15 | 0 | 2.130 | 3 | 0 | 3 |
| 2.112 | 11 | 2.112 | -3 | 14 | 1 | 2.112 | -9 | 4 | 0 |
| 2.107 | 10 | 2.106 | -9 | 4 | 1 | 2.107 | 8 | 5 | -2 |
| 2.098 | 07 | 2.098 | -1 | 13 | 2 | 2.098 | 6 | 0 | -3 |

34

Table 2.3.4.2. Representative X-ray diffraction pattern of schistose charoite (first 66 reflections).

MONOCLINIC CELL: $a$ =32.13 Å, $b$=19.64 Å, $c$=8.51 Å, $\beta$=95.23°

| $d_{obs.}$(Å) | $I$ | $d_{calc.}$(Å) | $h$ | $k$ | $l$ | $d_{obs.}$(Å) | $I$ | $d_{calc.}$(Å) | $h$ | $k$ | $l$ |
|---|---|---|---|---|---|---|---|---|---|---|---|
| **12.42** | **70** | **12.40** | **2** | **1** | **0** | **2.797** | **60** | **2.797** | **-2** | **1** | **3** |
| **9.83** | **40** | **9.82** | **0** | **2** | **0** | 2.767 | 25 | 2.766 | -3 | 1 | 3 |
| 9.38 | 25 | 9.37 | 3 | 1 | 0 | **2.716** | **70** | **2.716** | **-2** | **2** | **3** |
| 7.81 | 10 | 7.78 | 0 | 1 | 1 | 2.682 | 20 | 2.681 | 10 | 4 | 0 |
| 7.40 | 20 | 7.41 | 4 | 1 | 0 | 2.664 | 25 | 2.663 | 0 | 7 | 1 |
| 6.41 | 10 | 6.41 | 1 | 3 | 0 | 2.652 | 20 | 2.652 | 11 | 1 | 1 |
| 6.20 | 30 | 6.20 | 4 | 2 | 0 | 2.638 | 20 | 2.638 | 2 | 2 | 3 |
| **6.07** | **45** | **6.06** | **2** | **3** | **0** | 2.573 | 35 | 2.573 | 12 | 2 | 0 |
| 5.37 | 20 | 5.36 | 5 | 2 | 0 | 2.484 | 30 | 2.485 | -5 | 7 | 1 |
| 5.14 | 20 | 5.15 | 6 | 1 | 0 | 2.443 | 10 | 2.442 | 13 | 1 | 0 |
| 5.07 | 20 | 5.07 | 1 | 3 | 1 | 2.394 | 35 | 2.395 | -4 | 4 | 3 |
| 4.90 | 20 | 4.91 | 0 | 4 | 0 | 2.350 | 15 | 2.350 | -5 | 4 | 3 |
| **4.86** | **40** | **4.85** | **1** | **4** | **0** | 2.292 | 25 | 2.292 | 13 | 1 | 1 |
| 4.69 | 20 | 4.69 | 2 | 4 | 0 | 2.206 | 20 | 2.206 | 12 | 5 | 0 |
| 4.58 | 20 | 4.58 | 5 | 3 | 0 | 2.179 | 15 | 2.179 | 7 | 3 | 3 |
| 4.46 | 25 | 4.46 | -4 | 3 | 1 | 2.164 | 15 | 2.164 | -13 | 2 | 2 |
| 4.14 | 20 | 4.14 | 0 | 1 | 2 | 2.129 | 10 | 2.127 | -1 | 4 | 0 |
| 4.00 | 15 | 4.00 | 8 | 0 | 0 | 2.108 | 10 | 2.107 | 14 | 2 | 1 |
| 3.902 | 15 | 3.901 | -1 | 2 | 2 | 2.088 | 10 | 2.088 | 13 | 4 | 1 |
| **3.750** | **60** | **3.749** | **3** | **1** | **2** | 2.068 | 10 | 2.068 | -3 | 2 | 4 |
| 3.701 | 15 | 3.704 | 8 | 2 | 0 | 2.009 | 10 | 2.009 | 8 | 8 | 1 |
| 3.615 | 15 | 3.616 | 6 | 3 | 1 | **1.967** | **40** | **1.967** | **13** | **6** | **0** |
| 3.499 | 15 | 3.498 | 9 | 1 | 0 | 1.935 | 10 | 1.935 | -7 | 9 | 1 |
| 3.419 | 10 | 3.420 | -3 | 5 | 1 | 1.876 | 15 | 1.876 | 11 | 8 | 0 |
| **3.352** | **100** | **3.348** | **5** | **5** | **0** | 1.853 | 15 | 1.853 | 0 | 8 | 3 |
| **3.277** | **50** | **3.276** | **-6** | **2** | **2** | 1.805 | 10 | 1.805 | 8 | 0 | 4 |
| 3.205 | 35 | 3.205 | -9 | 2 | 1 | 1.778 | 35 | 1.778 | 16 | 4 | 1 |
| **3.131** | **95** | **3.132** | **-3** | **4** | **2** | 1.765 | 20 | 1.765 | -4 | 6 | 4 |
| 3.081 | 10 | 3.083 | 8 | 3 | 1 | 1.722 | 15 | 1.722 | 15 | 4 | 2 |
| 3.036 | 10 | 3.030 | 1 | 6 | 1 | 1.686 | 10 | 1.685 | -9 | 8 | 3 |
| **2.981** | **50** | **2.981** | **-8** | **4** | **1** | 1.662 | 10 | 1.662 | -14 | 8 | 1 |
| 2.917 | 35 | 2.918 | -7 | 3 | 2 | 1.640 | 10 | 1.640 | 8 | 5 | 4 |
| 2.875 | 25 | 2.875 | 10 | 1 | 1 | 1.633 | 10 | 1.633 | -7 | 1 | 5 |

Unit-cell parameters of mosaic-fibrous and schistose charoite were refined using different software packages based on least-squares methods, including ITO12 (Visser and Shirley 1998), DICVOL91 (Boultif & Louer 1991) and TREOR90 (Werner 1995). The X-ray diffraction patterns (*ca.* 100 reflections; Fig. 2.3.4.1) were subsequently indexed using the software package CELLSVD (Lowe-Ma 1993). For both varieties of charoite, the indexing yielded the best results using a primitive monoclinic cell with the following parameters: $a$ =19.86(1) Å, $b$=32.13(2) Å, $c$=7.952(9) Å, $\beta$=97.24° (mosaic-fibrous) and $a$ =32.13(2) Å, $b$=19.64(2) Å, $c$=8.509(6) Å, $\beta$=95.23° (schistose) (Tables 2.2.3.1, 2.3.4.1 and 2.3.4.2). Some of the XRD patterns of mosaic-fibrous charoite could also be refined on a triclinic cell ($a$ =19.96(1) Å, $b$ = 32.17(2) Å, $c$ =7.258(4) Å, $\alpha$=93.51°, $\beta$=99.45°, $\gamma$=89.50°), in which case, however, one strong reflection ($d$=7.85 Å, I=15) could not been indexed (Tables 2.2.3.1 and 2.3.4.1). According to the suggested earlier empirical formula of charoite (see Chapter 2.2.2), for both monoclinic and triclinic cells the number of formula units per unit-cell (estimated from the molecular weight and measured density) is close to 6.

Interestingly, two cell dimensions ($a$ and $b$) in all the samples are consistently refined to similar values regardless of the cell chosen and indexing program used. These parameters also correlate quite well with previously published data for charoite (Table 2.2.3.12.2.3.1). Differences between the alternative refinements arise mostly from the choice of parameter $c$ and $\beta$, and may indicate the existence of several polytypes of charoite. The uncertainty in $c$ may also result from remnant preferred orientation of the charoite fibres.

As the refinement of mosaic-fibrous charoite on the basis of a monoclinic cell gave the best correlation between the calculated and observed data, I chose these results for further analysis of the charoite structure.

### 2.3.5. *Transmission electron microscopy study*

TEM data for mosaic-fibrous and schistose charoite were provided by Dr. Roger H. Mitchell. The mineral was found to be very unstable under the electron beam. Most of the

36
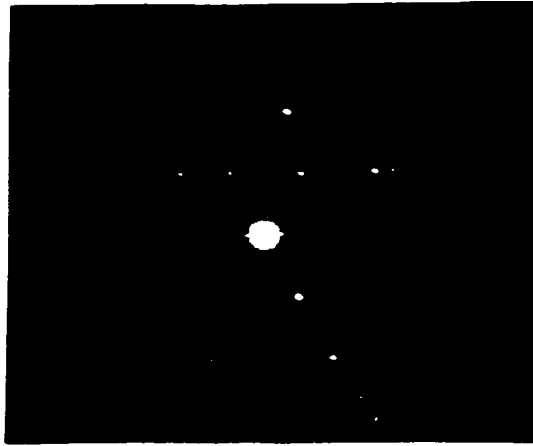
a
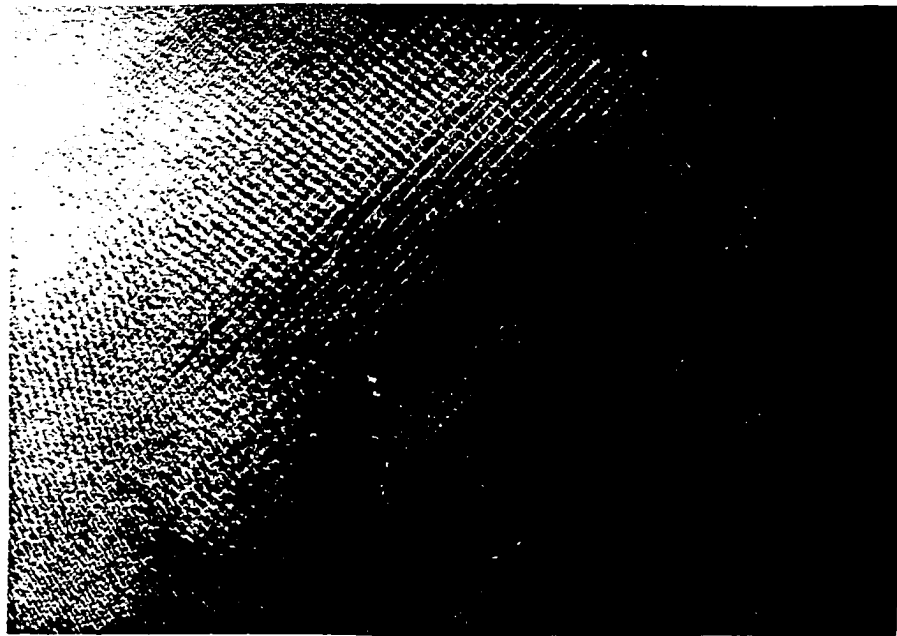


b

Fig. 2.3.5.1. TEM images of mosaic-fibrous charoite: a – SAED pattern;
b – High-resolution direct-lattice image.

37

selected-area electron diffraction (SAED) patterns show extremely weak, fuzzy or split reflections. Some of the SAED patterns and high-resolution (HR) direct lattice images are shown in Figures 2.3.5.1a,b and 2.3.5.2. Since the structure of the mineral is unknown, we could not estimate the exact orientation of TEM patterns. Our interpretation of TEM data was aimed at confirming unit-cell parameters of charoite obtained by XRD studies. The proportions between the parameters of monoclinic and triclinic reciprocal cells were estimated as follows:

$1/a : 1/b : 1/c = 1/19.86 : 1/32.13 : 1/7.95 = 1.6 : 1 : 4$ (mosaic-fibrous, monoclinic);

$1/a : 1/b : 1/c = 1/19.96 : 1/32.17 : 1/7.26 = 1.6 : 1 : 4.5$ (mosaic-fibrous, triclinic);

$1/a : 1/b : 1/c = 1/32.13 : 1/19.64 : 1/8.51 = 0.6 : 1 : 2.3$ (schistose, monoclinic).

Figure 2.3.5.1a shows a SAED pattern of mosaic-fibrous charoite taken along the fibres. Distances between the central reflection and two closest reflections relate to each other as 1.66, which is somewhat close to the $b/a$ ratio in both monoclinic and triclinic models. Distances between the lattice fringes on one of the high-resolution direct-lattice images of mosaic-fibrous charoite correspond to $ca.$ 8 Å and 10 Å (Fig. 2.3.5.1b). These numbers can be correlated with parameter $c$ (7.95 Å) and one half of parameter $a$ (19.87 Å) of the monoclinic cell.
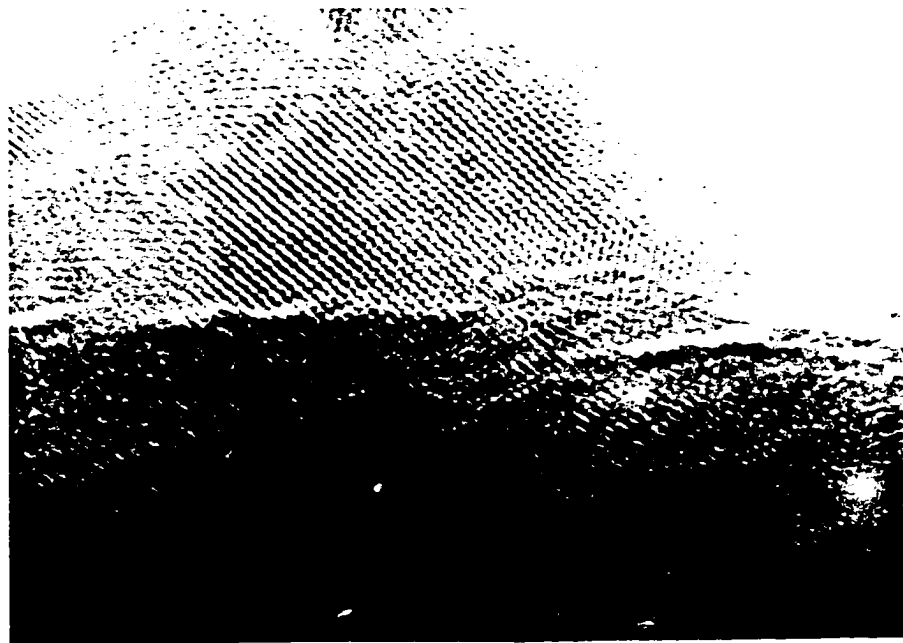


Fig. 2.3.5.2.    High-resolution direct-lattice image of schistose charoite.

38

Some of the high-resolution direct-lattice images of schistose charoite show lattice fringes with a spacing of approximately 7 Å resembling parameter $c$ of mosaic-fibrous charoite (Fig. 2.3.5.2).

## 2.4 Discussion and conclusions

### 2.4.1. Comparison of charoite, canasite and miserite structures

Taking into account the earlier-made proposals of structural similarities between charoite, canasite and miserite (see Chapter 2.2.3), I shall compare these three minerals from both compositional and structural standpoints (Table 2.4.1.1).

Compositionally similar charoite and canasite also have comparable unit-cell parameters $a$ (19.87 Å and 18.84 Å, respectively), and parameter $c$ of charoite (7.95 Å) and $b$ of canasite (7.24 Å) are also close. However, parameter $b$ of charoite (32.15 Å) is larger than $c$ of canasite (12.64 Å), resulting in the unit-cell volume of charoite being about 3 times greater than that of canasite (Table 2.4.1.1). If, according to Rogova $et$ $al.$ (1978), charoite and canasite have similar structural motifs, the structure of charoite should be composed of ($Si_{12}O_{30}$) tunnels interlayered with walls of cation-centred octahedra. Our analytical data (see Chapter 2.2.2), indicate that Na in charoite is present in minor amounts, and is prone to volatilisation under the electron beam. Hence, I assume that both K and Na atoms in charoite structure are accommodated at weakly bonded sites within the structural tunnels. For comparative purposes, I multiplied the formula of canasite by 3. As we can see (Table 2.4.1.1), the number of $SiO_4$ groups in both minerals is identical, as is the number of K atoms. However, the amount of octahedrally-coordinated cations is significantly greater in canasite than in charoite (48 and 30, respectively). Therefore, either the configuration of octahedral walls or the entire structural motif of charoite is different in comparison with canasite.

Compositionally, miserite and charoite are quite different (Table 2.1.1). The two minerals have different parameters $c$ (7.95 Å for charoite and 7.28 Å for miserite), whereas the $a$ and $b$ edges of the charoite cell (19.87 Å and 32.15Å) are nearly double those of miserite (10.10 Å and 16.01 Å). The cell volume of miserite is about 4.6 times smaller than

39

Table 2.4.1.1. Comparison of charoite, canasite and miserite.

| Mineral | Charoite | Canasite | Miserite |
|---|---|---|---|
| $a$, Å | 19.87 | 18.84 | 10.10 |
| $b$, Å | 32.15 | 7.24 | 16.01 |
| $c$, Å | 7.95 | 12.64 | 7.38 |
| $V(\text{Å}^3)$ | 5038 | 1601 | 1082 |
| Formula | $(K,Na)_3(Ca,Sr,Ba,Mn)_5Si_{12}O_{30}(OH,F)\cdot 3H_2O$ | $K_3Na_3Ca_5Si_{12}O_{30}(O,OH,F)_4$ | $KCa_5\square((Si_8O_{22})(OH)F$ |
| Z | 6 | 2 | 2 |
| Formula content | $(K,Na)_{18}(Ca,Sr,Ba,Mn)_{30}Si_{72}O_{180}(OH,F)_6\cdot 18H_2O$ | $K_6Na_6Ca_{10}Si_{24}O_{60}(O,OH,F)_8$ | $K_2Ca_{10}\square_2(Si_{16}O_{44})(OH)_2F_2$ |
| Formula extrapolated to a charoite-sized cell | $(K,Na)_{18}(Ca,Sr,Ba,Mn)_{30}Si_{72}O_{180}(OH,F)_6\cdot 18H_2O$ | $K_{18}Na_{18}Ca_{30}Si_{72}O_{180}(O,OH,F)_{24}$ | $K_{9.2}Ca_{46}\square_{9.2}(Si_{73.6}O_{202.4})(OH)_{9.2}F_{9.2}$ |
| | | $a_{char}/a_{can} \approx 1:1$ | $a_{char}/a_{mis} \approx 2:1$ |
| | | $b_{char}/c_{can} \approx 2.5:1$ | $b_{char}/b_{mis} \approx 2:1$ |
| | | $c_{char}/b_{can} \approx 1:1$ | $c_{char}/c_{mis} \approx 1:1$ |

40

that of charoite. As in the case of canasite (see above), miserite has a significantly lower relative proportion of $SiO_4$ tetrahedra to octahedrally-coordinated cations than charoite (Table 2.4.1.1). In addition, the number of K atoms in miserite (9.2) corresponds to nearly half the amount of (K,Na) atoms in charoite (18).

In order to simulate the structural motif of charoite, I attempted to change the configuration of the octahedral walls in miserite and canasite by removing some of the Ca octahedra and "straightening" the corrugated octahedral walls interlayered with the $(Si_{12}O_{30})$ tunnels. These attempts did not result in any realistic model which would allow us to achieve the desirable stoichiometry without drastic changes in the configuration of $(Si_{12}O_{30})$ tunnels. Therefore, we conclude that the structure of charoite probably shows very little affinity to those of canasite and miserite.

### 2.4.2. Speculations on the structure of charoite

A plausible structural model for charoite must account for the significantly high levels of "structural silica" in this mineral. The high relative proportion of $SiO_4$ tetrahedra to octahedrally-coordinated cations (predominantly Ca) observed in charoite is only found in phyllosilicates and related structures. As a simple analogy, let us consider the structure of micas. For the convenience of comparison to the formula of charoite, the general formula of trioctahedral micas can be written as: $K_{18}(Mg,Fe)_{54}(Si,Al)_{72}O_{180}(OH,F)_{36}$. From this formula, it is obvious that for each "unit" of seventy-two $(Si,Al)O_4$ tetrahedra, there are fifty-four octahedrally-coordinated cations (Mg,Fe). As there are significantly fewer octahedrally-coordinated cations available in charoite (see Chapter 2.4.1), the occurrence of continuous layers of edge-sharing octahedra (as in trioctahedral micas) is highly unlikely in the structure of charoite.

Among the phyllosilicates, the best correspondence in terms of the octahedral-to-tetrahedral cation ratio is observed between charoite and $[CaV^{4+}(Si_4O_{10})O \cdot 4H_2O]$. This compound crystallises in two structurally similar polymorphs, cavansite and pentagonite (Evans 1973). Both structures represent a network of 4-fold and 8-fold rings formed by $(SiO_3)$

41
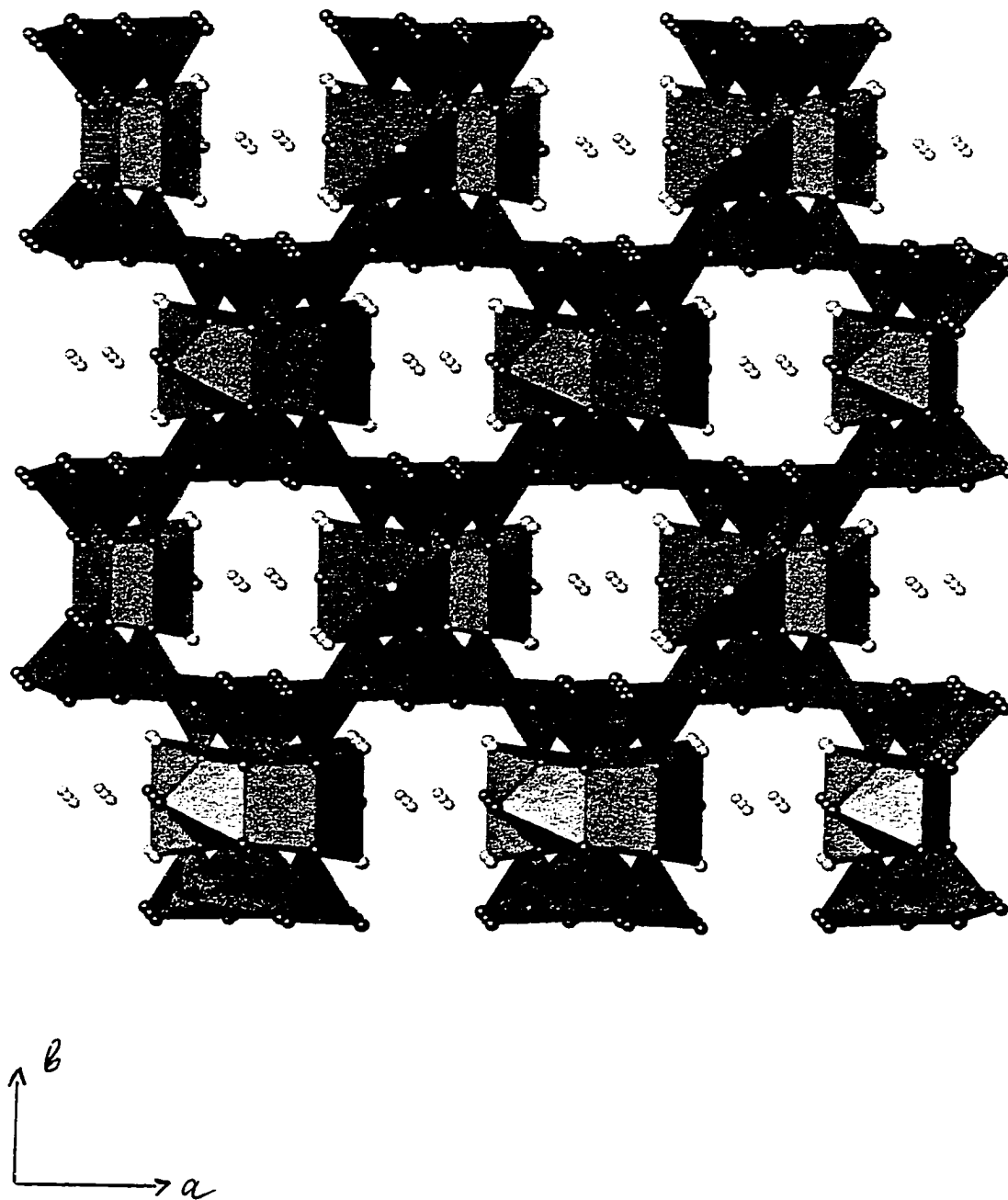
**Fig. 2.4.2.1.** Projection of cavansite structure on (001) (Evans, 1973). Sheets of $SiO_4$ tetrahedra (green) are interconnected by discontinuous layers of $CaO_7$ (red) and $VO_5$ (blue) polyhedra. Zeolitic $H_2O$ (yellow) is accommodated within the structural cavities.
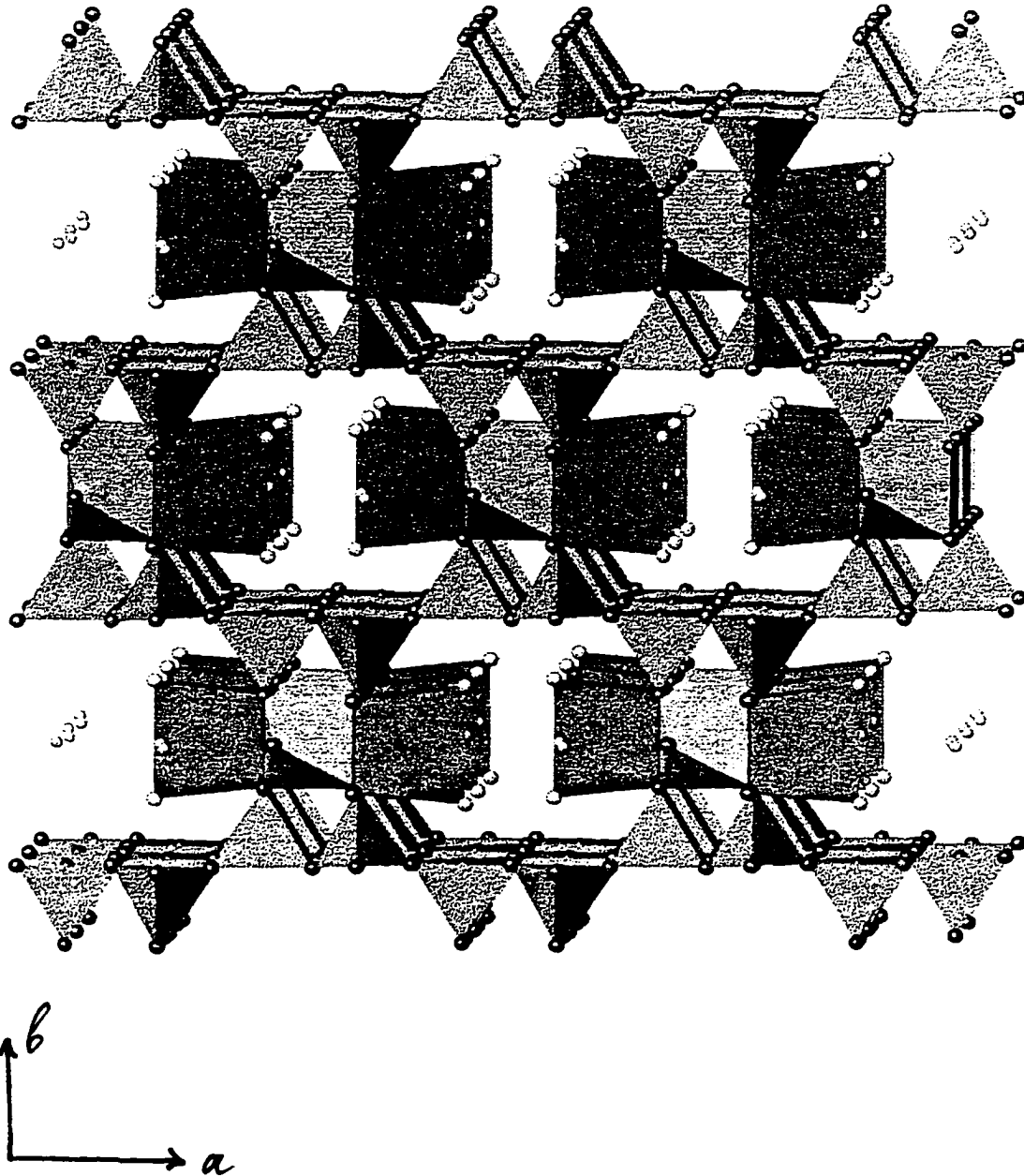
Fig. 2.4.2.2. Projection of pentagonite structure on (001) (Evans, 1973). Sheets of SiO₄ tetrahedra (green) are interconnected by discontinuous layers of CaO₇ (red) and VO₅ (blue) polyhedra. Purple − atoms of oxygen, yellow − H₂O.

43
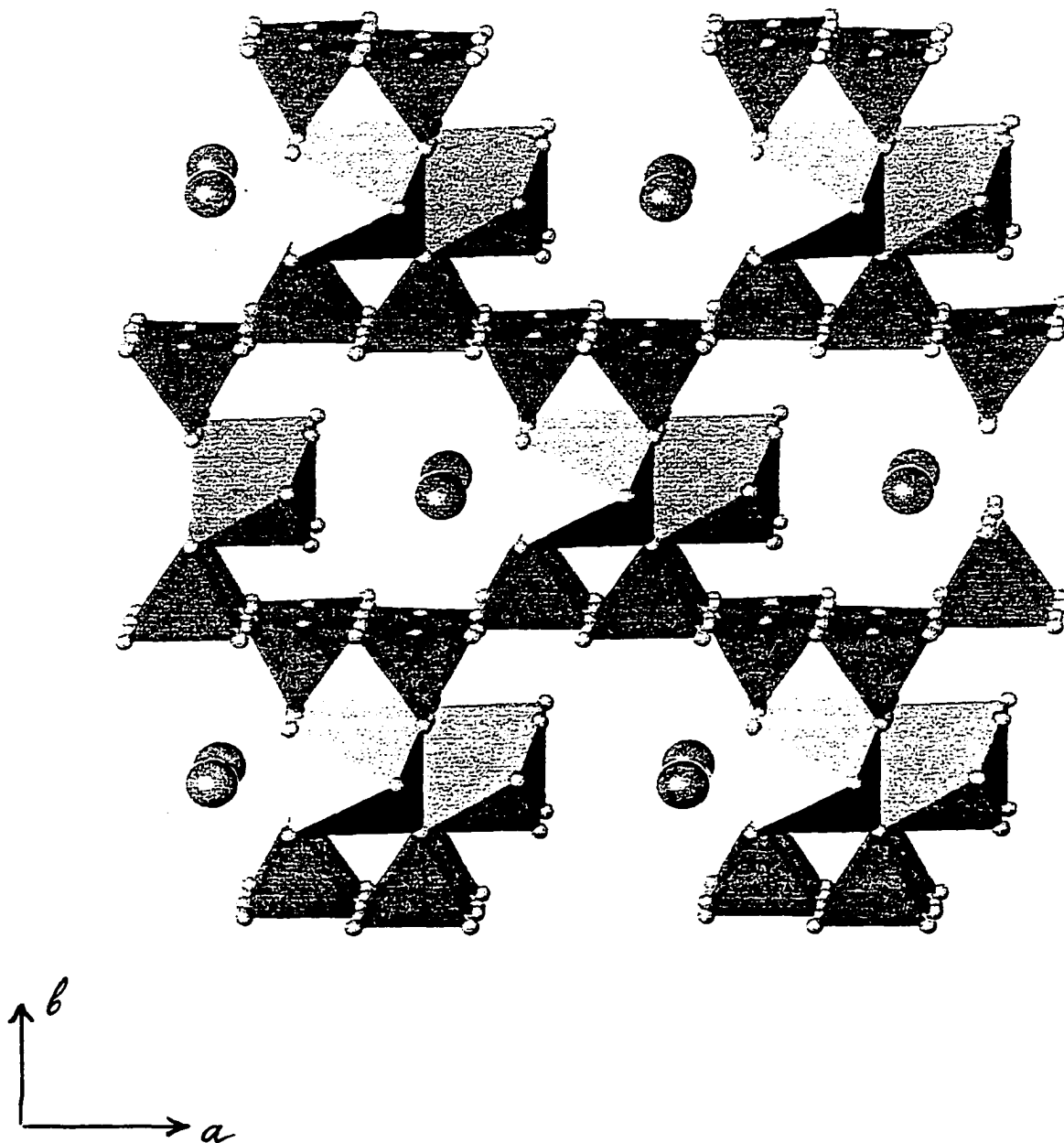
Fig. 2.4.2.3. Simulated structure of $(Ca,V)_{27}(Si_{72}O_{180})O_{18} \cdot 36H_2O$. $SiO_4$ tetrahedra (green) form sheets connected along [010] by layers of Ca (red) and V (blue) octahedra. Atoms of K (red) are accommodated within the structural channels.

44

chains linked into sheets parallel to (010). The silicate sheets are interconnected by discontinuous layers incorporating Ca and V atoms in a seven- and five-fold coordination, respectively (Figs. 2.4.2.1, 2.4.2.2). For further comparison, I favoured the structure of pentagonite as it is geometrically simpler than that of cavansite. In order to outline analogies between charoite and [$CaV^{4+}(Si_4O_{10})O \cdot 4H_2O$], I ignored three (K,Na) atoms in the charoite formula. I also "modified" the atomic coordinates in the structure of pentagonite (using the software ATOMS) so that both Ca and V became octahedrally-coordinated, forming double chains of octahedra between the silicate sheets. The modified formula of this hypothetical compound can be written as $(Ca,V)_{27}(Si_{72}O_{180})O_{18} \cdot 36H_2O$, i.e. there is twenty-seven octahedra per each "unit" of seventy-two $SiO_4$ tetrahedra. From interatomic distances in this structure, I expect that K can be accomodated between the chains of octahedra, within the structural channels (Fig. 2.4.2.3).

The results obtained in the present study have to be treated with caution. The model proposed is very approximate, and cannot be as yet used to refine the crystal structure of charoite from the powder-diffraction data. The importance of our findings is that we refined the empirical formula of charoite and demonstrated similarity between this mineral and phyllosilicates, as well as its differences relative to the "tube"-chain silicates of similar composition.

# CHAPTER 3.   Carbonatites.

## 3.1   Geological setting of the Murun carbonatites

The majority of carbonatite bodies are confined to the southern contact zone of the Little Murun with the Precambrian crystalline basement. Carbonatites occur in an aureole of aegirine-microcline fenites developed after Archean granite-gneisses, and Upper Proterozoic metasedimentary rocks (quartzites and sandstones) (Fig. 2.1.1). The carbonatites are closely associated with "torgolites" (quartz-carbonate rocks) and charoitites, and occupy an area of more than 10 km$^2$ (Vorob'ev & Malyshonok 1985). The carbonatites commonly form veins and lenses up to 0.5 m in thickness, or occur as cylindrical zoned bodies up to 1 m in diameter (Kogarko et al. 1995; Konev et al. 1996). According to some investigators (Vladykin & Tzaruk 1999), the main carbonatite body may reach up to 30 m in thickness, and is formed by interlayered pyroxene-, alkali feldspar-, and carbonate-rich zones. Several carbonatite bodies also occur in a contact zone of the Kedrovyi ("Cedar") syenite stock, some 5 km south-east of the Little Murun. These form veins or lenses (1-20 cm in thickness) in syenites, or occur as zoned bodies, several meters in size, with carbonates comprising up to 70 volumetric percent of the rock (Konev et al. 1996).

Previous studies have distinguished several varieties of carbonatites at the Murun complex (Vorob'ev & Malyshonok 1985; Konev et al. 1996). Two major types include calcite carbonatites and Ca-Sr-Ba carbonatites. The latter are divided into two groups: strontianite-barytocalcite and calcian-strontianite carbonatites (Konev et al. 1996). According to Konev et al. (1996), the majority of the calcite carbonatites and calcian-strontianite carbonatites are confined to the Kedrovyi massif, where they are closely associated with strontianite-barytocalcite carbonatites. Carbonatite bodies in the fenite aureole of the Malomurunskii massif are represented chiefly by the strontianite-barytocalcite variety.

46

## 3.2 Petrographic description of the samples studied

During the present study, twenty samples corresponding to various types of the Murun carbonate-rich rocks were examined. On the bases of their mineralogical and textural features, the samples were divided into four groups:

- *calcite carbonatite;*
- *Ba-Sr-Ca carbonatite;*
- *phlogopite-calcite carbonatite;*
- *quartz-feldspar-carbonate rock.*

*Calcite carbonatite* examined in the present study shows significant variation in the proportions of major and accessory mineral phases. The rock is composed mainly of carbonate (predominantly calcite), alkali feldspar and clinopyroxene. In the majority of samples, carbonates constitute from 25 to 80 vol.% of the rock, potassium feldspar from 10 to 70 vol.%, and clinopyroxene from 5-55 vol.%. Accessory minerals include titanite, quartz, dalyite, fluorapatite, barite, sulphides, tinaksite, zircon and turkestanite. In some samples (*e.g.* Mu-136/32, -136/33, -136/52), titanite and tinaksite gain the status of rock-forming minerals, and together comprise up to 70 vol.% of the rock. In these samples, fine-grained calcite and alkali feldspar are developed interstitially between titanite and tinaksite grains, and constitute only 10 to 30 vol.% of the rock. In hand specimens of the calcite carbonatites, carbonates occur as white to greyish-white aggregates, commonly replacing potassium feldspar. The latter commonly forms greenish-grey or brownish-green subhedral-to-euhedral grains up to 5 mm in size. Clinopyroxene occurs as dark green-to-almost black radial aggregates of elongated crystals up to 1.3 cm in diameter, or small (< 2 mm) anhedral grains in a carbonate matrix. In the titanite- and tinaksite-rich samples, titanite forms straw-yellow or brownish yellow elongate or wedge-shaped crystals up to 2 mm in size. Tinaksite forms acicular honey-yellow crystals up to 1.5 mm in length.

*Ba-Sr-Ca carbonatites* examined in the present study are composed mainly of carbonate, potassium feldspar and clinopyroxene. Accessory minerals include potassic

47

Fig. 3.2.1. Phenocryst of potassium feldspar in a carbonate matrix. Note a turbid altered core and inclusions of xenocrystic feldspar. Ba-Sr-Ca carbonatite (Mu-7). Field of view (FO V) 6 mm; (a) plane-polarized light, (b) crossed polars.

48
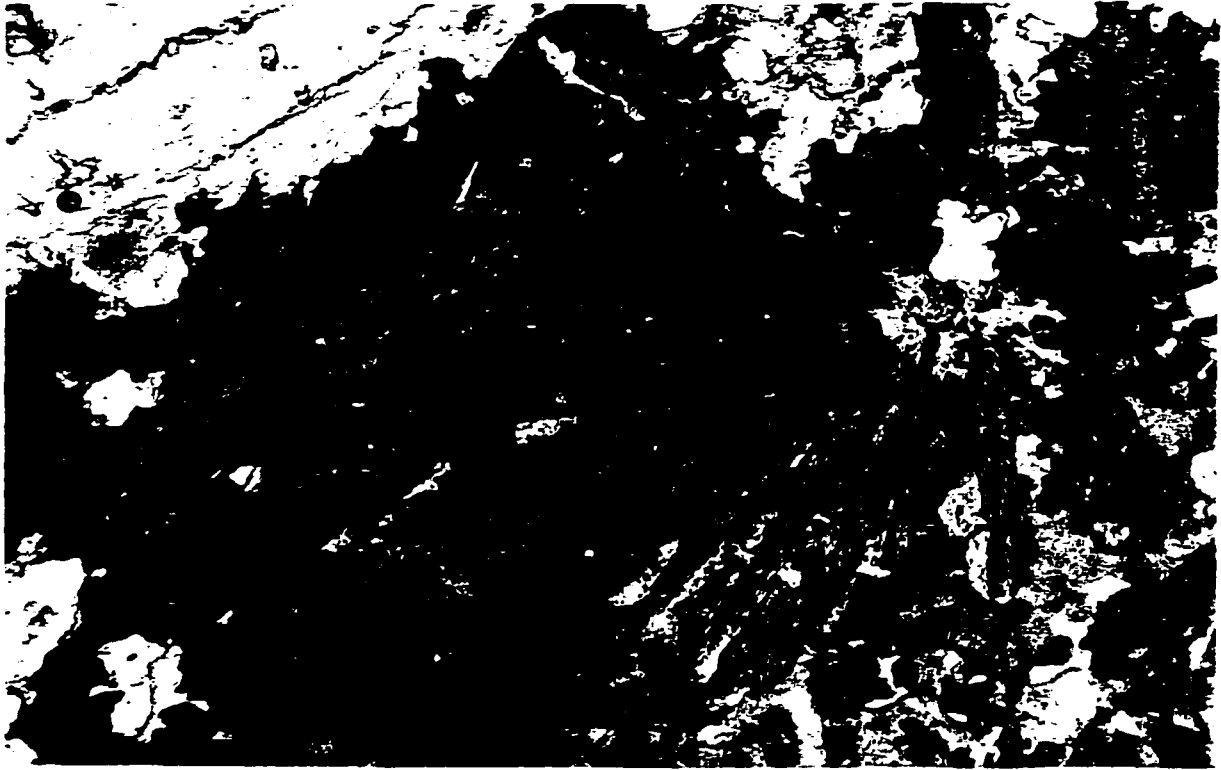
a
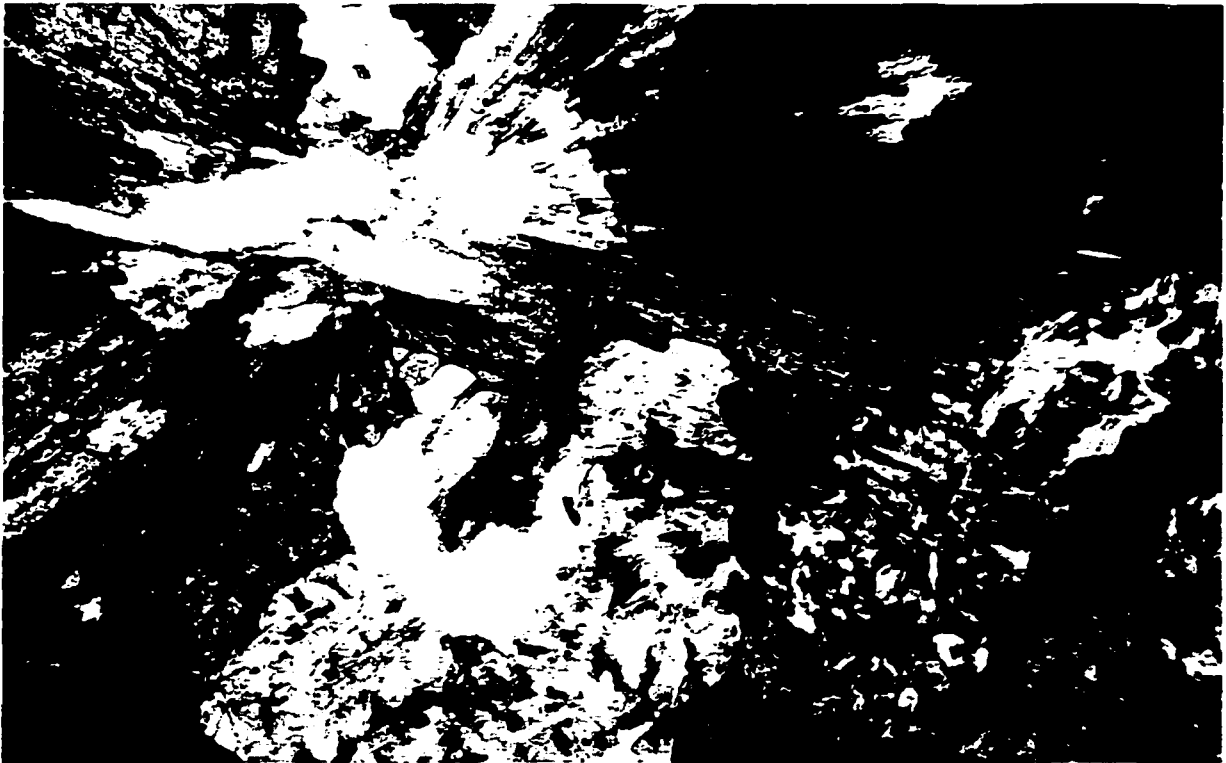


b

Fig. 3.2.2. Radial aggregates of clinopyroxene from Ba-Sr-Ca carbonatite, FOW 6 mm for both images. (a) Relict fragment of potassic richterite (pale blue) in clinopyroxene (green). (Mu-14); plane-polarized light. (b) Relationships between clinopyroxene, Fe-rich potassium feldspar (anomalous interference colour: ink-blue), and carbonates (white to grey) (Mu-180); crossed polars.

49

a
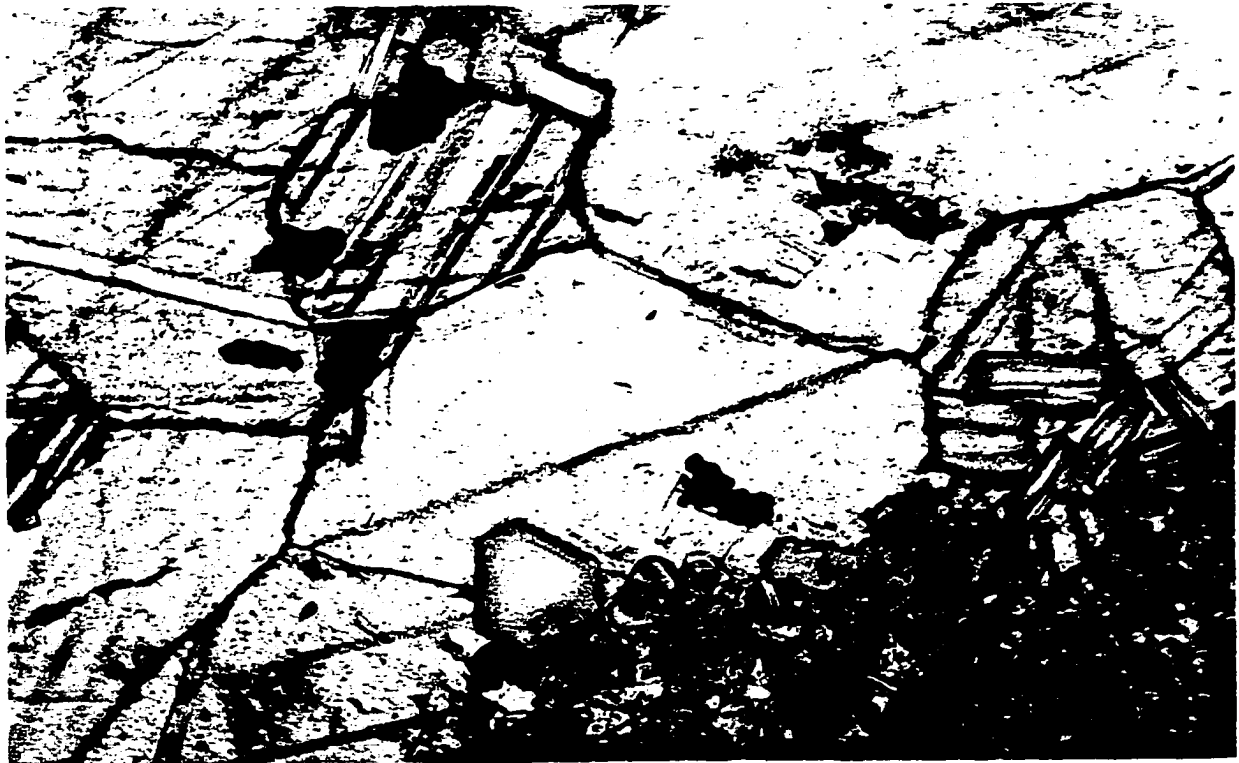


b

Fig. 3.2.3. Tabular crystals of phlogopite (pale orange-to-brownish yellow) in a mosaic of calcite crystals, phlogopite-calcite carbonatite (Mu-238). Note the presence of potassium feldspar (white, left) and sulphides (black). FOV 6 mm for both images; plane-polarised light.

50

richterite, dalyite, barite, fluorapatite, sulphides, fluorite and vanadinite. The modal composition of Ba-Sr-Ca carbonatites from the Murun complex is (vol.%): 45-40 carbonate, 25-20 alkali feldspar, 25-20 clinopyroxene, *ca. 5* apatite, <5 other accessory phases. However, the proportions of the major mineral phases vary significantly from one sample to another. The majority of the carbonatite samples examined have a layered texture formed by clinopyroxene- and potassium feldspar-rich zones in a carbonate matrix. Carbonate-rich zones of the rock are fine-grained, white to greyish-yellow with minor amounts (< 10 vol.%) of subhedral-to-anhedral clinopyroxene and potassium feldspar. Silicate-rich zones are composed of dark-green clinopyroxene and light yellow-to-greyish green, rarely apple-green (amazonite-like) potassium feldspar. The latter commonly occurs as euhedral crystals up to 6 mm with clear margins and a darker core, or clusters of euhedral-to-subhedral grains "cemented" by fine-grained carbonates (Fig. 3.2.1a,b). Clinopyroxene occurs as elongate crystals or radial aggregates of acicular crystals up to 1.5 cm in diameter in a carbonate matrix (Fig. 3.2.2a,b).

In *phlogopite-calcite* carbonatite, phlogopite comprises *ca.* 40 vol.% of the rock, carbonate (predominantly calcite) *ca.* 35 vol.%, and alkali feldspar less than 10 vol.% (Fig. 3.2.3a,b). Accessory phases include andradite, titanite, fluorapatite, rutile and sulphides.

*Quartz-feldspar-carbonate* rocks consist mainly of quartz (*ca.* 20 vol.%), calcite (*ca.* 30 vol.%), potassium feldspar (*ca.* 30 vol.%), and clinopyroxene (*ca.* 20 vol.%). The accessory mineral assemblage includes titanite, dalyite, sulphides and barite. In hand specimens, subhedral-to-euhedral grains of greenish potassium feldspar (up to 1.3 mm), and dark green acicular crystals and radial aggregates of clinopyroxene are distributed irregularly in a white fine-grained quartz-carbonate matrix.

## 3.3    Mineralogy of the carbonate-rich rocks

### 3.3.1  *Silicates*

*Potassium feldspar* is one of the major constituents of the examined rocks. In the majority of samples, the mineral forms subhedral-to-euhedral phenocrysts up to 6 mm in length, commonly with resorbed margins. Most of feldspar phenocrysts are fractured and

altered by carbonates to varying degrees. Large grains (>2 mm) commonly contain anhedral, highly-altered fragments of xenocrystic(?) feldspar. Grains of potassium feldspar less than 2 mm normally have a clear, fresh appearance. Some of the potassium feldspar crystals from the Ba-Sr-Ca carbonatite (*e.g.* Mu-7) show a prominent interpenetration twinning. The crystals from the calcite carbonatite commonly have a characteristic cross-hatched twinning. Potassium feldspar from the calcite carbonatite and Ba-Sr-Ca carbonatite commonly shows anomalous (ink-blue, brownish blue) interference colours, possibly arising from $Fe^{3+}$ in the structure (Figs. 3.2.2b and 3.3.1.1a,b).

Potassium feldspar from the Ba-Sr-Ca carbonatite, calcite carbonatite and quartz-feldspar-carbonate rock has very unusual composition. The mineral is highly enriched in Fe content, *i.e.* up to 7.5 wt.% or 0.27 atoms per formula unit (apfu) (Table 3.3.1.1, Fig. 3.3.1.2). In back-scattered electron images (BSE) and thin section, most of the feldspar phenocrysts exhibit a weak-to-moderate oscillatory or irregular zoning resulting from variations in $Fe_2O_3$ content (from 0.2-2.5 wt.% in low-average-atomic-number (*AZ*) zones to 3.0-7.5 wt.% in high-*AZ* zones; Table 3.3.1.1). The Fe/Al ratio varies from 0.06 to 0.40 among the zones. Such high concentrations of Fe are extremely rare in naturally-occurring alkali feldspar. Linthout and Lustenhouwer (1993) reported up to 14.5 wt.% $Fe_2O_3$ in high sanidine from Cancarix, Spain. It is noteworthy, however, that the highest $Fe_2O_3$ concentrations in Cancarix material were detected only in thin (< 3 μm) rims of sanidine crystals open into a miarolitic cavity occupied by aegirine grains, and that the central parts of the sanidine grains, as well as their rims not facing the cavity have only 1.0-3.6 wt.% $Fe_2O_3$. Most of the sanidine analyses with high Fe content given by Linthout and Lustenhouwer (1993) also have low totals (as low as 86.4 wt.%) and excess of Si in the empirical formulae (up to 3.13 apfu). Previously published data for potassium feldspar from the Murun complex (Konev *et al.* 1996) also indicate elevated concentrations of Fe in the samples from the calcite carbonatite (up to 2.6 wt.% $Fe_2O_3$) and from foyaites (up to 3.0 wt.% $Fe_2O_3$). Iron-rich alkali feldspar was also reported from several other localities, including Itrongay, Madagascar (up to 2.9 wt.% $Fe_2O_3$: Seto 1923, Nyfeler
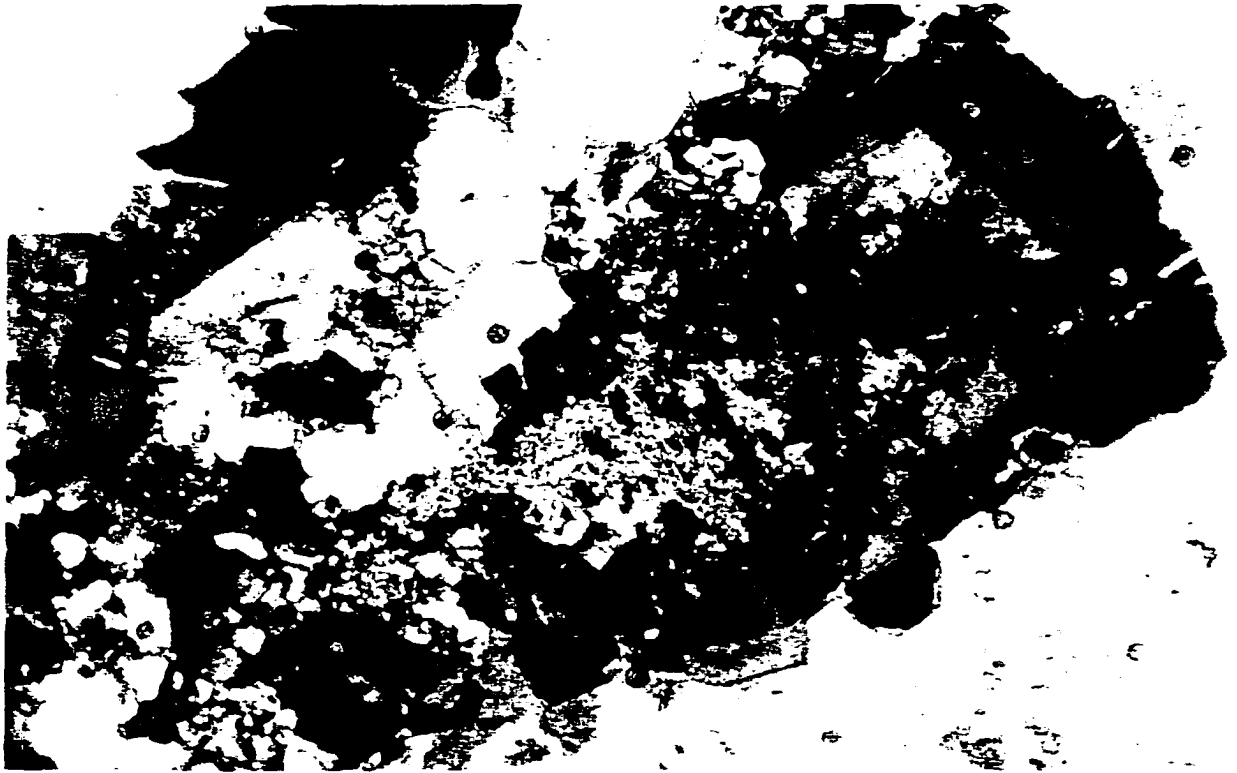
Fig. 3.3.1.1. Oscillatory-zoned crystals of potassium feldspar from the Ba-Sr-Ca carbonatite (Mu-14), crossed polars. (a) Phenocryst partially altered to a fine-grained carbonate aggregate, FOV 6 mm. (b) Cluster of crystals in a carbonate matrix; FOV 4.5 mm.

53
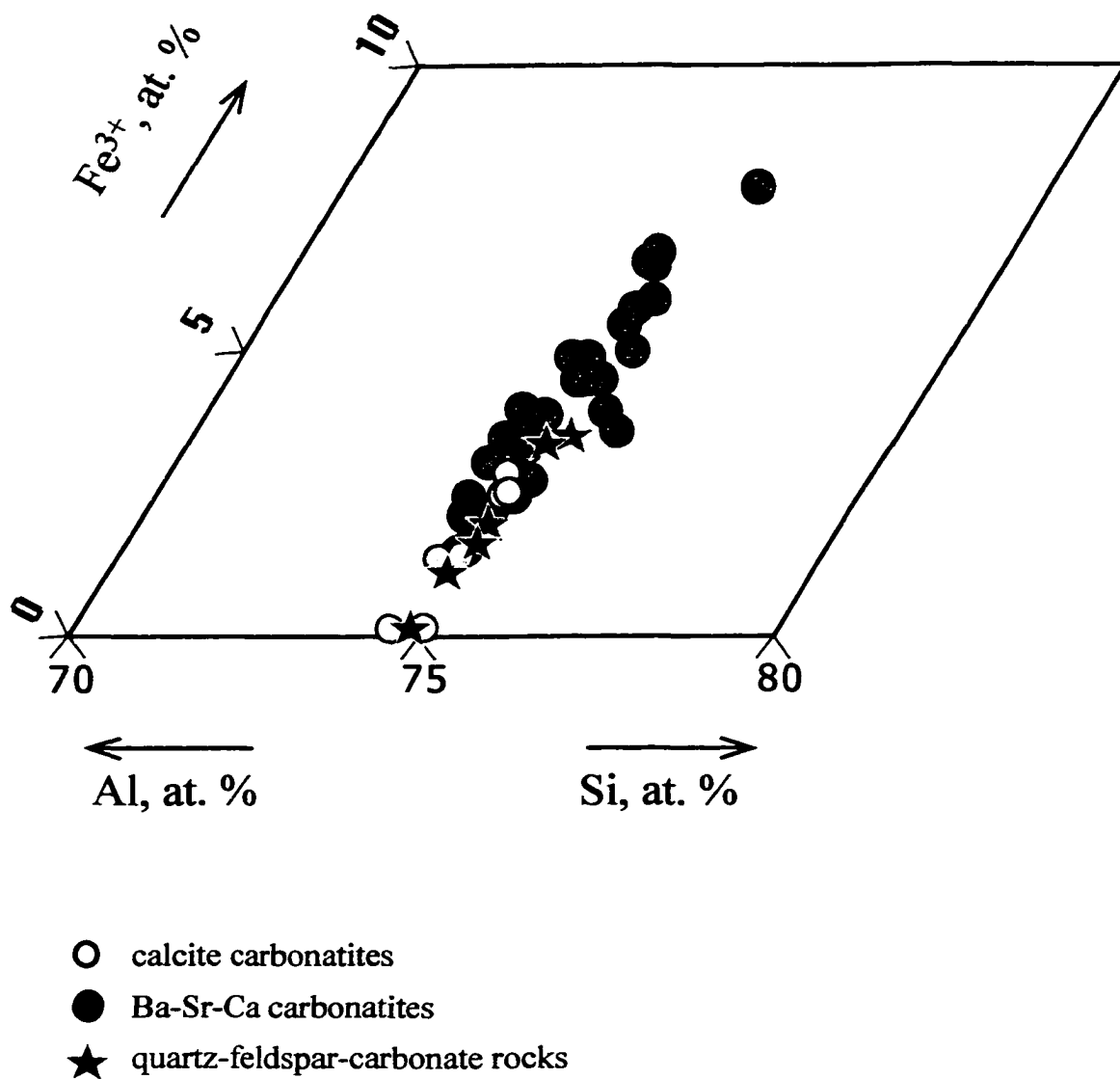
Fig. 3.3.1.2. Compositions of Fe-bearing potassium feldspar from carbonate-rich rocks of the Murun complex.

54

Table 3.3.1.1. Representative compositions of potassium feldspar from the carbonate-rich rocks.

| Wt. % | 1 | 2 | 3 | 4 | 5 | 6 | 7 | 8 | 9 | 10 | 11 |
|---|---|---|---|---|---|---|---|---|---|---|---|
| $SiO_2$ | 64.14 | 64.42 | 63.30 | 63.35 | 63.86 | 63.44 | 63.68 | 62.62 | 62.32 | 62.14 | 63.15 |
| $Al_2O_3$ | 17.26 | 15.44 | 13.45 | 15.78 | 14.64 | 16.78 | 16.00 | 13.73 | 13.13 | 11.98 | 15.81 |
| $Fe_2O_3$ | 1.57 | 4.50 | 6.52 | 3.70 | 5.55 | 2.74 | 3.83 | 6.03 | 7.24 | 7.50 | 3.69 |
| $Na_2O$ | 0.08 | n.d | n.d | n.d | n.d | n.d | n.d | n.d | n.d | n.d | n.d |
| $K_2O$ | 16.51 | 16.78 | 16.41 | 16.59 | 16.82 | 16.54 | 16.29 | 16.35 | 16.29 | 17.07 | 17.20 |
| Total | 99.56 | 101.14 | 99.68 | 99.42 | 100.87 | 99.50 | 99.80 | 98.95 | 98.98 | 98.69 | 99.85 |

Formulae calculated on the basis of 8 atoms of oxygen

| | 1 | 2 | 3 | 4 | 5 | 6 | 7 | 8 | 9 | 10 | 11 |
|---|---|---|---|---|---|---|---|---|---|---|---|
| Si | 2.998 | 2.998 | 3.011 | 2.992 | 2.995 | 2.982 | 2.990 | 3.000 | 2.996 | 3.016 | 2.982 |
| Al | 0.951 | 0.847 | 0.754 | 0.879 | 0.809 | 0.930 | 0.886 | 0.775 | 0.744 | 0.685 | 0.880 |
| $Fe^{3+}$ | 0.055 | 0.158 | 0.233 | 0.132 | 0.196 | 0.097 | 0.135 | 0.217 | 0.262 | 0.274 | 0.131 |
| Na | 0.007 | - | - | - | - | - | - | - | - | - | - |
| K | 0.984 | 0.996 | 0.996 | 1.000 | 1.006 | 0.992 | 0.976 | 0.999 | 0.999 | 1.057 | 1.036 |
| *Fe/Al* | *0.058* | *0.186* | *0.309* | *0.150* | *0.242* | *0.104* | *0.152* | *0.280* | *0.352* | *0.400* | *0.149* |

| Wt. % | 12 | 13 | 14 | 15 | 16 | 17 | 18 | 19 | 20 | 21 | 22 |
|---|---|---|---|---|---|---|---|---|---|---|---|
| $SiO_2$ | 64.60 | 64.78 | 64.87 | 64.46 | 63.54 | 63.86 | 63.47 | 63.49 | 61.77 | 62.15 | 60.88 |
| $Al_2O_3$ | 16.52 | 16.51 | 18.08 | 17.31 | 17.34 | 15.56 | 17.80 | 16.55 | 20.24 | 19.89 | 18.98 |
| $Fe_2O_3$ | 2.91 | 2.83 | 0.24 | 1.66 | 1.23 | 3.82 | 0.43 | 2.18 | n.d | n.d | n.d |
| BaO | n.d | n.d | n.d | n.d | n.d | n.d | n.d | n.d | 3.48 | 2.47 | 1.73 |
| $Na_2O$ | n.d | n.d | 0.37 | 0.69 | 0.19 | 0.50 | n.d | 0.47 | 0.98 | 0.71 | 0.94 |
| $K_2O$ | 17.32 | 17.37 | 16.07 | 15.59 | 15.98 | 15.60 | 16.86 | 16.23 | 14.64 | 15.00 | 14.85 |
| Total | 101.36 | 101.49 | 99.63 | 99.71 | 98.28 | 99.34 | 98.56 | 98.92 | 101.11 | 100.22 | 97.38 |

Formulae calculated on the basis of 8 atoms of oxygen

| | 12 | 13 | 14 | 15 | 16 | 17 | 18 | 19 | 20 | 21 | 22 |
|---|---|---|---|---|---|---|---|---|---|---|---|
| Si | 2.992 | 2.995 | 3.007 | 2.998 | 2.999 | 3.006 | 2.993 | 2.996 | 2.890 | 2.910 | 2.927 |
| Al | 0.902 | 0.900 | 0.988 | 0.949 | 0.965 | 0.863 | 0.989 | 0.921 | 1.116 | 1.098 | 1.076 |
| $Fe^{3+}$ | 0.101 | 0.098 | 0.008 | 0.058 | 0.044 | 0.135 | 0.015 | 0.077 | - | - | - |
| Ba | - | - | - | - | - | - | - | - | 0.064 | 0.045 | 0.033 |
| Na | - | - | 0.033 | 0.062 | 0.017 | 0.046 | - | 0.043 | 0.089 | 0.064 | 0.088 |
| K | 1.023 | 1.025 | 0.950 | 0.925 | 0.962 | 0.937 | 1.014 | 0.977 | 0.874 | 0.912 | 0.911 |
| *Fe/Al* | *0.112* | *0.109* | *0.008* | *0.061* | *0.046* | *0.156* | *0.015* | *0.084* | - | - | - |

n.d = not detected. Analyses 1-11: *Ba-Sr-Ca carbonatite* (1-3 − *Mu-8*; 4-5 − *Mu-14*; 6-9 − *Mu-15*; 10-11 − *Mu-151*); 12-15: *calcite carbonatite* (12 − *Mu-136/32*; 13 − *Mu-136/33*; 14-15 − *Mu-1052/20*); 16-19: *quartz-feldspar-carbonate rock* (16-17 − *Mu-136/46*; 18-19 − *Mu-145*); 20-22: *phlogopite-calcite carbonatite* (*Mu-238*).

55

1998) and Leucite Hills, Wyoming (up to 4.8 wt.% $Fe_2O_3$: Carmichael 1967). Several Fe-bearing phases with feldspar-type structure have been prepared synthetically. They include low-sanidine with the composition $K[Al_{0.72}Fe_{0.28}Si_3O_8]$ synthesised under hydrothermal conditions at 525°C (P=2 kbar) by Nadezhina *et al.* (1993), and $K[FeSi_3O_8]$ grown hydrothermally at P=1-2 kbars by Wones & Appleman (1961, 1963).

The compositions of the potassium feldspar examined in the present work show negative correlation between the Al and Fe contents (Fig. 3.3.1.2), suggesting the simple substitution scheme $Fe^{3+} \Leftrightarrow Al^{3+}$. The substitution mechanism and re-distribution of $Fe^{3+}$ among the $T_1$ and $T_2$ positions in natural feldspars was investigated previously by several researchers. These studies have shown that in low microcline and low albite, $Fe^{3+}$ is confined exclusively to the $T_1$ sites (Petrov *et al.* 1989). In low-sanidine, $Fe^{3+}$ ions occupy both $T_1$ and $T_2$ sites, with preference for $T_1$ (Petrov and Hafner 1988). Nyfeler *et al.* (1998) concluded that in high-sanidine, increasing Si - Al disorder is accompanied by more equal distribution of $Fe^{3+}$ between the $T_1$ and $T_2$ positions.

In contrast to other types of carbonate-rich rocks studied in the present work, potassium feldspar from the phlogopite-calcite carbonatite contains no detectable $Fe_2O_3$. Some phenocrysts, however, show a weak zoning resulting from enrichment of a rim in the celsian component (up to 6.6 mol.% $BaAl_2Si_2O_8$). BaO content varies from *ca.* 1.7 wt.% in the core to 3.5 wt.% in the outermost parts of the crystals, *i.e.* from 0.03 to 0.06 apfu (Table 3.3.1.1).

*Clinopyroxene* is found in the majority of the samples examined, with an exception of the phlogopite-calcite carbonatite. The mineral commonly occurs as coarse (*ca.* 1cm) prismatic crystals, or radial aggregates of elongate crystals up to 1.5 cm in diameter (Fig. 3.3.1.3a,b). The crystals of clinopyroxene are pleochroic from brownish yellow or orange brown to dark green or bluish green. Some of the crystals exhibit complex zoning (*e.g.* Mu-145; Fig. 3.3.1.3b) and twinning (*e.g.* Mu-8) in thin section. Radial aggregates of pyroxene may enclose anhedral fragments of highly-resorbed pyroxene, probably representing an earlier generation of the

56

a



b

Fig. 3.3.1.3. Complexly-zoned clinopyroxene from the quartz-feldspar-carbonate rock, plane-polarised light. (a) Clinopyroxene associated with quartz (below) and carbonates (upper right corner), Mu-136/46, FOV 6 mm; (b) phenocrysts of clinopyroxene and potassium feldspar in a quartz-carbonate matrix; Mu145; FOV 4.5 mm.

57

Table 3.3.1.2. Representative compositions of clinopyroxene from the carbonate-rich rocks.

| Wt. % | 1 | 2 | 3 | 4 | 5 | 6 | 7 | 8 | 9 | 10 | 11 | 12 | 13 | 14 | 15 |
|---|---|---|---|---|---|---|---|---|---|---|---|---|---|---|---|
| | core | | rim | | core | rim | relict | | host | | | | | | |
| $Na_2O$ | 8.03 | 8.30 | 9.63 | 4.50 | 7.81 | 10.32 | 6.27 | 8.07 | 9.24 | 9.07 | 11.86 | 4.73 | 6.08 | 9.62 | 11.81 |
| MgO | 2.83 | 2.87 | 2.94 | 7.55 | 3.80 | 2.65 | 1.75 | 1.42 | 2.62 | 0.92 | 1.89 | 6.79 | 4.41 | 0.73 | 1.87 |
| CaO | 10.17 | 9.38 | 8.01 | 15.91 | 9.45 | 6.30 | 11.85 | 8.81 | 6.81 | 7.09 | 2.67 | 15.98 | 13.40 | 6.93 | 3.09 |
| MnO | 0.50 | 0.47 | 0.40 | 0.26 | 0.62 | 0.41 | 1.07 | 0.67 | 0.61 | 1.16 | n.d | 0.35 | 0.41 | 0.57 | 0.17 |
| FeO* | 8.85 | 7.18 | 2.57 | 7.61 | 6.99 | 2.48 | 12.09 | 9.51 | 5.38 | 8.21 | 1.60 | 7.95 | 8.92 | 6.58 | 1.32 |
| $Fe_2O_3$* | 15.41 | 17.00 | 24.27 | 12.33 | 19.22 | 25.59 | 15.49 | 18.91 | 22.24 | 20.93 | 27.70 | 10.15 | 13.85 | 23.50 | 28.44 |
| $V_2O_3$ | 0.49 | 0.33 | 0.41 | n.d | 0.27 | 0.28 | 0.72 | 1.24 | 0.70 | 1.18 | 1.77 | 0.47 | 0.66 | 0.32 | 0.42 |
| $Al_2O_3$ | n.d | n.d | n.d | n.d | n.d | n.d | n.d | n.d | n.d | n.d | n.d | 0.38 | 0.37 | n.d | 0.26 |
| $TiO_2$ | 2.12 | 2.20 | 0.52 | 0.21 | 0.33 | 0.28 | 0.13 | 0.63 | 0.58 | 0.63 | 0.23 | 0.13 | 0.27 | 0.82 | 0.90 |
| $SiO_2$ | 52.49 | 51.27 | 52.41 | 52.18 | 52.20 | 52.93 | 50.54 | 50.90 | 51.62 | 51.52 | 52.84 | 52.44 | 52.12 | 51.19 | 52.47 |
| Total | 100.89 | 99.00 | 101.16 | 100.55 | 100.69 | 101.24 | 99.91 | 100.16 | 99.80 | 100.72 | 100.56 | 99.37 | 100.49 | 100.26 | 100.75 |
| Formulae calculated on the basis of 6 atoms of oxygen | | | | | | | | | | | | | | | |
| Na | 0.595 | 0.626 | 0.708 | 0.332 | 0.580 | 0.757 | 0.480 | 0.612 | 0.692 | 0.682 | 0.874 | 0.351 | 0.452 | 0.725 | 0.869 |
| Mg | 0.161 | 0.166 | 0.166 | 0.428 | 0.217 | 0.149 | 0.103 | 0.083 | 0.151 | 0.053 | 0.107 | 0.388 | 0.252 | 0.042 | 0.106 |
| Ca | 0.417 | 0.391 | 0.325 | 0.648 | 0.388 | 0.255 | 0.501 | 0.369 | 0.282 | 0.295 | 0.109 | 0.656 | 0.551 | 0.289 | 0.126 |
| Mn | 0.016 | 0.015 | 0.013 | 0.008 | 0.020 | 0.013 | 0.036 | 0.022 | 0.020 | 0.038 | - | 0.011 | 0.013 | 0.019 | 0.005 |
| $Fe^{2+}$ | 0.283 | 0.234 | 0.082 | 0.242 | 0.224 | 0.078 | 0.399 | 0.311 | 0.174 | 0.266 | 0.051 | 0.255 | 0.286 | 0.214 | 0.042 |
| $Fe^{3+}$ | 0.444 | 0.498 | 0.692 | 0.353 | 0.554 | 0.728 | 0.460 | 0.556 | 0.647 | 0.611 | 0.792 | 0.293 | 0.400 | 0.688 | 0.812 |
| V | 0.015 | 0.010 | 0.012 | - | 0.008 | 0.008 | 0.023 | 0.039 | 0.022 | 0.037 | 0.054 | 0.014 | 0.020 | 0.010 | 0.013 |
| Al | - | - | - | - | - | - | - | - | - | - | - | 0.017 | 0.017 | - | 0.012 |
| Ti | 0.061 | 0.064 | 0.015 | 0.006 | 0.010 | 0.008 | 0.040 | 0.019 | 0.017 | 0.018 | 0.007 | 0.004 | 0.003 | 0.024 | 0.026 |
| Si | 2.007 | 1.995 | 1.987 | 1.983 | 1.999 | 2.002 | 1.995 | 1.990 | 1.995 | 1.999 | 2.007 | 2.010 | 2.000 | 1.990 | 1.991 |
| Aeg | 49.95 | 55.42 | 73.65 | 34.49 | 55.68 | 76.18 | 47.83 | 58.57 | 66.56 | 65.66 | 83.37 | 31.30 | 42.61 | 72.85 | 84.61 |
| Di | 18.17 | 18.54 | 17.68 | 41.85 | 21.82 | 15.63 | 10.70 | 8.71 | 15.53 | 5.72 | 11.27 | 41.46 | 26.88 | 4.48 | 11.02 |
| Hed | 31.88 | 26.04 | 8.67 | 23.65 | 22.50 | 8.19 | 41.47 | 32.72 | 17.91 | 28.63 | 5.36 | 27.24 | 30.51 | 22.67 | 4.37 |

n.d = not detected; * $Fe^{2+}/Fe^{3+}$ ratio calculated from stoichiometry. Analyses 1-6: *Ba-Sr-Ca carbonatite (1-3 – Mu-8; 4 – Mu-14; 5-6 – Mu-151); 7-13: calcite carbonatite (7-9 – Mu-180; 10 – Mu-136/32; 11 – Mu-136/52; 12-13 – Mu-1052/20); 14-15: quartz-feldspar-carbonate rock (Mu-145).*
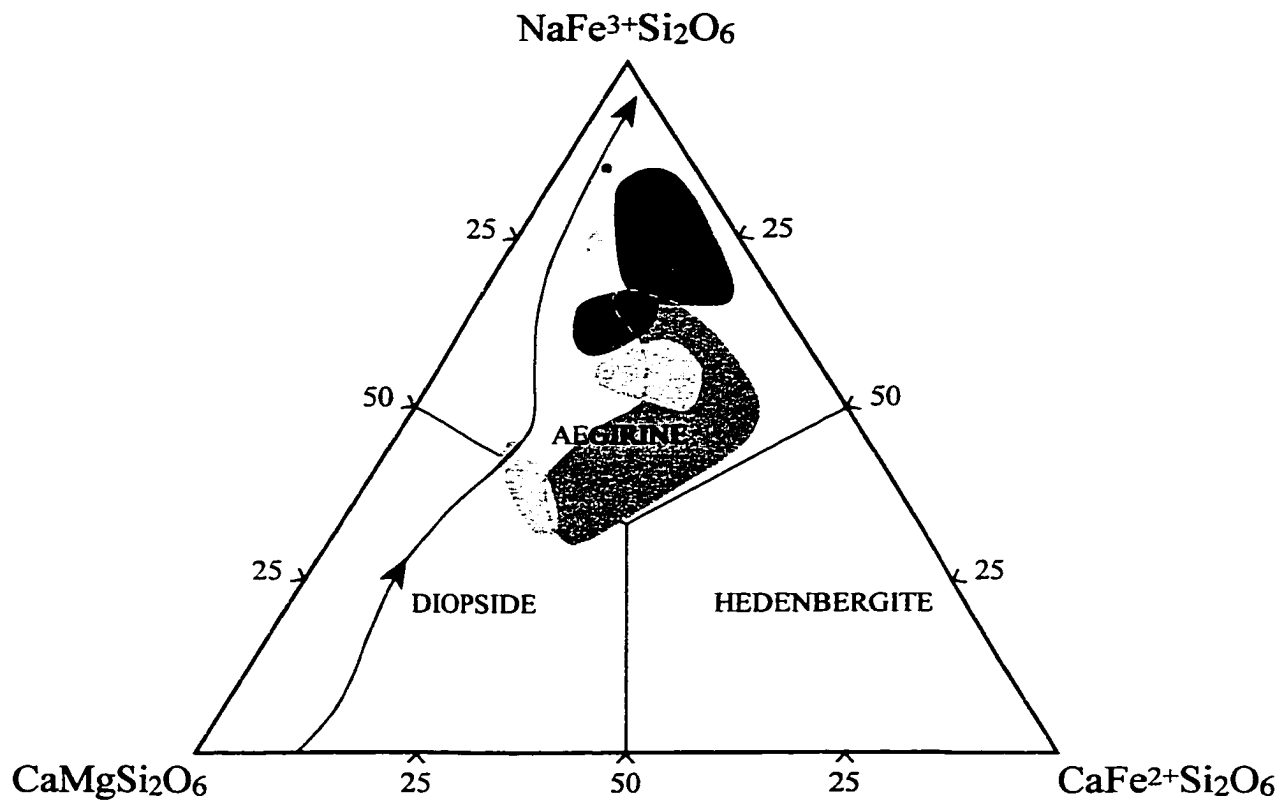
58

Fig. 3.3.1.4. Compositions of clinopyroxene from carbonate-rich rocks
of the Murun alkaline complex.

59

mineral. In a few cases, stellate aegirine aggregates contain anhedral fragments of potassic richterite (Fig. 3.2.2a). Compositionally, the bulk of the clinopyroxene crystals from the carbonatites correspond to aegirine and aegirine-augite (Table 3.3.1.2; Fig. 3.3.1.4). The fragments of early clinopyroxene from the Ba-Sr-Ca carbonatite and calcite carbonatite, however, have a preponderance of the diopside component (*ca.* 41.7 mol.% $CaMgSi_2O_6$; analyses 4 and 12 in Table 3.3.1.2). Most of the clinopyroxene is Al-poor with $TiO_2$ content varying from 0.2 to 2.2 wt.% in pyroxene from the Ba-Sr-Ca carbonatite, 0.7 to 1.8 wt.% from the calcite carbonatite, and 0.3 wt.% in pyroxene from the quartz-feldspar-carbonate rock. Most of the clinopyroxene crystals exhibit noticeable enrichment in $V_2O_3$ content (up to 1.2 wt.% in the Ba-Sr-Ca carbonatite; up to 1.8 wt.% in the calcite carbonatite and *ca.* 0.4 wt.% in the quartz-feldspar-carbonate rock). Those from the calcite carbonatite and Ba-Sr-Ca carbonatite show a significant compositional variation within the aegirine field (Fig. 3.3.1.4). The innermost parts of the crystals correspond to aegirine-augite (*ca.* 50 mol.% $NaFeSi_2O_6$), whereas rim zones contain *ca.* 73-83 mol.% $NaFeSi_2O_6$. Clinopyroxene from the quartz-feldspar-carbonate rock is the most evolved in terms of the aegirine content, containing up to 85 mol.% $NaFeSi_2O_6$ (Table 3.3.1.2, Fig. 3.3.1.4).

*Amphibole* is rare in the examined samples. The mineral probably represents remnants of an early paragenesis, as it occurs exclusively in the Ba-Sr-Ca carbonatite as anhedral resorbed fragments in the central parts of stellate aegirine aggregates (Fig. 3.2.2a). Amphibole is also found as subhedral-to-euhedral diamond-shaped crystals up to 0.6 mm enclosed in a carbonate matrix (Fig. 3.3.1.5). The mineral is slightly pleochroic from light blue to greyish blue.

According to the contemporary nomenclature (Leake *et al.* 1997), the amphibole corresponds to potassic richterite (Table 3.3.1.3), and commonly shows a core-to-rim zoning, with a core enriched in Fe, and depleted in Mg. The $\Sigma(FeO+Fe_2O_3)$ and MgO contents vary from *ca.* 17.2 and 12.6 wt.%, respectively in the cores to 11.2 and 16 wt.% in the peripheral

60

parts of the crystals. The amphibole is Ti-poor (< 0.6 wt.% $TiO_2$), and does not contain detectable Al. Initially, an attempt was made to recalculate the amphibole analyses on the basis of 13 small cations in the $C$- and $T$-sites (Mg+Fe+Mn+Ti+Si) and 23 negative charges. This recalculation method leads to unrealistic amounts of large cations (Na+K+Ca) in the $A$- and $B$-sites. Hence, we suggest that a small proportion of Ca may enter the $C$-site in the Murun richterite, as originally proposed for some sodic amphiboles by Hawthorne (1983). As the total number of cations cannot exceed 16, we recalculated the analyses assuming the complete occupancy at all cationic sites (Table 3.3.1.3).



Fig. 3.3.1.5. Euhedral crystal of potassic richterite (blue) and clinopyroxene (greenish brown) in a carbonate matrix (white), Ba-Sr-Ca carbonatite (Mu-151). FOV 6 mm; plane-polarised light.

61

Table 3.3.1.3. Representative compositions of potassic richterite
from Ba-Sr-Ca carbonatites.

| Wt. % | 1 | 2 | 3 | 4 | 5 | 6 | 7 |
|---|---|---|---|---|---|---|---|
| $SiO_2$ | 54.27 | 54.20 | 53.96 | 53.07 | 53.77 | 53.43 | 54.29 |
| $TiO_2$ | 0.51 | 0.53 | 0.20 | 0.20 | n.d | n.d | n.d |
| FeO* | 6.36 | 5.86 | 8.09 | 8.07 | 5.12 | 10.01 | 4.30 |
| $Fe_2O_3$* | 6.22 | 5.84 | 5.42 | 5.17 | 5.25 | 7.24 | 6.90 |
| MgO | 15.31 | 15.38 | 15.42 | 15.17 | 16.79 | 12.56 | 15.97 |
| MnO | 1.05 | 0.82 | 0.71 | 0.76 | 0.65 | 1.06 | 1.18 |
| CaO | 2.20 | 2.04 | 4.26 | 3.83 | 3.24 | 2.35 | 2.12 |
| $Na_2O$ | 6.30 | 6.43 | 4.90 | 4.89 | 5.73 | 6.06 | 6.29 |
| $K_2O$ | 4.89 | 4.90 | 5.44 | 5.32 | 4.59 | 5.04 | 5.02 |
| Total * | 97.11 | 96.00 | 98.40 | 96.48 | 95.15 | 97.75 | 96.07 |

Formulae calculated on the basis of 16 cations

| | 1 | 2 | 3 | 4 | 5 | 6 | 7 |
|---|---|---|---|---|---|---|---|
| Si | 7.953 | 7.998 | 7.881 | 7.899 | 7.964 | 7.947 | 7.986 |
| $Fe^{3+}_{IV}$ | 0.047 | 0.002 | 0.119 | 0.101 | 0.036 | 0.053 | 0.014 |
| $\Sigma$ | 8.000 | 8.000 | 8.000 | 8.000 | 8.000 | 8.000 | 8.000 |
| | | | | | | | |
| Ti | 0.056 | 0.059 | 0.022 | 0.022 | - | - | - |
| $Fe^{2+}$ | 0.779 | 0.723 | 0.988 | 1.005 | 0.634 | 1.245 | 0.530 |
| $Fe^{3+}_{VI}$ | 0.639 | 0.645 | 0.476 | 0.478 | 0.549 | 0.758 | 0.750 |
| Mg | 3.346 | 3.384 | 3.357 | 3.367 | 3.708 | 2.785 | 3.503 |
| Mn | 0.130 | 0.103 | 0.088 | 0.096 | 0.082 | 0.134 | 0.147 |
| $\Sigma$ | 4.950 | 4.914 | 4.931 | 4.968 | 4.973 | 4.922 | 4.930 |
| | | | | | | | |
| Na | 1.790 | 1.840 | 1.388 | 1.411 | 1.646 | 1.748 | 1.794 |
| K | 0.915 | 0.923 | 1.014 | 1.010 | 0.867 | 0.956 | 0.942 |
| Ca | 0.345 | 0.323 | 0.667 | 0.611 | 0.514 | 0.375 | 0.334 |
| $\Sigma$ | 3.050 | 3.086 | 3.069 | 3.032 | 3.027 | 3.078 | 3.070 |

n.d = not detected; * $Fe^{2+}/Fe^{3+}$ ratio calculated from stoichiometry.
Analyses 1-2: *Mu-8*; 3-5: *Mu-14*; 6-7: *Mu-151* (6 – core, 7 – rim).

*Phlogopite* is found only in the phlogopite-calcite carbonatite, where it forms polygranular aggregates of subhedral, commonly altered grains in a carbonate matrix, or occurs as euhedral tabular crystals up to 3 mm across (Fig. 3.2.3a,b). The majority of phlogopite crystals show distinct pleochroism from orange to light brown or from lettuce-green to brown. In BSE, the phlogopite commonly exhibits distinct zoning with a high-$AZ$ core and homogeneous or oscillatory zoned relatively low-$AZ$ rim. The difference in $AZ$ is created by variations in Ba/K and Fe/Mg proportions (Table 3.3.1.4). The core of phlogopite crystals contains up to 2.4 wt.% BaO, up to 11 wt.% FeO, 9.8 wt.% $K_2O$ and 20 wt.% MgO, as opposed to *ca.* 0.2 wt.% BaO, 7.7 wt.% FeO, 10.5 wt.% $K_2O$ and 22.5 wt.% MgO in the low-$AZ$ zones (Table 3.3.1.4). Some of the phlogopite also contains appreciable $TiO_2$ (up to 1.4 wt.%), and is slightly enriched in MnO (*ca.* 0.4 wt.%) and $V_2O_3$ (up to 0.2 wt.%; Table 3.3.1.4) contents. In terms of the composition, the Murun phlogopite is similar to micas from several other carbonatite occurrences, *e.g.* Mt. Weld (Australia), carbonatite complexes of Arkansas (U.S.A.), and Busumbu (Uganda) (Fig. 3.3.1.6a and references therein). Our material is unusual in containing high Ba coupled with negligible Na content (Fig. 3.3.1.6b).

*Titanite* is relatively common in the calcite carbonatite, and in some cases (e.g. Mu-136/33 and Mu-136/32), comprises 20 to 60 vol.% of the rock. The mineral occurs as subhedral-to-euhedral, elongated or wedge-shaped, straw-yellow crystals up to 1 mm in size, set in a carbonate matrix. The titanite is found in association with tinaksite, alkali feldspar, calcite, clinopyroxene and turkestanite. The mineral is commonly resorbed along fractures and margins by carbonates, barite and tinaksite (Figs. 3.3.1.7 and 3.3.1.8), and in some samples (e.g. Mu-114/2), is almost fully replaced by these minerals. In thin sections, the majority of the titanite crystals show distinct zoning, with red cores and colourless-to-grey rims (Fig. 3.3.1.9a.b). This zoning results from enrichment of the central parts of crystals in Nb (up to 1.7 wt.% $Nb_2O_5$) relative to the margins (*ca.* 0.5 wt.% $Nb_2O_5$) (Table 3.3.1.5). Some of the titanite from the calcite carbonatites also exhibits slight enrichment in Zr content (up to 0.7 wt.% $ZrO_2$). The titanite is Al-free, and contains moderate $Fe_2O_3$ (0.6 to 2.3 wt.%) and *ca.* 0.5 wt.%

63

Table 3.3.1.4. Representative compositions of phlogopite from the phlogopite-calcite carbonatite (Mu-238).

| Wt.% | 1 | 2 | 3 | 4 | 5 | 6 | 7 |
|---|---|---|---|---|---|---|---|
| $SiO_2$ | 39.61 | 41.37 | 41.91 | 37.30 | 37.23 | 40.61 | 39.19 |
| $TiO_2$ | 1.41 | 0.54 | 0.63 | 1.36 | 0.94 | 0.78 | 0.74 |
| $Al_2O_3$ | 12.96 | 11.57 | 10.87 | 13.33 | 13.05 | 11.50 | 11.66 |
| FeO* | 11.08 | 7.78 | 7.67 | 9.28 | 9.11 | 7.87 | 7.64 |
| $Fe_2O_3$* | n.d | n.d | n.d | n.d | n.d | 0.25 | 1.15 |
| $V_2O_3$ | 0.14 | n.d | 0.18 | n.d | n.d | n.d | n.d |
| MnO | 0.37 | 0.42 | 0.39 | 0.44 | 0.46 | 0.28 | 0.39 |
| MgO | 20.24 | 22.56 | 22.61 | 20.82 | 21.15 | 22.85 | 22.24 |
| $Na_2O$ | 0.25 | 0.03 | 0.15 | 0.12 | 0.29 | 0.04 | 0.14 |
| $K_2O$ | 9.97 | 10.25 | 10.12 | 9.77 | 9.78 | 10.68 | 10.41 |
| BaO | 0.35 | 0.24 | 0.33 | 2.12 | 2.36 | 0.23 | n.d |
| Total | 96.38 | 95.00 | 94.86 | 94.54 | 94.62 | 94.84 | 93.56 |

Formulae calculated on the basis of 11 atoms of oxygen

| | 1 | 2 | 3 | 4 | 5 | 6 | 7 |
|---|---|---|---|---|---|---|---|
| Si | 2.887 | 3.008 | 3.045 | 2.799 | 2.801 | 2.967 | 2.911 |
| $Ti_{IV}$ | - | - | 0.024 | 0.022 | 0.028 | 0.043 | 0.004 |
| Al | 1.113 | 0.992 | 0.931 | 1.179 | 1.157 | 0.990 | 1.021 |
| $Fe^{3+}$ | - | - | - | - | 0.014 | - | 0.064 |
| $\Sigma$ | *4.000* | *4.000* | *4.000* | *4.000* | *4.000* | *4.000* | *4.000* |
| $Fe^{2+}$ | 0.675 | 0.473 | 0.466 | 0.582 | 0.573 | 0.481 | 0.474 |
| $Ti_{VI}$ | 0.077 | 0.030 | 0.039 | 0.055 | 0.025 | - | 0.037 |
| V | 0.008 | - | 0.010 | - | - | - | - |
| Mg | 2.200 | 2.446 | 2.450 | 2.330 | 2.372 | 2.489 | 2.463 |
| Mn | 0.023 | 0.026 | 0.024 | 0.028 | 0.029 | 0.017 | 0.025 |
| $\Sigma$ | *2.983* | *2.975* | *2.989* | *2.995* | *2.999* | *2.987* | *2.999* |
| Na | 0.035 | 0.004 | 0.021 | 0.017 | 0.042 | 0.006 | 0.020 |
| K | 0.927 | 0.951 | 0.938 | 0.935 | 0.939 | 0.996 | 0.987 |
| Ba | 0.010 | 0.014 | 0.009 | 0.062 | 0.070 | 0.007 | - |
| $\Sigma$ | *0.972* | *0.969* | *0.968* | *1.014* | *1.051* | *1.009* | *1.007* |

n.d = not detected; * $Fe^{2+}/Fe^{3+}$ ratio calculated from stoichiometry; 1-3: weakly zoned grain; 4-7: strongly zoned grain (4-5 – core; 6-7 – rim).

**Fig. 3.3.1.6.** Compositional variation of phlogopite from several carbonatite complexes.

Legend:

Murun (this work)

Afrikanda (Chakhmouradian, unpublished data)

Arkansas (McCormick & Heathcote 1988)

Sukulu (McCormick & Le Bas 1996)

Busumbu (McCormick & Le Bas 1996)

Nooitgedacht (McCormick & Le Bas 1996)

Newania (Viladkar & Wimmenauer 1986)
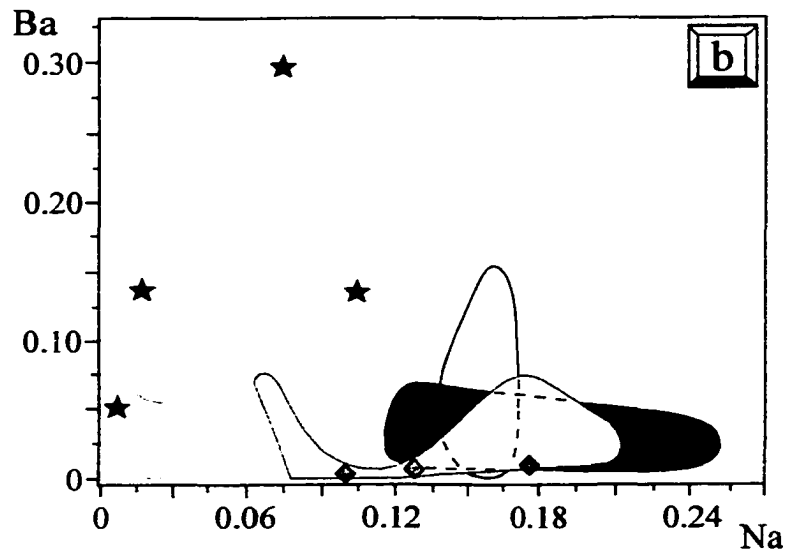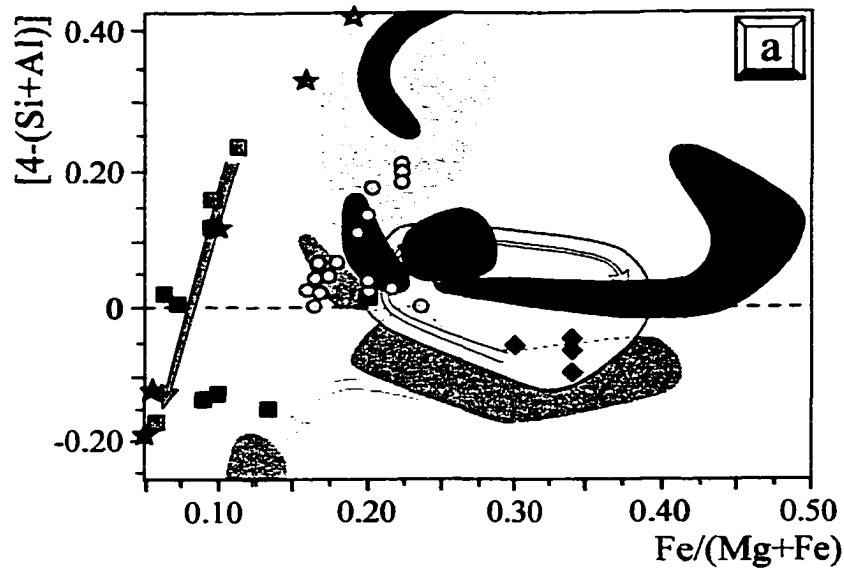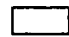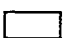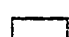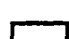
Dubrava (Skosyreva *et al.* 1988)

Mt. Weld (Middlemost 1990)

Fen (Mitchell 1980, Andersen 1989)

Loch Borralan (Young *et al.* 1994)

Uyaynah (Woolley *et al.* 1991)

Jacupiranga (Gaspar & Wyllie 1982)

Tapira (Brigatti *et al.* 1996)

Blackburn (Hogarth *et al.* 1988)

65

Fig. 3.3.1.7. Tinaksite and carbonates (white, pink, blue) developed interstitially and along the fractures in titanite (yellowish-grey). Calcite carbonatite (Mu-136/33); FOV 6 mm; crossed polars.



Fig. 3.3.1.8. BSE image of tinaksite (medium grey) developed interstitially with respect to potassium feldspar (dark grey) and titanite (light grey). Calcite carbonatite (Mu-136/33).

66
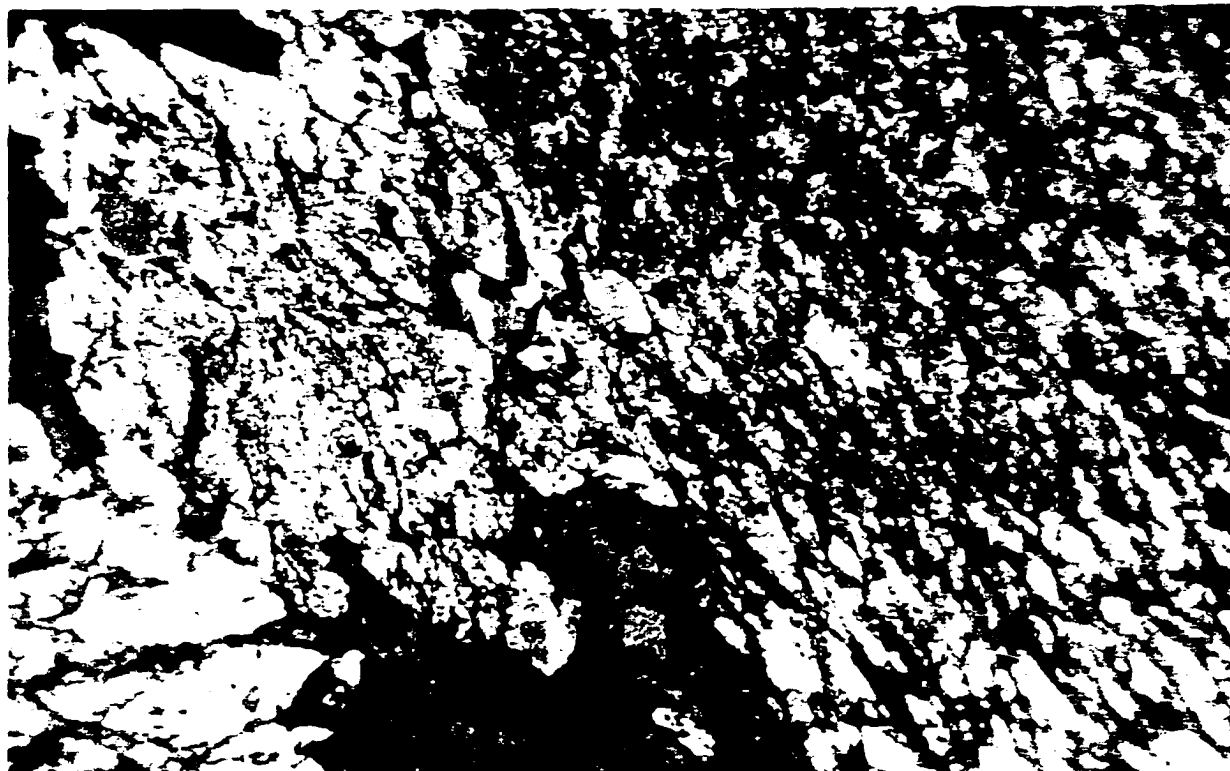
a



b

Fig. 3.3.1.9. Titanite crystals in the calcite carbonatite (Mu-136/33); plane polarised
light. (a) General view, FOV 6 mm; (b) Typical zonation pattern with cores
enriched in Nb (red), FOV 4.5 mm.

67

Table 3.3.1.5. Representative compositions of titanite from carbonatites

| Wt.% | 1 | 2 | 3 | 4 | 5 | 6 | 7 | 8 | 9 | 10 | 11 | 12 |
|---|---|---|---|---|---|---|---|---|---|---|---|---|
| $SiO_2$ | 30.52 | 30.36 | 30.08 | 30.56 | 30.33 | 30.24 | 30.73 | 30.18 | 30.59 | 29.45 | 29.55 | 30.25 |
| $Al_2O_3$ | n.d | n.d | n.d | n.d | n.d | n.d | n.d | n.d | n.d | 0.25 | 0.26 | 0.12 |
| $Fe_2O_3$ | 2.27 | 1.50 | 1.62 | 1.42 | 0.81 | 1.63 | 0.57 | 1.20 | 1.23 | 1.03 | 1.20 | 0.35 |
| $TiO_2$ | 37.42 | 37.13 | 36.36 | 38.00 | 39.10 | 37.50 | 39.15 | 37.47 | 37.82 | 38.46 | 38.53 | 38.47 |
| $ZrO_2$ | n.d | 0.44 | 0.22 | 0.64 | n.d | n.d | n.d | 0.67 | 0.53 | 1.43 | 2.04 | 0.21 |
| $Nb_2O_5$ | 0.84 | n.d | 1.21 | 0.79 | 0.64 | 0.56 | 1.73 | 0.43 | 0.65 | 0.17 | n.d | 1.05 |
| $CaO$ | 28.59 | 30.36 | 28.07 | 28.73 | 27.82 | 27.76 | 28.08 | 27.77 | 27.79 | 27.20 | 27.15 | 26.75 |
| $Na_2O$ | n.d | 0.34 | 0.44 | 0.41 | 0.68 | 0.38 | 1.23 | 0.58 | 0.57 | 0.29 | 0.36 | 1.24 |
| Total | 99.64 | 98.01 | 98.00 | 100.55 | 99.38 | 98.07 | 101.49 | 98.30 | 99.18 | 98.28 | 99.29 | 98.44 |
| Formulae calculated on the basis of $\Sigma$cations = 3 | | | | | | | | | | | | |
| Si | 1.002 | 1.006 | 1.000 | 0.992 | 0.992 | 1.003 | 0.982 | 0.999 | 1.004 | 0.982 | 0.979 | 0.995 |
| Al | - | - | - | - | - | - | - | - | - | 0.010 | 0.010 | 0.005 |
| Fe | 0.056 | 0.037 | 0.041 | 0.035 | 0.020 | 0.041 | 0.014 | 0.030 | 0.030 | 0.026 | 0.030 | 0.009 |
| Ti | 0.924 | 0.925 | 0.909 | 0.927 | 0.961 | 0.936 | 0.941 | 0.932 | 0.934 | 0.965 | 0.960 | 0.951 |
| Zr | - | 0.007 | 0.004 | 0.010 | - | - | - | 0.011 | 0.008 | 0.023 | 0.033 | 0.003 |
| Nb | 0.012 | - | 0.018 | 0.012 | 0.009 | 0.008 | 0.025 | 0.006 | 0.010 | 0.003 | - | 0.015 |
| Ca | 1.006 | 1.003 | 1.000 | 0.999 | 0.975 | 0.987 | 0.982 | 0.985 | 0.977 | 0.972 | 0.964 | 0.943 |
| Na | - | 0.022 | 0.028 | 0.025 | 0.043 | 0.025 | 0.076 | 0.037 | 0.037 | 0.019 | 0.024 | 0.079 |

n.d = not detected. Analyses 1-9: *Ca carbonatites (1 – Mu-114/2; 2 – Mu-136/32; 3-6 – Mu-136/33 [3-4 – core of a zoned crystal, 5-6 – rim]; 7 – Mu-136/52; 8-9 – Mu-1052/20); 10-11: phlogopite-calcite carbonatite (Mu-238); 12: quartz-feldspar-carbonate rocks (Mu-145).*

Na$_2$O (Table 3.3.1.5). At the Murun complex, Nb-rich titanite (4.0 wt.% Nb$_2$O$_5$) has been previously described from a quartz vein (Konev *et al.* 1996). However, the available compositional data on titanite from the Murun carbonatites lack detectable Nb$_2$O$_5$ (Konev *et al.* 1996). Significant enrichment in Nb$_2$O$_5$ contents (up to 6.2 wt.%) were observed in titanite from a granitic pegmatite of Zólkievka, Poland (Janeczek 1996). Coupled enrichment in Nb ($\leq$ 1.5 wt.% Nb$_2$O$_5$) and Zr (4.2 wt.% ZrO$_2$) was reported for titanite from nepheline syenite at Oldoinyo Lengai, Tanzania (Dawson *et al.* 1995).

Titanite is rare in the phlogopite-calcite carbonatite, where it occurs as anhedral-to-subhedral grains up to 50 $\mu$m across, commonly with rutile(?) rims. Relative to the calcite carbonatite, titanite from the phlogopite-calcite carbonatite is devoid of zoning, and has different compositional features. Here, titanite contains appreciable Zr (up to 2.0 wt.% ZrO$_2$) and is depleted in Nb ($\leq$ 0.17 wt.% Nb$_2$O$_5$) (Table 3.3.1.5). The Fe$_2$O$_3$ content in titanite from the phlogopite-calcite carbonatite varies from 1.0 to 1.2 wt.%. The mineral also contains minor Al$_2$O$_3$ (*ca.* 0.2 wt.%) and Na$_2$O (*ca.* 0.3 wt.%).

In the quartz-feldspar-carbonate rock, titanite is found as rare subhedral-to-euhedral oikocrysts up to 140 $\mu$m in size, highly-resorbed by carbonate minerals and barite. Here, titanite is commonly associated with rutile. Compositionally, the mineral corresponds to the empirical formula: (Ca$_{0.943}$Na$_{0.079}$)(Ti$_{0.951}$Fe$_{0.009}$Nb$_{0.015}$Zr$_{0.003}$)(Si$_{0.995}$Al$_{0.005}$)O$_5$.

*Tinaksite.* The Murun complex is the type-locality for tinaksite [NaK$_2$Ca$_2$Ti(Si$_7$O$_{19}$)(OH)] (Rogov *et al.* 1965). Here, the mineral occurs in a variety of rocks, including charoitites and carbonatites. In the samples examined, tinaksite was found predominantly in the calcite carbonatite (e.g. Mu-136/32, Mu-136/33), in association with titanite, potassium feldspar, carbonates, clinopyroxene, and quartz. The mineral forms subhedral-to-anhedral elongate crystals up to 1.5 mm in length, or radial aggregates of elongate crystals, and is commonly developed interstitially (Figs. 3.3.1.7 and 3.3.1.8), or along the fractures in titanite, and frequently contains resorbed fragments of clinopyroxene.

69

Table 3.3.1.6. Representative compositions of tinaksite from the calcite carbonatite and charoitite.

| Wt.% | 1 | 2 | 3 | 4 | 5 | 6 | 7 | 8 | 9□ |
|---|---|---|---|---|---|---|---|---|---|
| $SiO_2$ | 53.89 | 56.03 | 55.38 | 56.69 | 57.26 | 57.39 | 56.60 | 57.06 | 56.66 |
| $TiO_2$ | 8.40 | 9.13 | 9.95 | 8.73 | 9.78 | 10.36 | 9.42 | 8.32 | 10.26 |
| $Nb_2O_5$ | n.d | n.d | n.d | n.d | 0.60 | 0.38 | 0.50 | 0.29 | n.d |
| $Fe_2O_3$ | 3.09 | 2.49 | 0.91 | 1.42 | 1.41 | 0.93 | 1.32 | 1.56 | 0.37 |
| MnO | 1.68 | 1.97 | 1.16 | 1.37 | 0.45 | 0.37 | 1.03 | 0.80 | 0.42 |
| MgO | n.d | n.d | 0.12 | 0.14 | n.d | 0.13 | n.d | 0.48 | 0.35 |
| CaO | 13.76 | 14.53 | 13.26 | 14.02 | 14.33 | 14.54 | 14.06 | 14.81 | 14.96 |
| $Na_2O$ | 2.90 | 2.92 | 3.96 | 3.59 | 4.32 | 4.13 | 3.89 | 3.50 | 4.08 |
| $K_2O$ | 14.17 | 14.03 | 11.82 | 11.98 | 12.23 | 12.27 | 12.33 | 12.42 | 12.11 |
| Total | 97.89 | 101.10 | 96.56 | 97.94 | 100.38 | 100.50 | 99.15 | 99.24 | 99.22 |
| Formulae calculated on the basis of 19.5 atoms of oxygen | | | | | | | | | |
| Si | 6.917 | 6.932 | 7.035 | 7.103 | 7.012 | 7.005 | 7.030 | 7.065 | 7.004 |
| Ti | 0.811 | 0.849 | 0.951 | 0.823 | 0.901 | 0.951 | 0.880 | 0.776 | 0.954 |
| Nb | - | - | - | - | 0.033 | 0.021 | 0.028 | 0.016 | - |
| $Fe^{3+}$ | 0.298 | 0.232 | 0.087 | 0.134 | 0.130 | 0.085 | 0.123 | 0.146 | 0.034 |
| Mn | 0.183 | 0.206 | 0.125 | 0.145 | 0.047 | 0.038 | 0.108 | 0.084 | 0.044 |
| Mg | - | - | 0.023 | 0.026 | - | 0.024 | - | 0.089 | 0.065 |
| Ca | 1.892 | 1.926 | 1.805 | 1.882 | 1.880 | 1.902 | 1.871 | 1.967 | 1.981 |
| Na | 0.722 | 0.700 | 0.975 | 0.872 | 1.026 | 0.977 | 0.937 | 0.841 | 0.978 |
| K | 2.320 | 2.214 | 1.916 | 1.915 | 1.911 | 1.911 | 1.954 | 1.964 | 1.910 |

n.d = not detected. Analyses 1-6: *calcite carbonatite* (1-2 — *Mu-114/2*; 3-4 — *Mu-136/33*; 5-6 — *Mu-136/52*); 7-9: *charoitite* (7 — *Mu-13*; 8-*Mu-10*; 9 — *Mu-112*).

70

Compositionally, tinaksite from the calcite carbonatite is similar to the material from charoitites (Table 3.3.1.6), and shows rather noticeable intergranular variation in terms of MnO (0.4-2.0 wt.%) and $Fe_2O_3$ (0.9-3.1 wt.%) contents (Table 3.3.1.6). Some of the tinaksite grains are enriched in $Nb_2O_5$ (up to 0.6 wt.%).

*Dalyite* ($K_2Zr[Si_6O_{15}]$) was found in minor amounts in the majority of the rocks, with the exception of the phlogopite-calcite carbonatite. In the calcite carbonatite and Ba-Sr-Ca carbonatite, the mineral forms anhedral-to-subhedral elongate grains up to 0.6 mm in size, and is commonly developed interstitially or along fractures in potassium feldspar and calcite. In the quartz-feldspar-carbonate rock, the mineral is found in association with strontianite and ancylite-(Ce) as fracture fillings in low-Sr calcite, and prismatic grains ($\sim 30$ μm) confined to the boundaries between calcite and quartz grains. All dalyite compositions are enriched in the davanite component [up to 10 mol.% $K_2Ti(Si_6O_{15})$], and correspond to the empirical formula: $K_{1.85-2.00}(Zr_{0.90-0.99}Ti_{0.02-0.10})(Si_{5.97-6.02}O_{15})$. Previously, dalyite has been described in different rock types from the Murun complex, including fenites, charoitites, carbonatites, aegirinites, alkali syenites, and eudialyte-rich rocks (Konev *et al.* 1996). In the latter, dalyite was described as one of the rock-forming minerals. Ti-rich (up to 5.9 wt.% $TiO_2$, or *ca.* 40 mol.% $K_2Ti[Si_6O_{15}]$) varieties of the mineral were observed in the charoitites of the Murun complex (Konev *et al.* 1996).

*Turkestanite* [idealised structural formula $Th(Ca,Na)_2(K_{1-x} \square_x)(Si_8O_{20}) \cdot nH_2O$] was first described at the Dara-i-Pioz complex, Tajikistan (Pautov *et al.* 1997). The mineral represents a Ca-dominant analogue of steacyite [$Th(Na,Ca)_2(K_{1-x} \square_x)(Si_8O_{20})$]. Among our samples, the mineral is found only in the calcite carbonatite (Mu-136/33) as subhedral-to-euhedral prismatic crystals up to 0.4 mm in length commonly associated with titanite. Most of the turkestanite crystals are altered along fractures and margins (Fig. 3.3.1.10a,b). Fresh parts of the crystals are relatively uniform in composition (analyses 1-4 Table 3.3.1.7), and show slight enrichment in Na, K and Th, along with depletion in U and *LREE* contents relative to the material from Dara-

71

a

b

Fig. 3.3.1.10. Crystals of turkestanite enclosed in titanite (black). Calcite carbonatite (Mu-136/33). (a) BSE false colour image, F.O.V. 300 μm; (b) BSE image. Note a fresh core of the crystals (a — greenish yellow; b — medium $AZ$, grey), thin intermediate zone (a — greenish blue; b — low-$AZ$, dark grey), and an irregular rim (a — yellowish red; b — high-$AZ$, white) enriched in heavy elements (primarily Ba and Sr). For corresponding compositions, see Tables 3.3.1.7 & 3.3.1.8.

72

Table 3.3.1.7. Representative compositions of turkestanite.

| Wt.% | Murun this work (Mu-136/33) | | | | Dara-i-Pioz Pautov et al. (1997) | Reguir et al. (1999) | |
|---|---|---|---|---|---|---|---|
| | 1 | 2 | 3 | 4 | 5[#] | 6 | 7 |
| $SiO_2$ | 56.21 | 57.09 | 56.65 | 55.01 | 54.58 | 49.26 | 48.93 |
| $UO_2$ | n.d | n.d | n.d | n.d | 1.93 | 5.91 | 7.42 |
| $ThO_2$ | 27.06 | 27.63 | 26.64 | 28.13 | 23.43 | 22.00 | 21.38 |
| $Al_2O_3$ | n.d | n.d | n.d | n.d | 0.03 | 0.92 | 0.64 |
| $Y_2O_3$ | n.d | n.d | n.d | n.d | 0.05* | 0.17 | 0.33 |
| $La_2O_3$ | n.d | n.d | n.d | n.d | 0.36 | 1.09 | 0.74 |
| $Ce_2O_3$ | 0.67 | 0.82 | 0.80 | n.d | 0.58 | 2.00 | 1.82 |
| $Nd_2O_3$ | n.d | n.d | 0.74 | 0.77 | 0.31 | 0.56 | 0.95 |
| PbO | n.d | n.d | n.d | n.d | 0.94 | 5.09 | 5.11 |
| MgO | n.d | n.d | n.d | n.d | n.d | 0.14 | 0.04 |
| CaO | 7.41 | 7.53 | 7.17 | 7.10 | 7.56 | 7.91 | 8.16 |
| $Na_2O$ | 3.06 | 3.19 | 3.18 | 3.41 | 2.89 | 0.96 | 1.11 |
| $K_2O$ | 5.27 | 5.15 | 5.26 | 5.00 | 4.54 | 2.22 | 2.07 |
| Total | 99.68 | 101.41 | 100.44 | 99.42 | 99.39** | 98.23 | 98.70 |

Formulae calculated on the basis of 20 atoms of oxygen

| | 1 | 2 | 3 | 4 | 5 | 6 | 7 |
|---|---|---|---|---|---|---|---|
| Si | 8.066 | 8.061 | 8.071 | 8.009 | 8.067 | 7.816 | 7.817 |
| U | - | - | - | - | 0.033 | 0.108 | 0.136 |
| Th | 0.884 | 0.888 | 0.864 | 0.932 | 0.788 | 0.794 | 0.777 |
| Al | - | - | - | - | 0.005 | 0.172 | 0.121 |
| Y | - | - | - | - | 0.004* | 0.014 | 0.028 |
| La | - | - | - | - | 0.020 | 0.064 | 0.044 |
| Ce | 0.035 | 0.042 | 0.042 | - | 0.031 | 0.116 | 0.106 |
| Nd | - | - | 0.038 | - | 0.016 | 0.032 | 0.054 |
| Pb | - | - | - | - | 0.037 | 0.217 | 0.220 |
| Mg | - | - | - | - | - | 0.033 | 0.010 |
| Ca | 1.139 | 1.139 | 1.095 | 1.108 | 1.197 | 1.345 | 1.397 |
| Na | 0.851 | 0.873 | 0.878 | 0.963 | 0.828 | 0.295 | 0.344 |
| K | 0.965 | 0.928 | 0.956 | 0.929 | 0.856 | 0.449 | 0.422 |

n.d = not detected; [#] our recalculation of the original analytical data; * represents $\Sigma(Y+Yb)$; ** total also includes 0.01 wt.% MnO; 0.10 wt.% $Fe_2O_3$ (0.011 apfu $Fe^{3+}$); 0.07 wt.% $Pr_2O_3$ (0.004 apfu Pr); 0.05 wt.% $Sm_2O_3$ (0.003 apfu Sm); 0.06 wt.% [$Gd_2O_3$+ $Dy_2O_3$] (0.003 apfu [Gd+Dy]); 0.20 wt.% F, and 1.76 wt.% $H_2O^\tau$.

73

Table 3.3.1.8. Representative compositions of altered turkestanite.

| Wt.% | this work (Mu-136/33, see Fig. 3.1.10) | | | | Konev et al. (1996) |
|---|---|---|---|---|---|
| | medium-$AZ$ core | low-$AZ$ inter-mediate zone | high-$AZ$ marginal zone | | |
| | 1 | 2 | 3 | 4 | 5 |
| $SiO_2$ | 57.09 | 51.94 | 40.36 | 37.64 | 46.92 |
| $UO_2$ | n.d | n.d | n.d | 2.64 | |
| $ThO_2$ | 27.63 | 25.16 | 33.60 | 25.88 | 23.16 |
| $Y_2O_3$ | n.d | n.d | n.d | 0.97 | n.d |
| $La_2O_3$ | n.d | n.d | 0.33 | 1.59 | |
| $Ce_2O_3$ | 0.82 | 0.64 | 1.30 | 4.13 | 4.10[†] |
| $Nd_2O_3$ | n.d | n.d | n.d | 1.18 | |
| $Pr_2O_3$ | n.d | n.d | n.d | 0.27 | |
| $CaO$ | 7.53 | 7.22 | 3.96 | 3.43 | 7.19 |
| $SrO$ | n.d | 0.46 | 2.54 | 2.58 | 0.49 |
| $BaO$ | n.d | n.d | 6.85 | 5.02 | 0.32 |
| $Na_2O$ | 3.19 | n.d | n.d | n.d | 0.18 |
| $K_2O$ | 5.15 | 1.15 | 0.50 | 0.28 | 5.44 |
| Total | 101.41 | 86.57 | 89.44 | 85.61 | 87.85[##] |

n.d = not detected; [†] represents $\Sigma REE$; [##] Total also includes 0.05 wt.% FeO.

74

i-Pioz. Also, in contrast to the Dara-i-Pioz turkestanite, our material lacks detectable Pb, Mg, Al and Y. Altered parts of turkestanite grains have low analysis totals, and are impoverished in Na, K, Ca and Si, and enriched in Ba and Sr (Table 3.3.1.8). The low totals probably result from a significant amount of molecular $H_2O$ in the peripheral areas of the crystals. Previously published analytical data on turkestanite from the Murun complex exhibit similar compositional features (Konev *et al.* 1996; analysis 5 Table 3.3.1.8). Hydration of turkestanite, as well as leaching of the alkalis and Ca from its structure, and the increase in Ba and Sr contents may result from metamictisation of the mineral and its reaction with a late-stage interstitial fluid.

*Andradite* was found only in a sample of the phlogopite-calcite carbonatite (Mu-238). Here, the mineral forms rare anhedral-to-subhedral grains up to 40 $\mu$m in size. Andradite occurs in association with strontianite and Sr-rich calcite as fracture fillings in a feldspar matrix. The mineral commonly exhibits zoning with peripheral parts of the crystals (ca. 8 $\mu$m in width) enriched in $TiO_2$ (from ca. 1.0 wt.% in the core to ca. 2.2 wt.% in the rim). Enrichment in $TiO_2$ is accompanied by depletion in $Fe_2O_3$ content (from *ca.* 28.7 wt.% in the core to *ca.* 26.5 wt.% in the outermost parts). The complete compositional range of andradite can be expressed by the empirical formula: $(Ca_{2.94-3.01}Na_{0.01-0.06})(Fe^{3+}_{1.61-1.81}Fe^{2+}_{0.01-0.08}Al_{0.11-0.16}Ti_{0.05-0.16}Mg_{0.01-0.04}Mn_{0.02-0.06}V_{0.01-0.04})[Si_{2.94-3.01}O_{4.00}]$.

*Zircon* is very rare in the rocks examined, and found only in the calcite carbonatite (Mu-1052/20). Here, the mineral occurs as anhedral-to-subhedral grains (up to 30 $\mu$m in size) associated with potassium feldspar (Fig. 3.3.1.11). Compositionally, most of the zircon crystals correspond to nearly pure $ZrSiO_4$. In BSE, some of the grains exhibit irregular zoning with high-*AZ* zones enriched in $ThO_2$ (up to 3.0 wt.%) (Fig. 3.3.1.12).

75
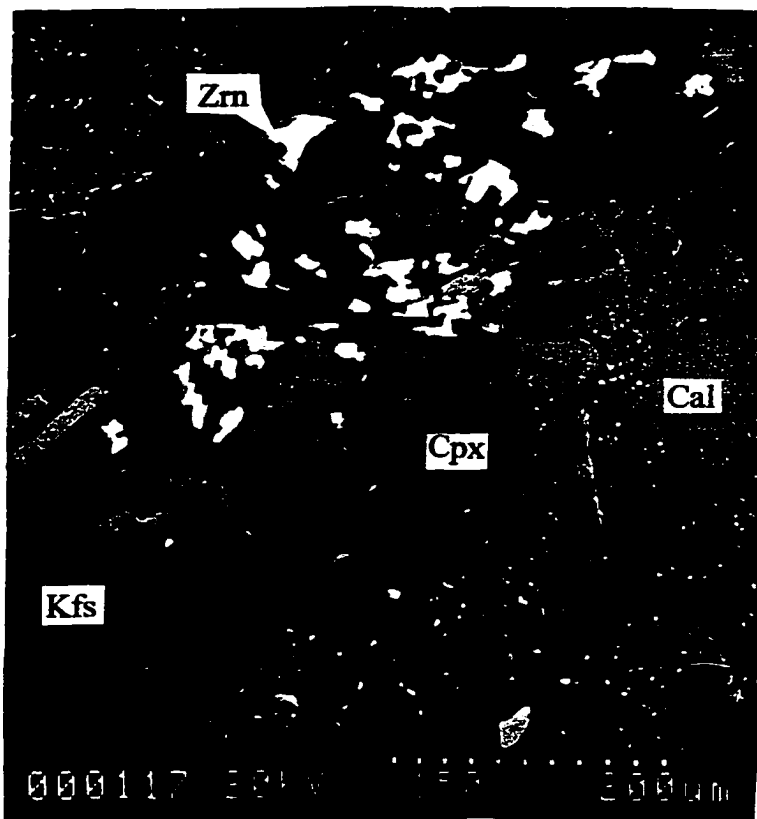
Fig. 3.3.1.11. BSE image of anhedral zircon (Zm) associated with laths of potassium feldspar (Kfs) and clinopyroxene (Cpx) in a carbonate matrix. Note that the crystal of calcite (Cal) has a homogeneous Sr-rich core and a Sr-depleted margin with inclusions of strontianite (white). (Mu-1052/20).



Fig. 3.3.1.12. BSE image of irregularly zoned crystal of zircon with high-$AZ$ areas enriched in Th; white spot at the bottom is barite, black background is Sr-rich calcite. Calcite carbonatite (Mu-1052/20).

### 3.3.2 *Carbonates*

<u>Carbonates with divalent cations</u>

*Calcite* is found in all four types of carbonate-rich rocks. The mineral is a major constituent of the calcite carbonatite, where it forms subhedral-to-euhedral grains up to 3 mm in size with a coarse cleavage and characteristic deformational twinning. Some of the calcite is developed interstitially or along fractures in feldspar, clinopyroxene, tinaksite and titanite. In some cases (*e.g.* Mu-136/32), the crystals of calcite are characterised by undulatory extinction and bent cleavage (Fig. 3.3.2.1).



Fig. 3.3.2.1. Bent cleavage in calcite, right top and left bottom – titanite (yellowish-grey). Calcite carbonatite (136/32); FOV 6 mm; plane-polarised light.

In BSE, Sr- and Ba-rich (up to 5.6 wt.% SrO, and 1.9 wt.% BaO: Table 3.3.2.1) high-*AZ* calcite from the calcite carbonatite commonly exhibits subsolidus re-equilibration textures resulting from depletion in Sr at the margin and along cleavage fractures (Fig. 3.3.2.2a). Low-

Sr (0.5-2.5 wt.% SrO) relatively low-$AZ$ calcite often occurs as intergrowths with minute anhedral grains of Ca-bearing strontianite and Sr-Ca-Ba carbonates of variable stoichiometry (Fig. 3.3.2.2b). These aggregates probably result from fluid-induced exsolution phenomena in the primary Sr-enriched calcite. In some cases, the mineral contains anhedral inclusions of burbankite, whose origin is uncertain.

In the Ba-Sr-Ca carbonatite, calcite occurs primarily in intricate intergrowths with Sr-Ca-Ba carbonates, Ca-enriched strontianite and $REE$-bearing carbonates (Fig. 3.3.2.3a,b). In thin section, these intergrowths appear as "patchy", commonly resembling a spider in shape, greyish aggregates of anhedral-to-subhedral grains. The identity of individual mineral phases cannot be readily determined. In BSE, calcite is conspicuous as low-$AZ$ lenticular, oval or elongate lamellae from a few μm to 100 μm in length, confined to the exsolution assemblage (Fig. 3.3.2.3a,b). In common with the calcite carbonatite, some calcite crystals from the Ba-Sr-Ca carbonatite occur as anhedral grains with Sr- and Ba-rich cores (up to 6.6 wt.% SrO and 2.0 wt.% BaO), and a re-equilibration assemblage confined to the margins of the crystals. This assemblage is composed of Sr- and Ba- depleted calcite, Ca-rich strontianite, and minute grains of Ba-Sr-Ca carbonates.

In the phlogopite-calcite carbonatite, calcite is the main carbonate phase. It forms a matrix of subhedral grains with characteristic twinning and rhombohedral cleavage (Fig. 3.2.3a,b). The mineral is also developed interstitially with respect to the phlogopite crystals, and as an alteration product after potassium feldspar. Some of the calcite grains contain minor inclusions of apatite and barite. Compositionally, the calcite is relatively uniform, and contains up to 6.5 wt.% SrO and $ca.$ 0.6 wt.% BaO (Table 3.3.2.1). In contrast to the calcite carbonatite, the exsolution textures composed of low-Sr calcite and Ca-rich strontianite are much less common in the phlogopite-calcite carbonatite.

Calcite from the quartz-feldspar-carbonate rock is similar to that from the calcite carbonatite in having a subsolidus re-equilibration texture. The mineral occurs as anhedral-to-subhedral grains, with Sr-rich high-$AZ$ cores (up to 5.3 wt.% SrO), and low-$AZ$ Sr-depleted

78
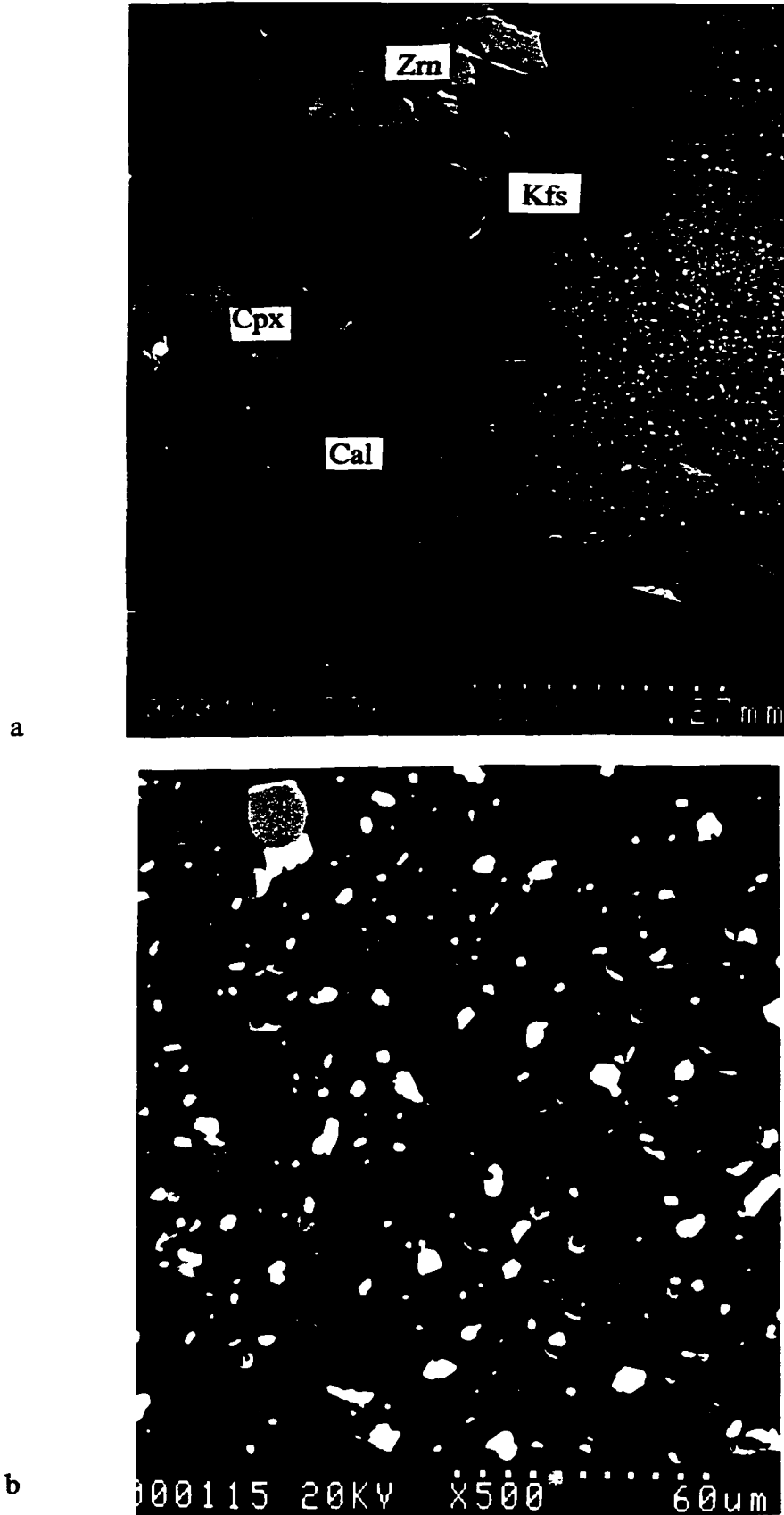
Fig. 3.3.2.2. Exsolution textures in the calcite carbonatite (Mu-1052/20), BSE images. (a) "Patches" of Sr-poor calcite and Ca-rich strontianite (speckled areas) along margins and fractures in primary Sr-rich calcite (Cal); for abbreviations see Fig. 15; (b) calcite (dark grey) – strontianite (white) exsolution aggregates, a medium grey grain in the top left corner is burbankite.

79
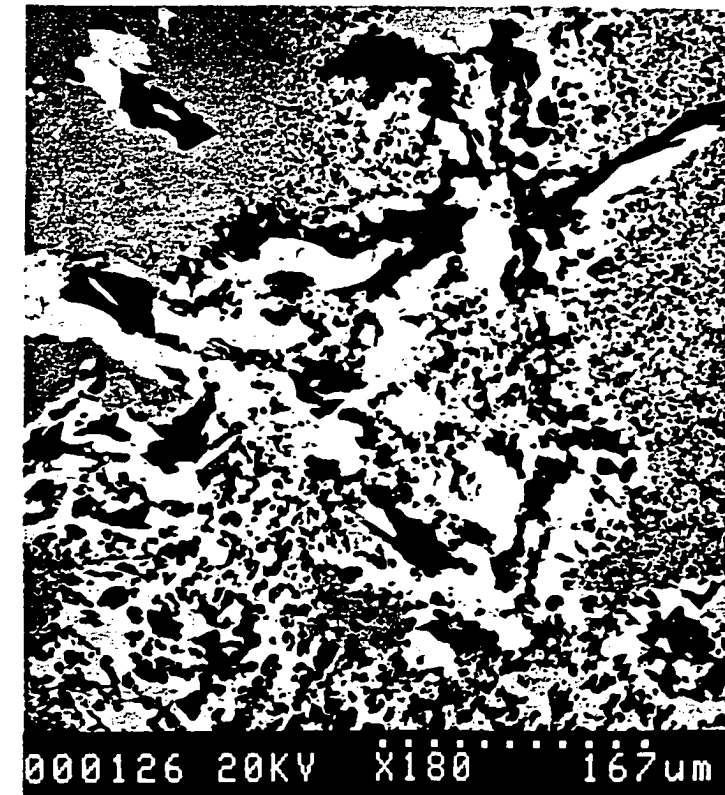
Fig. 3.3.2.3.BSE images of exsolution textures in the Ba-Sr-Ca carbonatite. (a) calcite (black)-barytocalcite (grey) aggregates with ancylite-(Ce) developed along fractures (white), Mu-14; (b) primary Sr-rich barytocalcite (medium grey) with exsolution textured margins of calcite (black) and barytocalcite (light grey), note grain coarsening toward the interstitial spaces. White spots are kukharenkoite. Mu-15.

80

Table 3.3.2.1. Representative compositions of strontian calcite.

| Wt. % | 1 | 2 | 3 | 4 | 5 | 6 | 7 | 8 | 9 | 10 | 11 | 12 |
|---|---|---|---|---|---|---|---|---|---|---|---|---|
| CaO | 50.05 | 53.39 | 49.86 | 51.61 | 48.98 | 53.63 | 51.41 | 54.54 | 52.40 | 50.75 | 50.88 | 52.08 |
| SrO | 5.98 | 1.11 | 6.60 | 4.62 | 6.62 | 0.68 | 4.85 | 0.56 | 3.92 | 5.58 | 4.79 | 5.00 |
| BaO | 1.65 | n.d | 1.59 | 1.00 | 1.99 | 1.67 | 0.79 | n.d | n.d | 1.91 | 1.55 | 0.60 |
| $CO_2$* | 42.29 | 42.37 | 42.39 | 42.75 | 41.82 | 42.86 | 42.63 | 43.04 | 42.79 | 42.75 | 42.41 | 43.18 |
| Total | 99.97 | 96.87 | 100.44 | 99.98 | 99.41 | 98.84 | 99.68 | 98.14 | 99.11 | 100.99 | 99.63 | 100.92 |
| Formulae calculated on the basis of 1 cation | | | | | | | | | | | | |
| Ca | 0.929 | 0.989 | 0.923 | 0.947 | 0.919 | 0.982 | 0.946 | 0.994 | 0.961 | 0.932 | 0.942 | 0.946 |
| Sr | 0.060 | 0.011 | 0.066 | 0.046 | 0.067 | 0.007 | 0.049 | 0.006 | 0.039 | 0.055 | 0.048 | 0.049 |
| Ba | 0.011 | - | 0.011 | 0.007 | 0.014 | 0.011 | 0.005 | - | - | 0.013 | 0.010 | 0.004 |
| $CO_3$ | 1.000 | 1.000 | 1.000 | 1.000 | 1.000 | 1.000 | 1.000 | 1.000 | 1.000 | 1.000 | 1.000 | 1.000 |

| Wt. % | 13 | 14 | 15 | 16 | 17 | 18 | 19 | 20 | 21 | 22[#] | 23[##] |
|---|---|---|---|---|---|---|---|---|---|---|---|
| CaO | 53.65 | 54.19 | 51.64 | 52.82 | 54.69 | 51.10 | 52.12 | 54.57 | 54.57 | 49.57 | 52.28 |
| SrO | 1.91 | 1.14 | 5.37 | 2.77 | 1.41 | 6.47 | 2.95 | 1.95 | 1.79 | 5.27 | 3.44 |
| BaO | n.d | n.d | 1.31 | n.d | n.d | 0.64 | 0.85 | 0.53 | n.d | 0.72 | n.d |
| $CO_2$* | 42.92 | 43.01 | 43.18 | 42.63 | 43.52 | 43.03 | 42.40 | 44.00 | 43.77 | 41.35 | 42.49 |
| Total | 8.48 | 98.34 | 101.50 | 98.22 | 99.62 | 101.24 | 98.32 | 101.37 | 100.43 | 96.91 | 98.21 |
| Formulae calculated on the basis of 1 cation | | | | | | | | | | | |
| Ca | 0.981 | 0.989 | 0.938 | 0.972 | 0.986 | 0.932 | 0.964 | 0.973 | 0.978 | 0.941 | 0.966 |
| Sr | 0.019 | 0.011 | 0.053 | 0.028 | 0.014 | 0.064 | 0.030 | 0.019 | 0.017 | 0.054 | 0.034 |
| Ba | - | - | 0.009 | - | - | 0.004 | 0.006 | 0.003 | - | 0.005 | - |
| $CO_3$ | 1.000 | 1.000 | 1.000 | 1.000 | 1.000 | 1.000 | 1.000 | 1.000 | 1.000 | 1.000 | 1.000 |

n.d = not detected; * calculated on the basis of stoichiometry; [#] analysis sum also includes 0.32 wt.% MnO, corresponding to 0.005 apfu; [##] analysis sum also includes 0.30 wt.% MnO, corresponding to 0.004 apfu. Analyses 1-7: *Ba-Sr-Ca carbonatite* (1-2 – *Mu-7*; 3-4 – *Mu-8*; 5-6 – *Mu-14*; 7 – *Mu-15*); 8-17: *calcite carbonatite* (8-9 – *Mu-114/2*; 10-11 – *Mu-136/32*; 12 – *Mu-180*; 13-14 – *Mu-136/33*; 15 – Mu-136/52; 16-17 – *Mu-1052/20*); 18 – *phlogopite-calcite carbonatite* (*Mu-238*); 19-23: *quartz-feldspar-carbonate rock* (19-21 – *Mu-145*; 22-23 – *Mu-136/46*).
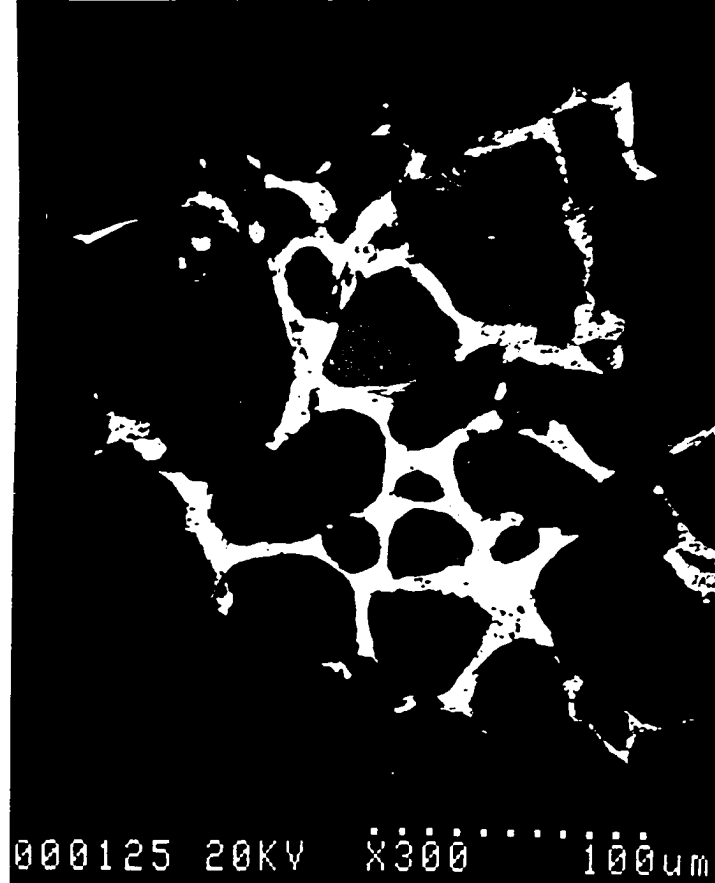
Fig. 3.3.2.4. Ancylite-(Ce) (white) developed interstitially with respect to quartz (dark grey) and Sr-rich calcite (grey); note ovoid inclusions of Sr-rich calcite in quartz. Quartz-feldspar-carbonate rock (Mu-145); BSE image.



Fig. 3.3.2.5. BSE image of kukharenkoite (white) with strontianite (grey) in calcite (black). Ba-Sr-Ca carbonatite (Mu-8).

82

margins (*ca.* 2.0 wt.% SrO). In common with the Ba-Sr-Ca carbonatite, calcite from the quartz-feldspar-carbonate rock forms intergrowths with Sr-Ca-Ba carbonates and minor strontianite. In contrast to the other carbonate-rich rocks examined, calcite in the quartz-feldspar-carbonate rock in some cases forms "graphic" intergrowths with quartz. Oval grains of calcite (up to 25 μm in diameter) are also found as inclusions in equant quartz crystals (Fig. 3.3.2.4). These inclusions contain *ca.* 3.5 wt.% SrO, and are compositionally similar to the high-*AZ* calcite.

S*trontianite* occurs in different proportions in all four rock types, but is especially abundant in the Ba-Sr-Ca carbonatite. As a part of the calcite-strontianite intergrowths (see above), strontianite is associated with minor Ba-Sr-Ca carbonates and barite, and forms anhedral grains up to 20 μm in the low-Sr parts of calcite grains (Fig. 3.3.2.2a,b). Here, the mineral is notably enriched in CaO (up to 22.5 wt.% in the calcite carbonatite and 20.2 wt.% in the phlogopite-calcite carbonatite: Table 3.3.2.2). In the Ba-Sr-Ca carbonatite, strontianite also occurs in complex intergrowths with Sr-Ca-Ba carbonates, calcite, and *REE* carbonates (Fig. 3.3.2.5). This strontianite shows a significant intergranular compositional variation in terms of CaO content (from 1.4 to 22.0 wt.%: Table 3.3.2.2). Strontianite is rare in the quartz-feldspar-carbonate rock, and is characterised by relatively low Ca content (3.2 to 5.5 wt.% CaO; Table 3.3.2.2). The amount of witherite component ($BaCO_3$) in strontianite varies from 1.0 to 7.4 mol.% in the calcite carbonatite; from 1.1 to 5.0 mol.% in the Ba-Sr-Ca carbonatite, from 0.6 to 2.3 mol.% in the phlogopite-calcite carbonatite, and from 1.2 to 8.6 mol.% in the quartz-feldspar-carbonate rock. Some strontianite crystals also contain appreciable $REE_2O_3$ ($\leq$ 2.5 wt.% in the calcite carbonatite; $\leq$ 3.9 wt.% in the Ba-Sr-Ca carbonatite; and $\leq$ 1.4 wt.% in the quartz-feldspar-carbonate rock: Table 3.3.2.2).

In thin section, *Sr-Ca-Ba carbonates* appear as anhedral-to-subhedral grains and oikokrysts ($\leq$ 0.5mm), with a coarse perpendicular cleavage and bronze-pinkish interference

Table 3.3.2.2. Representative compositions of calcian strontianite.

| Wt.% | 1 | 2 | 3 | 4 | 5 | 6 | 7 | 8 | 9 | 10 | 11 | 12 | 13 |
|---|---|---|---|---|---|---|---|---|---|---|---|---|---|
| CaO | 6.33 | 17.40 | 4.24 | 14.84 | 22.50 | 11.39 | 22.41 | 15.83 | 20.57 | 1.45 | 22.06 | 11.21 | 4.94 |
| SrO | 61.50 | 56.87 | 58.17 | 50.46 | 39.02 | 53.15 | 37.90 | 46.23 | 39.64 | 58.18 | 41.71 | 54.00 | 55.63 |
| BaO | 1.43 | 1.78 | 5.07 | 2.75 | 1.58 | 2.88 | 3.91 | 1.99 | 2.34 | 4.47 | 1.14 | 2.18 | 4.68 |
| $La_2O_3$ | n.d | n.d | 0.85 | n.d | n.d | n.d | n.d | n.d | n.d | 2.01 | n.d | n.d | 1.01 |
| $Ce_2O_3$ | n.d | n.d | 0.93 | n.d | n.d | n.d | n.d | n.d | n.d | 1.90 | n.d | n.d | 1.46 |
| $CO_2$* | 31.50 | 34.07 | 29.97 | 33.87 | 34.68 | 32.34 | 34.81 | 32.63 | 33.65 | 28.18 | 35.36 | 32.36 | 29.51 |
| Total | 100.76 | 100.12 | 99.23 | 101.92 | 97.78 | 99.76 | 99.03 | 96.68 | 96.20 | 96.19 | 100.27 | 99.75 | 97.23 |
| Formulae calculated on the basis 1 ($CO_3$) group | | | | | | | | | | | | | |
| Ca | 0.158 | 0.401 | 0.112 | 0.344 | 0.509 | 0.276 | 0.505 | 0.381 | 0.480 | 0.041 | 0.490 | 0.272 | 0.133 |
| Sr | 0.829 | 0.584 | 0.831 | 0.633 | 0.478 | 0.698 | 0.463 | 0.601 | 0.500 | 0.893 | 0.501 | 0.709 | 0.810 |
| Ba | 0.013 | 0.015 | 0.049 | 0.023 | 0.013 | 0.026 | 0.032 | 0.018 | 0.020 | 0.046 | 0.009 | 0.019 | 0.046 |
| La | - | - | 0.008 | - | - | - | - | - | - | 0.020 | - | - | 0.009 |
| Ce | - | - | 0.008 | - | - | - | - | - | - | 0.018 | - | - | 0.013 |
| $CO_3$ | 1.000 | 1.000 | 1.000 | 1.000 | 1.000 | 1.000 | 1.000 | 1.000 | 1.000 | 1.000 | 1.000 | 1.000 | 1.000 |

| Wt.% | 14 | 15 | 16 | 17 | 18 | 19 | 20 | 21 | 22 | 23 | 24 | 25 |
|---|---|---|---|---|---|---|---|---|---|---|---|---|
| CaO | 6.76 | 6.75 | 11.83 | 9.12 | 7.26 | 11.08 | 7.42 | 14.33 | 12.22 | 20.25 | 5.49 | 3.26 |
| SrO | 57.07 | 57.04 | 52.14 | 51.76 | 52.58 | 53.02 | 57.56 | 60.80 | 54.37 | 43.37 | 61.79 | 56.03 |
| BaO | 6.39 | 3.98 | 2.44 | 6.34 | 7.83 | 4.95 | 1.60 | n.d | 0.67 | 2.85 | 1.30 | 8.70 |
| $CO_2$* | 30.53 | 30.67 | 32.13 | 30.96 | 30.28 | 32.64 | 30.73 | 33.27 | 32.88 | 35.13 | 30.93 | 29.24 |
| Total | 98.75 | 98.44 | 98.54 | 98.18 | 97.95 | 101.69 | 97.31 | 100.70 | 100.14 | 101.60 | 99.51 | 98.67** |
| Formulae calculated on the basis 1 ($CO_3$) group | | | | | | | | | | | | |
| Ca | 0.174 | 0.173 | 0.289 | 0.231 | 0.188 | 0.266 | 0.189 | 0.303 | 0.292 | 0.452 | 0.139 | 0.088 |
| Sr | 0.766 | 0.790 | 0.689 | 0.710 | 0.738 | 0.690 | 0.796 | 0.697 | 0.702 | 0.525 | 0.849 | 0.819 |
| Ba | 0.060 | 0.037 | 0.022 | 0.059 | 0.074 | 0.044 | 0.015 | - | 0.006 | 0.023 | 0.012 | 0.086 |
| $CO_3$ | 1.000 | 1.000 | 1.000 | 1.000 | 1.000 | 1.000 | 1.000 | 1.000 | 1.000 | 1.000 | 1.000 | 1.000 |

n.d = not detected. * calculated on the basis of stoichiometry; ** Total also includes 0.41 wt.% $La_2O_3$ (0.004 apfu La) and 1.03 wt.% $Ce_2O_3$ (0.010 apfu Ce). Analyses 1-11: Ba-Sr-Ca carbonatite (1-2 – Mu-7; 3-5 – Mu-8; 6-7 – Mu-14; 8-9 – Mu-15; 10-11 – Mu-151); 12-20: calcite carbonatite (12 – Mu-114/2; 13 – Mu-180; 14-16 – Mu-136/32; 17-19 – Mu-136/33; 20 – Mu-1052/20); 21-23 – phlogopite-calcite carbonatite (Mu-238); 24-25: quartz-feldspar-carbonate rock (24 – Mu-136/46; 25 – Mu-145).

84

colours (Figs. 3.3.2.6, 3.3.2.7 and 3.3.2.8). The minerals also occur interstitially with respect to feldspar, clinopyroxene, titanite and tinaksite.



Fig. 3.3.2.6. Oikocryst of Ba-Sr-Ca carbonate (yellow, pink) enclosing grains of potassium feldspar (grey) and clinopyroxene (black, elongate) in a quartz matrix (white). Quartz-feldspar-carbonate rock (Mu-136/46); FOV 6 mm; crossed polars.

In BSE, Sr-Ca-Ba carbonates are discernible as a constituent of the complex exsolution aggregates with strontianite, calcite and *REE* carbonates (see above) (Fig. 3.3.2.3a,b), here, the Ba-Sr-Ca phases occur as anhedral grains from 5 to 50 μm in size, and calcite-free aggregates (up to 3mm in size) of variable composition. In minor amounts, Sr-Ca-Ba carbonates occur in the calcite-strontianite exsolution aggregates in the calcite carbonatite (see above), where they form anhedral grains up to 10-20 μm. The Ba-Ca-Sr carbonates exhibit a wide compositional variation (Table 3.3.2.3), ranging from almost pure [CaBa(CO₃)₂] (e.g. analyses 1 and 4 Table 3.3.2.3), to Sr-rich varieties (e.g. analyses 2, 5 and 9 Table 3.3.2.3). Some of the grains

85
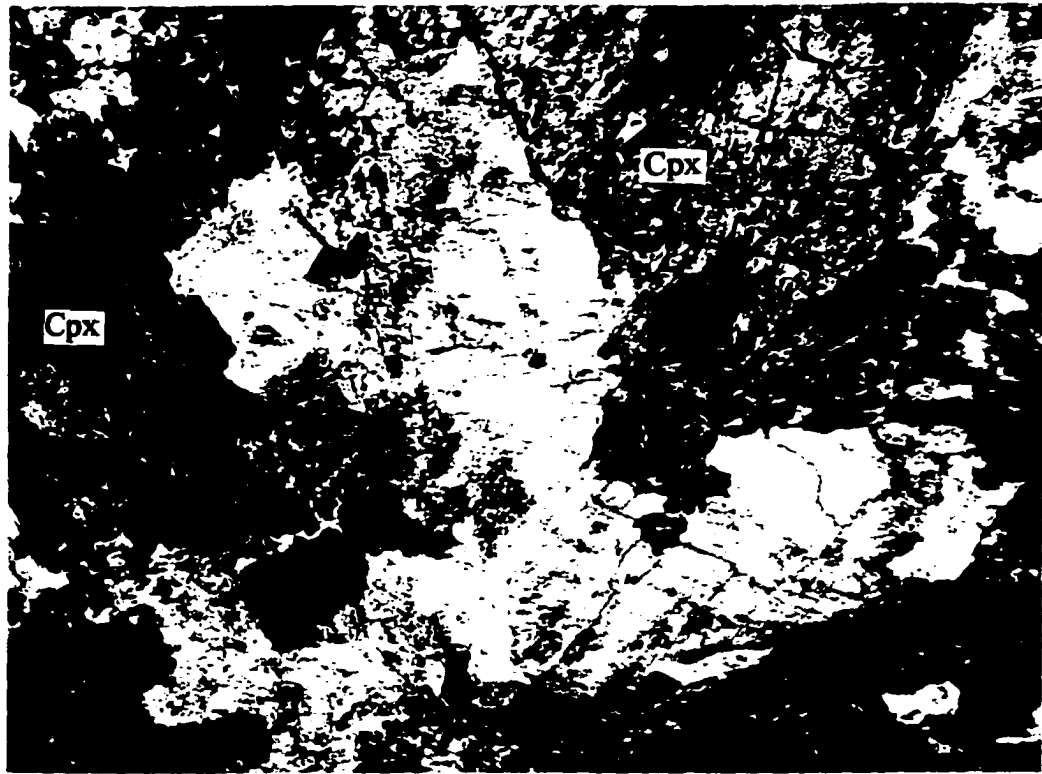
Fig. 3.3.2.7. Ba-Sr-Ca carbonates (pink, light green) with clinopyroxene (Cpx) in the Ba-Sr-Ca carbonatite (Mu-151). FOV 6 mm; crossed polars.



Fig. 3.3.2.8. Primary barytocalcite with coarse cleavage (bronze yellow; bottom right) associated with zoned potassium feldspar (light grey) and stellite clinopyroxene (dark green). Ba-Sr-Ca carbonatite (Mu-15). FOV 6 mm; crossed polars.

86

Table 3.3.2.3. Representative compositions of Ba-, Sr-, Ca-bearing carbonates.

| Wt. % | 1 | 2 | 3 | 4 | 5 | 6 | 7 | 8 | 9 | 10 | 11 | 12 | 13 | 14 |
|---|---|---|---|---|---|---|---|---|---|---|---|---|---|---|
| CaO | 18.87 | 18.44 | 20.99 | 18.67 | 18.87 | 22.34 | 21.39 | 18.44 | 19.25 | 19.46 | 22.68 | 18.43 | 19.19 | 20.61 |
| SrO | 1.23 | 2.61 | 11.09 | 0.31 | 2.97 | 12.50 | 17.03 | 1.72 | 5.16 | 9.18 | 11.58 | 1.67 | 4.15 | 12.09 |
| BaO | 49.72 | 47.17 | 36.55 | 50.34 | 46.69 | 33.43 | 30.22 | 47.78 | 43.68 | 38.07 | 32.68 | 48.81 | 44.46 | 34.22 |
| $CO_2$* | 29.60 | 29.12 | 31.67 | 29.23 | 29.47 | 32.44 | 32.69 | 28.92 | 29.84 | 30.10 | 32.10 | 29.18 | 29.58 | 31.13 |
| Total | 99.42 | 97.34 | 100.30 | 98.55 | 98.00 | 100.71 | 101.33 | 96.86 | 97.93 | 96.81 | 99.04 | 98.09 | 97.38 | 98.05 |

Formulae calculated on the basis of 2 cations

| | 1 | 2 | 3 | 4 | 5 | 6 | 7 | 8 | 9 | 10 | 11 | 12 | 13 | 14 |
|---|---|---|---|---|---|---|---|---|---|---|---|---|---|---|
| Ca | 1.001 | 0.994 | 1.040 | 1.002 | 1.005 | 1.081 | 1.027 | 1.001 | 1.013 | 1.015 | 1.109 | 0.991 | 1.018 | 1.039 |
| Sr | 0.035 | 0.076 | 0.297 | 0.009 | 0.086 | 0.327 | 0.442 | 0.051 | 0.147 | 0.259 | 0.307 | 0.049 | 0.119 | 0.330 |
| Ba | 0.964 | 0.930 | 0.663 | 0.989 | 0.909 | 0.592 | 0.531 | 0.948 | 0.840 | 0.726 | 0.584 | 0.960 | 0.863 | 0.631 |
| $CO_3$ | 2.000 | 2.000 | 2.000 | 2.000 | 2.000 | 2.000 | 2.000 | 2.000 | 2.000 | 2.000 | 2.000 | 2.000 | 2.000 | 2.000 |

| Wt. % | 15 | 16 | 17 | 18 | 19 | 20 | 21 | 22 | 23 | 24 | 25 | 26 | 27 | 28 | 29 |
|---|---|---|---|---|---|---|---|---|---|---|---|---|---|---|---|
| CaO | 18.13 | 22.15 | 19.69 | 22.82 | 6.95 | 20.97 | 19.01 | 22.28 | 19.11 | 24.05 | 21.56 | 18.50 | 23.11 | 8.77 | 19.11 |
| SrO | 2.89 | 10.33 | 2.04 | 7.45 | 52.55 | 13.26 | 2.32 | 9.55 | 2.41 | 8.12 | 11.56 | 1.58 | 10.84 | 48.51 | 2.41 |
| BaO | 48.26 | 35.02 | 48.92 | 35.40 | 9.55 | 33.50 | 46.46 | 33.56 | 46.76 | 34.68 | 32.73 | 48.36 | 34.12 | 10.11 | 46.76 |
| $CO_2$* | 29.31 | 31.82 | 30.36 | 31.23 | 30.52 | 31.70 | 29.24 | 31.17 | 29.44 | 32.76 | 31.22 | 29.07 | 32.53 | 30.39 | 29.44 |
| Total | 98.59 | 99.32 | 101.01 | 96.90 | 99.57 | 99.43 | 97.03 | 96.56 | 97.72 | 100.81 | 97.07 | 97.51 | 100.60 | 97.78 | 97.72 |

Formulae calculated on the basis of 2 cations

| | 15 | 16 | 17 | 18 | 19 | 20 | 21 | 22 | 23 | 24 | 25 | 26 | 27 | 28 | 29 |
|---|---|---|---|---|---|---|---|---|---|---|---|---|---|---|---|
| Ca | 0.971 | 1.092 | 1.018 | 1.147 | 0.357 | 1.038 | 1.021 | 1.122 | 1.019 | 1.152 | 1.084 | 0.999 | 1.115 | 0.226 | 1.019 |
| Sr | 0.084 | 0.276 | 0.057 | 0.203 | 1.463 | 0.355 | 0.067 | 0.260 | 0.070 | 0.210 | 0.314 | 0.046 | 0.283 | 0.678 | 0.070 |
| Ba | 0.945 | 0.632 | 0.925 | 0.650 | 0.180 | 0.607 | 0.912 | 0.618 | 0.911 | 0.608 | 0.602 | 0.955 | 0.602 | 0.096 | 0.911 |
| $CO_3$ | 2.000 | 2.000 | 2.000 | 2.000 | 2.000 | 2.000 | 2.000 | 2.000 | 2.000 | 2.000 | 2.000 | 2.000 | 2.000 | 2.000 | 2.000 |

* calculated on the basis of stoichiometry. Analyses 1-16: *Ba-Sr-Ca carbonatite* (1-3 – *Mu-7*; 4-7 – *Mu-8*; 8-11 – *Mu-14*; 12-14 – *Mu-15*;15-16 - *Mu-151*); 17-25: *calcite carbonatite* (17-19 – *Mu-114/2*; 20 – *Mu-136/32*; 21-22 – *Mu-136/33*; 23-25 – *Mu-136/52*); 26-29: *quartz-feldspar-carbonate rock* (26-28 – *Mu-136/46*; 29 – *Mu-145*).

correspond to olekminskite [(Sr,Ca,Ba) $CO_3$], a mineral first described from the Murun complex by Konev *et al.* (1991) (*e.g.* analyses 17 and 28 Table 3.3.2.3).

Carbonates of rare-earth elements.

*Ancylite-(Ce)* [SrCe($CO_3$)$_2$(OH)· $H_2O$] is one of the most abundant *REE*-bearing carbonates in our samples. The mineral is found predominantly in the Ba-Sr-Ca carbonatite, and in lesser amounts, in the calcite carbonatite and quartz-feldspar-carbonate rock. Ancylite-(Ce) occurs as anhedral-to-subhedral discrete crystals up to 170 μm in size or aggregates of anhedral grains commonly confined to the interstitial spaces and fractures in the exsolution aggregates. In the quartz-feldspar-carbonate rock, ancylite-(Ce) also forms stellate aggregates of elongate crystals up to 60 μm across, and is associated with strontianite or developed interstitially relative to calcite and quartz (Fig. 3.3.2.4). The ancylite-(Ce) shows a notable intergranular variation in composition (Table 3.3.2.4). In terms of the proportions of individual *REE*, the Murun ancylite is similar to that from Narssârssuk (Greenland), and low-Nd ancylite-(Ce) from the Bearpaw Mts. (Montana, U.S.A.) (Fig. 3.3.2.9). In terms of Sr-Ca-$\Sigma REE$ contents, our data are similar to those for the material from Khibina (Kola Peninsula, Russia), Bearpaw Mts., and some of the ancylite-(Ce) from Narssârssuk. (Fig. 3.3.2.9, and references therein).


*Burbankite* [(Na,Ca)$_3$(Sr,Ca,*REE*,Ba)$_3$($CO_3$)$_5$] was first described by Pecora & Kerr (1953) in carbonatites from the Bearpaw Mountains, Montana. Subsequently, the mineral was found in several other occurrences, including carbonatites of the Khibina complex (Zaitzev *et al.* 1998) and Chipman Lake complex (Platt & Woolley 1990), nepheline-syenitic rocks of Mont Saint-Hilaire (Chen & Chao 1974) and Eastern Ukraine (Litvin *et al.* 1998). Recently, burbankite has been described in fluid inclusions in quartzites bordering the Kalkfeld carbonatite complex (Bühn *et. al* 1999).

88

Fig. 3.3.2.9. Compositional variation of ancylite.
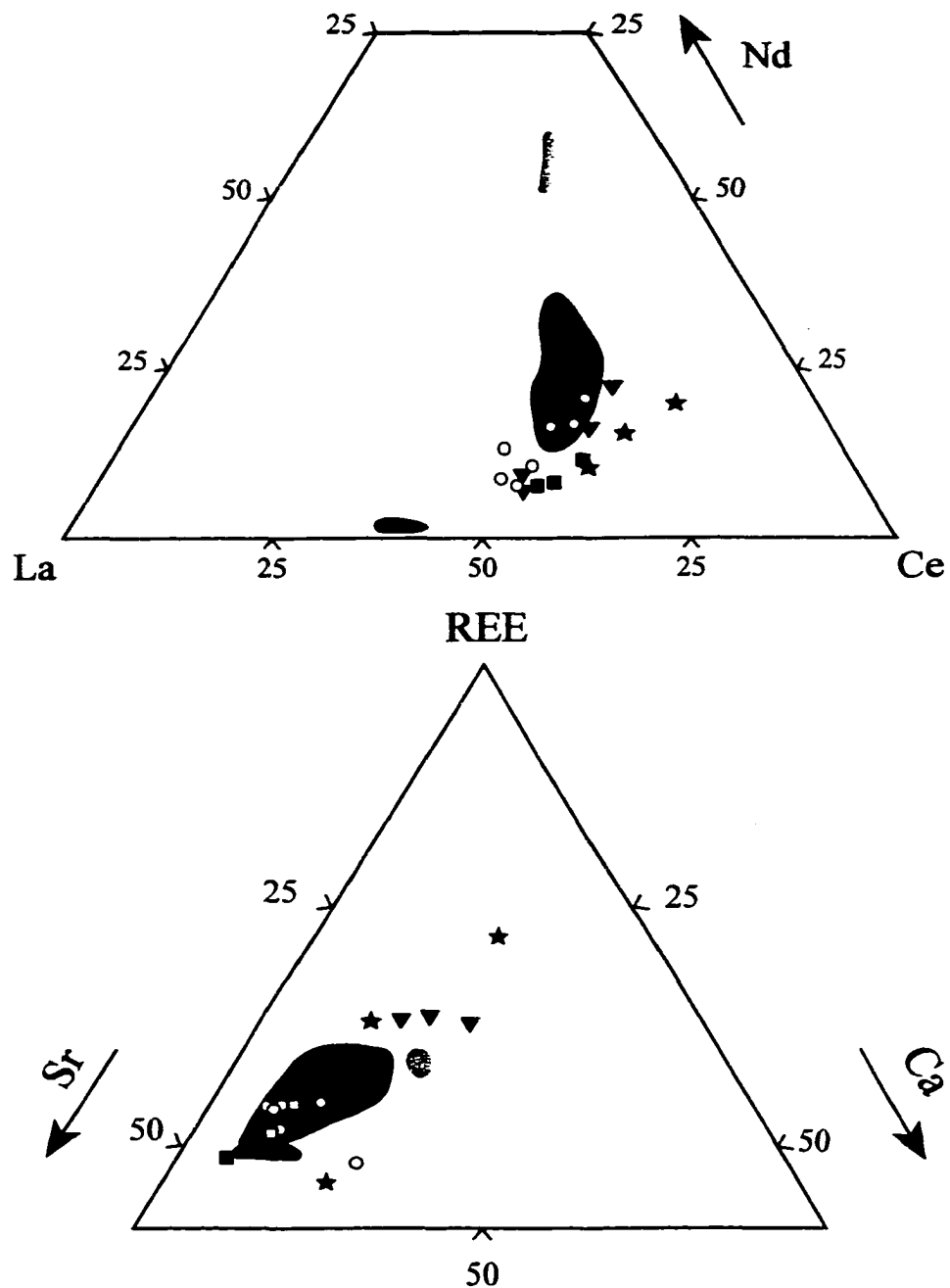
Ancylite-(Ce)

○      Murun, this work

■      Bearpaw Mountains (Reguir & Mitchell 2000)

■      Khibina (Zaitsev *et al.* 1998)

▼      Narssarssuk (Pekov *et al.* 1997)

★      Benfontein (Mitchell 1995)

Ancylite-(La)

■      Khibina (Yakovenchuk *et al.* 1997)

"Ancylite-(Nd)"

▒      Bearpaw Mountains (Reguir & Mitchell 2000)

Table 3.3.2.4. Representative compositions of ancylite-(Ce) from carbonate-rich rocks and charoitites.

| Wt. % | 1 | 2 | 3 | 4 | 5 | 6 | 7 | 8 | 9 | 10 |
|---|---|---|---|---|---|---|---|---|---|---|
| CaO | 1.79 | 2.26 | 1.53 | 1.87 | 1.64 | 3.88 | 2.08 | 2.37 | 1.82 | 0.80 |
| SrO | 20.23 | 19.30 | 23.72 | 19.90 | 20.68 | 19.00 | 20.52 | 16.43 | 17.63 | 21.92 |
| BaO | 1.50 | 1.23 | n.d | 0.93 | 2.25 | 1.93 | 2.82 | n.d | n.d | n.d |
| $La_2O_3$ | 15.81 | 18.29 | 11.21 | 13.35 | 15.98 | 13.12 | 16.84 | 11.75 | 11.83 | 11.20 |
| $Ce_2O_3$ | 21.80 | 22.20 | 21.81 | 23.80 | 20.00 | 20.00 | 21.85 | 28.00 | 27.95 | 24.36 |
| $Pr_2O_3$ | 1.17 | 0.86 | 1.71 | 1.88 | 3.35 | 4.33 | 0.60 | 2.07 | 2.58 | 1.73 |
| $Nd_2O_3$ | 5.38 | 4.31 | 8.14 | 7.25 | 6.17 | 6.18 | 3.76 | 8.92 | 9.40 | 8.39 |
| $Sm_2O_3$ | n.d | n.d | n.d | n.d | n.d | n.d | n.d | 0.25 | 0.91 | 0.75 |
| $ThO_2$ | 2.32 | 1.81 | 0.93 | n.d | n.d | n.d | n.d | 1.44 | 1.46 | n.d |
| $CO_2$* | 22.65 | 22.88 | 22.89 | 22.57 | 22.90 | 23.35 | 22.71 | 22.71 | 23.23 | 23.34 |
| Total | 92.65 | 93.14 | 91.94 | 91.55 | 92.97 | 91.79 | 91.18 | 93.94 | 96.81 | 91.49 |

Formulae calculated on the basis of 2 cations

| | 1 | 2 | 3 | 4 | 5 | 6 | 7 | 8 | 9 | 10 |
|---|---|---|---|---|---|---|---|---|---|---|
| Ca | 0.124 | 0.155 | 0.105 | 0.130 | 0.113 | 0.261 | 0.144 | 0.164 | 0.129 | 0.056 |
| Sr | 0.759 | 0.717 | 0.880 | 0.749 | 0.767 | 0.691 | 0.767 | 0.615 | 0.645 | 0.833 |
| Ba | 0.038 | 0.031 | - | 0.024 | 0.056 | 0.047 | 0.071 | - | - | - |
| La | 0.377 | 0.432 | 0.264 | 0.320 | 0.377 | 0.304 | 0.401 | 0.280 | 0.275 | 0.272 |
| Ce | 0.516 | 0.520 | 0.511 | 0.565 | 0.468 | 0.459 | 0.516 | 0.660 | 0.645 | 0.585 |
| Pr | 0.028 | 0.020 | 0.040 | 0.044 | 0.078 | 0.099 | 0.014 | 0.049 | 0.059 | 0.041 |
| Nd | 0.124 | 0.099 | 0.186 | 0.168 | 0.141 | 0.139 | 0.087 | 0.205 | 0.212 | 0.196 |
| Sm | - | - | - | - | - | - | - | 0.006 | 0.020 | 0.017 |
| Th | 0.034 | 0.026 | 0.014 | - | - | - | - | 0.021 | 0.021 | - |
| $CO_3$ | 2.000 | 2.000 | 2.000 | 2.000 | 2.000 | 2.000 | 2.000 | 2.000 | 2.000 | 2.000 |

* calculated on the basis of stoichiometry; n.d - not detected; analyses 1-4: *Ba-Sr-Ca carbonatite* (1-3 — *Mu-7*; 4 — *Mu-14*; 5 — *Mu-151*); 6: *calcite carbonatite* (*Mu-180*); 7: *quartz-feldspar-carbonate rock* (*Mu-145*); 8-10: *charoitite* (*Mu-198*).

Burbankite is rare in the rocks examined, and is found only in the calcite carbonatite and quartz-feldspar-carbonate rock. The mineral occurs as anhedral-to-subhedral elongate grains up to 30 μm enclosed by the calcite-strontianite exsolution aggregates (Fig. 3.3.2.2b), or as fracture filings. Burbankite is also found in Ba-Sr-Ca carbonate-dominated exsolution aggregates in tinaksite-rich samples of the calcite carbonatite (sample Mu-114/2), where it is associated with calcite, strontianite and kukharenkoite. Recalculation of the microprobe analyses of burbankite to structural formulae invariably results in somewhat low cation total in the A-site (Na+Ca) (Table 3.3.2.5), possibly indicating the presence of vacancies. However, the low cation totals may be merely an artefact resulting from vaporisation of Na under the electron beam. Burbankite from the examined samples exhibits noticeable intergranular compositional variation, especially in terms of Sr-Ba-REE proportions in the B-site (Table 3.3.2.5). SrO and BaO contents vary from 33.5-44.0 wt.% and 0-8.0 wt.%, respectively (Table 3.3.2.5). Some of the burbankite grains are REE-free, whereas in other crystals, $REE_2O_3$ reaches 4.8 wt.%. It is noteworthy, that although most burbankite shows a preponderance of Ce among the rare-earth elements, in some of the crystals, La is a dominant REE (e.g. analysis 3 Table 3.3.2.5). In terms of (Na+Ca)-(Sr+Ba)-REE proportions, the Murun burbankite is similar to the material from Mount St.Hilaire, the Azov region, and some samples from the Khibina complex, Chipman Lake and the Bearpaw Mountains (Fig. 3.3.2.10 and references therein). Burbankite from the Kalkfeld massif and most of the samples from the Khibina complex (Zaitsev et al. 1998) is depleted in BaO, and significantly enriched in $Na_2O$ and $REE_2O_3$ relative to our material (Fig. 3.3.2.10).

Kukharenkoite-(Ce) [$Ba_2Ce(CO_3)_3F$] is rare in the rocks examined. This mineral was first described from carbonatites of the Khibina alkaline complex (Zaitzev et al. 1996). Kukharenkoite-(Ce) has also been found in carbonatites of the Vuorijärvy complex, Russia, at the Mont Saint-Hilaire alkaline complex and the Saint-Amable nepheline syenite sill, Canada (Zaitzev et al. 1996). To our knowledge, it has not been previously observed at Murun.

Table 3.3.2.5. Representative compositions of burbankite from the calcite carbonatite.

| Wt. % | 1 | 2 | 3 | 4 | 5 | 6 | 7 | 8 | 9 |
|---|---|---|---|---|---|---|---|---|---|
| $Na_2O$ | 9.08 | 9.49 | 7.39 | 8.47 | 8.68 | 7.99 | 8.54 | 7.92 | 7.21 |
| CaO | 9.93 | 10.39 | 11.20 | 11.47 | 11.85 | 15.87 | 12.36 | 13.52 | 12.34 |
| SrO | 33.47 | 34.92 | 36.07 | 38.47 | 39.27 | 34.78 | 41.22 | 44.07 | 43.93 |
| BaO | 8.07 | 6.94 | 8.15 | 7.98 | 6.26 | 2.56 | n.d | n.d | n.d |
| $La_2O_3$ | 2.08 | 1.74 | 2.40 | n.d | n.d | 1.55 | 0.82 | n.d | 0.35 |
| $Ce_2O_3$ | 2.73 | 2.90 | 2.19 | n.d | 0.24 | 2.16 | 1.56 | 0.74 | 0.66 |
| $CO_2$* | 32.71 | 33.59 | 33.55 | 33.65 | 34.04 | 35.13 | 34.23 | 35.25 | 33.87 |
| | | | | | | | | | |
| Total | 98.07 | 99.97 | 100.95 | 100.04 | 100.34 | 100.04 | 98.73 | 101.50 | 98.36 |

Formulae calculated on the basis of 15 atoms of oxygen:

| | 1 | 2 | 3 | 4 | 5 | 6 | 7 | 8 | 9 |
|---|---|---|---|---|---|---|---|---|---|
| Na | 1.971 | 2.006 | 1.564 | 1.788 | 1.811 | 1.615 | 1.772 | 1.595 | 1.512 |
| Ca | 0.916 | 0.905 | 1.127 | 1.106 | 1.089 | 1.122 | 1.067 | 1.188 | 1.224 |
| $\Sigma A$ cations | 2.877 | 2.911 | 2.691 | 2.894 | 2.900 | 2.737 | 2.839 | 2.783 | 2.736 |
| | | | | | | | | | |
| Ca | 0.275 | 0.309 | 0.183 | 0.232 | 0.277 | 0.651 | 0.350 | 0.317 | 0.205 |
| Sr | 2.173 | 2.208 | 2.283 | 2.428 | 2.450 | 2.102 | 2.557 | 2.655 | 2.755 |
| Ba | 0.354 | 0.297 | 0.349 | 0.340 | 0.264 | 0.105 | - | - | - |
| La | 0.086 | 0.070 | 0.097 | - | - | 0.060 | 0.032 | - | 0.014 |
| Ce | 0.112 | 0.116 | 0.088 | - | 0.009 | 0.082 | 0.061 | 0.028 | 0.026 |
| $\Sigma B$ cations | 3.000 | 3.000 | 3.000 | 3.000 | 3.000 | 3.000 | 3.000 | 3.000 | 3.000 |
| | | | | | | | | | |
| $\Sigma (A+B)$ cat. | 5.877 | 5.911 | 5.691 | 5.894 | 5.900 | 5.737 | 5.839 | 5.783 | 5.736 |
| | | | | | | | | | |
| $CO_3$ | 5.000 | 5.000 | 5.000 | 5.000 | 5.000 | 5.000 | 5.000 | 5.000 | 5.000 |

* calculated on the basis of stoichiometry; n.d = not detected; 1-5: *Mu-114/2*; 6-9: *Mu-1052-20*.
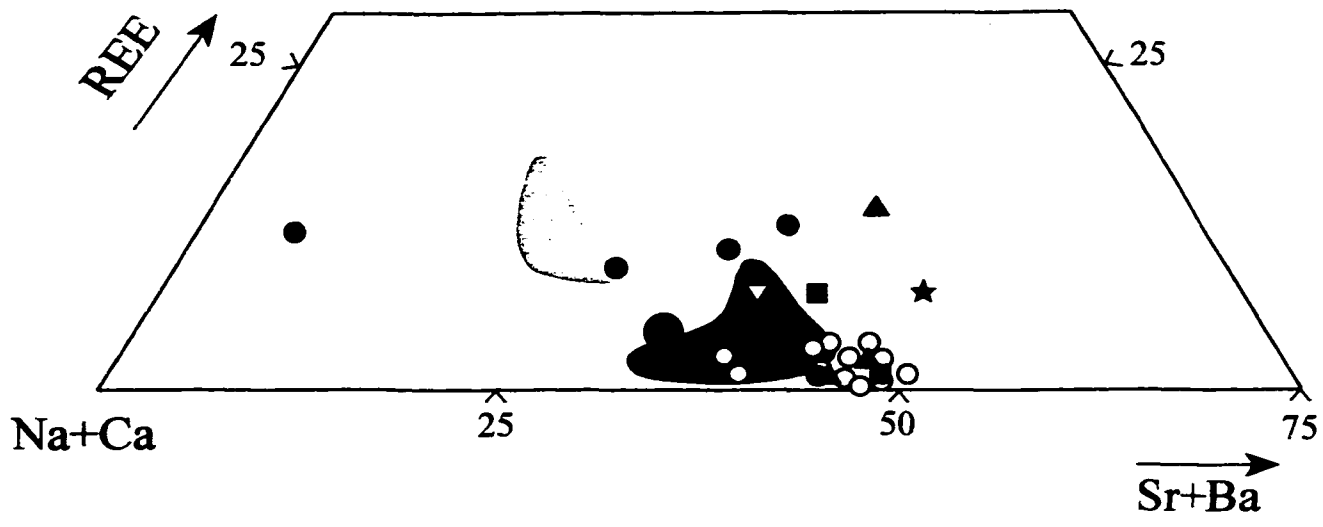
O　　　Murun, this work

★　　　Murun (Konev *et al.*, 1996)

▮　　　Bearpaw Mountains (Reguir & Mitchell, 2000)

▽　　　Bearpaw Mountains (Effenberger *et al.*, 1985)

●　　　Khibina (Belovitskaya *et al.*, 1998)

▢　　　Khibina (Zaitsev *et al.*, 1998)

■　　　Chipman Lake (Platt & Wooley, 1990)

●　　　Kalkfeld (Buhn *et al.*, 1999)

▲　　　Azov region (Litvin *et al.*, 1998)

■　　　Mont St. Hilaire (Chen & Chao, 1974)

Fig. 3.3.2.10.　Compositional variation in burbankite.

Table 3.3.2.6. Representative compositions of kukharenkoite.

| Wt.% | 1 | 2 | 3 | 4 | 5** | 6** | 7** | 8 | 9 | 10 | 11 | 12 | 13 |
|---|---|---|---|---|---|---|---|---|---|---|---|---|---|
| $Na_2O$ | 0.36 | 0.24 | 0.46 | 0.41 | n.d | 0.08 | n.d | 0.41 | n.d | n.d | n.d | n.d | 0.62 |
| $CaO$ | 1.54 | 1.80 | 1.61 | 1.23 | 0.39 | 0.05 | 0.06 | 1.62 | 2.80 | 2.28 | 2.05 | 1.26 | 2.17 |
| $SrO$ | 2.69 | 2.72 | 2.76 | 2.22 | 1.55 | 0.42 | 0.05 | 2.44 | 3.41 | 3.96 | 6.51 | 6.69 | 4.15 |
| $BaO$ | 42.94 | 43.41 | 41.90 | 42.72 | 47.39 | 48.93 | 50.07 | 40.72 | 39.14 | 40.39 | 38.80 | 39.64 | 38.29 |
| $La_2O_3$ | 10.40 | 9.67 | 9.02 | 8.63 | 6.61 | 6.16 | 10.27 | 13.88 | 19.30 | 20.29 | 12.84 | 14.52 | 17.62 |
| $Ce_2O_3$ | 13.39 | 12.75 | 13.41 | 11.83 | 15.30 | 15.12 | 14.32 | 12.12 | 1.74 | 2.49 | 9.14 | 9.02 | 1.91 |
| $Pr_2O_3$ | 0.99 | 0.93 | 0.84 | 0.81 | 1.19 | 1.49 | 0.37 | 0.77 | 1.13 | 1.18 | 1.30 | 1.67 | 1.36 |
| $Nd_2O_3$ | 2.84 | 2.57 | 2.76 | 3.53 | 4.26 | 4.08 | 1.47 | 1.95 | 1.65 | 1.02 | 1.29 | 1.00 | 2.67 |
| $Y_2O_3$ | n.d | n.d | n.d | n.d | n.d | n.d | n.d | n.d | n.d | 0.46 | n.d | 0.76 |  |
| $ThO_2$ | n.d | n.d | n.d | 0.42 | n.d | 0.10 | n.d | n.d | n.d | n.d | n.d | n.d | 0.18 |
| $F$ | 0.56 | 0.67 | 0.60 | 0.83 | 3.18 | 3.20 | 3.14 | 0.32 | n.a | n.a | n.a | n.a | n.a |
| $CO_2*$ | 22.59 | 22.32 | 22.09 | 21.47 | 21.95 | 21.74 | 21.54 | 22.29 | 21.29 | 21.97 | 22.11 | 21.69 | 21.70 |
| $-F=O_2$ | 0.24 | 0.28 | 0.25 | 0.35 | 1.34 | 1.35 | 1.32 | 0.13 | - | - | - | - | - |
| Total | 98.06 | 96.80 | 95.20 | 93.75 | 100.63 | 100.28# | 99.97 | 96.39 | 90.46 | 94.04 | 94.04 | 93.25 | 90.67 |
| **Formulae calculated on the basis of 3 cations** | | | | | | | | | | | | | |
| Na | 0.068 | 0.046 | 0.089 | 0.081 | - | 0.016 | - | 0.078 | - | - | - | - | 0.122 |
| Ca | 0.160 | 0.190 | 0.172 | 0.135 | 0.042 | 0.005 | 0.007 | 0.171 | 0.309 | 0.245 | 0.218 | 0.136 | 0.235 |
| Sr | 0.152 | 0.155 | 0.159 | 0.132 | 0.090 | 0.025 | 0.003 | 0.139 | 0.204 | 0.230 | 0.375 | 0.393 | 0.244 |
| Ba | 1.636 | 1.675 | 1.633 | 1.714 | 1.859 | 1.938 | 2.002 | 1.573 | 1.583 | 1.583 | 1.511 | 1.454 | 1.519 |
| La | 0.373 | 0.351 | 0.331 | 0.326 | 0.244 | 0.230 | 0.386 | 0.505 | 0.735 | 0.748 | 0.471 | 0.543 | 0.658 |
| Ce | 0.477 | 0.460 | 0.488 | 0.443 | 0.561 | 0.560 | 0.534 | 0.437 | 0.066 | 0.091 | 0.332 | 0.335 | 0.071 |
| Pr | 0.035 | 0.033 | 0.030 | 0.030 | 0.043 | 0.055 | 0.014 | 0.028 | 0.042 | 0.043 | 0.047 | 0.062 | 0.050 |
| Nd | 0.099 | 0.090 | 0.098 | 0.129 | 0.152 | 0.147 | 0.054 | 0.069 | 0.061 | 0.036 | 0.046 | 0.036 | 0.097 |
| Y |  |  |  |  |  |  |  |  |  | 0.024 |  | 0.041 |  |
| Th |  |  |  | 0.010 |  | 0.002 |  |  |  |  |  |  | 0.004 |
| F | 0.172 | 0.209 | 0.189 | 0.269 | 1.007 | 1.023 | 1.013 | 0.100 | - | - | - | - | - |
| $CO_3$ | 3.000 | 3.000 | 3.000 | 3.000 | 3.000 | 3.000 | 3.000 | 3.000 | 3.000 | 3.000 | 3.000 | 3.000 | 3.000 |
| *ΣA cations* | *2.016* | *2.066* | *2.053* | *2.062* | *1.991* | *2.006##* | *2.012* | *1.961* | *2.096* | *2.057* | *2.104* | *1.984* | *2.120* |
| *ΣB cations* | *0.984* | *0.934* | *0.947* | *0.938* | *1.009* | *0.994* | *0.988* | *1.039* | *0.904* | *0.943* | *0.896* | *1.016* | *0.880* |

* calculated on the basis of stoichiometry; n.d - not detected; n.a = not analysed; ** our recalculation of the original analytical data; # Total also includes 0.26 wt.% MnO; ## sum also includes 0.022 apfu $Mn^{2+}$. Analyses 1-8: kukharenkoite-(Ce) (1-4 – Ba-Sr-Ca carbonatite [Mu-8]; 5-7 – Zaitzev et al.,1998); 8-13: "kukharenkoite-(La)" (8 – Ba-Sr-Ca carbonatite [Mu-114/2]; 9-12 – calcite carbonatite [Mu-15]; 13 – charoitite [Mu-13]).

94

Fig. 3.3.2.11.. Compositional variation of kukharenkoite.
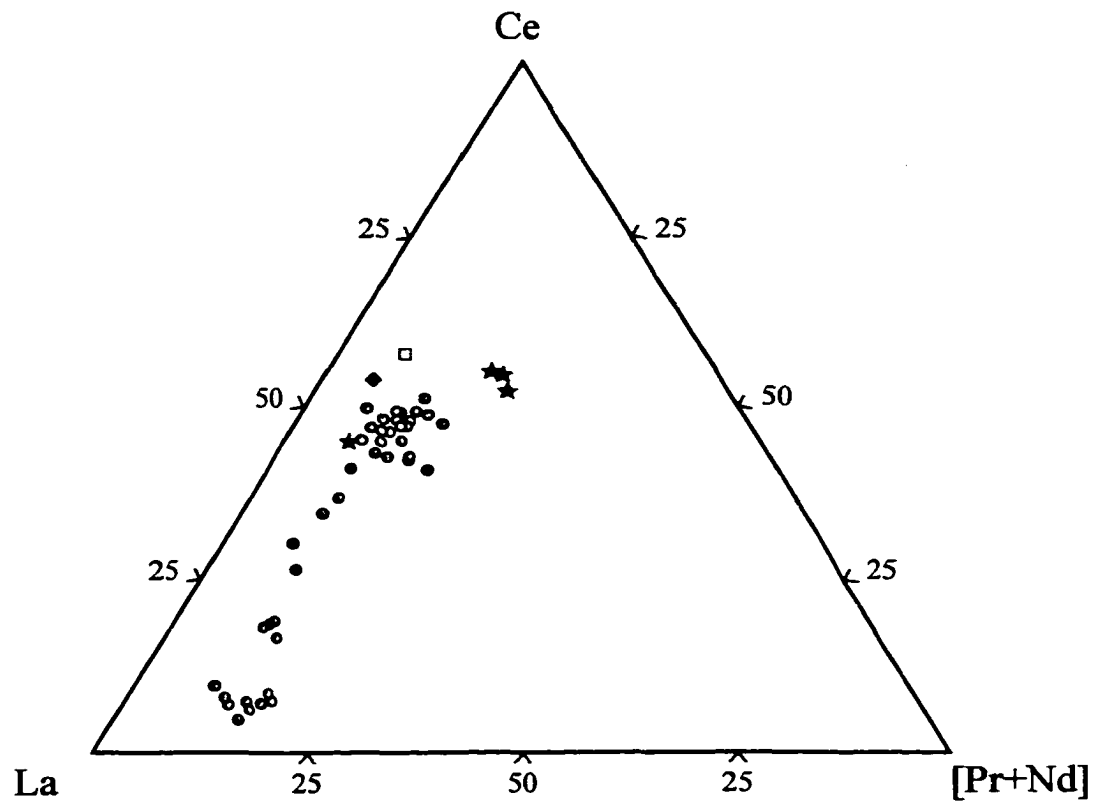
- Murun, this work
★ Khibina (Zaitsev *et al.* 1998)
◆ Vuorijärvy (Zaitsev *et al.* 1998)
□ Mont St. Hilaire (Zaitsev *et al.* 1998)

Kukharenkoite-(Ce) is found as anhedral grains (15-100 μm in size) embedded in the exsolution aggregates (Figs. 3.3.2.3b and 3.3.2.5), where it is commonly associated with burbankite. In contrast to the type material, kukharenkoite from Murun exhibits significant intergranular compositional variation, especially in terms of the Ce/La proportion. The majority of compositions are very similar to the data of Zaitsev *et al.* (1996), but some samples differ from the type material in being significantly enriched in La (Table 3.3.2.6, Fig. 3.3.2.11). A few compositions correspond to a distinct mineral species, *i.e.* "*kukharenkoite-(La)*" (Table 3.3.2.6, Fig. 3.3.2.11).

### 3.3.3 *Quartz*

Quartz is found predominantly in the quartz-feldspar-carbonate rock (Mu-145 and Mu-136/46), where this mineral comprises 15-20 vol.% of the rock.



Fig. 3.3.3.1. Relationships of quartz (grey) with potassium feldspar (crosshatched) and calcite (fine-grained, multicoloured). Quartz-feldspar-carbonate rock (Mu-145); FOV 6 mm; crossed polars.

96

Here, quartz occurs as oikocrysts enclosing euhedral crystals of potassium feldspar, clinopyroxene and calcite (Figs. 3.3.3.1 and 3.3.2.6) or as graphic intergrowths with calcite. Some of the quartz grains contain inclusions of relatively high-Sr calcite (Fig. 3.3.2.4). Quartz is also found in minute amounts in the Ba-Sr-Ca carbonatite and calcite carbonatite, where it is developed interstitially and as fracture fillings in the earlier-crystallised phases.

### 3.3.4 Fluorapatite

*Fluorapatite* is found as a ubiquitous constituent in all types of rocks examined in the present study. In the Ba-Sr-Ca carbonatite and quartz-feldspar-carbonate rock, the mineral forms subhedral-to-euhedral prismatic (up to 100 µm in length) or rounded (up to 50 µm in diameter) crystals embedded in the carbonates, or developed interstitially and along the fractures in feldspar and other earlier-crystallised minerals. In calcite carbonatite, fluorapatite is found in cavities and fractures in the calcite-strontianite intergrowths. In the phlogopite-calcite carbonatite, fluorapatite occurs as anhedral-to-subhedral grains and aggregates of subhedral crystals (up to 230 µm in size) in a phlogopite matrix. The mineral is generally enriched in SrO and is characteristically devoid of Si. In the calcite carbonatite and Ba-Sr-Ca carbonatite, flourapatite commonly shows a weak-to-moderate irregular zoning, with high-$AZ$ zones enriched in SrO (up to 6.7 wt.%: Table 3.3.4.1). Some apatite crystals from the quartz-feldspar-carbonate rock and calcite carbonatite show a different zonation pattern, with high-$AZ$ zones enriched in $LREE$ (up to 1.5 wt.%; analyses 6, 8 and 9, Table 3.3.4.1). In contrast to the other examined carbonate-rich rocks, some of the fluorapatite crystals from the quartz-feldspar-carbonate rock contain appreciable Na (up to 0.5 wt.%; Table 3.3.4.1).

Previously, Sr-rich apatite has been described from many carbonatite occurrences worldwide, including Gatineau, Quebec (4.7 wt.%: Hogarth *et al.* 1985) and Oldoinyo Lengai, Tanzania (2.2-4.6 wt.%; Dawson 1993). Chakhmouradian & Mitchell (1998) have observed extremely Sr-rich (up to 12.8 wt.% SrO) fluorapatite in dolomite carbonatites of Lesnaya Varaka, Russia.

97

Table 3.3.4.1. Representative compositions of fluorapatite from carbonatites.

| Wt. % | 1 low-Az | 2 high-Az | 3 low-Az | 4 high-Az | 5 low-Az | 6 high-Az | 7 low-Az | 8 high-Az | 9 high-Az |
|---|---|---|---|---|---|---|---|---|---|
| $P_2O_5$ | 41.60 | 40.56 | 42.35 | 41.74 | 41.76 | 41.92 | 41.47 | 41.46 | 41.13 |
| $La_2O_3$ | n.d | n.d | n.d | n.d | n.d | n.d | n.d | 0.49 | 0.50 |
| $Ce_2O_3$ | n.d | n.d | n.d | n.d | n.d | 0.22 | n.d | 1.00 | 0.93 |
| CaO | 52.63 | 51.37 | 52.85 | 50.71 | 54.78 | 53.00 | 53.63 | 52.21 | 52.21 |
| SrO | 5.24 | 6.72 | 4.58 | 6.65 | 2.76 | 4.72 | 2.75 | 2.80 | 2.57 |
| $Na_2O$ | n.d | n.d | n.d | n.d | n.d | n.d | n.d | n.d | 0.47 |
| F | 1.59 | 1.88 | 1.23 | 1.71 | 3.20 | 2.22 | 1.69 | 1.75 | 1.87 |
| $-O=F_2$ | 0.67 | 0.79 | 0.52 | 0.72 | 1.35 | 0.93 | 0.71 | 0.74 | 0.79 |
| Total | 100.39 | 99.74 | 100.49 | 100.09 | 101.15 | 101.15 | 98.83 | 98.97 | 98.89 |

Formulae calculated on the basis of 8 cations

| | 1 | 2 | 3 | 4 | 5 | 6 | 7 | 8 | 9 |
|---|---|---|---|---|---|---|---|---|---|
| La | - | - | - | - | - | - | - | 0.016 | 0.016 |
| Ce | - | - | - | - | - | 0.007 | - | 0.031 | 0.029 |
| Ca | 4.766 | 4.721 | 4.762 | 4.647 | 4.909 | 4.777 | 4.882 | 4.801 | 4.777 |
| Sr | 0.257 | 0.334 | 0.223 | 0.330 | 0.134 | 0.230 | 0.135 | 0.139 | 0.127 |
| Na | - | - | - | - | - | - | - | - | 0.078 |
| $\Sigma$ | 5.023 | 5.055 | 4.985 | 4.977 | 5.043 | 5.014 | 5.017 | 4.987 | 5.027 |
| P | 2.977 | 2.945 | 3.015 | 3.023 | 2.957 | 2.986 | 2.983 | 3.013 | 2.973 |
| F | 0.425 | 0.510 | 0.327 | 0.463 | 0.846 | 0.591 | 0.454 | 0.475 | 0.505 |

n.d = not detected. Analyses 1-4: *Ba-Sr-Ca carbonatite* (1-2 − *Mu-8*; 3-4 − *Mu-15*); 5-6: *calcite carbonatite (Mu-1052/20)*; 7-9: *quartz-feldspar-carbonate rock (Mu-145)*.

### 3.3.5 *Barite*

Barite is a common late-stage mineral in the samples examined. The mineral forms subhedral-to-euhedral crystals up to 50 μm across that are typically confined to cavities and fractures. It also occurs among alteration products developed after earlier-crystallised minerals (*e.g.* titanite). Barite commonly occurs in the calcite-strontianite and Ba-Sr-Ca carbonate-calcite-strontianite intergrowths, where it is associated with kukharenkoite, ancylite-(Ce) and burbankite. Compositionally, barite from the Murun carbonatites shows slight enrichment in SrO and CaO contents (both ≤ 1.0 wt.%).

### 3.3.6 *Fluorite*

This mineral occurs in aggregates (up to 200 μm in size) of anhedral grains developed interstitially or along fractures in potassium feldspar and carbonates, and was found only in one sample the Ba-Sr-Ca carbonatite (Mu-180).

### 3.3.7 *Sulphides*

In the samples examined, sulphides are found in subordinate amounts. *Pyrrhotite* and *pyrite* occur predominantly in the phlogopite-calcite carbonatite. Here, pyrrhotite forms anhedral-to-subhedral, commonly elongate grains up to 250 μm in size, commonly containing inclusions of potassium feldspar, titanite, and apatite. Pyrite occurs as subhedral crystals up to 150 μm in size generally confined to cavities and fractures.

*Chalcopyrite* occurs in most of the examined rocks as anhedral-to-subhedral, rarely diamond-shaped grains up to 100 μm across, typically showing an alteration rim. The mineral is associated with galena, bornite and sphalerite.

*Bornite* forms subhedral grains up to 200 μm, commonly with exsolution lammelae of an unidentified phase, and in few cases, is altered to barite along fractures and margins.

*Galena* and *sphalerite* are found predominantly as rare minute (*ca.* 40 μm) inclusions in chalcopyrite. Galena occurs predominantly in the quartz-feldspar-carbonate rock, where it forms anhedral grains, commonly with an alteration rim.

Diggenite [$Cu_9S_5$] occurs chiefly in the Ba-Sr-Ca carbonatite as rare anhedral grains up to 170 μm in size, confined to fractures in the carbonates and clinopyroxene.

Most of the sulphide minerals are poor in minor elements and typically correspond to the ideal compositions. Sphalerite and digenite may contain appreciable Fe (*ca.* 0.2 wt.% and 1 wt.%, respectively).

### 3.3.8   *Vanadates*

*Vanadinite* [$Pb_5(VO_4)_3Cl$] is extremely rare in the rocks examined, and was found only in a sample of the Ba-Sr-Ca carbonatite (Mu-151), where it forms anhedral-to-subhedral interstitial grains *ca.* 20 μm in size. The mineral exhibits relative enrichment in CuO (up to 1.26 wt.%), BaO (up to 1.2 wt.%) and FeO (up to 0.6 wt.%) (Table 3.3.8.1).

Vanadinite occurs in intimate intergrowths with an unidentified Pb- and Cu-bearing vanadate with composition corresponding to the general empirical formula: (Pb, Cu,Ba,Ca)$_2$(VO$_4$)(OH) (Table 3.3.8.1). Unlike in mottramite [$PbCu(VO_4)(OH)$], the vanadate of the current study has a Pb:Cu proportion that is close to 2:1. This mineral also contains appreciable BaO (1.3-1.5 wt.%), FeO (≤ 0.7 wt.%) and, in some cases, MnO (1.0 wt.%) (Table 3.3.8.1). The low analyses totals may reflect the presence of some amount of molecular water.

100

Table 3.3.8.1. Representative compositions of vanadinite and an unidentified Pb-Cu vanadate from Ba-Sr-Ca carbonatite (Mu-151).

| | 1 | 2 | 3 | 4 | 5 | 6 | 7 |
|---|---|---|---|---|---|---|---|
| $SiO_2$ | n.d | n.d | n.d | n.d | 0.25 | 0.52 | 0.60 |
| FeO | 0.55 | 0.57 | 0.43 | 0.19 | 0.66 | 0.57 | 0.51 |
| $V_2O_5$ | 18.26 | 18.38 | 18.25 | 18.83 | 21.93 | 21.49 | 21.2 |
| PbO | 79.30 | 78.97 | 79.64 | 78.43 | 59.29 | 59.54 | 59.48 |
| CaO | 0.23 | n.d | 0.11 | 0.28 | 0.52 | 0.59 | 0.63 |
| MnO | n.d | n.d | n.d | n.d | n.d | n.d | 1.00 |
| CuO | n.d | n.d | 0.41 | 1.26 | 11.89 | 11.96 | 11.10 |
| BaO | n.d | 1.17 | 0.73 | 0.99 | 1.26 | 1.54 | 1.36 |
| Cl | 2.37 | 2.27 | 2.52 | 2.14 | n.d | n.d | n.d |
| -O=F | 0.53 | 0.51 | 0.57 | 0.48 | - | - | - |
| $H_2O^*$ | - | - | - | - | 3.39 | 2.24 | 1.90 |
| Total | 100.18 | 100.85 | 101.52 | 101.64 | 98.19 | 98.45 | 97.78 |

Formulae calculated on the basis of:

| | 13 anions | | | | 3 cations | | |
|---|---|---|---|---|---|---|---|
| Si | - | - | - | - | 0.018 | 0.038 | 0.043 |
| $Fe^{2+}$ | 0.110 | 0.114 | 0.085 | 0.037 | 0.040 | 0.034 | 0.041 |
| $V^{5+}$ | 2.892 | 2.898 | 2.861 | 2.897 | 1.053 | 1.027 | 1.013 |
| Pb | 5.118 | 5.073 | 5.087 | 4.916 | 1.160 | 1.158 | 1.158 |
| Ca | 0.059 | - | 0.028 | 0.070 | 0.040 | 0.046 | 0.049 |
| Mn | - | - | - | - | - | - | 0.061 |
| Cu | - | - | 0.073 | 0.222 | 0.653 | 0.653 | 0.606 |
| Ba | - | 0.109 | 0.068 | 0.090 | 0.036 | 0.044 | 0.039 |
| Cl | 0.963 | 0.918 | 1.013 | 0.845 | - | - | - |
| OH | - | - | - | - | 1.159 | 1.080 | 0.916 |

n.d = not detected; * calculated from stoichiometry. Analyses 1-4: vanadinite; 5-7: unidentified vanadate. For analyses 5-7, S, As and P were sought, but not found.

101

## 3.4    Discussion and conclusions

### 3.4.1    *Genesis of the Murun carbonatites and related rocks*

Sr- and Ba-rich carbonatites from Murun alkaline complex represent a compositionally and mineralogically unique rock type, and have no direct analogues. In addition to Ca- rich strontianite, calcite with elevated Sr contents, olekminskite [(Sr,Ca,Ba) $CO_3$], and Ba-Ca-Sr carbonates with the general formula $(Ca_{0.97-1.15}Ba_{0.53-0.99}Sr_{0.01-0.44})(CO_3)_2$, several rare minerals have been found in the examined rocks. These include burbankite, ancylite-(Ce) and kukharenkoite; the latter has not been previously described from the Murun rocks. In the present work we distinguished three mineralogical types of carbonatites: calcite carbonatite (i), Ba-Sr-Ca carbonatite (ii), and phlogopite-calcite carbonatite (iii).

In the carbonatites of types (i) and (ii), the earliest mineral paragenesis to crystallise includes potassium feldspar, followed by aegirine-augite, and a primary Ca-Sr-Ba carbonate (strontian calcite or barytocalcite). In some samples, the early mineral assemblage also includes titanite, zircon, potassic richterite, and strontian apatite. The late stage mineral assemblage is composed of stellite aegirine, products of exsolution in primary carbonates, fluorite, dalyite, barite, sulphides, *REE*-bearing carbonates, vanadinite, and in the calcite carbonatite, tinaksite and turkestanite.

The calcite-carbonatite and Ba-Sr-Ca carbonatite differ noticeably in terms of the composition of rock-forming silicates (Figs. 3.3.1.2 and 3.3.1.4). Potassium feldspar from the Ba-Sr-Ca carbonatite is significantly enriched in $Fe^{3+}$ (0.06-0.27 apfu) in comparison with the calcite-carbonatite (0.01-0.10 apfu). This compositional dissimilarity clearly results from different $f(O_2)$ in two types of parental magma. However in both cases, the crystals of potassium feldspar show oscillatory zoning with some variation in Fe/Al among the zones (Fig. 3.4a,b), indicating fluctuations in $f(O_2)$ throughout the crystallisation span of the feldspar.

In the ternary system $CaFe^{2+}Si_2O_2–CaMgSi_2O_6–NaFe^{3+}Si_2O_6$, the compositions of clinopyroxene from the two types of carbonatites define subparallel, partially overlapping trends, indicating that these carbonatites evolved independently and cannot represent differentiates from a single parental carbonatitic magma (Fig. 3.3.1.4). The early clinopyroxene

102

from the calcite carbonatite is represented by sodic diopside and aegirine-augite depleted in hedenbergite component relative to the aegirine-augite from the Ba-Sr-Ca carbonatite. The observed difference in $Fe^{2+}$/Mg ratio may result from (i) different oxygen fugacities during the crystallisation of the two types of clinopyroxene, or (ii) competition for Mg or $Fe^{2+}$ between clinopyroxene and other mafic minerals (*e.g.*, Mitchell & Vladykin 1996; Piilonen *et al.* 1998). As the Ba-Sr-Ca carbonatite crystallised in a more oxidised environment (see above), we suggest that the generally higher $Fe^{2+}$/Mg ratio in the clinopyroxene from this carbonatite resulted from sequestration of Mg by alternative hosts such as amphibole. This conclusion is further supported by the occurrence of relict richterite in some samples of Ba-Sr-Ca carbonatite (Figs. 3.2.2a and 3.3.1.5).

The major mineralogical difference between the carbonatites of type (i) and (ii) is the nature of primary carbonates. In type (i), the primary carbonate is a Sr-rich calcite with relatively low Ba contents ($\leq$ 1.9 wt.% BaO), whereas the rocks of type (ii) contain barytocalcite as a major carbonate phase, and only minor Ba-rich calcite as a part of the subsoludus mineral assemblage. In both cases, the primary carbonates became unstable upon cooling and underwent complex exsolution processes. Typical exsolution textures consist of primary carbonates in a core, and the subsolvus mineral assemblage confined to marginal parts of the crystal. The composition of the primary carbonates becomes progressively depleted in "impurity" components (Ba + Sr in calcite, and Sr in barytocalcite) towards the margin. In our opinion, this indicates that interstitial fluids played an important role in the onset of exsolution processes promoting an outward diffusion of components in the peripheral zones of carbonate crystals. The mineralogy of the exsolution assemblage is strikingly similar in the two types of carbonatites (Fig. 3.4.1.1), whereas the proportion among the three principle constituents (calcite, strontianite, and barytocalcite) is very different. During the exsolution process light rear earth elements (*LREE*) present in the primary carbonates in trace amounts, were incorporated in kukharenkoite and partly in strontianite (up to 3.9 wt. % $LREE_2O_3$).

103
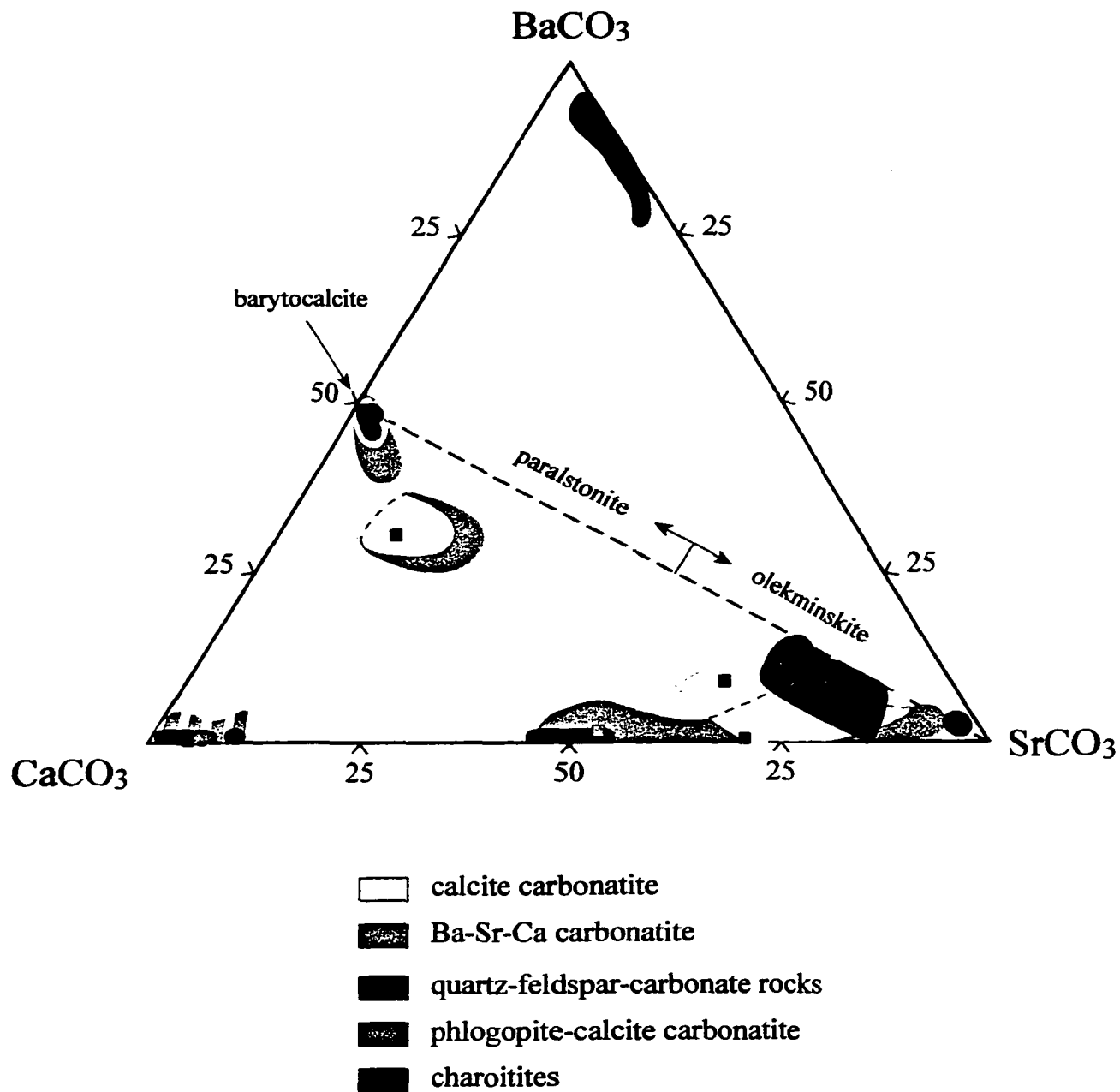
Fig. 3.4.1.1. Compositional variations of Ca-, Sr- and Ba-bearing carbonates from the carbonate-rich rocks of the Murun complex.

104

In the carbonatites of type (i), the primary Sr-rich calcite contains 5-6 mol.% $SrCO_3$. If we neglect the effect of Sr removal by diffusion during the exsolution process, the composition of the primary Sr-rich calcite attests to crystallisation temperatures in excess of 650° C (Fig. 3.4.1.2a). At lower temperatures, pressures greater than 4 kbar are required for incorporation of significant Sr into calcite. As the subsolvus calcite and, especially, strontianite show a significant variation in composition, the exsolution probably occurred over a range of temperatures. Comparatively low Ca contents (< 30 mol.% $CaCO_3$) in strontianite indicate total pressures not exceeding 2 kbar and temperatures generally below 350° C (Fig. 3.4.1.2b).

Crystallisation conditions for the carbonatites of type (ii) cannot be readily inferred from the available experimental data because the system $CaCO_3$–$SrCO_3$–$BaCO_3$ has not been studied in sufficient detail. There is complete miscibility between witherite and strontianite at all temperatures and pressures, whereas in the system $BaCO_3$–$CaCO_3$, a complete solid solution exists only above 850° C (Fig. 3.4.1.3). Below 500° C, the system incorporates two solvii separating orthorhombic witherite and rhombohedral calcite from monoclinic barytocalcite [$CaBa(CO_3)_2$]. At ambient pressures, the barytocalcite-type structure is stable in a relatively narrow range of compositions, and only a few mol.% of $SrCO_3$ can be incorporated into this structure. The solubility of $SrCO_3$ in barytocalcite increases with pressure (Chang 1965); however, even pressures in excess of 20 kbar cannot account for 13-22 mol.% $SrCO_3$ present in the primary barytocalcite from Murun.

In the phlogopite-calcite carbonatite [type (iii)], the early mineral assemblage includes phlogopite, primary Sr-rich calcite, potassium feldspar, apatite, and subordinate amounts of andradite and titanite. The late-stage mineral assemblage is composed of sulphides (mostly pyrite and pyrrhotite), rutile (rimming titanite), and secondary carbonates exsolved from the Sr-rich calcite. In contrast to the calcite-dominant carbonatites of type (i), this type is devoid of clinopyroxene and Ba-Sr-Ca carbonates. The two types of carbonatites also differ in the composition of feldspar phenocrysts. In the phlogopite-bearing type, potassium feldspar lacks detectable Fe, and contains appreciable Na and Ba contents (0.7-1.2 and 1.7-3.5 wt.%
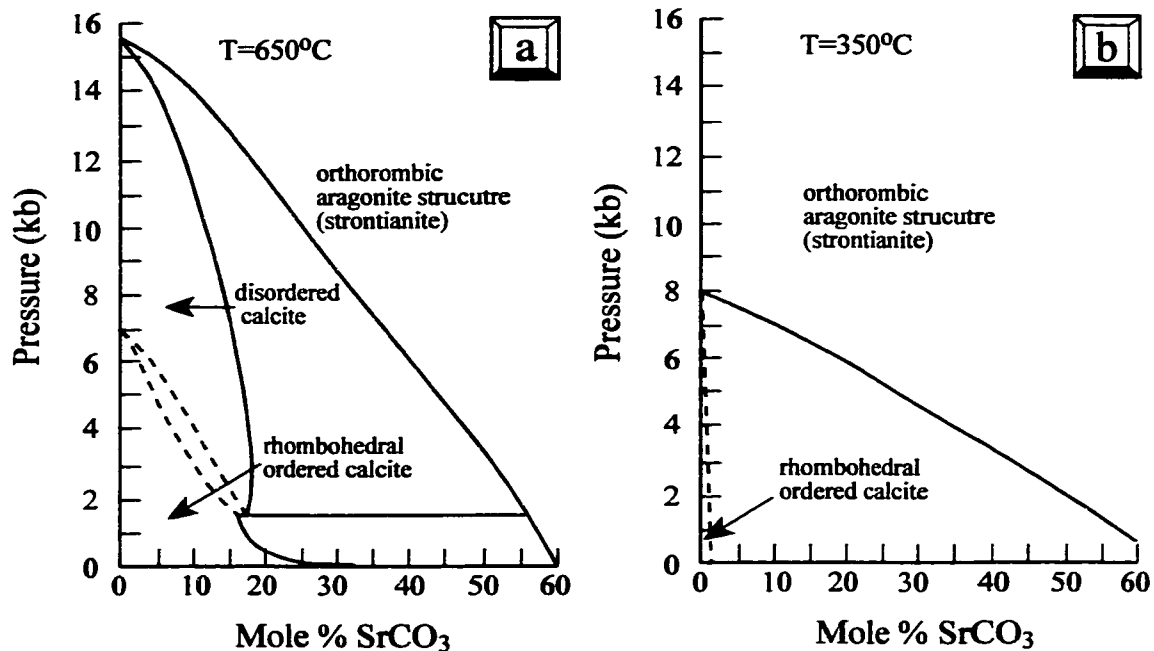
Fig. 3.4.1.2. Isothermal sections of 650°C and 350°C in the system CaCO3-SrCO3 (after Carlson, 1988).
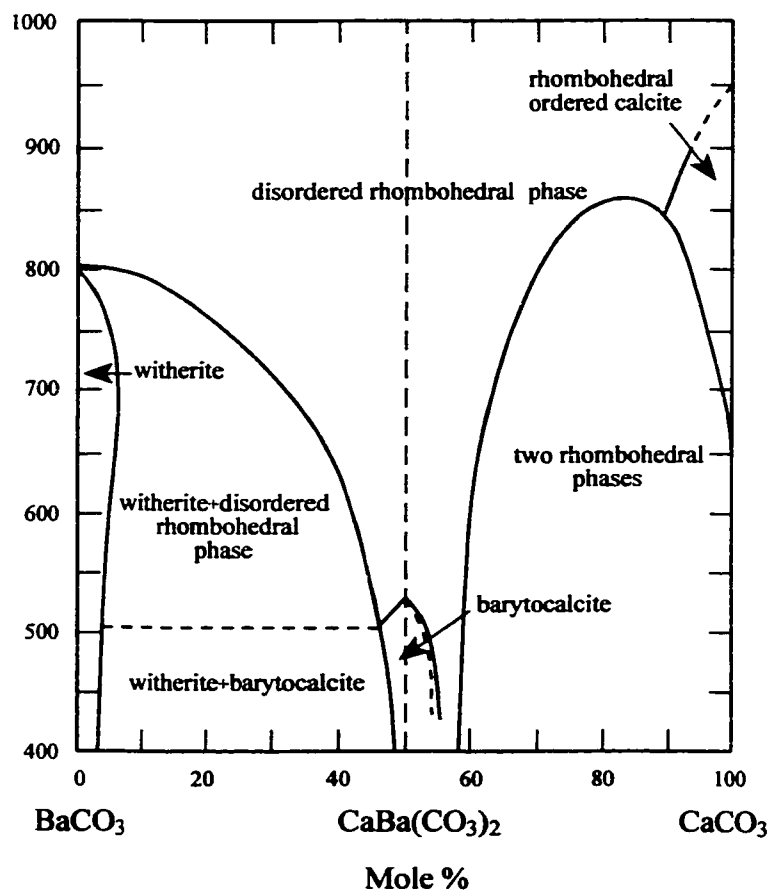


Fig. 3.4.1.3. Subsolidus phase relations in the system BaCO3-CaCO3.

106

respective oxides). In common with potassium feldspar, phlogopite from the type-(iii) carbonatite is enriched in Ba (up to 2.4 wt.% BaO). Both minerals exhibit a similar core-to-rim zonation pattern of decreasing Ba content. This indicates that early sequestration of Ba in the silicates precluded crystallisation of primary Ba carbonates such as barytocalcite. The mineralogical differences between the carbonatites of types (i) and (iii) clearly indicate that the latter crystallised from a volatile-rich magma depleted in Na, and under more reducing conditions. In the phlogopite carbonatite, exsolution textures are much less common than in the calcite carbonatite, and contain strontianite comparatively enriched in Ca (30-45 mol. % $CaCO_3$). The above observations may indicate that the carbonatites of type (iii) crystallised at greater depths (at $P \geq 4$ kbar), and upon crystallisation, underwent a rapid loss of residual volatiles.

In addition to the three types of carbonatites, we classify the quartz-feldspar-carbonate rock as a distinct lithological type. This rock is generally similar to the calcite-dominant carbonatite of type (i), but contains large modal proportions of quartz. This mineral crystallised late in the evolutionary history of the rock forming oikocrysts, graphic intergrowths with calcite and equant crystals with abundant calcite inclusions. These textural features suggest that the quartz-feldspar-carbonate rock is transitional from carbonatites to quartz-calcite rocks locally known as "torgolites" (Konev et al. 1996). The "torgolites" are essentially bimodal rocks with about 60-70 vol.% of quartz and 30-40 vol.% of calcite intergrown in a manner reminiscent of the graphic texture in pegmatites. Konev et al. (1996) interpret these unusual rocks as a product of eutectic crystallisation of quartz and calcite. Although such a genetic interpretation is thermodynamically plausible (Lee & Wyllie 1998), and consistent with some textural characteristics of the quartz-calcite rocks, it does not explain the presence of ovoid calcite inclusions in quartz oikocrysts, nor the large modal proportions of alkali feldspar and aegirine in these rocks. In terms of composition, the carbonates and feldspar from the quartz-feldspar-carbonate rocks are almost identical to their counterparts in the calcite-carbonatites of type (i) (Figs. 3.3.1.2 and 3.4.1.1), whereas the clinopyroxene is significantly richer in the aegirine

107

component (Fig. 3.3.1.4). The above observations may indicate that the calcite-carbonatites and quartz-carbonate rocks are cognate, but the latter crystallised from a more evolved source enriched in alkalis and silica. Such processes as assimilation of wall-rock material and anatexis may have contributed to the formation of the quartz-feldspar-carbonate rocks and "torgolites".

For comparative purposes, we also plotted on Figure 3.4.1.1 the compositions of carbonates from the charoitites. In these rocks, Sr-rich calcite, Ca-rich strontianite, barytocalcite and witherite occur as strings of anhedral grains embedded in charoite (see also Chapter 2.1). Compositionally, these minerals are very similar to their counterparts in the Ba-Sr-Ca carbonatite, and may represent derivatives from the same source. Although we did not observe witherite in our carbonatite samples, Konev et al. (1996) describe this mineral as a product of exsolution of the primary strontian barytocalcite $Ca_{0.76}Sr_{0.44}Ba_{0.80}(CO_3)_2$.

### 3.4.2 Comparison with other carbonatite complexes

In addition to the Murun complex, Sr-rich carbonatites have been observed only at a few other occurrences worldwide. In the majority of these, high *REE* and relatively low Ba levels accompany the general enrichment of carbonatites in Sr. A Sr-rich carbonatite dyke has been described at Sarnu-Dandali alkaline complex, Rajasthan, India (Wall et al. 1993). In contrast to the carbonate-rich rocks from Murun, the carbonatite at Sarnu-Dandali is *REE*-rich and Ba-poor. This carbonatite is composed of exceptionally Sr-rich calcite (up to 13 wt.% SrO) occurring in two major parageneses, i.e. in exsolution aggregates with carbocernaite [(Ca,Na)(Sr,Ce,Ba)(CO_3)_2], and in a complex cotectic intergrowth with carbocernaite and Ca-rich (19 wt.% CaO) strontianite. Both calcite and strontianite from the Sarnu carbonatite are Ba-poor, and only in few cases, incorporate appreciable BaO (up to 1.0 wt.% in calcite, and up to 2.5 wt. % in strontianite). On the basis of compositions of coexisting calcite and strontianite, Wall et al. (1993) suggested that the Rajastan carbonatite dyke formed at T=500°C and P=2kbar. These data are in general agreement with the P-T conditions inferred in this work for the Murun calcite carbonatite.

108

Carbonatites from the Bearpaw Mt. (Montana) represent another example of Sr-rich carbonate rocks associated with alkaline complexes (Reguir & Mitchell 2000). The Bearpaw carbonatites contain Sr-rich calcite (5.5 wt.% SrO) that forms exsolution aggregates with Ca-rich strontianite ($\leq$ 7.2 wt.% CaO) resembling those found in the Murun calcite carbonatites. In contrast to the carbonate-rich rocks of the Murun complex, the Bearpaw carbonatites are devoid of primary Ba-rich carbonate minerals (*i.e.* barytocalcite). At Bearpaw, Ba is concentrated predominantly in late-stage *REE*-bearing carbonates, including carbocernaite $[(Ca,Na)(Sr,Ce,Ba)(CO_3)_2]$, burbankite $[(Na,Ca)_3(Sr,Ca,REE,Ba)_3(CO_3)_5]$ and huanghoite-(Ce) $[BaCe(CO_3)_2F]$.

Sr- and Ba-rich calcite carbonatites have been recently described at the Dunkeldyksky alkaline complex, Tajikistan (Faiziev *et al.* 1998). Here, Ba, Sr and *REE* are incorporated in Ba- and *REE*-bearing strontian calcite (*ca.* 0.2 wt.% BaO, 0.2 wt.% $REE_2O_3$, and 6.2 wt.% SrO), strontianite, celestine, barite, fluorite (up to 0.8 wt.% $REE_2O_3$), and several *REE*-bearing fluorcarbonates. As suggested by Faiziev *et al.* (1998), all these minerals were formed during the exsolution processes in hypothetical primary Ca-, Sr, Ba-, *REE*-, F- and $SO_4$-rich carbonates. However, the diversity of the minerals in the "exsolution" assemblage and some textural features of the Dunkeldyksky carbonatites (in particular, confinement of the late-stage phases to cleavage surfaces in the primary carbonates) suggest that the genetical model proposed by Faiziev *et al.* (1998) is unrealistic, and that the role of fluids in the crystallisation of fluorite and sulphates was underestimated.

# CHAPTER 4. Hypabyssal and Volcanic Rocks

## 4.1 Geological setting of the studied hypabyssal and volcanic rocks

The youngest igneous suite at Murun is represented mostly by dykes and sills (up to 20 m in thickness) cross-cutting phlogopite clinopyroxenite, kalsilite clinopyroxenite, kalsilite syenite and shonkinite in the north-eastern part of the complex. They also intrude volcanic rocks (leucite tinguaite, phonolite, solvsbergite and trachyte) in the north-central part of the complex, as well as charoitites and rocks of the exo- and endocontact (Mitchell and Vladykin 1996; Panina 1997).

Mitchell and Vladykin (1996) distinguish three mineralogically distinct types of the hypabyssal rocks at Murun: (1) phlogopite-rich rocks containing potassium batisite, potassium richterite and wadeite; (2) agpaitic dykes with kalsilite, potassium feldspar, barytolamprophyllite and eudialyte; (3) tausonite-, wadeite- and barytolamprophyllite-bearing dykes. Type (1), as well as potassium richterite–phlogopite–leucite lava flows associated with leucite phonolite were originally described as lamproites by Vladykin (1985), and subsequently studied as such by Orlova et al. (1992), Panina and Vladykin (1994), Vladykin (1997), and Panina (1997). On the contrary, Mitchell and Bergman (1991), and Mitchell and Vladykin (1996) showed that the compositional features of mica and clinopyroxene from the phlogopite-rich rocks of type (1) correlate well with those from the mica-rich plutonic rocks, and that the "lamproite-like" dykes, in fact, represent a lamprophyric facies of the plutonic suite.

Two other types of "lamproites" were described from the phlogopite pyroxenites and shonkinites of the "Martov anomaly" in the northern part of the Murun complex (Panina and Vladykin 1994). These "lamproites" are represented by the phlogopite-rich olivine-clinopyroxene-pseudoleucite rocks forming an intrusive body (up to 100 m in thickness), and by dykes (up to 3 m in thickness) of phlogopite-rich pseudoleucite-richterite rocks with clinopyroxene and batisite.

Lamproites were also described from several other localities in the Aldan shield, including Yakokutskii alkaline massif, Ryabinovyi massif, Molbo River area and Upper Yakutian depression (Panina and Vladykin 1994).

110

## 4.2    Petrographic description of the samples studied

In the present work, twenty samples representing various types of the Murun hypabyssal and volcanic rocks were examined. Because the major rock-forming minerals of these rocks (clinopyroxene, mica and amphibole) were characterised in detail by Mitchell & Vladykin (1996), the emphasis of the study is on their accessory mineralogy.

On the basis of the textural features and mineralogical composition, we divided the samples into following eight groups:

1 - *lamprophyre* (Mu-215, -150, -232, -241, -3/100, -231/13);

2 - *pseudoleucite syenite* (Mu-216, -167/19);

3 - *pseudoleucite italite* (Mu-235);

4 - *kalsilite melasyenite* (Mu-172);

5 - *eudialyte-bearing syenite* (Mu-245, -196, -175, -194);

6 - *"potassium-batisite" synite* (Mu-186/6, -237, -171);

7 - *lamprophyllite- and barytolamprophyllite-bearing syenite* (Mu-236, -184/11);

8 - *aegirinite* (Mu-190).


Group (1) lamprophyre is composed mainly of biotite (15-45 vol.% of the rock), clinopyroxene (5-40 vol.%), amphibole (5-30 vol.%), potassium feldspar (5-35 vol.%), and, in some examples, olivine (up to 15 vol.%). In the majority of samples (*e.g.* Mu-232, -231/13), biotite, clinopyroxene and/or amphibole form phenocrysts (up to 3mm in size) set in a fine-grained potassium feldspar-biotite-clinopyroxene-amphibole-apatite groundmass (Figs. 4.2.1, 4.2.2). In some samples (*e.g.* Mu-150, -3/100), phenocrysts of biotite are accompanied by macrocrysts of olivine (Fig. 4.2.3). The accessory mineral assemblage of the lamprophyre includes apatite-group minerals, wadeite, tetra-ferriphlogopite, titanite, ilmenite, zircon, titanomagnetite, quartz, rutile (?), talc, monazite-(Ce), sulphides, barite and carbonates.

111

Fig. 4.2.1. Phenocrysts of biotite (yellow), amphibole (colourless) and clinopyroxene
(pale green) in a fine-grained groundmass. Lamprophyre, Mu-231/13. FOV
3.5 mm; plane-polarised light.



Fig. 4.2.2. Phenocrysts of biotite (cream and greenish yellow) and amphibole
(greenish blue and purplish-blue) in a fine-grained groundmass.
Lamprophyre, Mu-232. FOV 3.5 mm; plane-polarised light.

112
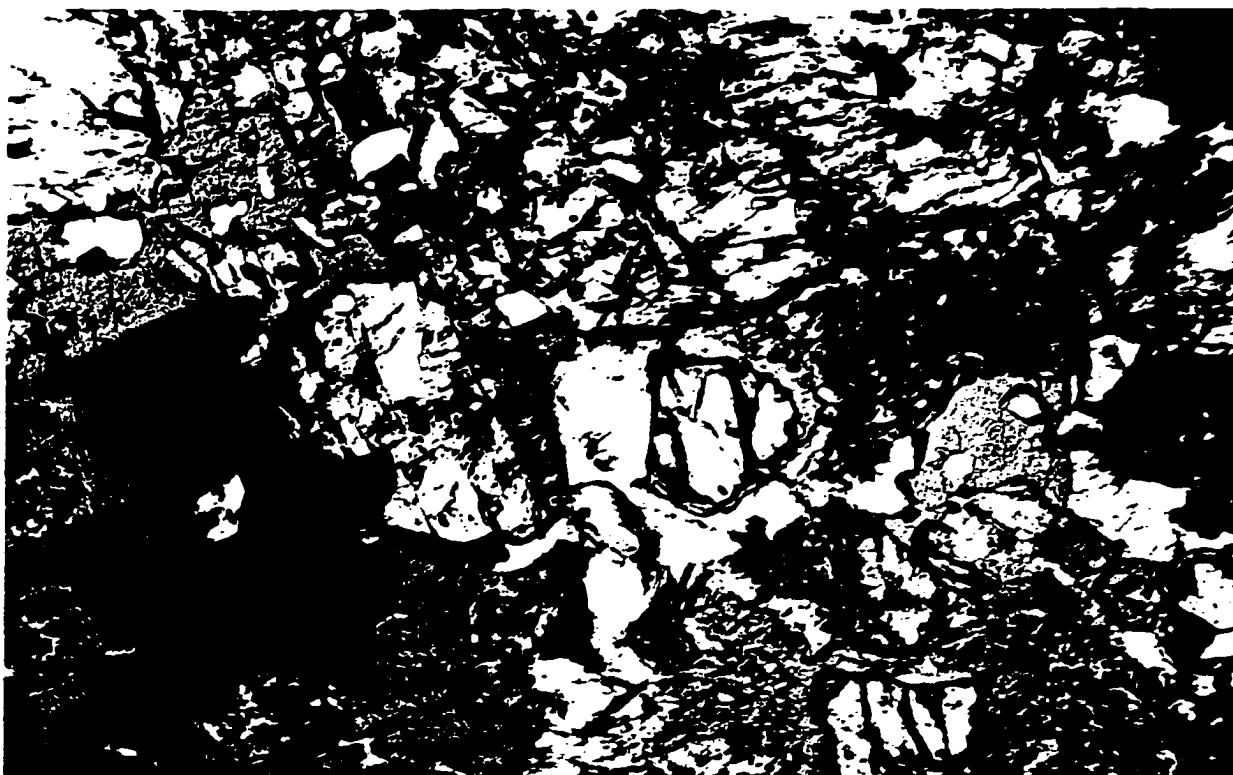
Fig. 4.2.3. Phenocrysts of biotite (reddish brown), clinopyroxene (pale green) and olivine (white grains with high relief) in a potassium feldspar-clinopyroxene-biotite groundmass. Lamprophyre, Mu-3/100. FOV 3.5 mm; plane-polarised light.

Pseudoleucite syenite of group (2) incorporates pseudoleucite sodalite syenite (*e.g.* Mu-216) and garnet-pseudoleucite syenite (*e.g.* Mu-167/19). In the pseudoleucite sodalite syenite, phenocrysts of clinopyroxene (up to 0.4 mm) and rounded pseudomorphs of potassium feldspar plus sodalite (up to 0.7 mm in diameter) developed after leucite phenocrysts, are set in a fine-grained groundmass (Fig. 4.2.4). In some cases, anhedral-to-subhedral grains of clinopyroxene are enclosed by the sodalite pseudomorphs. Sodalite and potassium feldspar pseudomorphs comprise about 20 vol.% of the rock, phenocrysts of clinopyroxene 5 vol.%, and the groundmass accounts for 75 vol.%. The groundmass is composed mainly of clinopyroxene, potassium feldspar and biotite, with subordinate barytolamprophyllite, a cancrinite-group mineral and kalsilite. Accessory minerals also include titanite, sulphides, and barite. In the garnet-pseudoleucite syenite, phenocrysts of leucite and garnet are replaced by potassium

113
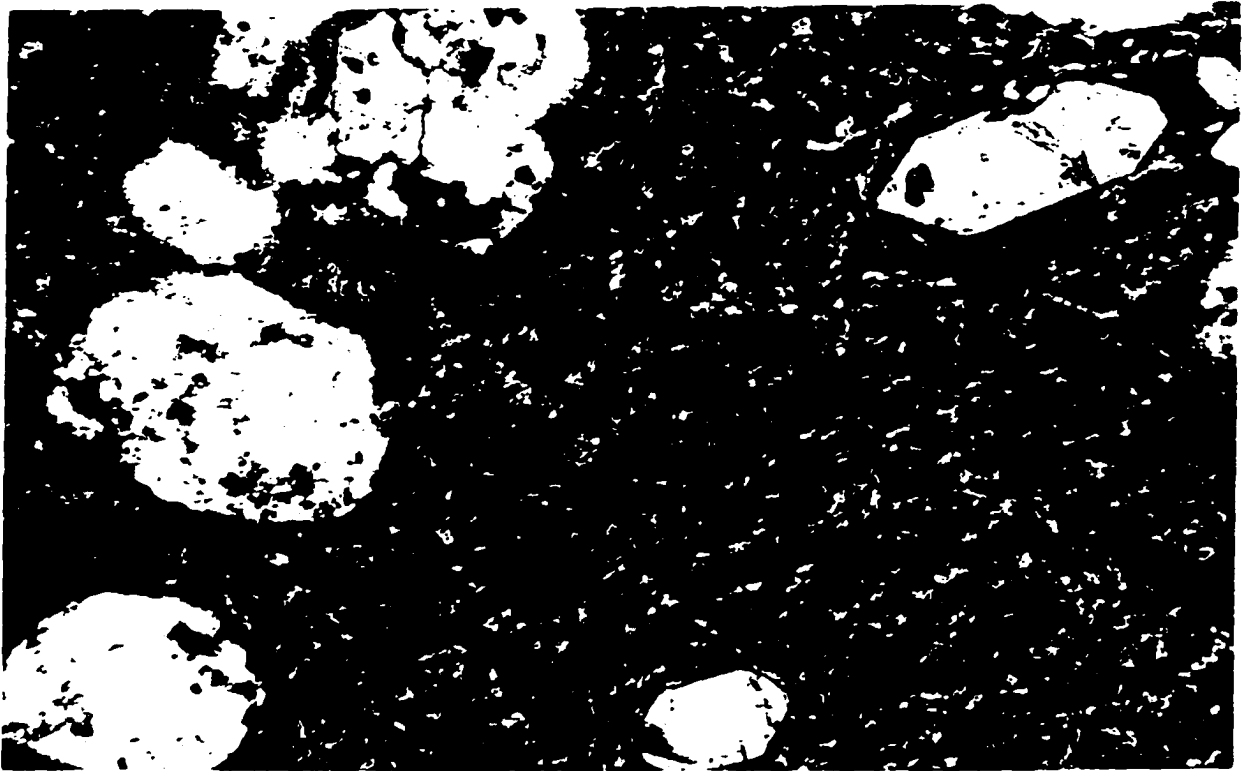
Fig. 4.2.4. Phenocrysts of clinopyroxene (greenish yellow) and pseudomorphs of sodalite after leucite in a fine-grained groundmass. Pseudoleucite sodalite syenite, Mu-216. FOV 3.5 mm; plane-polarised light.
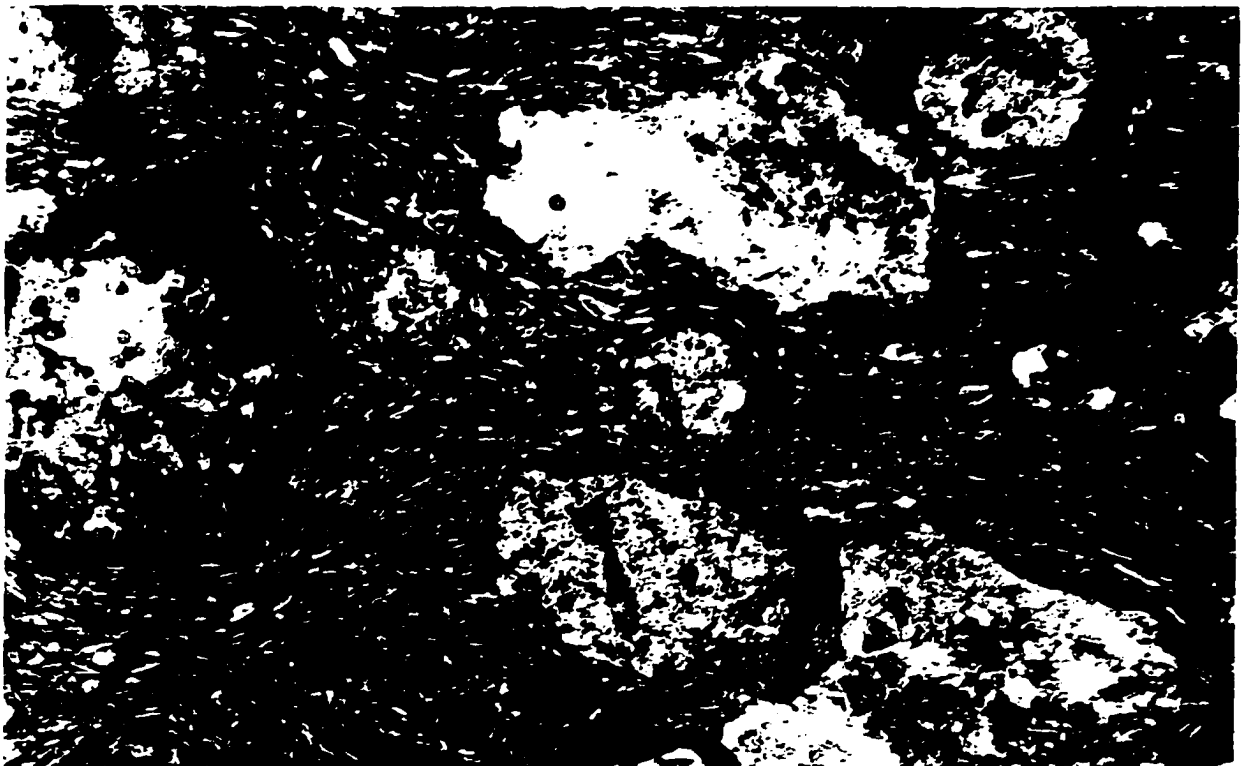


Fig. 4.2.5. Phenocrysts of garnet (hexagonally-shaped, left) and pseudoleucite in the fine-grained clinopyroxene-potassium feldspar groundmass exhibiting flow texture. Garnet-pseudoleucite syenite, Mu-167/19. FOV 3.5 mm; plane-polarised light.

114

feldspar, carbonates and other secondary minerals (20 vol.%) set in a fine-grained clinopyroxene-potassium feldspar groundmass (80 vol.%) showing a flow texture (Fig. 4.2.5). The pseudomorphs and groundmass are extensively altered to Fe-Ti oxides/hydroxides, muscovite, ferripyrophyllite and jarosite. The latter mineral commonly occurs as fracture fillings-linings in elongate cavities possibly left after the decomposition of the clinopyroxene. Accessory minerals also include quartz, sulphides and barite.

In the pseudoleucite italite (e.g. Mu-235), potassium feldspar pseudomorphs after leucite (ca. 35 vol.%), phenocrysts of clinopyroxene (ca. 20 vol.%), and rare phenocrysts of biotite (<5 vol.%) are set in a clinopyroxene-biotite-apatite groundmass (ca. 40 vol.%) (Fig. 4.2.6). The phenocrysts of clinopyroxene and the groundmass are strongly altered to a mixture of carbonates (predominantly barytocalcite). Accessory minerals also include ilmenite and barite.

The kalsilite melasyenite (e.g. Mu-172) is composed of phenocrysts of biotite and diopside (each about 25 vol.% of the rock), fluorapatite (ca. 10 vol.%), and fine-grained kalsilite-potassium feldspar aggregates (ca. 40 vol.%) developed interstitially between the phenocrysts (Fig. 4.2.7). The kalsilite-potassium feldspar aggregates also contain minor amounts of aegirine, fluorapatite and quartz. Accessories also include magnetite, chromite, barite and Fe-hydroxides.

The eudialyte-bearing syenite of group (5), is divided into two subgroups: eudialyte aegirine syenite (e.g. Mu-245) and eudialyte-bearing nepheline syenite (e.g. Mu-196). In the eudialyte aegirine syenite, aegirine comprises 70 vol.% of the rock, potassium feldspar about 10 vol.%, eudialyte 10 vol.%, and nepheline less than 5 vol.%. Aegirine forms radial and fibrous aggregates of small (ca. 100 µm in length) acicular crystals, and large (up to 2 mm in length) subhedral relicts commonly enclosed by the fine-grained aggregates of the mineral (Fig. 2.4.8). Coarse (up to 2 mm in size) prismatic crystals of potassium feldspar and eudialyte are developed interstitially between the aegirine aggregates. Accessory minerals include lamprophyllite, sulphides, strontianite and an unidentified Na-Fe-Sr silicate. Eudialyte-bearing

115
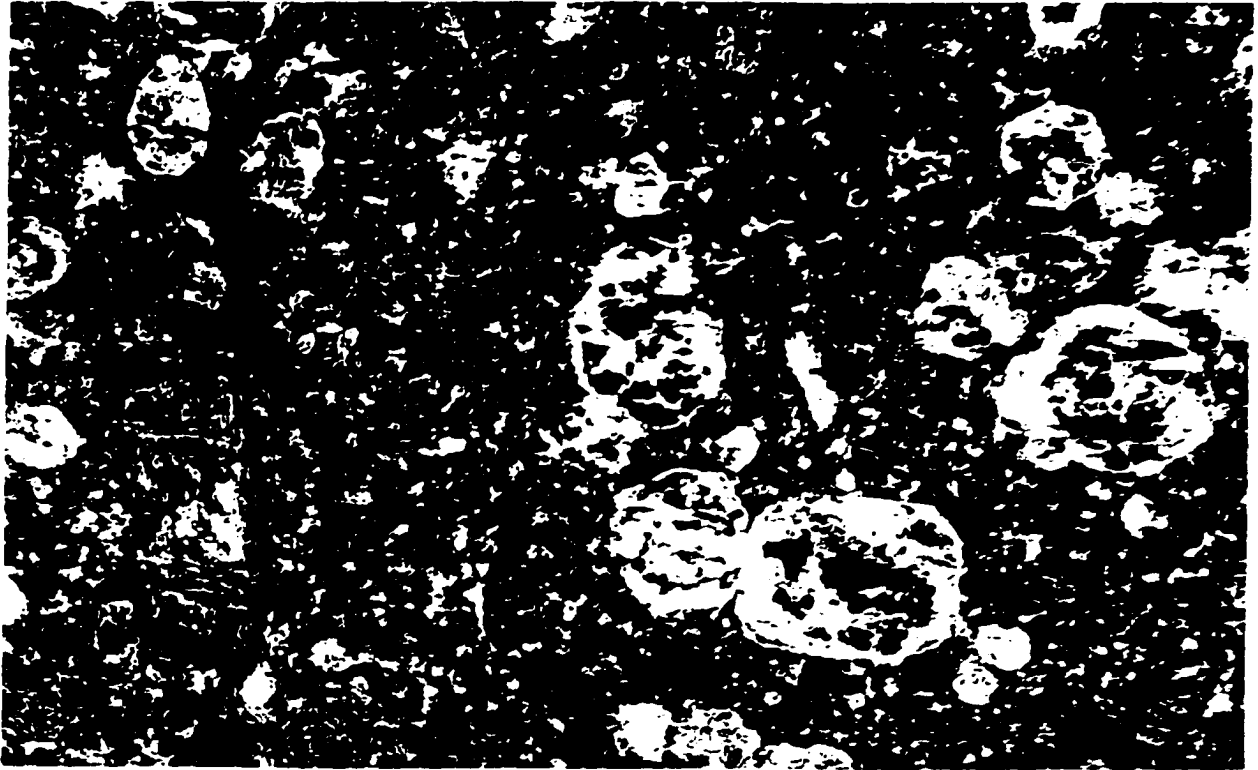
Fig. 4.2.6. Pseudomorphs of potassium feldspar after leucite (greyish white) and altered phenocrysts of clinopyroxene (yellowish grey) in a fine-grained biotite-clinopyroxene-apatite groundmass. Pseudoleucite italite, Mu-235. FOV 3.5 mm; plane-polarised light.



Fig. 4.2.7. Phenocrysts of biotite (yellowish brown), clinopyroxene (greyish, fractured) and apatite (colourless) in a groundmass composed of kalsilite-potassium feldspar intergrowths. Kalsilite melasyenite, Mu-172. FOV 3.5 mm; plane-polarised light.

116
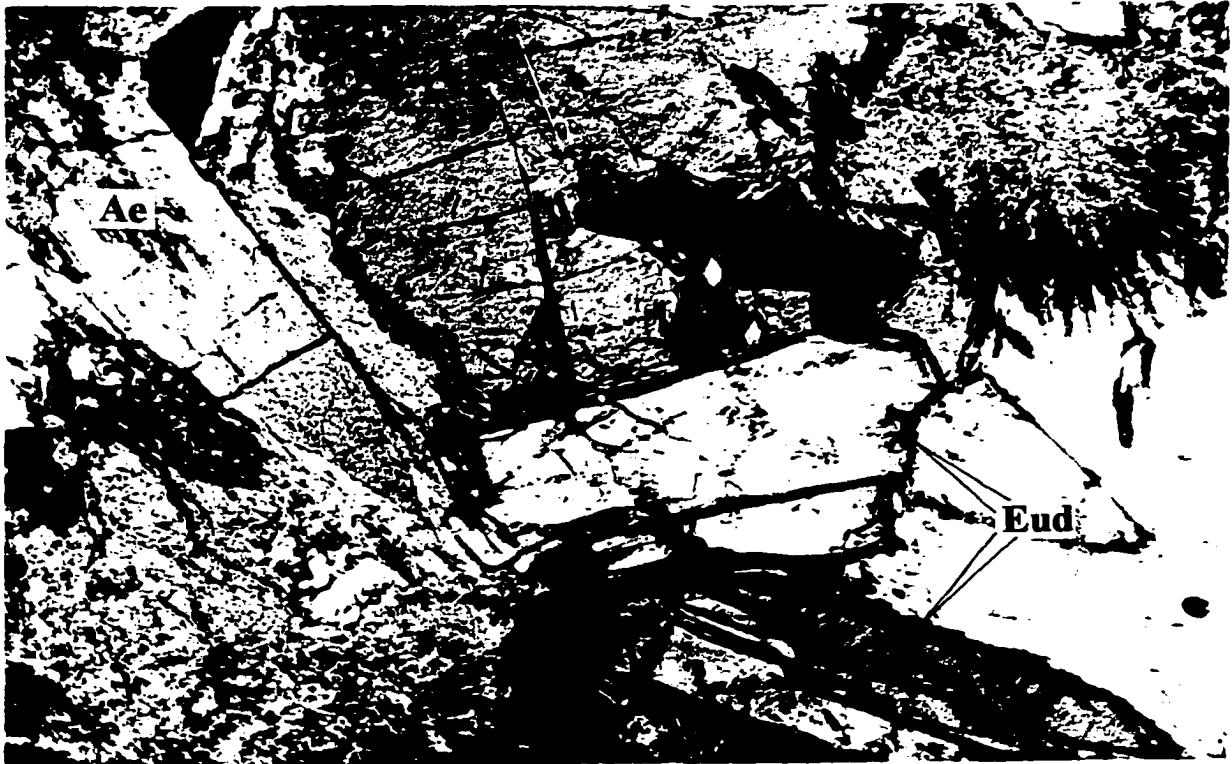
Fig. 4.2.8.  Relict of prismatic clinopyroxene (Ae) enclosed by fibrous clinopyroxene (bright yellowish, bluish and pinkish green), also present are prismatic crystals of eudialyte (Eud) and potassium feldspar (grey, top). Eudialyte aegirine syenite, Mu-245. FOV 3.5 mm; crossed polars.
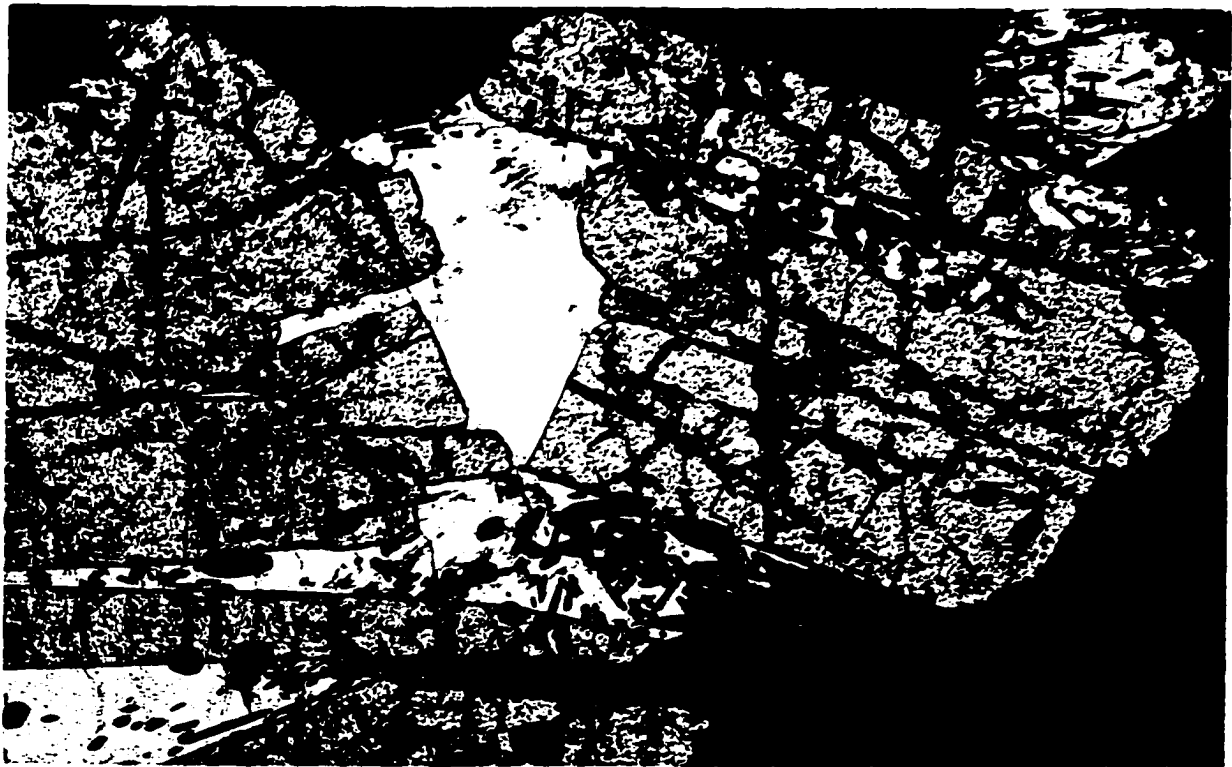


Fig. 4.2.9.  Clusters of "potassium-batisite" crystals (grey), fibrous clinopyroxene (green), and interstitial potassium feldspar (colourless). "Potassium-batisite" syenite, Mu-237. FOV 3.5 mm; plane-polarised light.

117

nepheline syenite is composed mainly of fine-grained (100-200 μm) aggregates of aegirine crystals comprising about 75 vol.% of the rock, and subhedral nepheline grains (20 vol.%). Prismatic crystals of eudialyte (up to 0.5 mm in length) are developed in the nepheline matrix, and are commonly replaced by strontianite and wadeite. Other accessory minerals include potassium feldspar, lamprophyllite, titanite, apatite-group minerals and galena.

"Potassium-batisite" syenite is composed mainly of thin prismatic or rectangular crystals and radial aggregates of clinopyroxene (50-55 vol.% of the rock), coarse (up to 1.2 cm in length) elongate crystals of "potassium batisite" (20-30 vol.%), and subhedral-to-euhedral grains of potassium feldspar (ca. 20-30 vol.%) developed interstitially between the clinopyroxene and "potassium batisite" (Fig. 4.2.9). Acicular crystals of clinopyroxene commonly penetrate "potassium-batisite" grains. The accessory mineral assemblage includes titanite, wadeite, muscovite, barytolamprophyllite, rutile (?), hollandite-type minerals, and in some samples (e.g. Mu-186/6), an unidentified Ti-Pb silicate and thorianite.

In the lamprophyllite- and barytolamprophyllite-bearing syenite of group (7), clinopyroxene comprises 50-70 vol.% of the rock, lamprophyllite or barytolamprophyllite 10-20 vol.%, potassium feldspar with kalsilite 15-20 vol.%, and wadeite 10-15 vol.%. Thin elongate laths of barytolamprophyllite and lamprophyllite (up to 0.5 cm in length) are commonly overgrown by fibrous aggregates of clinopyroxene. The latter mineral also forms radial aggregates (up to 2 mm in diameter) and discrete acicular grains in the potassium feldspar-kalsilite-clinopyroxene matrix. Large (up to 3 mm) prismatic grains of wadeite are commonly found intergrown with lamprophyllite and barytolamprophyllite (Fig. 4.2.10). Accessory minerals include nepheline, apatite-group minerals, sulphides, barite, an unidentified Pb-Al silicate, and in some cases (e.g. Mu-184/11), tausonite (Fig. 4.2.11).

Aegirinite is composed of 90 vol.% of fine-grained clinopyroxene. Potassium feldspar is developed interstitially between the clinopyroxene grains and commonly altered to carbonates and muscovite. Accessory minerals are wadeite, celadonite, rutile (?), magnetite, sulphides, and an unidentified Ba-Ti Al-silicate.
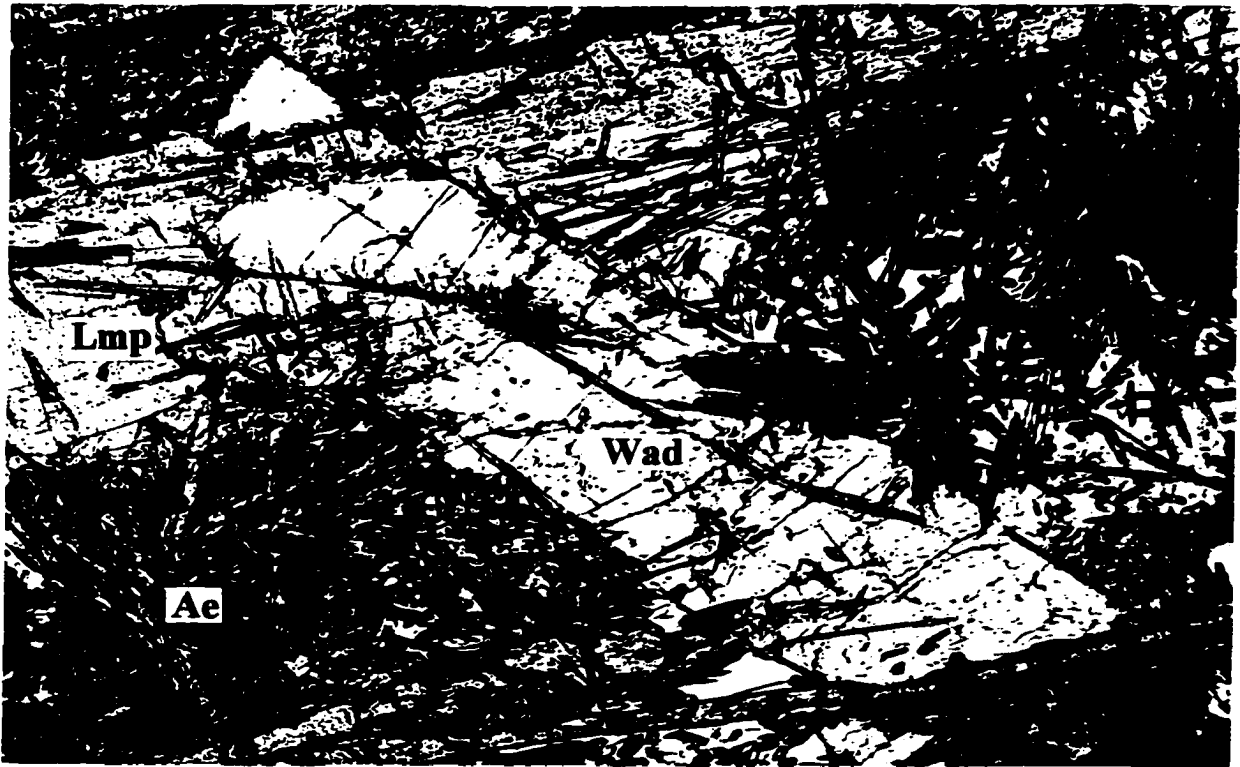
Fig. 4.2.10. Relationship between wadeite (Wad), lamprophyllite (yellow) and acicular clinopyroxene; matrix – potassium feldspar (colourless). Lamprophyllite-bearing syenite, Mu-184/11. FOV 3.5 mm; plane-polarised light.
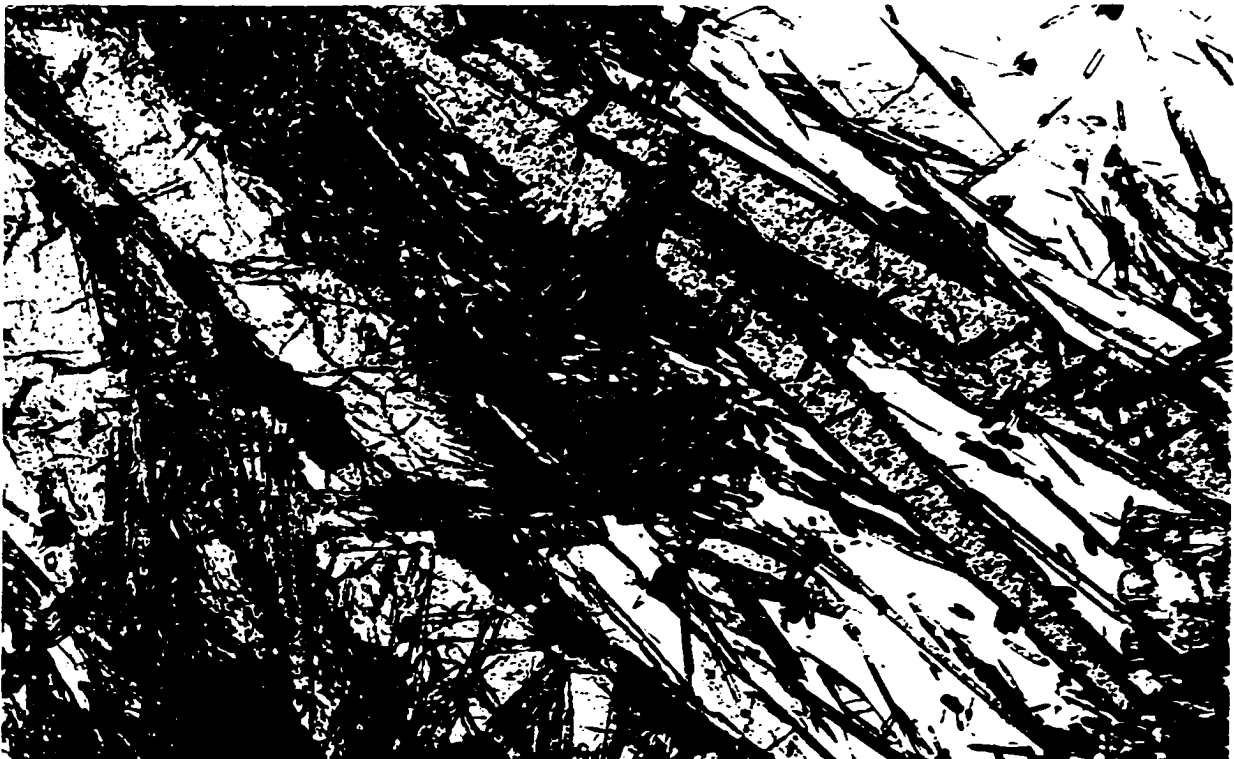


Fig. 4.2.11. Tausonite (opaque) developed along fractures in lamprophyllite (yellow). Green – clinopyroxene, colourless – potassium feldspar. Lamprophyllite-bearing syenite, Mu-184/11. FOV 3.5 mm; plane-polarised light.

119

## 4.3 Mineralogy of the examined rocks

### 4.3.1 Silicates

*Clinopyroxene* is one of the major constituents of the examined rocks. In the majority of the lamprophyre samples, the mineral occurs as brownish or olive-green to dark green, anhedral-to-subhedral elongate grains (*ca.* 100 μm in length) in the groundmass. In some samples (*e.g.* Mu-241, -150, 3/100), clinopyroxene also forms subhedral-to-euhedral elongate (up to 0.8 mm in length and up to 1 mm across) phenocrysts. Most of the phenocrysts are slightly pleochroic from pale green to yellowish green, and are commonly resorbed by mica and carbonate minerals (Fig. 4.3.1.1).



Fig. 4.3.1.1. Phenocrysts of clinopyroxene (green) partly replaced by biotite and carbonates, and phenocrysts of phlogopite (reddish yellow). Left – part of an alteration "corona" around olivine. Lamprophyre, Mu-150. FOV 3.5 mm; plane-polarised light.

In the pseudoleucite syenite (group 2) and pseudoleucite italite (group 3), clinopyroxene occurs as subhedral to anhedral phenocrysts (up to 0.7 mm in length), and forms anhedral-to-subhedral grains (50-100 μm in size) in the groundmass. The phenocrysts are commonly zoned, with colourless or pale yellow core and yellowish green rim (Fig. 4.2.4). The phenocrysts are commonly strongly altered by carbonates, muscovite and barite, and in some cases (*e.g.* Mu-167/19), almost fully replaced by jarosite, ferripyrophyllite and muscovite (Fig. 4.3.1.2).
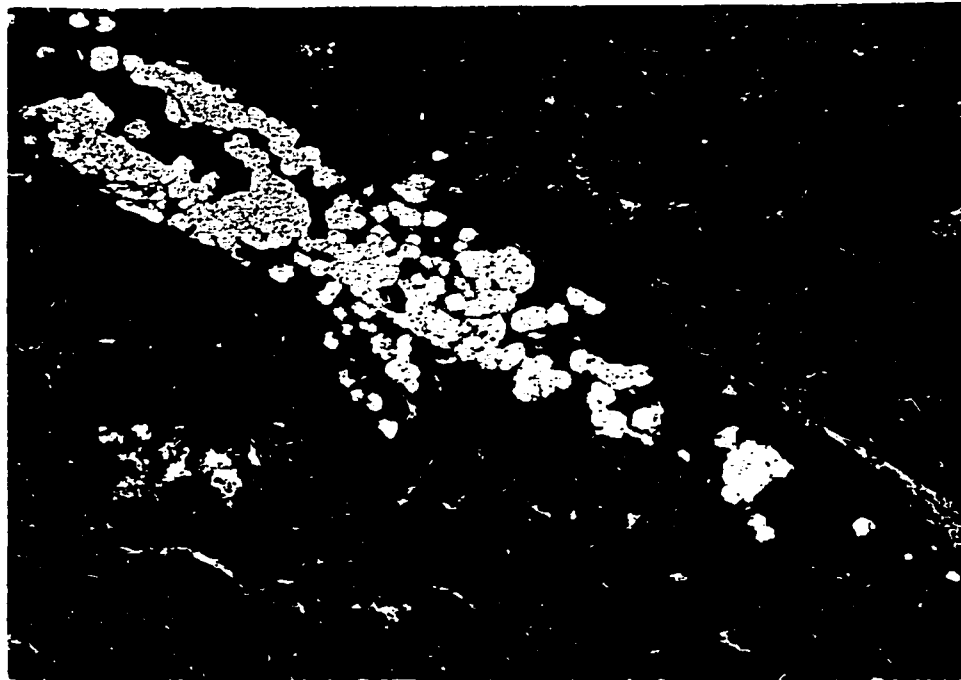


Fig. 4.3.1.2. Equant crystals of jarosite (white) and ferripyrophyllite (dark grey) filling cavities with relicts of clinopyroxene. Matrix – potassium feldspar. Pseudoleucite syenite 167/19. BSE image.

In the kalsilite melasyenite (group 4), colourless to pale yellowish green clinopyroxene forms subhedral-to-euhedral, elongate (up to 1.5 mm in length and up to 0.4 mm across)

121

phenocrysts (Fig. 4.2.7). Minor amounts of olive-green clinopyroxene are found in the fine-grained kalsilite-potassium feldspar groundmass.

In the eudialyte-bearing syenite (group 5), "potassium-batisite" syenite (group 6), and barytolamprophyllite- and lamprophyllite-bearing syenite (group 7), clinopyroxene forms fibrous or radial aggregates (up to several mm in diameter) of yellowish-green to olive-green acicular crystals, or occurs as subhedral elongate or rectangular relicts enclosed by these aggregates (Fig. 4.2.8). In the group 6 and 7 rocks, acicular crystals of clinopyroxene commonly penetrate coarse grains of "potassium batisite", and barytolamprophyllite or lamprophyllite, respectively (Figs. 4.2.10, 4.2.11). In some samples of the barytolamprophyllite- and lamprophyllite-beraing syenite (e.g. Mu-236), clinopyroxene also forms elongate (up to 0.3 mm in length) subhedral-to-euhedral grains in the feldspar-kalsilite matrix.

In the aegirinite, greenish-yellow to dark green clinopyroxene forms fibrous aggregates of fine (ca. 100 μm in size) grains.

Compositionally, clinopyroxene from the lamprophyre ranges from diopside (phenocrysts in Mu-3/100 and Mu-150) to aegirine-augite (groundmass in Mu-150), and to aegirine (groundmass in Mu-241). Most of the compositions from the lamprophyre have ≤ 12 mol.% of hedenbergite component and lie close to the overall trend of pyroxene from Little Murun, as given by Mitchell and Vladykin (1996), (Table 4.3.1.1, Fig. 4.3.1.3).

The majority of the compositions of clinopyroxene from the pseudoleucite italite, eudialyte-bearing syenite, lamprophyllite- and barytolamprophyllite-bearing syenite, and aegirinite correspond to aegirine, with ≤ 8.5 mol.% $CaMgSi_2O_6$ and ≤ 13 mol.% $CaFeSi_2O_6$ (Table 4.3.1.1, Fig. 4.3.1.3).

Compositions of clinopyroxene from the "potassium-batisite" syenite show noticeable variation within the aegirine field. The innermost parts of the crystals contain ca. 70 mol.% $NaFeSi_2O_6$ and ca. 8 mol.% $CaFeSi_2O_6$, whereas their rims are depleted in hedenbergite (ca. 2 mol. %) and enriched in aegirine (up to 86 mol.%).

Table 4.3.1.1. Representative compositions of clinopyroxene.

| Wt. % | 1 | 2 | 3 | 4 | 5 | 6 | 7 | 8 | 9 | 10 | 11 | 12 |
|---|---|---|---|---|---|---|---|---|---|---|---|---|
| $SiO_2$ | 54.99 | 55.24 | 51.56 | 54.15 | 54.07 | 52.94 | 51.39 | 51.99 | 51.65 | 51.61 | 51.81 | 52.55 |
| $TiO_2$ | 0.25 | 0.43 | 1.32 | 0.45 | 0.39 | 0.61 | 1.06 | 0.71 | 0.86 | 2.24 | 0.39 | 1.64 |
| $ZrO_2$ | n.d | n.d | 0.37 | n.d | n.d | n.d | n.d | n.d | n.d | n.d | n.d | n.d |
| $Al_2O_3$ | 0.10 | n.d | 0.81 | 0.19 | 0.58 | 0.48 | 0.18 | 0.07 | 0.33 | n.d | 0.14 | 0.21 |
| $V_2O_3$ | n.d | n.d | 0.32 | 0.21 | n.d | 1.02 | 0.16 | 0.11 | 0.23 | 0.33 | 0.37 | n.d |
| $Fe_2O_3$* | 11.95 | 1.55 | 31.09 | 4.11 | 3.19 | 27.58 | 18.03 | 20.80 | 23.82 | 24.04 | 29.77 | 28.31 |
| FeO* | 1.63 | 2.45 | 2.19 | 3.48 | 2.53 | 2.00 | 5.37 | 4.68 | 4.35 | 2.50 | 0.70 | 3.13 |
| MnO | n.d | n.d | n.d | 0.16 | n.d | n.d | 0.30 | 0.26 | 0.40 | 0.25 | 0.18 | 0.24 |
| MgO | 10.83 | 17.36 | 0.65 | 14.04 | 15.46 | 2.01 | 4.60 | 4.14 | 3.22 | 3.34 | 2.01 | 1.24 |
| CaO | 16.19 | 22.35 | 0.20 | 21.63 | 23.70 | 2.59 | 10.33 | 9.59 | 7.32 | 5.81 | 4.17 | 2.77 |
| $Na_2O$ | 5.24 | 0.95 | 12.82 | 1.89 | 0.98 | 11.85 | 7.61 | 8.17 | 9.20 | 10.26 | 11.321 | 1.90 |
| Total* | 101.18 | 100.33 | 101.33 | 100.31 | 100.90 | 101.08 | 99.03 | 100.62 | 101.38 | 100.38 | 100.76 | 101.99 |
| Formulae calculated on the basis of 6 atoms of oxygen | | | | | | | | | | | | |
| Si | 2.012 | 2.000 | 1.960 | 1.991 | 1.968 | 1.998 | 1.986 | 1.982 | 1.963 | 1.965 | 1.971 | 1.982 |
| Ti | 0.007 | 0.012 | 0.038 | 0.012 | 0.011 | 0.017 | 0.031 | 0.020 | 0.025 | 0.064 | 0.011 | 0.047 |
| Zr | - | - | 0.007 | - | - | - | - | - | - | - | - | - |
| Al | 0.004 | - | 0.036 | 0.008 | 0.025 | 0.021 | 0.008 | 0.003 | 0.015 | - | 0.006 | 0.009 |
| V | - | - | 0.010 | 0.006 | - | 0.031 | 0.005 | 0.003 | 0.007 | 0.010 | 0.011 | - |
| $Fe^{3+}$ | 0.329 | 0.042 | 0.890 | 0.114 | 0.087 | 0.784 | 0.524 | 0.597 | 0.681 | 0.689 | 0.852 | 0.804 |
| $Fe^{2+}$ | 0.050 | 0.074 | 0.070 | 0.107 | 0.077 | 0.063 | 0.174 | 0.149 | 0.138 | 0.080 | 0.022 | 0.099 |
| Mn | - | - | - | 0.005 | 0.007 | - | 0.010 | 0.008 | 0.013 | 0.008 | 0.006 | 0.008 |
| Mg | 0.591 | 0.937 | 0.037 | 0.770 | 0.839 | 0.113 | 0.265 | 0.235 | 0.182 | 0.190 | 0.114 | 0.070 |
| Ca | 0.635 | 0.867 | 0.008 | 0.852 | 0.924 | 0.105 | 0.428 | 0.392 | 0.298 | 0.237 | 0.170 | 0.112 |
| Na | 0.372 | 0.067 | 0.945 | 0.135 | 0.069 | 0.867 | 0.570 | 0.604 | 0.678 | 0.758 | 0.835 | 0.870 |

123

Table 4.3.1.1. (Continued).

| Wt. % | 13 | 14 | 15 | 16 | 17 | 18 | 19 | 20 | 21 | 22 | 23 | 24 |
|---|---|---|---|---|---|---|---|---|---|---|---|---|
| $SiO_2$ | 51.68 | 51.95 | 52.57 | 52.26 | 51.20 | 50.46 | 53.35 | 50.83 | 51.24 | 51.44 | 52.63 | 52.31 |
| $TiO_2$ | 0.39 | 1.18 | 1.25 | 0.35 | 0.81 | 2.74 | 1.04 | 0.96 | 0.73 | 3.17 | 0.37 | 0.50 |
| $ZrO_2$ | n.d | n.d | n.d | n.d | n.d | n.d | n.d | n.d | n.d | 1.17 | n.d | n.d |
| $Al_2O_3$ | 0.16 | 0.02 | 0.25 | 0.45 | 0.41 | 0.75 | 0.51 | 0.24 | 0.28 | 0.02 | 0.32 | 0.17 |
| $V_2O_3$ | 0.11 | n.d | 0.15 | n.d | n.d | 0.20 | n.d | n.d | n.d | 0.27 | 0.59 | 0.76 |
| $Fe_2O_3$* | 30.62 | 27.04 | 29.74 | 3.54 | 9.19 | 25.49 | 23.39 | 31.82 | 29.43 | 27.29 | 30.61 | 33.22 |
| FeO* | 2.72 | 3.33 | 2.39 | 6.64 | 7.34 | 5.60 | 1.67 | 2.21 | 2.94 | 2.26 | - | 0.18 |
| MnO | 0.11 | 0.33 | 0.12 | 0.35 | 0.31 | 0.43 | 0.45 | 0.40 | 1.31 | n.d | n.d | n.d |
| MgO | 0.62 | 1.37 | 0.94 | 12.54 | 9.21 | 0.25 | 4.38 | 0.28 | 0.52 | 0.57 | 0.25 | 0.34 |
| CaO | 2.38 | 3.43 | 1.90 | 23.50 | 19.90 | 4.51 | 6.68 | 1.77 | 3.53 | n.d | n.d | 0.17 |
| $Na_2O$ | 11.85 | 11.36 | 12.37 | 0.72 | 2.67 | 10.90 | 9.97 | 12.13 | 11.26 | 13.32 | 13.62 | 13.37 |
| Total* | 100.60# | 100.01 | 101.68 | 100.35 | 101.04 | 101.33 | 101.44 | 100.64 | 101.24 | 99.51 | 98.39 | 101.02 |
| Formulae calculated on the basis of 6 atoms of oxygen | | | | | | | | | | | | |
| Si | 1.984 | 1.998 | 1.987 | 1.956 | 1.935 | 1.938 | 1.992 | 1.959 | 1.967 | 1.983 | 1.985 | 1.988 |
| Ti | 0.011 | 0.034 | 0.036 | 0.010 | 0.023 | 0.079 | 0.029 | 0.028 | 0.021 | 0.092 | 0.010 | 0.014 |
| Zr | - | - | - | - | - | - | - | - | - | 0.022 | - | - |
| Al | 0.007 | 0.001 | 0.011 | 0.020 | 0.018 | 0.034 | 0.022 | 0.011 | 0.013 | 0.001 | 0.014 | 0.008 |
| V | 0.011 | - | 0.005 | - | - | 0.006 | - | - | - | 0.008 | 0.018 | 0.023 |
| $Fe^{3+}$ | 0.885 | 0.782 | 0.846 | 0.100 | 0.261 | 0.737 | 0.657 | 0.923 | 0.850 | 0.792 | 0.966 | 0.950 |
| $Fe^{2+}$ | 0.087 | 0.107 | 0.076 | 0.208 | 0.232 | 0.180 | 0.052 | 0.071 | 0.094 | 0.073 | - | 0.006 |
| Mn | 0.004 | 0.011 | 0.004 | 0.011 | 0.010 | 0.014 | 0.014 | 0.013 | 0.043 | - | - | - |
| Mg | 0.035 | 0.079 | 0.053 | 0.700 | 0.519 | 0.014 | 0.244 | 0.016 | 0.030 | 0.033 | 0.014 | 0.019 |
| Ca | 0.098 | 0.141 | 0.077 | 0.943 | 0.806 | 0.186 | 0.267 | 0.073 | 0.145 | - | - | 0.007 |
| Na | 0.882 | 0.847 | 0.907 | 0.052 | 0.196 | 0.812 | 0.722 | 0.906 | 0.838 | 0.996 | 0.996 | 0.985 |

n.d = not detected; * $Fe^{2+}/Fe^{3+}$ ratio calculated from stoichiometry; # Total also includes 0.07 wt.% $K_2O$ (0.003 apfu K). Analyses 1-6: lamprophyre (1-2 – Mu-150, 3 – Mu-241; 4-5 – Mu-3/100; 6 – Mu-232); 7-11: batisite/shcherbakovite syenite (7-8 – Mu-171; 9 – Mu-237; 10-11 – Mu-186/6: 10 – core, 11 – rim); 12: barytolamprophyllite-and lamprophyllite-bearing syenite (12 – Mu-184/11; 13 – Mu-236); 14-15: aegirinite (Mu-190); 16-18: pseudoleucite sodalite syenite (Mu-216, 16 – low-AZ; 17 – medium-AZ; 18 – high-AZ); 19: garnet-pseudoleucite syenite (Mu-167/19); 20-21: eudialite-bearing syenite (20 – Mu-245; 21 – Mu-196); 22-24: pseudoleucite italite (Mu-235).

AEGIRINE　DIOPSIDE

25

25

$CaFe^{2+}Si_2O_6$

25　50　25

$NaFe^{3+}Si_2O_6$

$CaMgSi_2O_6$

## This work:

*lamprophyre:*

■ Mu-215

□ Mu-3/100

■ Mu-241, -232

■ Mu-150

*barytolamprophyllite- and
lamprophyllite-bearing syenite:*

■ Mu-184/11

■ Mu-236

*"potassium-batisite" syenite:*

▨ Mu-186/6

*aegirinite:*

□ Mu-190

*pseudoleucite syenite:*

▨ Mu-216

■ Mu-167/19

*eudialyte-bearing syenite;
pseudoleucite italite:*

■ Mu-196, -245;
Mu-235

## Mitchell & Vladykin (1996):

▨ *yakutite (kalsilite
pyroxenite)*

▨ *phlogopite
pyroxenite*

▨ *centre-I
shonkinite*

---► overall compositional trend
of pyroxene occuring in
Little Murun plutonic rocks

Fig. 4.3.1.3. Compositions of clinopyroxene from Murun
hypabyssal and volcanic rocks

125

Compositionally, clinopyroxene from the pseudoleucite syenite varies from diopside to aegirine (Table 4.3.1.1, Fig. 4.3.1.3). The mineral from the pseudoleucite sodalite syenite (*e.g.,* Mu-216) has the highest amount of the hedenbergite component (up to 30 mol.%) among the rocks studied. Cores of the clinopyroxene phenocrysts from the sample Mu-216 contain *ca.* 25 mol.% of $NaFeSi_2O_6$ and *ca.* 50 mol.% $CaMgSi_2O_6$. Some of the phenocrysts have irregularly-zoned rims with high-*AZ* zones containing up to 80 mol.% of $NaFeSi_2O_6$ and only 1.5 mol.% $CaMgSi_2O_6$, and low-*AZ* zones containing as low as 10 mol.% of $NaFeSi_2O_6$ and up to 70 mol.% $CaMgSi_2O_6$ (Table 4.3.1.1, Fig. 4.3.1.3). In the garnet-pseudoleucite syenite (*e.g.* Mu-167/19), the composition of strongly altered clinopyroxene crystals varies from having only 15 mol.% of $NaFeSi_2O_6$ and as much as 65 mol.% $CaMgSi_2O_6$ to nearly pure aegirine with only 4 mol.% of $CaMgSi_2O_6$ and 5 mol. % of $CaFeSi_2O_6$ components (Table 4.3.1.1, Fig. 4.3.1.3).

The majority of the clinopyroxene compositions from the rocks examined show noticeable enrichment in $V_2O_3$ (up to 1.0 wt.% in the lamprophyre and 0.8 wt.% in the pseudoleucite italite). Typically, $Al_2O_3$ ranges from 0.1 to 0.4 wt.%, but in some cases (*e.g.,* lamprophyre, Mu-241; pseudoleucite sodalite syenite, Mu-216) may reach 0.8 wt.% (Table 4.3.1.1). $TiO_2$ content varies from 0.4 to 1.3 wt.% in the lamprophyre, from 0.4 to 2.7 wt.% in the pseudoleucite syenite, from 0.4 to 3.2 wt.% in the pseudoleucite italite, from 0.4 to 2.2 wt.% in the "potassium-batisite" syenite, from 0.4 to 1.6 wt.% in the lamprophyllite- and barytolamprophyllite-bearing syenite, and is about 0.8 wt.% in the eudialyte syenite, and 1.2 wt.% in the aegirinite (Table 4.3.1.1).

*Mica.*

Biotite is one of the major constituents of the group 1 lamprophyre. Here, it occurs as platy phenocrysts up to 4 mm in length, short prismatic subhedral-to-euhedral crystals in the groundmass (*ca.* 100 μm in length) and in some cases, as an alteration rim (*e.g.* Mu-3/100, Fig. 4.3.1.4) or as a part of a thick "corona" around olivine macrocrysts (*e.g.* Mu-150, Fig. 4.3.1.5). The majority of the biotite phenocrysts are distinctly pleochroic from light yellow to greenish

Fig. 4.3.1.4. Biotite rims (reddish brown) around olivine macrocrysts (colourless). Left – phenocryst of clinopyroxene (pale green). Lamprophyre, Mu-3/100. FOV. 3.5 mm, plane-polarised light.



Fig. 4.3.1.5. "Corona" of tetra-ferriphlogopite (orange-red), potassic richterite (white), and biotite (orange-yellow) on altered olivine (grey). Lamprophyre, Mu-3/100. FOV. 3.5 mm, plane-polarised light.

127

yellow, or from orange yellow to reddish yellow and brownish red. The phenocrystic and groundmass biotite is commonly resorbed by carbonates. Biotite is also found in the pseudoleucite sodalite syenite (group 2) and pseudoleucite italite (group 3). In the pseudoleucite sodalite syenite (e.g. Mu-216), biotite occurs in a fine-grained clinopyroxene-potassium feldspar groundmass as anhedral-to-subhedral grains up to 100 μm. In the pseudoleucite italite (e.g. Mu-235), biotite forms rare yellowish orange to red phenocrysts up to 150 μm in length, and dark red subhedral-to-euhedral grains in a clinopyroxene-biotite-apatite groundmass (Fig. 4.2.6).

All compositions of the phenocrysts from the lamprophyre correspond to intermediate members of the phlogopite-annite series (Table 4.3.1.2). The majority of these phenocrysts show a core-to-rim zoning with a core enriched in MgO (up to 26.2 wt. %), and depleted in $FeO_T$ (< 3.9 wt. %) and $TiO_2$ (< 0.7 wt.%), where $FeO_T$ is total Fe expressed as FeO. Rims of the phenocrysts contain up to 33.4 wt.% $FeO_T$ (e.g. Mu-215), 5.9 wt.% $TiO_2$, and are relatively poor in MgO (< 5.0 wt.%). "Depletion" in MgO is commonly coupled with a decreasing $Al_2O_3$ content (from 13.2 wt.% in the core to 7.6 wt.% in the rim; Table 4.3.1.2). Some of the phenocrysts show slight enrichment in BaO (up to 1.2 wt.%). The groundmass biotite from the lamprophyre (Table 4.3.1.2; analyses 3, 10 and 12) is relatively depleted in Al, and enriched in Ti and Fe in comparison with the phenocrysts. The groundmass biotite from the pseudoleucite syenite shows preponderance of the annite component, and contains only ca. 3.5 wt.% MgO (Table 4.3.1.2; analysis 13). Biotite phenocrysts from the pseudoleucite italite (Table 4.3.1.2; analyses 14 and 15) are zoned with a core containing up to 19.4 wt.% MgO, 12.3 wt.% $FeO_T$, 0.9 wt.% $TiO_2$, 9.4 wt.% $Al_2O_3$, and a rim enriched in $FeO_T$ (up to 21.6 wt.%) and $TiO_2$ (up to 2.7 wt.%), and depleted in MgO (to 14.7 wt.%) and $Al_2O_3$ (to 6.0 wt.%). Biotite compositions from each of the samples studied form distinct evolutionary trends (Fig. 4.3.1.6). Also shown on Figure 4.3.1.6 are compositional data for mica from the plutonic rocks and some of the hypabyssal rocks of the Little Murun massif (as determined by Mitchell and Bergman 1991, and Mitchell and Vladykin 1996). Most of the biotite compositions obtained in this work fall

Table 4.3.1.2. Representative compositions of mica and ferripyrophyllite.

| Wt.% | 1# | 2** | 3** | 4# | 5# | 6** | 7# | 8# | 9# | 10# | 11** | 12# | 13# |
|---|---|---|---|---|---|---|---|---|---|---|---|---|---|
| $SiO_2$ | 41.98 | 40.39 | 38.81 | 40.45 | 41.30 | 37.57 | 34.01 | 37.32 | 40.68 | 40.54 | 38.64 | 37.54 | 34.83 |
| $TiO_2$ | 0.97 | 0.83 | 1.00 | 1.43 | 0.73 | 2.50 | 5.91 | 2.83 | 1.24 | 1.33 | 1.86 | 1.94 | 3.48 |
| $Al_2O_3$ | 12.51 | 12.10 | 9.87 | 10.08 | 10.97 | 12.28 | 7.94 | 13.19 | 11.24 | 10.12 | 10.60 | 7.63 | 7.50 |
| $Fe_2O_3$ | n.d | 3.34 | 1.25 | n.d | n.d | 0.12 | n.d | n.d | n.d | n.d | n.d | 0.02 | n.d |
| FeO | 8.17 | 0.90 | 14.26 | 11.36 | 9.38 | 15.69 | 33.38 | 14.05 | 11.58 | 9.54 | 8.93 | 22.28 | 34.21 |
| MnO | n.d | n.d | 0.15 | n.d | n.d | 0.13 | 0.31 | 0.17 | 0.24 | n.d | n.d | 0.24 | 1.22 |
| MgO | 22.23 | 26.19 | 18.21 | 21.12 | 21.92 | 17.46 | 4.99 | 16.58 | 20.76 | 22.04 | 22.67 | 14.15 | 3.54 |
| $Na_2O$ | 0.83 | 0.67 | 0.02 | n.d | n.d | n.d | 0.27 | 0.31 | n.d | 0.74 | 0.61 | 0.65 | 0.34 |
| $K_2O$ | 8.52 | 8.87 | 9.90 | 10.21 | 10.31 | 9.58 | 8.50 | 9.33 | 10.51 | 10.17 | 10.17 | 9.30 | 9.57 |
| BaO | n.d | n.d | n.d | n.d | n.d | 1.17 | n.d | 0.99 | n.d | n.d | 1.09 | 0.48 | n.d |
| Total | 95.21 | 93.29 | 93.47 | 94.65 | 94.61 | 96.50 | 95.31 | 94.77 | 96.25 | 94.48 | 94.57 | 94.23 | 94.69 |
| Formulae calculated on the basis of 11 atoms of oxygen | | | | | | | | | | | | | |
| Si | 3.003 | 2.897 | 2.974 | 2.999 | 3.025 | 2.819 | 2.829 | 2.840 | 2.970 | 2.992 | 2.880 | 2.988 | 2.958 |
| Ti | 0.052 | 0.045 | 0.058 | 0.080 | 0.040 | 0.141 | 0.370 | 0.162 | 0.068 | 0.074 | 0.104 | 0.116 | 0.222 |
| Al | 1.055 | 1.023 | 0.892 | 0.881 | 0.947 | 1.086 | 0.778 | 1.183 | 0.967 | 0.881 | 0.931 | 0.716 | 0.751 |
| $Fe^{3+}$ | - | 0.180 | 0.071 | - | - | 0.007 | - | - | - | - | - | 0.001 | - |
| $Fe^{2+}$ | 0.489 | 0.054 | 0.915 | 0.704 | 0.575 | 0.985 | 2.322 | 0.894 | 0.707 | 0.589 | 0.557 | 1.483 | 2.430 |
| Mn | - | - | 0.010 | - | - | 0.008 | 0.022 | 0.011 | 0.015 | - | - | 0.016 | 0.088 |
| Mg | 2.371 | 2.801 | 2.081 | 2.335 | 2.394 | 1.954 | 0.619 | 1.881 | 2.260 | 2.426 | 2.519 | 1.679 | 0.448 |
| Na | 0.115 | 0.093 | 0.003 | - | - | - | 0.044 | 0.046 | - | 0.106 | 0.088 | 0.100 | 0.056 |
| K | 0.778 | 0.812 | 0.968 | 0.966 | 0.963 | 0.917 | 0.902 | 0.906 | 0.979 | 0.958 | 0.967 | 0.944 | 1.037 |
| Ba | - | - | - | - | - | 0.034 | - | 0.030 | - | - | 0.032 | 0.015 | - |

129

Table 4.3.1.2 (Continued).

| Wt. % | 14[#] | 15[#] | 16** | 17* | 18** | 19* | 20** | 21** | 22** | 23** | 24* | 25* |
|---|---|---|---|---|---|---|---|---|---|---|---|---|
| $SiO_2$ | 41.06 | 37.88 | 41.63 | 45.18 | 43.81 | 43.99 | 45.19 | 44.00 | 53.36 | 55.50 | 55.34 | 50.74 |
| $TiO_2$ | 0.88 | 2.66 | 0.07 | n.d | n.d | 0.43 | n.d | n.d | 1.12 | 1.22 | 1.15 | 0.48 |
| $Al_2O_3$ | 9.36 | 6.05 | 0.27 | 36.39 | 35.80 | 32.22 | 36.52 | 36.17 | 0.28 | 0.29 | 0.25 | 3.23 |
| $Fe_2O_3$ | n.d | n.d | 14.99 | 4.25 | 3.99 | 4.51 | 0.89 | 2.38 | 16.91 | 16.83 | 17.52 | 24.60 |
| FeO | 12.26 | 21.58 | 1.48 | n.d | n.d | 0.02 | n.d | 0.96 | 9.85 | 12.02 | 9.89 | n.d |
| $V_2O_3$ | n.d | n.d | n.d | n.d | n.d | n.d | n.d | n.d | 0.63 | 0.16 | 0.48 | n.d |
| MnO | 0.33 | 0.47 | n.d | n.d | n.d | n.d | n.d | n.d | n.d | n.d | n.d | n.d |
| MgO | 19.44 | 14.71 | 27.37 | n.d | n.d | 0.84 | 0.11 | n.d | 4.29 | 2.93 | 4.03 | 1.46 |
| $Na_2O$ | 0.21 | n.d | n.d | 0.21 | 0.18 | 0.12 | 0.07 | 0.80 | 0.32 | 0.05 | 0.15 | 0.30 |
| $K_2O$ | 10.07 | 9.41 | 10.54 | 11.69 | 11.58 | 11.39 | 11.75 | 11.48 | 10.56 | 10.42 | 10.50 | 0.38 |
| Total | 93.61 | 94.31[†] | 96.35 | 97.72 | 95.36 | 93.52 | 94.53 | 95.79 | 99.32 | 99.42 | 99.31 | 82.34[††] |

Formulae calculated on the basis of 11 atoms of oxygen

| | 14 | 15 | 16 | 17 | 18 | 19 | 20 | 21 | 22 | 23 | 24 | 25 |
|---|---|---|---|---|---|---|---|---|---|---|---|---|
| Si | 3.091 | 3.032 | 3.057 | 2.973 | 2.957 | 3.035 | 3.037 | 2.959 | 3.936 | 3.965 | 3.936 | 3.997 |
| Ti | 0.050 | 0.160 | 0.004 | - | - | 0.022 | - | - | 0.060 | 0.066 | 0.062 | 0.028 |
| Al | 0.830 | 0.571 | 0.023 | 2.823 | 2.848 | 2.620 | 2.893 | 2.867 | 0.023 | 0.024 | 0.021 | 0.300 |
| $Fe^{3+}$ | - | - | 0.828 | 0.210 | 0.203 | 0.234 | 0.045 | 0.121 | 0.905 | 0.905 | 0.938 | 1.458 |
| $Fe^{2+}$ | 0.772 | 1.444 | 0.091 | - | - | 0.001 | - | 0.054 | 0.586 | 0.718 | 0.589 | - |
| $V^{6+}$ | - | - | - | - | - | - | - | - | 0.036 | 0.009 | 0.027 | - |
| Mn | 0.021 | 0.032 | - | - | - | - | - | - | - | - | - | - |
| Mg | 2.182 | 1.755 | 2.997 | - | - | 0.086 | 0.011 | - | 0.455 | 0.312 | 0.427 | 0.172 |
| Na | 0.031 | - | - | 0.027 | 0.024 | 0.016 | 0.009 | 0.104 | 0.044 | 0.007 | 0.021 | 0.046 |
| K | 0.967 | 0.961 | 0.987 | 0.981 | 0.997 | 1.003 | 1.007 | 0.985 | 0.958 | 0.950 | 0.953 | 0.038 |

n.d = not detected. [†] Total also includes 1.55 wt.% BaO (0.049 apfu Ba); [††] Total also includes 1.15 wt.% CaO (0.097 apfu Ca). [#] All Fe is given as FeO, stoichiometry suggests that no $Fe^{3+}$ is present; * All Fe is given as $Fe_2O_3$, stoichiometry suggests that no $Fe^{2+}$ is present. ** The $Fe^{2+}/Fe^{3+}$ ratio is calculated from stoichiometry. Analyses 1-15 – *biotite*: 1-12 – *lamprophyre* (1-3 – *Mu-150*: 1,2 – zoned phenocryst, 3 - groundmass; 4-5 – *Mu-3/100*: zoned phenocryst; 6-7 – *Mu-215*: zoned phenocryst; 8 – *Mu-232*: phenocryst, 9-10 – *Mu-231/13*: 9 – phenocryst, 10 – groundmass; 11-12 – *Mu-241*: 11 – phenocryst, 12 – groundmass); 13: *pseudoleucite syenite* (*Mu-216*, groundmass); 14-15: *pseudoleucite italite* (*Mu-235*: zoned phenocryst); 16 – *tetra-ferriphlogopite*: *lamprophyre* (*Mu-150*); 17-21 – *muscovite*: 17-18 – *aegirinite* (*Mu-190*); 19-20 – *garnet-pseudoleucite syenite* (*Mu-167/19*), 21 – *batisite/shcherbakovite syenite* (*Mu-186/6*); 22-24 – *celadonite*: *aegirinite* (*Mu-190*); 25 – *ferripyrophyllite*: *garnet-pseudoleucite syenite* (*Mu-167/19*).

within the field of the Murun plutonic rocks. However, some of the lamprophyre samples (*e.g.* Mu-215) exhibit noticeable enrichment in $TiO_2$ content (Fig. 4.3.1.6).

<u>Muscovite</u> is found in the garnet-pseudoleucite syenite (group 2, Mu-167/19), "potassium-batisite" syenite (group 6, Mu-186/6), and aegirinite (group 8, Mu-190), where it forms as an alteration product of clinopyroxene and potassium feldspar. The mineral contains up to 4.5 wt.% $Fe_2O_3$ (0.23 *apfu* $Fe^{3+}$), and in case of the garnet-pseudoleucite syenite, up to 0.8 wt.% MgO (0.09 *apfu* Mg) (Table 4.3.1.2).

<u>Tetra-ferriphlogopite</u> [$KMg_3Fe^{3+}Si_3O_{10}(OH)_2$] is found only in one sample of the lamprophyre (Mu-150). The mineral forms pinkish-yellow to dark red elongate grains, and is confined to a central part (*ca.* 0.5 mm in thickness) of an alteration "corona" around olivine macrocrysts (Fig. 4.3.1.5). This tetra-ferriphlogopite has nearly ideal composition with only 0.1 wt.% $TiO_2$ and 0.3 wt.% $Al_2O_3$ (Table 4.3.1.2; analysis 16).

<u>Celadonite</u> [$KFe^{3+}(Mg,Fe^{2+})$ $Si_4O_{10}(OH)_2$] occurs only in a sample of aegirinite (Mu-190), where it forms clusters of platy and acicular grains up to 180 μm in length, and is confined to cavities and fractures in the aegirine mesostasis. The mineral is associated with calcite, potassium feldspar, rutile (?), and pyrite. To our knowledge, celadonite has not been previously identified at Murun.

The identification of celadonite and tetra-ferriphlogopite has been made only on the basis of electron-microprobe analyses (Table 4.3.1.2); hence structural studies are required to confirm these identifications.

*Ferripyrophyllite* [$Fe^{3+}_2Si_4O_{10}(OH)_2$] occurs as an alteration product in the garnet-pseudoleucite syenite (Mu-167/19). Here, the mineral occurs along fractures and in cavities, and is commonly associated with jarosite and muscovite (Fig. 4.3.1.2). A representative composition of ferripyrophyllite is given in Table 4.3.1.2. Ferripyrophyllite is a rare mineral species and, prior to our study, had not been recognised at Murun.

131

This work:

*lamprophyre:*

| | | | | |
|---|---|---|---|---|
| ■ | Mu-150 | ▦ | Mu-3/100 | |
| ■ | Mu-231/13 | □ | Mu-215 | |
| ■ | Mu-232 | ■ | Mu-241 | |

*pseudoleucite italite:*

■ Mu-235

*pseudoleucite syenite:*

▨ Mu-216

Mitchell & Vladykin (1996):

▦ Murun plutonic rocks

⬭ Compositional fields for mica from "lamproite-like" hypabyssal rocks
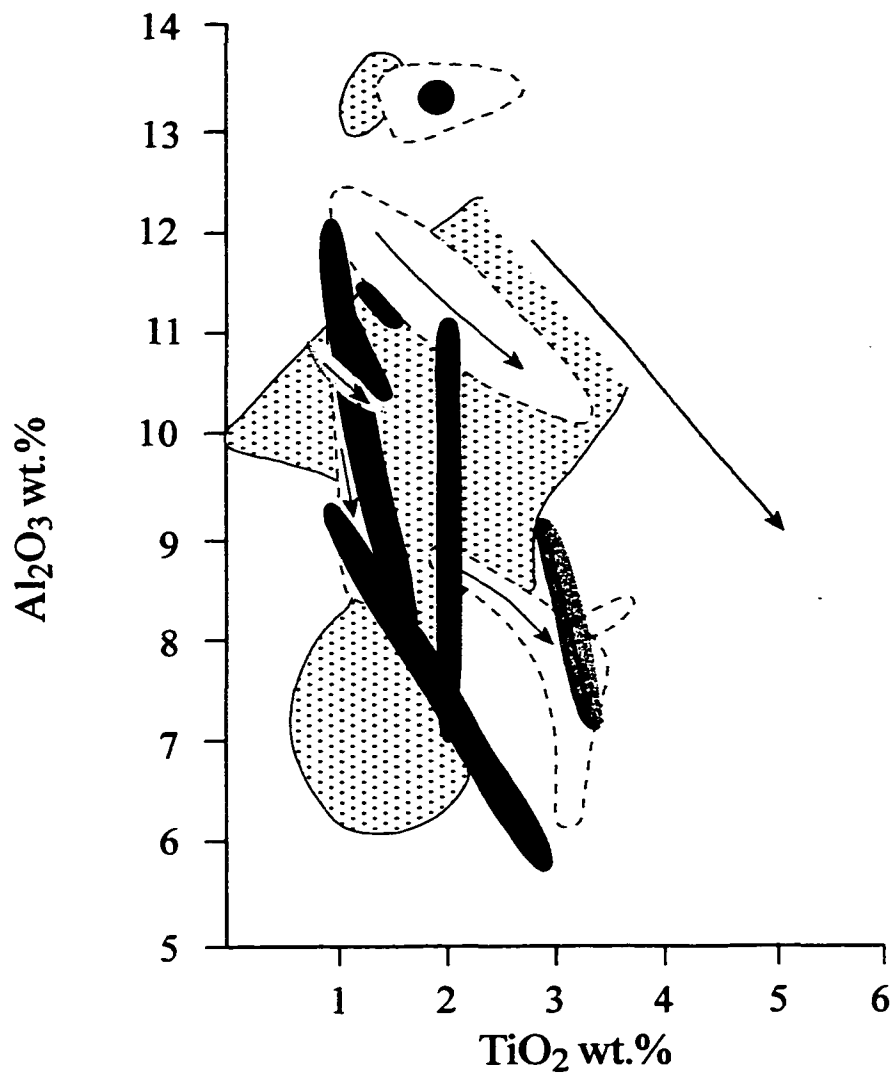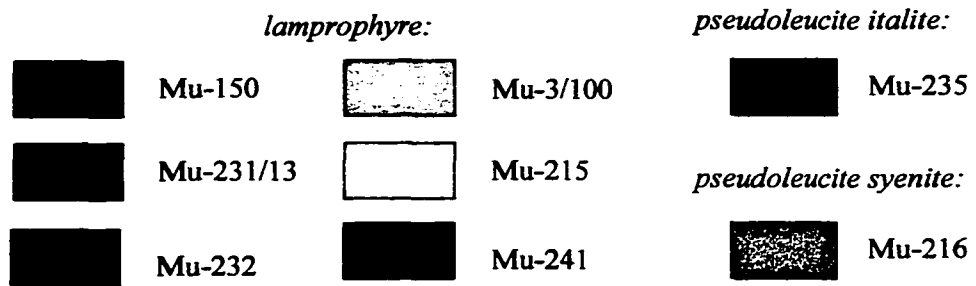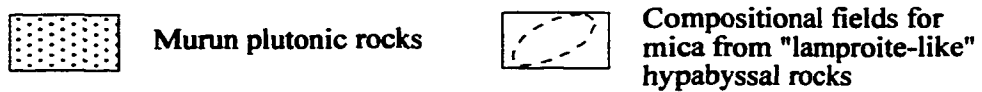
Fig. 4.3.1.6. Compositional variation of mica.

132

*Feldspar*

Potassium feldspar. In the lamprophyre, potassium feldspar occurs predominantly as anhedral grains (up to 60 µm across) in the groundmass. In some cases (*e.g.* Mu-215), the mineral also forms coarse (up to 1mm in size) subhedral-to-euhedral grains in the biotite-clinopyroxene-potassium feldspar mesostasis, and is strongly resorbed by carbonates (Fig. 4.3.1.7). In the pseudoleucite syenite and pseudoleucite italite, potassium feldspar forms pseudomorphs after leucite, and is commonly altered to Fe-Ti oxides/hydroxides, carbonates, muscovite and ferripyrophyllite. The mineral from the pseudoleucite syenite is also found as minute (*ca.* 40 µm across) anhedral grains in the fine-grained potassium feldspar-clinopyroxene matrix. In the kalsilite melasyenite, potassium feldspar is found exclusively as fine-grained intergrowths with kalsilite (Fig. 4.3.1.8). In the eudialyte-bearing syenite, "potassium-batisite" syenite, and lamprophyllite- and barytolamprophyllite-bearing syenite, potassium feldspar forms coarse subhedral or euhedral prismatic crystals (up to 2.5 mm in length) commonly replaced by carbonates (Fig. 4.2.8). In the lamprophyllite- and barytolamprophyllite-bearing syenite, and in some samples of the "potassium-batisite" syenite (*e.g.* Mu-186/6), anhedral-to-subhedral grains of the mineral also develop interstitially with respect to clinopyroxene, lamprophyllite and "potassium batisite" (Figs. 4.2.10, 4.2.11, 4.3.1.9). In the aegirinite, potassium feldspar is rare, it occurs interstitially with respect to aegirine grains, and is commonly altered to carbonates plus muscovite.

Representative compositions of potassium feldspar from the examined rocks are given in Table 4.3.1.3. Typically, $Fe_2O_3$ content varies from 0.3 to 0.9 wt.%, but in some samples may reach 1.4 wt.% (lamprophyre, Mu-3/100), and 1.8 wt.% ("potassium-batisite" syenite, Mu-186/6). BaO varies from below the detection limit (0.2 wt.%) to 2.1 wt.% in the lamprophyre, 1.5 wt.% in the pseudoleucite syenite, 3.0 wt.% in the "potassium-batisite" syenite, and 1.6 wt.% in the lamprophyllite- and barytolamprophyllite-bearing syenite. Potassium feldspar from the pseudoleucite italite, eudialyte syenite and aegirinite is devoid of

133

Fig. 4.3.1.7. Altered potassium feldspar (brownish; top left), prismatic grains of calcite (greyish white), phenocrysts of biotite (elongate colourless), and clinopyroxene (green to dark green). Lamprophyre, Mu-215. FOV. 3.5 mm, plane-polarised light.
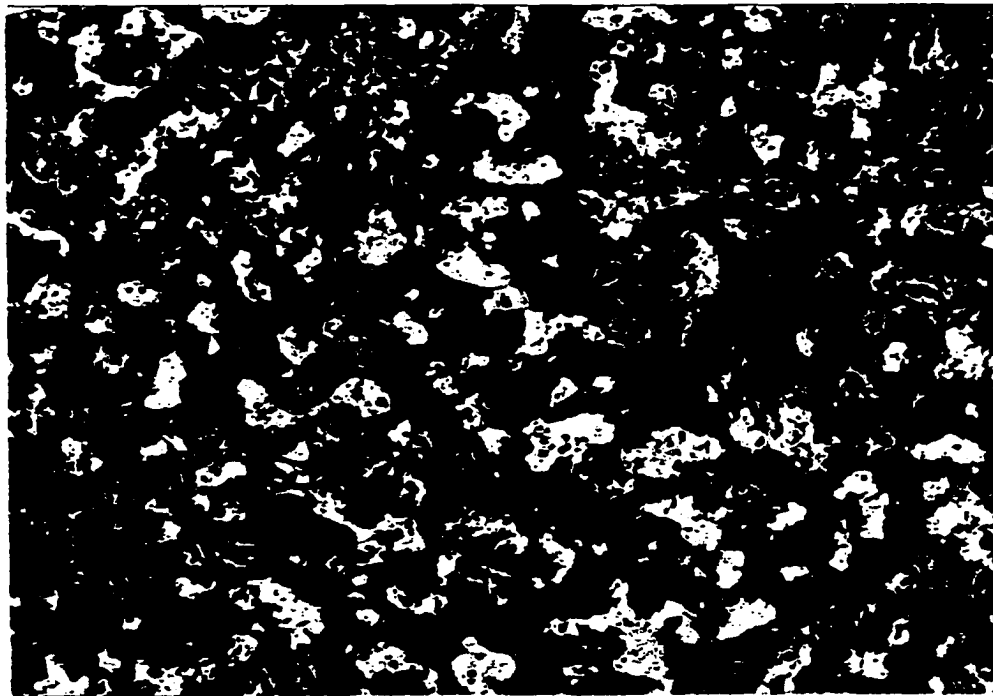


Fig. 4.3.1.8. Kalsilite-potassium feldspar intergrowths. FOV 100 μm. Kalsilite melasyenite, Mu-172. BSE image.

134

Table 4.3.1.3. Representative compositions of potassium feldspar.

| Wt.% | 1 | 2 | 3 | 4 | 5 | 6 | 7 | 8 | 9 |
|---|---|---|---|---|---|---|---|---|---|
| $SiO_2$ | 63.89 | 65.38 | 62.37 | 65.19 | 63.39 | 64.30 | 64.02 | 64.18 | 64.78 |
| $Al_2O_3$ | 18.19 | 18.33 | 17.81 | 18.56 | 18.87 | 18.36 | 18.54 | 18.12 | 18.34 |
| $Fe_2O_3$ | 0.40 | 0.61 | 1.39 | 0.45 | 0.79 | 0.79 | 0.78 | 0.41 | 0.28 |
| BaO | n.d | n.d | 2.07 | n.d | 1.53 | n.d | n.d | n.d | n.d |
| $Na_2O$ | n.d | n.d | 0.43 | n.d | 0.17 | n.d | n.d | n.d | n.d |
| $K_2O$ | 16.86 | 16.33 | 15.14 | 16.55 | 16.34 | 16.77 | 17.11 | 16.49 | 16.36 |
| Total | 99.34 | 99.94 | 99.21 | 100.75 | 101.15 | 100.39 | 100.45 | 99.20 | 99.96 |

Formulae calculated on the basis of 8 atoms of oxygen

| | 1 | 2 | 3 | 4 | 5 | 6 | 7 | 8 | 9 |
|---|---|---|---|---|---|---|---|---|---|
| Si | 2.986 | 2.993 | 2.958 | 2.993 | 2.944 | 2.977 | 2.967 | 2.996 | 2.997 |
| Al | 1.002 | 1.000 | 0.996 | 1.004 | 0.968 | 0.990 | 1.013 | 0.997 | 1.000 |
| $Fe^{3+}$ | 0.014 | 0.021 | 0.050 | 0.016 | 0.028 | 0.028 | 0.027 | 0.141 | 0.010 |
| Ba | - | - | 0.038 | - | 0.028 | - | - | - | - |
| Na | - | - | 0.040 | - | 0.015 | - | - | - | - |
| K | 1.005 | 0.964 | 0.916 | 0.969 | 0.968 | 0.990 | 1.012 | 0.982 | 0.966 |

| Wt.% | 10 | 11 | 12 | 13 | 14 | 15 | 16 | 17 | 18 |
|---|---|---|---|---|---|---|---|---|---|
| $SiO_2$ | 63.96 | 63.86 | 62.84 | 62.29 | 61.77 | 64.66 | 62.08 | 16.52 | 68.00 |
| $Al_2O_3$ | 17.43 | 17.20 | 17.81 | 17.80 | 17.59 | 18.32 | 17.88 | 18.52 | 19.01 |
| $Fe_2O_3$ | 0.81 | 1.18 | 1.18 | 0.84 | 1.81 | 0.60 | 0.90 | 0.47 | n.d |
| BaO | n.d | 0.58 | 2.97 | 0.98 | 2.40 | n.d | 1.65 | n.d | n.d |
| CaO | n.d | n.d | n.d | n.d | n.d | n.d | n.d | n.d | 0.31 |
| $Na_2O$ | n.d | n.d | n.d | 0.43 | 0.23 | n.d | 0.20 | 0.47 | 11.53 |
| $K_2O$ | 16.45 | 16.21 | 14.94 | 16.06 | 15.05 | 17.12 | 15.86 | 17.02 | n.d |
| Total | 98.65 | 99.03 | 99.74 | 98.44 | 99.05 | 100.70 | 98.37 | 101.13 | 98.85 |

Formulae calculated on the basis of 8 atoms of oxygen

| | 10 | 11 | 12 | 13 | 14 | 15 | 16 | 17 | 18 |
|---|---|---|---|---|---|---|---|---|---|
| Si | 3.007 | 3.005 | 2.971 | 2.965 | 2.948 | 2.985 | 2.964 | 2.988 | 3.004 |
| Al | 0.966 | 0.954 | 0.993 | 0.999 | 0.989 | 0.997 | 1.006 | 1.002 | 0.990 |
| $Fe^{3+}$ | 0.029 | 0.042 | 0.042 | 0.030 | 0.065 | 0.021 | 0.032 | 0.016 | - |
| Ba | - | 0.011 | 0.055 | 0.018 | 0.045 | - | 0.031 | - | - |
| Ca | - | - | - | - | - | - | - | - | 0.015 |
| Na | - | - | - | 0.040 | 0.021 | - | 0.018 | 0.043 | 0.987 |
| K | 0.987 | 0.973 | 0.901 | 0.975 | 0.916 | 1.008 | 0.966 | 0.996 | - |

n.d=not detected. Analyses 1-4: *biotite-rich rock* (1: *Mu-231/13*, 2: *Mu-241*, 3-4: *Mu-3/100*); 5-7 — *pseudoleucite syenite* (5-6: *Mu-167/19*, 7: *Mu-216*); 8 — *pseudoleucite italite* (*Mu-235*); 9 — *eudialyte syenite* (*Mu-245*); 10-14 — *batisite/shcherbakovite syenite* (10-12: *Mu-171*, 13-14: *Mu-186/6*); 15-16 — *barytolamprophyllite- and lamprophyllite-bearing syenite* (15: *Mu-184/11*, 16: *Mu-236*); 17 — *aegirinite* (*Mu-190*).

detectable Ba (Table 4.3.1.3). Generally, this mineral contains less than 0.5 wt.% $Na_2O$, *i.e.* less than 5 mol.% albite).

Fig. 4.3.1.9. Potassium feldspar (grey) developed interstitially with respect to lamprophyllite (coarse lammelae) and fibrous clinopyroxene. Lamprophyllite-bearing syenite, Mu-184/11. F.O.V. 3.5 mm, plane-polarised light.

Albite is found only in one sample of the lamprophyre (Mu-232), where it occurs as a groundmass mineral associated with potassium feldspar and biotite. Albite forms anhedral-to-subhedral grains up to 70 $\mu$m in size. Compositionally, the mineral corresponds to nearly pure albite with ≤ 0.35 wt.% CaO (< 2 mol.% anorthite) (Table 4.3.1.3).

*Nepheline* is found only in the eudialyte-bearing nepheline syenite (Mu-196) and some samples of barytolamprophyllite-and lamprophyllite-bearing syenite (*e.g.* Mu-236 and –

136

Table 4.3.1.4. Representative compositions of kalsilite and nepheline.

| Wt.% | 1 | 2 | 3 | 4 | 5 | 6 | 7 | 8 |
|---|---|---|---|---|---|---|---|---|
| $SiO_2$ | 37.04 | 36.99 | 36.75 | 40.04 | 40.43 | 40.13 | 40.91 | 40.81 |
| $Al_2O_3$ | 30.25 | 30.05 | 28.45 | 33.55 | 34.40 | 33.19 | 33.18 | 33.34 |
| $Fe_2O_3$ | 2.91 | 3.34 | 4.20 | 1.40 | 1.08 | 1.73 | 2.41 | 2.16 |
| $Na_2O$ | 0.42 | n.d | 0.10 | 15.64 | 15.57 | 15.90 | 16.08 | 16.03 |
| $K_2O$ | 28.65 | 28.78 | 28.80 | 8.37 | 8.06 | 7.83 | 7.66 | 7.58 |
| Total | 99.27 | 99.16 | 98.30 | 99.00 | 99.54 | 98.78 | 100.24 | 99.92 |

Formulae calculated on the basis of 4 atoms of oxygen

| | 1 | 2 | 3 | 4 | 5 | 6 | 7 | 8 |
|---|---|---|---|---|---|---|---|---|
| Si | 0.991 | 0.991 | 1.000 | 0.992 | 0.991 | 0.995 | 1.000 | 0.999 |
| Al | 0.954 | 0.949 | 0.912 | 0.980 | 0.994 | 0.970 | 0.956 | 0.962 |
| $Fe^{3+}$ | 0.059 | 0.067 | 0.086 | 0.026 | 0.020 | 0.032 | 0.044 | 0.040 |
| Na | 0.022 | - | 0.005 | 0.751 | 0.740 | 0.763 | 0.762 | 0.761 |
| K | 0.978 | 0.984 | 1.000 | 0.265 | 0.252 | 0.248 | 0.239 | 0.237 |

n.d = not detected. Analyses 1-3: *kalsilite* (1-2 – barytolamprophyllite-bearing syenite, *Mu-236*; 3 – kalsilite melasyenite, Mu-172); 4-8: *nepheline* (4-5 – barytolamprophyllite-bearing syenite, *Mu-236*; 6-8 – eudialyte-bearing syenite, 6-7: *Mu-245*; 8: *Mu-196*).

137

the eudialyte-bearing nepheline syenite, white subhedral fractured crystals of the mineral (up to 1 mm in length) are developed interstitially relative to clinopyroxene and eudialyte. In the barytolamprophyllite- and lamprophyllite-bearing syenite, nepheline is extremely rare, and forms strongly altered anhedral-to-subhedral grains (up to 150 µm across) in the potassium feldspar-kalsilite-clinopyroxene matrix.

Nepheline contains 7.7 to 8.4 wt.% $K_2O$ (24 to 26 mol.% $KAlSiO_4$). All compositions plot close to the $NaAlSiO_4$ - $KAlSiO_4$ join within the Morozewicz-Buerger convergence field of Tilley (1954) for plutonic nepheline, suggesting low crystallisation temperatures or equilibration (Hamilton 1961, Mitchell & Platt 1979). Nepheline is somewhat enriched in $Fe^{3+}$ (up to 1.4 wt.% in barytolamprophyllite- and lamprophyllite-bearing syenite, and 2.4 wt.% in the eudialyte-bearing syenite, Table 4.3.1.4).

*Kalsilite* is found in the kalsilite melasyenite, and some samples of the barytolamprophyllite-bearing syenite (*e.g.* Mu-236) and pseudoleucite syenite (*e.g.* Mu-216). In the kalsilite melasyenite, the mineral occurs in the vermiform intergrowths with potassium feldspar, developed interstitially with respect to biotite and diopside (Fig. 4.3.1.8). In the barytolamprophyllite-bearing syenite and pseudoleucite syenite, kalsilite forms anhedral grains (up to 150 µm) in the groundmass. Kalsilite from the pseudoleucite syenite is typically altered to an unidentified cancrinite-group mineral.

Kalsilite from the barytolamprophyllite-bearing syenite and kalsilite melasyenite is noticeably enriched in $Fe_2O_3$ (up to 3.3 wt.% $Fe_2O_3$ or 0.07 *apfu* $Fe^{3+}$, and 4.2 wt.% or 0.09 *apfu* $Fe^{3+}$, respectively; Table 4.3.1.4). $Na_2O$ content varies from below the detection limit to 0.4 wt.% $Na_2O$ (< 2 mol.% nepheline) in kalsilite from the barytolamprophyllite-bearing syenite, and 0.1 wt.% (< 1 mol.% nepheline) from the kalsilite melasyenite (Table 4.3.1.4). Previous studies of the Murun kalsilite from kalsilite syenites, yakutites, tinguaites and synnyrites showed that the $Na_2O$ content typically does not exceed 0.1 wt.% (or 0.01 apfu Na), and that the mineral can contain up to 3.2 wt.% $Fe_2O_3$ (or 0.06 apfu $Fe^{3+}$) (Samsonova &

138

Donakov 1968; Konev *et al.* 1996). Similarly to the Murun material, kalsilite from the pseudoleucite syenites and synnyrites of the Southern Sakun massif (western Aldan shield is Na-poor (< 0.1 wt.% $Na_2O$), however, the $Fe_2O_3$ content is noticeably lower (< 1.1 wt. %) than that of the Murun mineral (Kononova *et al.* 1997).

*Amphibole* is found exclusively in the lamprophyre. In sample Mu-150, colourless elongate and diamond-shaped (in cross-section) crystals of amphibole occur in "coronas" around olivine (Fig. 4.3.1.5). Amphibole from sample Mu-3/100 forms thin (*ca.* 100 μm in thickness) alteration rims on olivine. In sample 231/13, amphibole occurs as slightly pleochroic (from colourless to pale greenish blue) subhedral-to-euhedral prismatic phenocrysts up to 0.8 mm in length (Fig. 4.2.1) commonly exhibiting a prominent parallel twinning. Amphibole from sample Mu-232 is strongly pleochroic from greenish-blue to purplish-blue. The mineral forms prismatic (up to 1.2 mm in length and 0.7 mm across) phenocrysts (Fig. 4.2.1), and small (*ca.* 50 μm across) anhedral grains in the potassium feldspar-biotite-clinopyroxene-apatite groundmass. The phenocrysts are partly altered to clinopyroxene along the rim and fractures.

According to the existing nomenclature (Leake *et al.* 1997), all amphibole compositions from samples Mu-150, 3/100, and 231/13 correspond to potassic richterite (Table 4.3.1.5). It is noteworthy, however, that they exhibit a significant variation within the potassic-richterite field. The $FeO_T$ and MgO contents correspond to *ca.* 1.5 and 22.9 wt.%, respectively in amphibole from the "corona" (Mu-150), 6.9 and 19.7 in samples from the alteration rim on olivine (Mu-3/100), and 8.5 and 18.8 wt.% in the phenocrystic amphibole (Mu-231/13). Typically, this amphibole is Al-poor (< 0.2 wt.% $Al_2O_3$), but in some cases (*e.g.* Mu-3/100), may contain up to 1.0 wt.% $Al_2O_3$ (Table 4.3.1.5). $TiO_2$ content varies from negligible (*e.g.* Mu-3/100) to 0.5 wt.% (*e.g.* Mu-150). The amphibole from sample Mu-232 corresponds to magnesioriebeckite (Table 4.3.1.5, analyses 6-7). In BSE, the mineral exhibits an irregular zoning with high-*AZ* zones enriched in $FeO_T$ (up to 21.3 wt.%), and impoverished in MgO (to 11.6 wt.%) relative to the low-*AZ* areas (*ca.* 16.2 wt.% $FeO_T$ and 14.0 wt.% MgO).

## Table 4.3.1.5. Representative compositions of amphiboles from lamprophyre.

| Wt. % | 1 | 2 | 3 | 4 | 5 | 6 | 7 |
|---|---|---|---|---|---|---|---|
| SiO$_2$ | 54.28 | 55.63 | 57.2 | 55.82 | 54.58 | 54.54 | 55.35 |
| TiO$_2$ | 0.28 | 0.35 | 0.53 | 0.25 | n.d | 0.67 | 0.24 |
| Al$_2$O$_3$ | 0.18 | n.d | n.d | 0.75 | 0.97 | 0.24 | 0.28 |
| Fe$_2$O$_3$ | 4.56 | 1.48 | 1.54 | 2.14 | 2.55 | 10.58 | 13.81 |
| FeO | 3.95 | n.d | 0.69 | 4.55 | 4.58 | 5.63 | 7.46 |
| MnO | 0.06 | 0.17 | n.d | n.d | 0.18 | 0.21 | 0.15 |
| MgO | 18.76 | 22.92 | 23.22 | 20.10 | 19.26 | 14.02 | 11.62 |
| CaO | 4.24 | 6.20 | 6.24 | 6.00 | 5.81 | 2.70 | 0.57 |
| Na$_2$O | 5.02 | 4.13 | 4.62 | 5.26 | 5.15 | 6.28 | 7.80 |
| K$_2$O | 4.86 | 4.75 | 4.6 | 3.45 | 3.39 | 0.59 | 0.19 |
| Total | 96.19 | 95.63 | 98.64 | 98.32 | 96.47 | 95.46 | 97.47 |

Formulae calculated on the basis of 23 oxygens
($Fe^{2+}/Fe^{3+}$ ratio − from stoichiometry)

| | 1 | 2 | 3 | 4 | 5 | 6 | 7 |
|---|---|---|---|---|---|---|---|
| Si | 7.887 | 7.925 | 7.914 | 7.864 | 7.854 | 7.959 | 8.000 |
| Al$_{IV}$ | 0.032 | - | - | 0.125 | 0.146 | 0.041 | - |
| Fe$^{3+}$$_{IV}$ | 0.081 | 0.075 | 0.086 | 0.011 | - | - | - |
| Σ | 8.000 | 8.000 | 8.000 | 8.000 | 8.000 | 8.000 | 8.000 |
| | | | | | | | |
| Ti | 0.030 | 0.037 | 0.055 | 0.026 | - | 0.074 | 0.026 |
| Al$_{VI}$ | - | - | - | - | 0.018 | - | 0.048 |
| Fe$^{3+}$$_{VI}$ | 0.417 | 0.083 | 0.074 | 0.216 | 0.276 | 1.162 | 1.502 |
| Fe$^{2+}$ | 0.481 | - | 0.080 | 0.536 | 0.551 | 0.687 | 0.902 |
| Mg | 4.064 | 4.869 | 4.791 | 4.222 | 4.133 | 3.051 | 2.504 |
| Mn | 0.008 | 0.021 | - | - | 0.022 | 0.026 | 0.018 |
| Σ | 5.000 | 5.010 | 5.000 | 5.000 | 5.000 | 5.000 | 5.000 |
| | | | | | | | |
| Ca | 0.660 | 0.946 | 0.925 | 0.906 | 0.896 | 0.422 | 0.088 |
| Na | 1.340 | 1.054 | 1.075 | 1.094 | 1.104 | 1.578 | 1.912 |
| Σ | 2.000 | 2.000 | 2.000 | 2.000 | 2.000 | 2.000 | 2.000 |
| | | | | | | | |
| Na | 0.074 | 0.087 | 0.164 | 0.343 | 0.333 | 0.199 | 0.274 |
| K | 0.902 | 0.863 | 0.812 | 0.620 | 0.622 | 0.110 | 0.035 |
| Σ | 0.976 | 0.950 | 0.976 | 0.963 | 0.955 | 0.309 | 0.309 |

n.d = not detected. Analyses 1-5: *potassic richterite* (1: phenocryst, *Mu-231/13*; 2-3 − "corona" on olivine, *Mu-150*; 4-5 − alteration rim on olivine, *Mu-3/100*); 6-7: *magnesioriebeckite* (zoned phenocryst, Mu-232: 6 − low-*AZ*, 7 − high-*AZ*).

140

*Olivine* is found only in two samples of the lamprophyre (Mu-150 and 3/100). In sample Mu-150, the mineral forms anhedral greyish-green macrocrysts (up to 3 mm across) surrounded by a thick (up to 2 mm in thickness) "corona" composed (from the olivine outwards) of tetra-ferriphlogopite, potassic richterite, and biotite (Fig. 4.3.1.5). In sample Mu-3/100, olivine occurs as colourless to very pale green anhedral-to-subhedral phenocrysts (up to 0.7 mm across) commonly mantled by phlogopite (Figs. 4.2.3, 4.3.1.4).

Compositionally, olivine from sample 3/100 shows the preponderance of the forsterite component (from 70.2 to 75.8 mol.% $Mg_2SiO_4$, Table 4.3.1.6). The fayalite and tephroite components vary from 23.6 to 28.9, and from 0.6 to 0.9 mol. %, respectively. Some of the olivine compositions exhibit slight enrichment in Ca (up to 0.2 wt.% CaO or 0.3 mol.% $Ca_2SiO_4$; Table 4.3.1.6). Compositions of the macrocrysts of olivine strongly altered by talc from the sample Mu-150 could not been determined.

Table 4.3.1.6. Representative compositions of olivine from lamprophyre.

| Wt. % | 1 | 2 | 3 | 4 | 5 | 6 |
|---|---|---|---|---|---|---|
| SiO2 | 37.50 | 37.55 | 37.98 | 38.34 | 38.04 | 38.04 |
| FeO | 26.38 | 25.28 | 22.70 | 21.91 | 22.97 | 25.22 |
| MnO | 0.85 | 0.71 | 0.50 | 0.53 | 0.54 | 0.81 |
| MgO | 35.97 | 36.27 | 38.85 | 39.51 | 38.54 | 36.95 |
| CaO | n.d | n.d | 0.13 | n.d | 0.20 | 0.15 |
| Total | 100.70 | 99.81 | 100.16 | 100.29 | 100.29 | 101.17 |

Formulae calculated on the basis of 4 atoms of oxygen

| | | | | | | |
|---|---|---|---|---|---|---|
| Si | 0.991 | 0.995 | 0.990 | 0.993 | 0.992 | 0.994 |
| Fe | 0.583 | 0.560 | 0.495 | 0.475 | 0.501 | 0.551 |
| Mn | 0.019 | 0.016 | 0.011 | 0.012 | 0.012 | 0.018 |
| Mg | 1.417 | 1.433 | 1.510 | 1.527 | 1.498 | 1.439 |
| Ca | - | - | 0.004 | n.d | 0.006 | 0.004 |
| *Σcations* | 3.010 | 3.005 | 3.010 | 3.007 | 3.009 | 3.006 |

End-member components (mol.%)

| | | | | | | |
|---|---|---|---|---|---|---|
| *Forsterite* | 70.19 | 71.33 | 74.77 | 75.83 | 74.30 | 71.52 |
| *Fayalite* | 28.87 | 27.88 | 24.50 | 23.59 | 24.84 | 27.38 |
| *Tephroite* | 0.94 | 0.79 | 0.55 | 0.58 | 0.59 | 0.89 |
| *Larnite* | - | - | 0.18 | - | 0.28 | 0.21 |

n.d = not detected.

141

*Sodalite* is found exclusively in the samples of pseudoleucite sodalite syenite (*e.g.* Mu-216). The mineral forms rounded pseudomorphs (up to 0.7 mm in diameter) after leucite phenocrysts set in a fine-grained groundmass (Fig. 4.2.4). The mineral has nearly ideal composition with slight enrichment in $Fe_2O_3$ (up to 0.4 wt.%), and nosean component (up to 0.6 wt.% $SO_3$) (Table 4.3.1.7).

A *cancrinite-group mineral* is an accessory phase in the pseudoleucite sodalite syenite (Mu-216). The mineral is commonly developed as fracture fillings in clinopyroxene, in association with barite and barytolamprophyllite. The cancrinite-group mineral has relatively uniform composition (Table 4.3.1.7), with the Na content exhibiting the most signifiant variation (from 4.91 *apfu* to 5.50 *apfu*). The stoichiometry of this mineral exhibits clear similarities with the $K-SO_4$-rich members of the cancrinite group, pitiglianoite $[K_2Na_6Si_6Al_6O_{24}(SO_4)\cdot 2H_2O]$ and giuseppettite $[(Na,K,Ca)_{7-8}(Si,Al)_{12}O_{24}(SO_4,Cl)_{1-2}$.

*Eudialyte* [ideally, $Na_{15}Ca_6(Fe^{2+},Mn^{2+})_3Zr_3(Si,Nb)(Si_{25}O_{73})(O,OH,H_2O)_3(Cl,OH)_2$] occurs exclusively in the samples of eudialyte-bearing syenite (group 5). In the eudialyte-aegirine syenite (*e.g.* Mu-245), the mineral forms subhedral-to-euhedral prismatic crystals up to 2 mm in length (Fig. 4.2.8). Eudialyte from the eudialyte-bearing nepheline syenite (*e.g.* Mu-196) occurs as euhedral prismatic crystals up to 0.5 mm in length, partially replaced by strontianite and wadeite (Fig. 4.3.1.10).

In BSE, the mineral commonly exhibits an oscillatory zoning with high-*AZ* zones enriched in Zr and Mn and proportionally depleted in Ti and $Fe^{2+}$ (Table 4.3.1.7, analyses 4-7). The ZrO and MnO contents vary from 11.2 and 4.2 wt.% (respectively) in the low-*AZ* zones, to 12.3 and 6.3 wt.% in the high-*AZ* zones, respectively, whereas the $TiO_2$ and FeO contents are *ca.* 1.1 and 5.4 wt.% in the low-*AZ* zones, and *ca.* 0.6 and 4.2 wt.% in the high-*AZ* zones (Table 4.3.1.7). The high-*AZ* zones also contain elevated levels of Nb (up to 1.7 wt.% $Nb_2O_5$, or 0.41 *apfu* Nb), whereas the low-*AZ* zones lack detectable Nb.

142

## Table 4.3.1.7. Representative compositions of sodalite, cancrinite-group mineral and eudialyte.

| Wt. % | 1 | 2 | 3 | 4 low-$AZ$ | 5 high-$AZ$ | 6 low-$AZ$ | 7 high-$AZ$ |
|---|---|---|---|---|---|---|---|
| $SiO_2$ | 37.25 | 33.88 | 34.00 | 50.65 | 48.77 | 49.99 | 47.56 |
| $TiO_2$ | n.d | n.d | n.d | 1.05 | 0.60 | 1.15 | 0.57 |
| $Al_2O_3$ | 31.49 | 28.64 | 28.17 | n.d | n.d | n.d | n.d |
| FeO | - | - | - | 5.25 | 4.07 | 5.49 | 4.12 |
| $Fe_2O_3$ | 0.36 | 0.41 | 0.33 | - | - | - | - |
| $Nb_2O_5$ | n.d | n.d | n.d | n.d | 1.01 | n.d | 1.69 |
| ZrO | n.d | n.d | n.d | 11.58 | 12.34 | 11.25 | 11.95 |
| MnO | n.d | n.d | n.d | 1.58 | 2.35 | 1.75 | 2.87 |
| SrO | n.d | n.d | n.d | 4.42 | 6.34 | 4.17 | 5.33 |
| CaO | n.d | 0.47 | 1.19 | 11.11 | 11.33 | 10.89 | 10.39 |
| $Na_2O$ | 24.29 | 16.06 | 14.26 | 9.96 | 10.18 | 9.58 | 9.88 |
| $K_2O$ | 0.16 | 9.49 | 9.12 | 1.97 | 1.76 | 1.63 | 1.37 |
| $SO_3$ | 0.56 | 6.45 | 7.15 | n.d | n.d | n.d | n.d |
| Cl | 7.27 | n.d | n.d | 0.38 | 0.31 | 0.57 | 0.36 |
| $-O=Cl_2$ | 1.64 | - | - | 0.09 | 0.07 | 0.13 | 0.08 |
| Total | 100.12* | 95.40 | 94.22 | 97.86 | 98.99 | 96.34 | 96.01 |

### Formulae calculated on the basis of:

| | 6 oxygens | $\Sigma(Si+Al+Fe^{3+})=12$ | | $\Sigma(Si+Ti+Al+Zr+Nb)=29$ | | | |
|---|---|---|---|---|---|---|---|
| Si | 5.971 | 5.984 | 6.049 | 25.730 | 25.394 | 25.731 | 25.270 |
| Ti | - | - | - | 0.401 | 0.235 | 0.445 | 0.228 |
| Al | 5.949 | 5.962 | 5.907 | - | - | - | - |
| $Fe^{2+}$ | - | - | - | 2.230 | 1.772 | 2.363 | 1.831 |
| $Fe^{3+}$ | 0.043 | 0.054 | 0.044 | - | - | - | - |
| Nb | - | - | - | - | 0.238 | - | 0.406 |
| Zr | - | - | - | 2.869 | 3.133 | 2.824 | 3.096 |
| Mn | - | - | - | 0.680 | 1.036 | 0.763 | 1.292 |
| Sr | - | - | - | 1.302 | 1.914 | 1.245 | 1.642 |
| Ca | - | 0.089 | 0.227 | 6.047 | 6.321 | 6.006 | 5.915 |
| Na | 7.549 | 5.500 | 4.912 | 9.811 | 10.278 | 9.561 | 10.179 |
| K | 0.033 | 2.138 | 2.070 | 1.277 | 1.169 | 1.070 | 0.929 |
| $S^{6+}$ | 0.067 | 0.855 | 0.955 | - | - | - | - |
| Cl | 1.975 | - | - | 0.327 | 0.274 | 0.497 | 0.324 |

n.d = not detected. * Total also includes 0.38 wt.% MgO (0.091 apfu Mg). Analyses 1: *sodalite* (*pseudoleucite sodalite syenite, Mu-216*); 2-3: *cancrinite-group mineral* (*pseudoleucite sodalite syenite, Mu-216*); 4-7: *eudialyte* (*4-5 − eudialyte syenite, Mu-245*; 6-7 − *eudialyte-bearing nepheline syenite, Mu-196*).
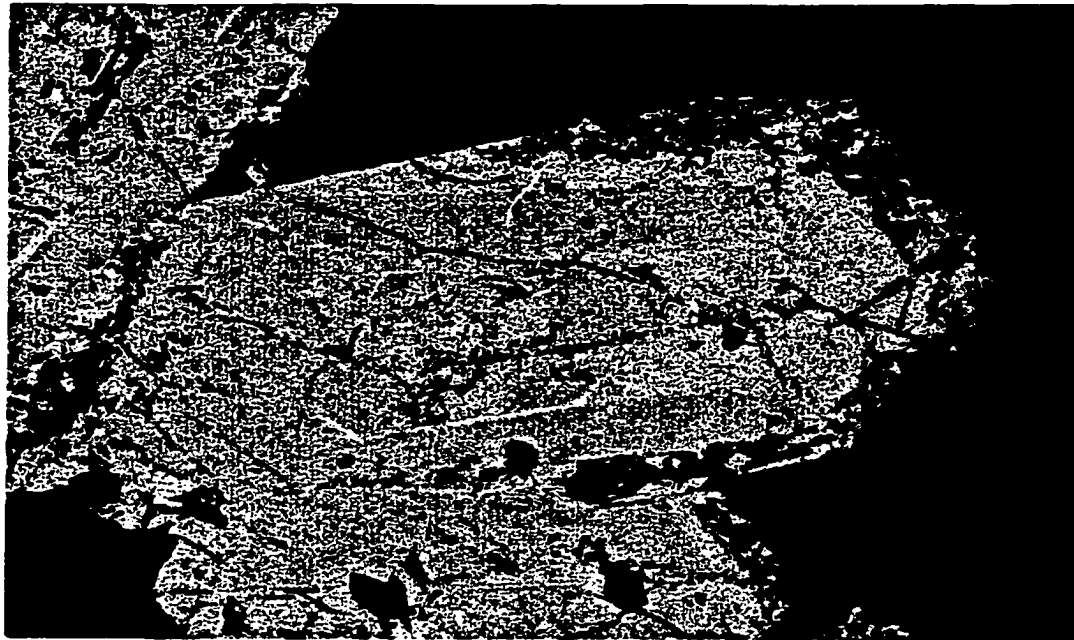
Fig. 4.3.1.10. Zoned eudialyte crystals with alteration rims. Pink — wadeite, white — strontianite, black — nepheline. Eudialyte-bearing nepheline syenite, Mu-196. F.O.V. 0.8 mm. False-colour BSE image.

The Murun eudialyte has unusually high $K_2O$ contents, varying from 1.4 to 2.0 wt.% (0.9 to 1.3 *apfu* K). Previous studies of the eudialyte-type minerals showed that $K_2O$ content in these minerals usually does not exceed 0.5 wt.% $K_2O$ (Johnsen & Grice 1999), and only rarely reaches 0.6 wt.% (Temiscaminque County, Quebec; Johnsen & Grice 1999). In addition, the eudialyte studied in this work is also enriched in Sr (up to 6.3 wt.% SrO or 1.9 *apfu* Sr). SrO concentrations in eudialyte-type minerals typically do not exceed 0.5 wt.% (Johnsen & Grice 1999). High SrO contents in eudialyte-type minerals were previously reported from several occurrences, including manganokhomyakovite [$Na_{12}Sr_3Ca_6Mn_3Zr_3W(Si_{25}O_{73})(O,OH,H_2O)_3$ $(Cl,OH)_2$] from Mont Saint-Hilaire, Quebec (9.6 wt.%; Johnsen *et al.* 1999), material from the Gardiner complex, East Greenland (4.1 wt.%), Khibina massif, Kola Peninsula, Russia (2.0 wt.%) and Burpala massif, Siberia, Russia (1.7 wt.%) (Johnsen & Grice 1999).

*Garnet* is found exclusively in the samples of garnet-pseudoleucite syenite, where it forms hexagonally-shaped phenocrysts (up to 0.4 mm in diameter) profusely altered to a

144

Table 4.3.1.8. Representative compositions of titanian andradite from the garnet-pseudoleucite syenite (*Mu-167/19*).

| Wt. % | 1 | 2 | 3 | 4 | 5 |
|---|---|---|---|---|---|
| $SiO_2$ | 31.12 | 31.01 | 30.81 | 30.93 | 31.43 |
| $TiO_2$ | 10.39 | 8.98 | 9.47 | 9.49 | 9.02 |
| $Al_2O_3$ | 0.58 | 0.90 | 0.80 | 0.64 | 0.80 |
| FeO | 3.09 | 3.33 | 2.05 | 1.96 | 2.62 |
| $Fe_2O_3$ | 23.10 | 23.00 | 24.37 | 24.01 | 23.97 |
| $V_2O_3$ | 0.50 | 0.44 | 0.52 | n.d | 0.60 |
| MnO | 0.49 | 0.24 | 0.31 | 0.37 | 0.39 |
| MgO | 0.38 | 0.56 | 0.48 | 0.47 | 0.29 |
| CaO | 31.92 | 31.35 | 31.98 | 31.64 | 31.82 |
| $Na_2O$ | 0.30 | 0.09 | 0.25 | 0.39 | 0.30 |
| Total | 101.87 | 99.90 | 101.04 | 99.90 | 101.24 |
| Formulae calculated on the basis of 8 cations | | | | | |
| Si | 2.600 | 2.637 | 2.592 | 2.627 | 2.638 |
| $Fe^{3+}$ | 0.400 | 0.363 | 0.408 | 0.373 | 0.362 |
| Σ | *3.000* | *3.000* | *3.000* | *3.000* | *3.000* |
| Ti | 0.653 | 0.575 | 0.599 | 0.606 | 0.570 |
| Al | 0.057 | 0.090 | 0.079 | 0.064 | 0.079 |
| $Fe^{3+}$ | 1.052 | 1.109 | 1.135 | 1.161 | 1.152 |
| $Fe^{2+}$ | 0.205 | 0.196 | 0.145 | 0.139 | 0.159 |
| $V^{3+}$ | 0.033 | 0.030 | 0.035 | - | 0.040 |
| Mg | - | - | 0.007 | 0.030 | - |
| Σ*B* | *2.000* | *2.000* | *2.000* | *2.000* | *2.000* |
| Ca | 2.857 | 2.856 | 2.883 | 2.879 | 2.862 |
| Na | 0.049 | 0.015 | 0.041 | 0.064 | 0.049 |
| Mn | 0.035 | 0.017 | 0.022 | 0.027 | 0.028 |
| Mg | 0.047 | 0.071 | 0.054 | 0.030 | 0.036 |
| $Fe^{2+}$ | 0.012 | 0.041 | - | - | 0.025 |
| Σ*A* | *3.000* | *3.000* | *3.000* | *3.000* | *3.000* |

n.d = not detected.

145

mixture of Fe-Ti oxides and hydroxides, relict garnet, muscovite and barite (Fig. 4.2.5). Compositionally, the garnet corresponds to titanian andradite with the general formula $(Ca_{2.87}Mg_{0.05}Na_{0.04}Mn_{0.02}Fe^{2+}_{0.02})_{\Sigma 3.00}(Fe^{3+}_{1.12}Ti_{0.61}Fe^{2+}_{0.17}Al_{0.07}V^{3+}_{0.03})_{\Sigma 2.00}(Si_{2.62}Fe^{3+}_{0.38})_{\Sigma 3.00}O_{12}$ (Table 4.3.1.8).

*Barytolamprophyllite* [ideally, $(Na,Ca)_2(Ba,Ca,Sr)_2(Ti,Fe)_3(SiO_4)_4(O,OH)_2$] and *lamprophyllite* [ideally, $(Na,Ca)_2(Sr,Ba,Ca)_2(Ti,Fe)_3(SiO_4)_4(OH,F)_2$] are among the major rock-forming minerals in the lamprophyllite- and barytolamprophyllite-bearing syenite. They occur as slightly pleochroic (from brownish yellow to greenish yellow) laths up to 2 cm in length commonly intergrown with clinopyroxene and wadeite (Fig.4.2.10). In some cases (*e.g.* Mu-184/11), tausonite and clinopyroxene are developed along fractures in the lamprophyllite (Fig. 4.2.11). Barytolamprophyllite is also found as an accessory phase in the eudialyte-bearing syenite, where it occurs as subhedral elongate crystals up to 0.5 mm in length developed interstitially with respect to nepheline, or overgrowths on eudialyte crystals. In some samples of the "potassium-batisite" syenite (*e.g.* Mu-237), fine-grained aggregates of barytolamprophyllite in association with rutile (?) are developed as cavity fillings in the clinopyroxene matrix. In the pseudoleucite syenite (*e.g.* Mu-216), barytolamprophyllite and lamprophyllite occur as radial aggregates of elongate crystals (up to 70 μm in diameter) commonly mantled by calcite (Fig. 4.3.1.11a,b). In these aggregates, the core is composed essentially of lamprophyllite, whereas the rim consists of barytolamprophyllite. In the pseudoleucite syenite, barytolamprophyllite also forms re-equilibration rims on titanite (Fig. 4.3.1.12).

Chemical data on barytolamprophyllite and lamprophyllite from the rocks examined are given in Table 4.3.1.9 and Fig. 4.3.1.13. Also shown on Fig. 4.3.1.13 are the compositions of lamprophyllite-group minerals from peralkaline rocks world-wide (after Chakhmouradian & Mitchell 1999).

146
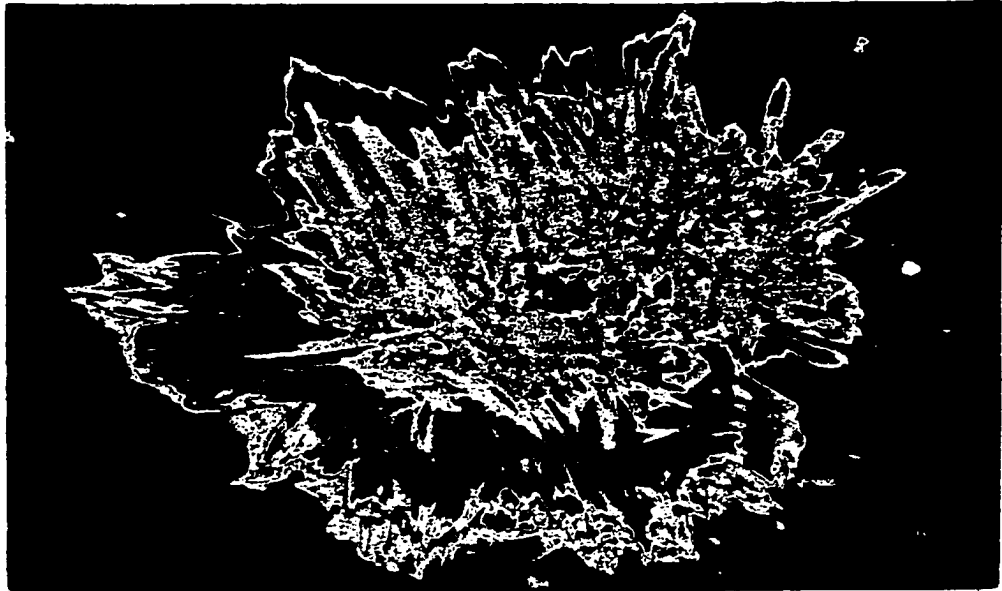
a
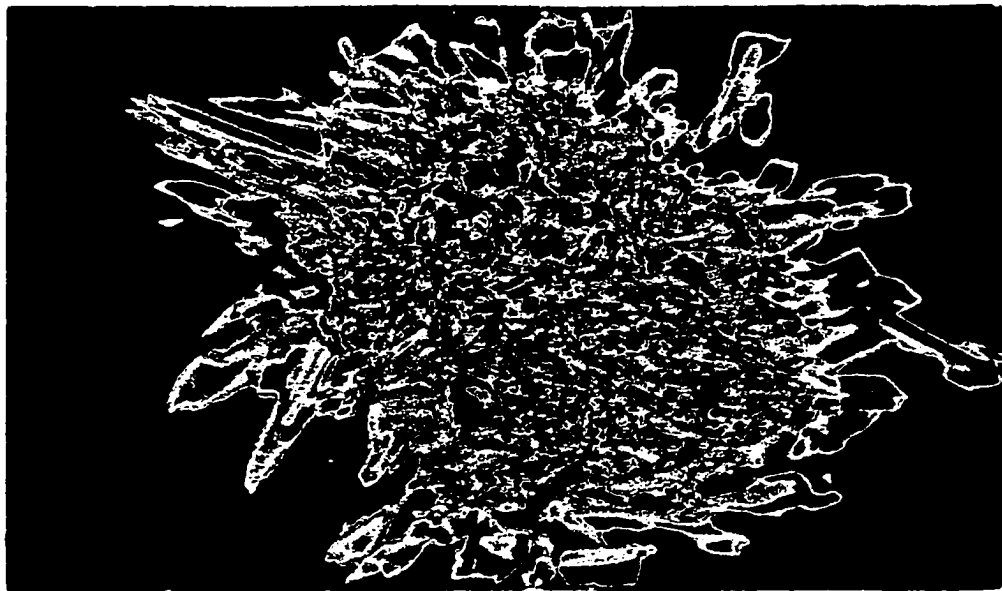


b

Fig. 4.3.1.11. Radial aggregates of lamprophyllite (green) and barytolamprophyllite (red) crystals. In (a), note a calcite rim on barytolamprophyllite (light blue). Pseudoleucite syenite, Mu-216. FOV. 80 μm. False colour BSE image.

147

Fig. 4.3.1.12. Re-equilibration rim of lamprophyllite (white) on titanite (grey). Pseudoleucite syenite, Mu-216. BSE image.

In the barytolamprophyllite-bearing syenite (*e.g.* Mu-236), most compositions correspond to barytolamprophyllite with *ca.* 15.8 wt.% BaO and 5.8 wt.% SrO. In the lamprophyllite-bearing type (*e.g.* Mu-184/11), the majority of crystals contain *ca.* 16.9 wt.% SrO and 2.0 wt.% BaO (Table 4.3.1.9, Fig. 4.3.1.13). The sum of Ca and alkalies (*apfu*) is slightly higher in the lamprophyllite (*ca.* 13.6 wt.%) than in the baryolamprophyllite (*ca.* 12.7 wt.%). Most lamprophyllite from the eudialyte-bearing syenite is enriched in Sr (19.0-20.9 wt.% SrO), depleted in Ba (0.9-1.9 wt.% BaO), and has the lowest $\Sigma$(Na+K+Ca) content among the rocks studied (Table 4.3.1.9, Fig. 4.3.1.13). In the "potassium-batisite" syenite, all compositions fall within the barytolamprophyllite field with 12.8-15.8 wt.% BaO and 5.0-7.9 wt.% SrO. The $\Sigma$(Na+K+Ca) content is slightly higher than that of the mineral from the barytolamprophyllite-bearing syenite, *i.e.* *ca.* 13.2 wt.% (Table 4.3.1.9, Fig. 4.3.1.13). Lamprophyllite from the cores of the radial aggregates from the pseudoleucite syenite is

148

Table 4.3.1.9. Representative compositions of lamprophyllite-group minerals.

| Wt.% | 1 | 2 | 3 | 4 | 5 | 6 | 7 | 8 | 9 | 10 | 11 | 12 | 13 | 14 | 15 |
|---|---|---|---|---|---|---|---|---|---|---|---|---|---|---|---|
| $SiO_2$ | 31.67 | 31.57 | 31.58 | 30.90 | 31.26 | 30.95 | 30.83 | 33.20 | 29.03 | 27.84 | 28.14 | 28.38 | 29.31 | 30.67 | 29.31 |
| $TiO_2$ | 28.19 | 27.55 | 27.87 | 28.03 | 28.69 | 28.43 | 28.36 | 24.16 | 22.33 | 24.85 | 25.28 | 26.81 | 25.63 | 25.87 | 24.71 |
| $ZrO_2$ | 0.37 | n.d | 0.54 | n.d | n.d | 0.63 | 0.74 | n.d | n.d | 0.50 | 0.28 | n.d | n.d | n.d | n.d |
| $Al_2O_3$ | n.d | n.d | 0.04 | n.d | n.d | n.d | n.d | 0.70 | 0.69 | 0.09 | 0.09 | 0.17 | n.d | n.d | n.d |
| $Fe_2O_3$* | 3.01 | 3.57 | 3.58 | 3.44 | 2.83 | 2.53 | 3.04 | 6.31 | 7.55 | 2.96 | 4.77 | 5.12 | 4.37 | 4.53 | 4.65 |
| MnO | 2.28 | 2.17 | 2.03 | 2.83 | 2.76 | 2.40 | 2.21 | 3.01 | 2.98 | 0.09 | 1.95 | 2.62 | 2.51 | 3.93 | 4.05 |
| MgO | 0.69 | 0.53 | 0.50 | 0.29 | 0.32 | 0.30 | 0.31 | 0.53 | 0.36 | 0.28 | 0.43 | 0.17 | 0.47 | 0.77 | 0.68 |
| CaO | 1.14 | 1.17 | 1.19 | 1.16 | 1.02 | 0.84 | 1.12 | 1.20 | 0.79 | 1.89 | 1.18 | 1.33 | 1.00 | 0.84 | 1.00 |
| SrO | 16.82 | 17.34 | 16.69 | 19.03 | 19.31 | 20.85 | 19.88 | 11.63 | n.d | 0.40 | 6.13 | 7.05 | 5.45 | 7.85 | 4.97 |
| BaO | 2.05 | 1.60 | 2.88 | 0.92 | 1.37 | 1.86 | 1.131 | 5.24 | 23.83 | 27.83 | 16.03 | 13.67 | 18.13 | 12.79 | 15.78 |
| $K_2O$ | 2.20 | 2.06 | 2.08 | 1.31 | 1.34 | 0.85 | 1.12 | 3.00 | 3.69 | 2.13 | 2.73 | 2.64 | 2.93 | 3.79 | 3.90 |
| $Na_2O$ | 10.40 | 10.37 | 10.31 | 10.12 | 10.18 | 10.37 | 10.39 | 11.08 | 7.25 | 9.47 | 8.48 | 8.92 | 8.96 | 8.63 | 8.31 |
| Total | 98.82 | 97.93 | 99.29 | 98.03 | 99.08 | 100.01 | 99.26 | 100.06 | 98.50 | 98.43** | 95.49 | 96.88 | 98.76 | 99.67 | 97.36 |
| Structural formulae calculated on the basis of 4 atoms of Si. | | | | | | | | | | | | | | | |
| Si | 4.000 | 4.000 | 4.000 | 4.000 | 4.000 | 4.000 | 4.000 | 4.000 | 4.000 | 4.000 | 4.000 | 4.000 | 4.000 | 4.000 | 4.000 |
| Ti | 2.678 | 2.694 | 2.712 | 2.729 | 2.761 | 2.791 | 2.781 | 2.189 | 2.314 | 2.685 | 2.703 | 2.842 | 2.631 | 2.537 | 2.536 |
| Zr | 0.023 | - | 0.034 | - | - | 0.040 | 0.047 | - | - | 0.035 | 0.019 | - | - | - | - |
| Al | - | - | 0.096 | - | - | - | - | 0.099 | 0.112 | 0.015 | 0.015 | 0.028 | - | - | - |
| $Fe^{3+}$ | 0.286 | 0.349 | 0.349 | 0.335 | 0.273 | 0.249 | 0.298 | 0.572 | 0.783 | 0.320 | 0.510 | 0.543 | 0.449 | 0.445 | 0.478 |
| Mn | 0.244 | 0.239 | 0.223 | 0.310 | 0.299 | 0.265 | 0.244 | 0.307 | 0.348 | 0.011 | 0.235 | 0.313 | 0.290 | 0.434 | 0.468 |
| Mg | 0.130 | 0.103 | 0.096 | 0.056 | 0.061 | 0.058 | 0.060 | 0.095 | 0.074 | 0.060 | 0.091 | 0.036 | 0.096 | 0.150 | 0.138 |
| Ca | 0.154 | 0.163 | 0.165 | 0.216 | 0.140 | 0.117 | 0.175 | 0.155 | 0.117 | 0.291 | 0.180 | 0.201 | 0.146 | 0.117 | 0.146 |
| Sr | 1.232 | 1.308 | 1.252 | 1.429 | 1.433 | 1.578 | 1.503 | 0.813 | - | 0.033 | 0.505 | 0.576 | 0.431 | 0.594 | 0.393 |
| Ba | 0.101 | 0.082 | 0.146 | 0.047 | 0.069 | 0.095 | 0.058 | 0.247 | 1.287 | 1.567 | 0.893 | 0.755 | 0.970 | 0.654 | 0.844 |
| K | 0.354 | 0.342 | 0.343 | 0.216 | 0.219 | 0.142 | 0.186 | 0.461 | 0.649 | 0.390 | 0.495 | 0.475 | 0.510 | 0.631 | 0.679 |
| Na | 2.547 | 2.615 | 2.587 | 2.540 | 2.526 | 2.625 | 2.627 | 2.588 | 1.937 | 2.638 | 2.337 | 2.438 | 2.371 | 2.182 | 2.199 |

n.d = not detected; * Total Fe given as $Fe_2O_3$; ** Total also includes 0.10 wt.% $Nb_2O_5$ (0.006 apfu Nb). Analyses 1-8: *lamprophyllite* (1-3 – *lamprophyllite-bearing syenite*: Mu-184/11; 4-5 – *eudialyte-bearing syenite*: 4-5 – Mu-245, 6-7 – Mu-196; 8 – *pseudoleucite syenite*: Mu-216, core of a radial aggregate); 9-15: *barytolamprophyllite* (9-10 – *pseudoleucite syenite*: Mu-216, 9 – rim of a radial aggregate, 10 – intergrowth with clinopyroxene; 11-13 – *barytolamprophyllite-bearing syenite*: Mu-236; 14-15 – *"potassium batisite" syenite*: Mu-237).

149

Fig. 4.3.1.13. Compositions of lamprophyllite and barytolamprophyllite from Murun and other occurrences.

enriched in Ba relative to the other rock types, and contains *ca.* 5.2 wt.% BaO and *ca.* 10.3 wt.% SrO (Table 4.3.1.9, Fig. 4.3.1.13). Barytolamprophyllite from the outermost parts of these aggregates is Sr-poor, with *ca.* 22.9 wt.% BaO and only 0.2 wt.% SrO. The overall evolutionary trend shown on Fig. 4.3.1.14 is almost parallel to the re-equilibration trend determined for the zoned crystals from Pegmatite Peak (Chakhmouradian & Mitchell 1999). However, the $\Sigma$(Na+K+Ca) content is noticeably higher in the compositions from the pseudoleucite syenite (*ca.* 13.5 wt.%), than in those from Pegmatite Peak (*ca.* 11.9 wt.%). The re-equilibration rims on titanite from the pseudoleucite syenite correspond to barytolamprophyllite with less than 0.3 wt.% SrO and, in terms of Ba-Sr-$\Sigma$(Na+K+Ca) proprtions, fall close to the barytolamprophyllite from the radial aggregates (Fig. 4.3.1.13). In lamprophyllite and barytolamprophyllite from the rocks studied, MnO content is typically about 2.3 wt.%, but in some cases, reaches 3.3 wt.% (outermost parts of the radial aggregates from the pseudoleucite syenite). Some of the compositions exhibit noticeable enrichment in $ZrO_2$ content (up to 0.5 wt.% in barytolamprophyllite from the pseudoleucite syenite, and up to 0.7 wt.% in lamprophyllite from the eudialyte-bearing syenite). The $Al_2O_3$ contents in both minerals are typically low, not exceeding 0.2 wt.%.

In the examined samples, "*potassium batisite*" occurs exclusively in the "potassium-batisite" syenite. In samples Mu-237 and 186/6, the mineral forms greyish elongate (up to 3 mm in length and 0.3 mm in thickness) or oval crystals, as well as their parallel intergrowths (Fig. 4.2.9). "Potassium batisite" from sample Mu-171 forms coarse prismatic grains up to 1.2 cm in length. The mineral is commonly associated with titanite (Fig. 4.3.1.14), and typically replaced along the rim and fractures by a $TiO_2$ phase, an unidentified Ti-Pb silicate, hollandite-type minerals and thorianite.

Fig. 4.3.1.14. "Potassium batisite" (white) in association with titanite (light grey), clinopyroxene (grey), hollandite-type mineral (indicated by an arrow) and potassium feldspar (dark grey). Mu-237, BSE image.

Compositionally, the "potassium batisite" from Murun corresponds to neither shcherbakovite nor batisite *sensu stricto*. In batisite $[Na(Na,K)(Ba,K)Ti_2(Si_4O_{12})O_2]$, Na fully occupies one structural site, and prevails over K in the other, so that $Na_\Sigma > K_\Sigma$ (Nikitin & Belov 1962, Schmahl & Tillmanns 1987). In shcherbakovite $[Na(K,Na)(K,Ba)Ti_2(Si_4O_{12})O_2]$, K predominates over Na in one of the alkali-cation sites and prevails over Ba in the third site, *i.e.* $K_\Sigma > Na_\Sigma$ and $K_\Sigma > Ba_\Sigma$ (Kostyleva-Labuntsova *et al.* 1978). In common with shcherbakovite, the mineral studied in this work clearly shows the preponderance of K in one of the alkali-cation sites, but contains more Ba than K in the third site (Table 4.3.1.10). A mineral with similar composition was previously described from the Walgidee Hills lamproites (Australia) under the name "noonkanbahite" (Prider 1965). Unfortunately, this name was subsequently discredited without a proper consideration of cation ordering. Lazebnik & Lazebnik (1986) and Konev *et al.* (1996) refer to the Murun material as "K-batisite", but this name has not been approved by IMA as a valid term. The mineral studied in this work contains *ca.* 3.9 wt.%

152

Table 4.3.1.10. Representative compositions of "potassium batisite".

| Wt.% | 1 | 2 | 3 | 4 | 5 | 6 | 7 | 8 | 9 |
|---|---|---|---|---|---|---|---|---|---|
| $Nb_2O_5$ | n.d | n.d | n.d | n.d | n.d | 0.25 | n.d | n.d | n.d |
| $SiO_2$ | 38.25 | 38.97 | 38.90 | 38.33 | 38.28 | 38.96 | 38.83 | 39.08 | 38.59 |
| $TiO_2$ | 21.30 | 22.34 | 22.22 | 20.29 | 19.67 | 20.12 | 19.43 | 18.84 | 18.35 |
| $ZrO_2$ | 1.77 | 2.18 | 1.69 | 0.58 | 2.76 | 0.82 | 1.09 | 0.60 | 0.84 |
| $Fe_2O_3$ | 4.07 | 3.64 | 4.00 | 4.22 | 3.41 | 3.95 | 3.61 | 4.11 | 3.89 |
| MnO | 0.25 | n.d | n.d | n.d | n.d | n.d | 0.21 | n.d | n.d |
| MgO | n.d | n.d | n.d | n.d | 0.19 | n.d | 0.18 | 0.41 | 0.21 |
| CaO | 0.99 | 0.60 | 0.49 | 0.47 | 0.90 | 1.38 | 1.14 | 0.99 | 0.93 |
| SrO | 1.99 | 1.95 | 0.90 | n.d | 0.63 | 0.65 | 0.76 | n.d | n.d |
| BaO | 15.64 | 16.04 | 17.46 | 20.48 | 17.63 | 18.12 | 18.55 | 21.53 | 21.38 |
| $Na_2O$ | 5.30 | 4.87 | 5.59 | 5.62 | 5.02 | 5.14 | 5.24 | 5.25 | 5.34 |
| $K_2O$ | 8.78 | 8.67 | 8.27 | 7.91 | 8.60 | 8.20 | 8.21 | 7.94 | 7.81 |
| Total | 98.34 | 99.26 | 99.52 | 97.90 | 97.09 | 97.59 | 97.25 | 98.75 | 97.34 |

Formulae calculated on the basis of 9 cations

| | 1 | 2 | 3 | 4 | 5 | 6 | 7 | 8 | 9 |
|---|---|---|---|---|---|---|---|---|---|
| Nb | - | - | - | - | - | 0.013 | - | - | - |
| Si | 3.902 | 3.979 | 3.946 | 3.985 | 3.996 | 4.032 | 4.031 | 4.040 | 4.051 |
| Ti | 1.634 | 1.716 | 1.695 | 1.586 | 1.544 | 1.566 | 1.517 | 1.465 | 1.449 |
| Zr | 0.088 | 0.109 | 0.085 | 0.029 | 0.141 | 0.040 | 0.055 | 0.031 | 0.042 |
| $Fe^{3+}$ | 0.312 | 0.280 | 0.305 | 0.330 | 0.268 | 0.308 | 0.282 | 0.320 | 0.307 |
| Mn | 0.022 | - | - | - | - | - | 0.018 | - | - |
| Mg | - | - | - | - | 0.030 | - | 0.028 | 0.063 | 0.033 |
| Ca | 0.108 | 0.066 | 0.053 | 0.052 | 0.101 | 0.153 | 0.127 | 0.110 | 0.105 |
| Sr | 0.118 | 1.115 | 0.053 | - | 0.038 | 0.039 | 0.046 | - | - |
| Ba | 0.625 | 0.642 | 0.694 | 0.835 | 0.721 | 0.735 | 0.755 | 0.872 | 0.880 |
| Na | 1.048 | 0.964 | 1.099 | 1.133 | 1.016 | 1.031 | 1.055 | 1.052 | 1.087 |
| K | 1.143 | 1.129 | 1.070 | 1.049 | 1.145 | 1.083 | 1.087 | 1.047 | 1.046 |

n.d = not detected. 1-4: *Mu-186/6*, 5-7: *Mu-237*, 8-9: *Mu-171*.

153

Fe$_2$O$_3$, and is typically Nb-poor ($\leq$ 0.3 wt.% Nb$_2$O$_5$). ZrO$_2$ content varies from 0.6 to 2.8 wt.% (Table 4.3.1.10). Some of the "potassium-batisite" grains contain minor Mn ($\leq$ 0.2 wt.% MnO) and Mg ($\leq$ 0.4 wt.% MgO). SrO and CaO contents vary from below the detection limit to 2.0 wt.%, and from 0.5 to 1.4 wt.%, respectively (Table 4.3.1.10).

*Wadeite* [K$_2$ZrSi$_3$O$_9$] is relatively common in the lamprophyllite- and barytolamprophyllite-bearing syenite where it occurs as colourless subhedral-to-euhedral prismatic crystals up to 3 mm in length (Fig. 4.3.1.15). Wadeite is commonly intergrown with elongate crystals of lamprophyllite and barytolamprophyllite; rarely, it forms anhedral-to-subhedral poikilitic crystals hosting inclusions of clinopyroxene and kalsilite (Fig. 4.3.1.16). In the "potassium-batisite" syenite, wadeite is less abundant, and occurs as subhedral-to-euhedral prismatic crystals (up to 1 mm in length) in the clinopyroxene-potassium feldspar matrix. The mineral commonly associated with "potassium batisite" and hollandite-type titanates. Wadeite is also found in some samples of the eudialyte-bearing syenite (*e.g.* Mu-196), where it forms rare anhedral-to-subhedral grains (up to 100 μm across) confined to the alteration rims around eudialyte crystals (Fig. 4.3.1.10). In the aegirinite (Mu-190), wadeite is extremely rare. Here, anhedral grains of the mineral occur as a part of an alteration assemblage developed after the clinopyroxene and potassium feldspar. In the aegirinite, wadeite is closely associated with calcite, ancylite-(Ce), and an unidentified Ba-Ti silicate. Wadeite has not been found in the samples of the lamprophyre.

Compositional data for wadeite from the rocks examined are given in Table 4.3.1.11. Some of the crystals exhibit slight enrichment in FeO (up to 0.6 wt.% in the lamprophyllite- and barytolamprophyllite-bearing syenite, 0.3 wt.% in the "potassium-batisite" syenite, and 0.2 wt.% in the eudialyte-bearing synite). Na$_2$O is minor and does not exceed 0.4 wt.%. Wadeite from the "potassium-batisite" syenite, and lamprophyllite- and barytolamprophyllite-bearing syenite is unusually rich in Ti (up to 3.0, and 1.0 wt.% TiO$_2$, respectively), whereas samples from eudialyte-bearing syenite and aegirinite are Ti-poor (Table 4.3.1.11). Previously published

154
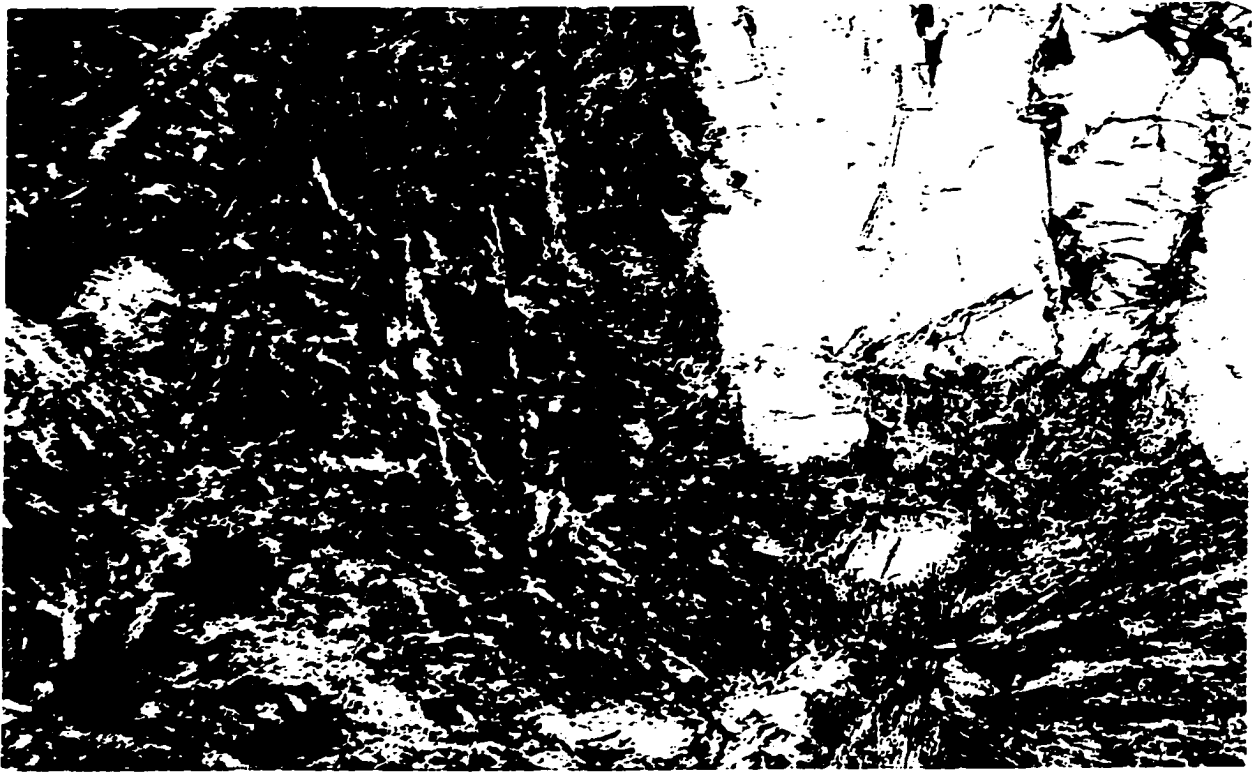
Fig. 4.3.1.15. Wadeite (colourless) and lamprophyllite (pinkish-yellow) surrounded by undulatory-fibrous aggregates of aegirine (green). Dark brown to opaque – tausonite. Lamprophyllite-bearing syenite, Mu-184/11. FOV. 3.5 mm. Plane-polarised light.
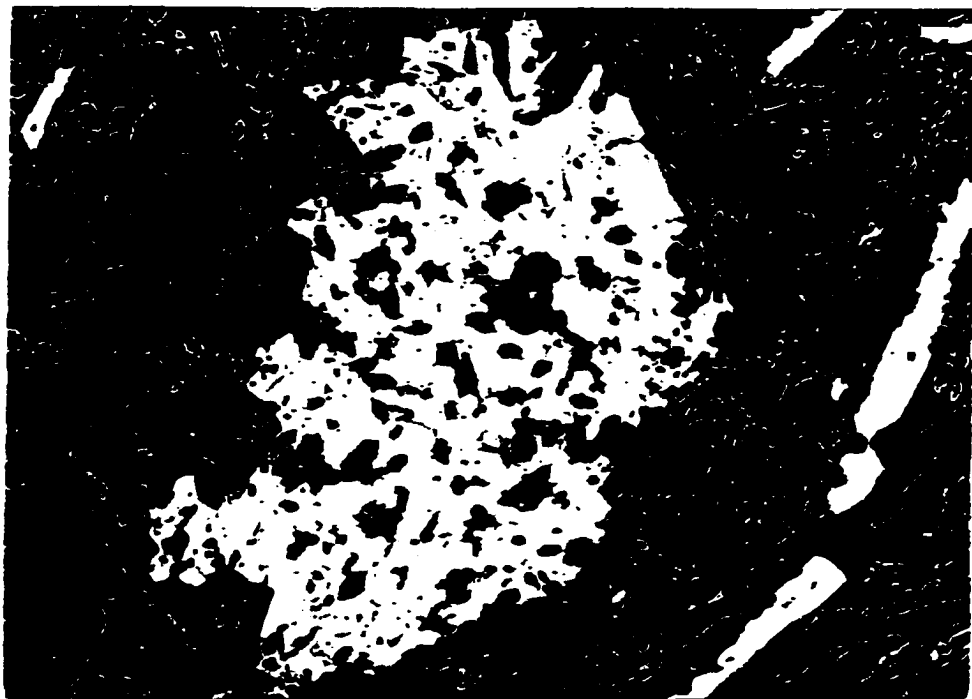


Fig. 4.3.1.16. Poikilocrystal of wadeite (light grey) with inclusions of clinopyroxene (grey). White elongate crystals – barytolamprophyllite, dark grey – potassium feldspar. Barytolamprophyllite-bearing syenite, Mu-236. BSE image.

155

Table 4.3.1.11. Representative compositions of wadeite.

| Wt.% | 1 | 2 | 3 | 4 | 5 | 6 | 7 | 8 |
|------|------|------|------|------|------|------|------|------|
| $SiO_2$ | 45.07 | 45.08 | 45.45 | 45.76 | 45.09 | 44.88 | 45.68 | 46.51 |
| $TiO_2$ | 1.00 | 0.87 | 2.05 | 2.94 | 1.14 | 2.11 | n.d | n.d |
| $ZrO_2$ | 31.02 | 30.06 | 28.87 | 26.82 | 30.39 | 29.15 | 32.51 | 32.19 |
| FeO | n.d | 0.59 | 0.20 | 0.34 | n.d | n.d | 0.23 | n.d |
| $Na_2O$ | n.d | 0.39 | 0.23 | 0.44 | n.d | n.d | n.d | 0.13 |
| $K_2O$ | 23.73 | 22.92 | 23.35 | 23.39 | 23.47 | 23.40 | 23.09 | 22.40 |
| Total | 100.82 | 99.91 | 100.15 | 99.69 | 100.09 | 99.54 | 101.51 | 101.22 |

Formulae calculated on the basis of 9 atoms of oxygen

| | 1 | 2 | 3 | 4 | 5 | 6 | 7 | 8 |
|------|------|------|------|------|------|------|------|------|
| Si | 2.960 | 2.977 | 2.977 | 2.990 | 2.973 | 2.964 | 2.979 | 3.015 |
| Ti | 0.049 | 0.043 | 0.101 | 0.144 | 0.057 | 0.105 | - | - |
| Zr | 0.994 | 0.968 | 0.922 | 0.855 | 0.977 | 0.939 | 1.034 | 1.018 |
| $Fe^{2+}$ | - | 0.033 | 0.011 | 0.019 | - | - | 0.013 | - |
| Na | - | 0.050 | 0.029 | 0.056 | - | - | - | 0.016 |
| K | 1.988 | 1.931 | 1.951 | 1.950 | 1.974 | 1.971 | 1.921 | 1.853 |

n.d = not detected. Analyses 1-2: *barytolamprophyllite-* and *lamprophyllite-bearing* syenite (1 – Mu-184/11, 2 – Mu-236); 3-6: *"potassium batisite" syenite* (3-4 – Mu-186/6; 5-6 – Mu-237); 7: *eudialyte-bearing syenite* (Mu-196); 8: *aegirinite* (Mu-190).

156

data show that the $TiO_2$ content in the Murun wadeite is typically below 0.6 wt.% (Mitchell & Vladykin 1993; Konev *et al.* 1996). Ti-rich wadeite (up to 2.8 wt.% $TiO_2$) was reported from the Leucite Hill lamproites, Wyoming (Charmichael 1967; Mitchell & Bergman 1991). Subsequently, an unnamed Ti-analogue of wadeite with the formula $[K_2(Ti,Zr)Si_3O_9]$ containing up to 22.4 wt.% $TiO_2$ and only 0.7 wt.% $ZrO_2$ was found in the intergrowths with wadeite-type phases of variable $TiO_2$ contents in a groundmass of lamproites from the same locality (Mitchell & Steele 1992). These authors suggested the presence of a limited solid solution between the Zr- and Ti-dominant end-members.

*Titanite* is relatively rare in the hypabyssal rocks. In the lamprophyre (*e.g.* Mu-231/13), this mineral forms euhedral wedge-shaped crystals (up to 20 μm across) or anhedral-to-subhedral grains (up to 200 μm in size) in the clinopyroxene-biotite-potassium feldspar matrix. Anhedral-to subhedral grains of titanite from the pseudoleucite syenite (Mu-216) are commonly mantled by re-equilibration rims of barytolamprophyllite (Fig. 4.3.1.13). In this rock, minute (< 20 μm across) grains of titanite also occur as inclusions in pyrite. Titanite is a characteristic accessory mineral in the "potassium-batisite" syenite (Mu-237, 186/6), where it forms elongate commonly fractured grains (up to 0.4 mm) in the potassium feldspar-clinopyroxene matrix (Fig. 4.3.1.11). The mineral is closely associated with "potassium batisite" and hollandite-type phases. In the eudialyte-bearing syenite (Mu-196), titanite occurs as extremely rare anhedral grains up to 50 μm in size.

The titanite is relatively poor in minor elements (Table 4.3.1.12). The mineral from the "potassium-batisite" syenite is Al-free, whereas titanite from the lamprophyre and pseudoleucite syenite is slightly enriched in $Al_2O_3$ (up to 0.1 and 0.3 wt.%, respectively). $Fe_2O_3$ content is *ca.* 1.4 wt.% in samples from the lamprophyre, *ca.* 2.2 wt.% in the pseudoleucite syenite, and 0.9-2.2 wt.% in titanite from the "potassium-batisite" syenite. Typically, the Murun titanite is devoid of detectable Nb, but in some cases contains up to 0.6 wt.% $Nb_2O_5$ ("potassium-batisite" syenite). The mineral from the lamprophyre and pseudoleucite synite is

157

Table 4.3.1.12. Representative compositions of titanite.

| Wt.% | 1 | 2 | 3 | 4 | 5 | 6 |
|---|---|---|---|---|---|---|
| $SiO_2$ | 30.55 | 29.85 | 30.13 | 29.98 | 29.93 | 29.99 |
| $Al_2O_3$ | 0.09 | 0.32 | n.d | n.d | n.d | n.d |
| $TiO_2$ | 38.80 | 37.85 | 37.45 | 38.91 | 36.78 | 36.71 |
| $Fe_2O_3$ | 1.38 | 2.19 | 1.46 | 0.88 | 1.48 | 2.25 |
| $ZrO_2$ | n.d | n.d | n.d | n.d | 0.52 | n.d |
| $Nb_2O_5$ | 0.13 | n.d | n.d | n.d | 0.61 | n.d |
| CaO | 28.23 | 28.35 | 27.02 | 27.47 | 26.66 | 27.15 |
| SrO | n.d | n.d | 0.66 | 1.12 | 1.12 | 1.04 |
| $Na_2O$ | 0.22 | n.d | 0.67 | 0.46 | 0.82 | 0.42 |
| $K_2O$ | 0.07 | n.d | n.d | n.d | n.d | n.d |
| Total | 99.47 | 98.56 | 97.39 | 98.82 | 97.92 | 97.56 |

Formulae calculated on the basis of $\Sigma$cations = 3

| | 1 | 2 | 3 | 4 | 5 | 6 |
|---|---|---|---|---|---|---|
| Si | 0.999 | 0.987 | 1.004 | 0.990 | 0.997 | 1.002 |
| Al | 0.003 | 0.012 | - | - | - | - |
| Ti | 0.955 | 0.941 | 0.938 | 0.966 | 0.922 | 0.922 |
| $Fe^{3+}$ | 0.034 | 0.055 | 0.037 | 0.022 | 0.037 | 0.057 |
| Zr | - | - | - | - | 0.008 | - |
| Nb | 0.002 | - | - | - | 0.009 | - |
| Ca | 0.990 | 1.005 | 0.965 | 0.972 | 0.952 | 0.972 |
| Sr | - | - | 0.013 | 0.021 | 0.022 | 0.020 |
| Na | 0.014 | - | 0.043 | 0.029 | 0.053 | 0.027 |
| K | 0.003 | - | - | - | - | - |

n.d = not detected. Analyses 1: *lamprophyre* (Mu-231/13); 2: *pseudoleucite syenite* (Mu-216) 3-6: *"potassium batisite syenite"* (3-5 — Mu-186/6; 6 — Mu-237).

158

Sr- and Na-poor, whereas titanite from the "potassium-batisite" syenite is somewhat enriched in SrO (up to 1.1 wt.%) and $Na_2O$ (up to 0.8 wt.%) contents (Table 4.3.1.12).

Unidenified silicates

*Ba-Ti Al-silicate* occurs in the aegirinite (Mu-190) as radial aggregates (up to 0.2 mm in diameter) of thin fibrous crystals. The mineral is undoubtedly part of an alteration assemblage, and is commonly associated with calcite, ancylite-(Ce), and rutile (?). Compositionally, this mineral corresponds to the general empirical formula $(K,Ba)_3Fe^{2+}AlTiSi_{5.6}O_{26}$ (Table 4.3.1.13, analyses 3 and 4; Fig. 4.3.1.17).

*Ti-Pb silicate* is found in the "potassium-batisite" syenite (Mu-186/6). The mineral forms anhedral grains less than 30 µm across developed along fractures in the "potassium batisite" (Figs. 4.3.1.18, 4.3.1.19).



Fig. 4.3.1.18. Unidentified Ti-Pb silicate (red) developed along the fracture in the "potassium batisite" (yellow). Dark blue – potassium feldspar, green – titanite, light blue – clinopyroxene. "Potassium-batisite" syenite, Mu-186/6. F.O.V. 180 µm. False colour BSE image.

159
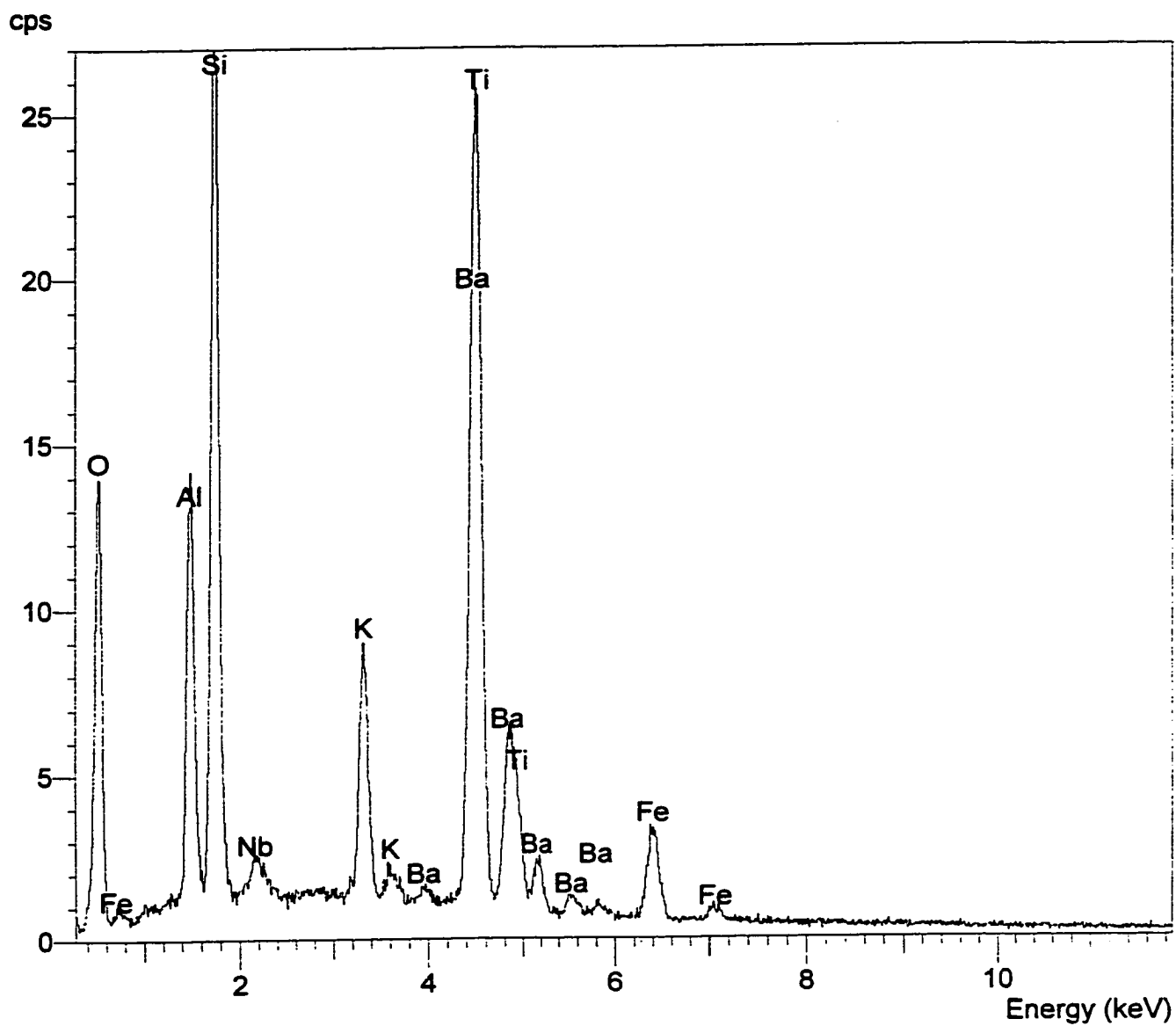
Fig. 4.3.1.17. EDS spectrum of an unidentified Ba-Ti Al-silicate
from the aegirinite (Mu-190).

160
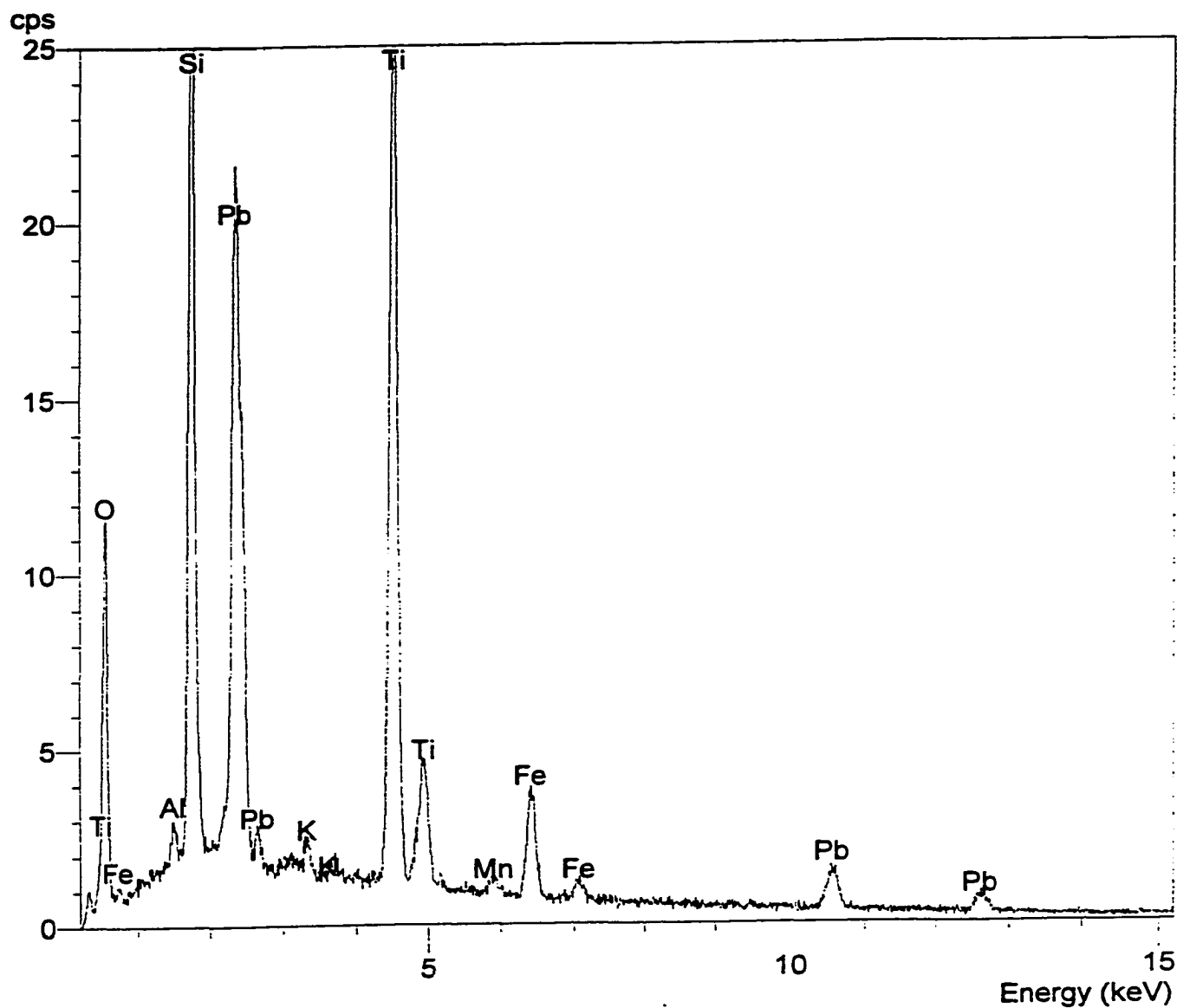
**4.3.1.19 . EDS spectrum of an unidentified Ti-Pb silicate from the "potassium batisite" syenite (Mu-186/6).**

161

Table 4.3.1.13. Representative compositions of unidentified silicates.

| Wt. % | 1 | 2 | 3 | 4 | 5 | 6 |
|---|---|---|---|---|---|---|
| $Nb_2O_5$ | n.d | n.d | 1.75 | 1.65 | n.d | n.d |
| $SiO_2$ | 22.12 | 21.22 | 26.96 | 28.03 | 43.52 | 43.07 |
| $TiO_2$ | 32.25 | 31.55 | 19.59 | 19.56 | 0.21 | n.d |
| $ZrO_2$ | n.d | n.d | n.d | 0.63 | 1.44 | 1.28 |
| $Al_2O_3$ | 0.97 | 0.99 | 12.65 | 13.33 | 1.79 | 1.47 |
| $Ce_2O_3$ | n.d | 0.78 | n.d | n.d | n.d | 0.54 |
| FeO | 4.99 | 4.97 | 5.74 | 5.55 | 7.57 | 8.43 |
| MnO | 0.64 | 0.66 | 0.32 | 0.36 | 2.30 | 1.50 |
| MgO | n.d | n.d | 0.36 | 0.27 | 0.33 | 0.25 |
| SrO | 0.65 | 0.71 | n.d | n.d | 33.27 | 32.67 |
| BaO | 2.73 | 1.43 | 22.27 | 21.99 | n.d | n.d |
| PbO | 30.42 | 29.90 | n.d | n.d | n.d | n.d |
| CaO | 0.22 | 0.39 | 0.25 | 0.22 | 3.57 | 3.28 |
| $Na_2O$ | 0.37 | 0.18 | 0.24 | 0.54 | 7.67 | 7.88 |
| $K_2O$ | 0.70 | 0.43 | 4.58 | 4.52 | 0.11 | 0.14 |
| Total | 96.06 | 93.21 | 94.71 | 96.65 | 101.78 | 100.51 |

n.d. = not detected. 1-2: *Ti-Pb silicate* ("potassium-batisite" syenite, Mu-186/6); 3-4: *Ba-Ti Al-silicate* (aegirinite, Mu-190); 5-6: *Na-Fe-Sr silicate* (eudialyte aegirine syenite, Mu-245).

162

· The mineral contains major Si, Ti and Pb, and has relatively uniform composition (Table 4.3.1.13, analyses 1-2). Some crystals also contain significant amounts of FeO (up to 5.0 wt.%) and BaO (up to 3.0 wt.%). Other elements present in minor quantities include K, Na, Al, Sr, Mn, Ca, and in some cases Ce (Table 4.3.1.13). The general empirical formula of this mineral can be written as $(Pb,Ba)(Ti,Fe^{3+})_3(Si,Al,Fe^{3+})_3(O,OH)_{13}$.

*Na-Fe-Sr silicate* is found in the eudialyte-aegirine syenite (*e.g.* Mu-245), where it occurs as subhedral rectangular crystals (up to 80 µm across) developed interstitially with respect to nepheline, and commonly associated with strontianite. Representative compositions of this mineral are given in Table 4.3.1.13 (analyses 5-6). The empirical formula of the mineral is $(Na,K)_2(Sr,Ca)_3(Fe^{3+},Mn)(Si,Al,Fe^{3+})_6O_{17}$.

### 4.3.2 Oxides

*Magnetite* is found in some of the samples of the lamprophyre (*e.g.* Mu-3/100, -232), kalsilite melasyenite (*e.g.* Mu-172), and aegirinite (Mu-190). The mineral typically forms anhedral-to-subhedral elongate or rounded grains up to 80 µm across developed inerstitially or along fractures in olivine (lamprophyre) or clinopyroxene (aegirinite). In the kalsilite melasyenite, magnetite also occurs as rare minute (< 20 µm in size) grains in the kalsilite-potassium feldspar aggregates. In the lamprophyre, magnetite also forms intergrowths with rutile (?). Representative compositions of the mineral are given in Table 4.3.2.1. Magnetite from the aegirinite is enriched in $Cr_2O_3$ (up to 14.8 wt.%) and depleted in $TiO_2$ ($\leq$ 0.7 wt.%) relative to the crystals from the lamprophyre (*ca.* 4.5 and 7.8 wt.%, respectively), and kalsilite melasyenite (*ca.* 2.1 and 1.8 wt.%, respectively). Samples from the lamprophyre and kalsilite melasyenite typically contains minor MnO ($\leq$ 0.5 wt.%) and MgO ($\leq$ 0.9 wt.%).

163

Table 4.3.2.1. Representative compositions of magnetite and chromite.

| Wt.% | 1 | 2 | 3 | 4 | 5 | 6 |
|---|---|---|---|---|---|---|
| $SiO_2$ | n.d | 0.30 | 0.34 | 0.90 | n.d | n.d |
| $Al_2O_3$ | 0.16 | n.d | n.d | n.d | 0.11 | 0.25 |
| $TiO_2$ | 1.82 | 4.49 | 4.16 | 0.65 | 1.59 | 1.64 |
| $Fe_2O_3$* | 62.63 | 59.93 | 53.34 | 50.36 | 32.64 | 31.38 |
| FeO* | 30.57 | 35.76 | 33.71 | 32.98 | 30.59 | 30.09 |
| $Cr_2O_3$ | 2.05 | n.d | 7.80 | 14.81 | 32.50 | 34.45 |
| MnO | 0.41 | n.d | 0.59 | n.d | 0.95 | 1.34 |
| MgO | 0.87 | n.d | 0.94 | n.d | 1.30 | 1.58 |
| Total* | 98.51 | 100.18 | 100.53 | 98.70 | 96.78 | 97.90 |

Formulae calculated on the basis of 4 atoms of oxygen

| | | | | | | |
|---|---|---|---|---|---|---|
| Si | - | 0.011 | 0.013 | 0.034 | - | - |
| Al | 0.007 | - | - | - | 0.005 | 0.011 |
| Ti | 0.053 | 0.129 | 0.118 | 0.019 | 0.045 | 0.045 |
| $Fe^{3+}$ | 1.824 | 1.720 | 1.508 | 1.447 | 0.918 | 0.871 |
| $Fe^{2+}$ | 0.989 | 1.140 | 1.059 | 1.053 | 0.956 | 0.928 |
| Cr | 0.063 | - | 0.232 | 0.447 | 0.960 | 1.004 |
| Mn | 0.013 | - | 0.019 | - | 0.030 | 0.042 |
| Mg | 0.050 | - | 0.053 | - | 0.070 | 0.087 |

n.d = not detected; * $Fe^{2+}/Fe^{3+}$ ratio calculated from stoichiometry. Analyses 1-4: *magnetite* (1: kalsilite melasyenite, *Mu-172*; 2-3: lamprophyre, 2 – Mu-232; 3 – Mu-3/100; 4: aegirinite, Mu-190); 5-6: *chromite* (5 – core, 6 – rim of a zoned crystal; Mu-172).

164

*Chromite* is found exclusively in the kalsilite melasyenite (Mu-172). The mineral occurs as rare minute ($\leq 20$ $\mu$m in size) inclusions in clinopyroxene. The inclusions commonly exhibit a weak variation in $Cr_2O_3$, MnO and MgO (Table 4.3.2.1).

*Ilmenite* is rare in the rocks examined. The mineral occurs as anhedral grains (up to 120 $\mu$m in size) developed interstitially in the biotite-clinopyroxene-potassium feldspar groundmass in the lamprophyre (*e.g.* Mu-241) and pseudoleucite italite (*e.g.* Mu-235). Ilmenite from both rock types has elevated MnO contents (up to 5.6 wt.% or 0.12 *apfu* Mn in the lamprophyre, and 6.5 wt.% or 0.14 *apfu* Mn in the psedoleucite syenite; Table 4.3.2.2).

*Rutile(?)* is found in the majority of the rocks examined (except the pseudoleucite italite, kalsilite melasyenite, and eudialyte-bearing syenite). The mineral occurs as anhedral-to-subhedral grains up to 100 $\mu$m in size commonly associated with titanite and sulphides. Rutile has nearly ideal composition; only in a few cases (*e.g.* aegirinite, Mu-190) does it exhibit noticeable enrichment in $Fe_2O_3$ (up to 2.1 wt.%) and $Nb_2O_5$ (up to 1.6 wt.%; Table 4.3.2.2).

*Hollandite-type K-Ba-Fe titanates* are relatively common in the "potassium-batisite" syenite (Mu-237 and 186/6). These minerals form rare anhedral-to-subhedral grains (up to 50 $\mu$m in size), and are confined to cavities and fractures in the "potassium batisite" and titanite (Fig. 4.3.2.1). The titanates are commonly associated with rutile (?), an unidentified Pb-Ti silicate, and wadeite. The latter mineral, in some cases, forms a rim on crystals of titanates.

The hollandite-type minerals from Murun have been previously described by Lazebnik *et al.* (1985), Mitchell &Vladykin (1993), and Chakhmouradian & Evdokimov (1997). These studies demonstrate that the Murun hollandites (*sensu lato*) are essentially members of the pseudobinary system $K_{2-x}(Ti,Fe)_8O_{16}$ - $Ba_{2-x}(Ti,Fe)_8O_{16}$. Both K- and Ba-dominant minerals contain only negligible amounts of other *B*-site cations such as Mn or Cr.

Table 4.3.2.2. Representative compositions of ilmenite and rutile (?).

| Wt.% | 1* | 2** | 3* | 4 | 5 | 6 |
|------|-----|------|------|------|------|------|
| $SiO_2$ | n.d | 0.29 | 0.27 | 0.93 | n.d | 0.41 |
| $TiO_2$ | 58.83 | 51.93 | 52.12 | 95.78 | 97.92 | 97.00 |
| $Fe_2O_3$ | n.d | 0.16 | n.d | 0.99 | 2.07 | 1.95 |
| FeO | 40.29 | 40.79 | 40.27 | n.d | n.d | n.d |
| $Nb_2O_5$ | n.d | n.d | n.d | 0.27 | 1.39 | 1.58 |
| MnO | 5.58 | 6.18 | 6.51 | n.d | n.d | n.d |
| Total | 99.70 | 99.35 | 99.17 | 97.97 | 101.38 | 101.14 |

Formulae calculated on the basis of:

| | 3 atoms of oxygen | | | 2 atoms of oxygen | | |
|------|------|------|------|------|------|------|
| Si | - | 0.007 | 0.007 | 0.013 | - | 0.005 |
| Ti | 1.017 | 0.991 | 0.995 | 0.978 | 0.974 | 0.967 |
| $Fe^{3+}$ | - | 0.003 | - | 0.010 | 0.021 | 0.019 |
| $Fe^{2+}$ | 0.847 | 0.866 | 0.855 | - | - | - |
| Nb | - | - | - | 0.002 | 0.008 | 0.009 |
| Mn | 0.119 | 0.133 | 0.140 | - | - | - |

n.d = not detected; * All Fe given as FeO, stoichiometry suggests that no $Fe_2O_3$ is present; ** $Fe^{3+}/Fe^{2+}$ ratio calculated from stoichiometry. Analyses 1-3: *ilmenite* (1: lamprophyre, Mu-241; 2-3: pseudoleucite italite, Mu-235); 4-6: *rutile* (?) (aegirinite, Mu-190).

Compositionally, the hollandite-type phases studied in this work can be divided into two groups: Pb-free and Pb-bearing (K,Ba)-Fe titanates. In BSE, the Pb-free hollandite commonly exhibits a core-to-rim zoning with a low-$AZ$ core and a high-$AZ$ rim (Fig. 4.3.2.2). Compositionally, the core of the crystals shows the preponderance of the K-dominant (i.e. priderite) component (Norrish 1954; Sinclair & McLaughlin 1982), whereas the peripheral zone corresponds to henrymeyerite [$BaFe^{2+}Ti_7O_{16}$] (Mitchell et al. 2000) (Table 4.3.2.3). The Pb-free titanate from sample Mu-186/6 exhibits noticeable enrichment in Mn and V. MnO and $V_2O_3$ contents vary from 0.2 and 0.6 wt.% in the cores of the crystals to 0.9 and 1.0 wt.% in the peripheral zones, respectively (Table 4.3.2.3).

The Pb-bearing "hollandite" is found exclusively in sample Mu-186/6. In BSE, this mineral commonly exhibits an irregular zoning resulting from variations in the Pb/(Ba+K) ratio (Fig. 4.3.2.3). The Pb-bearing compositions show the preponderance of Ba (ca. 9.7 wt.% BaO, 0.52 apfu Ba) over K (ca. 1.4 wt.% $K_2O$, 0.25 apfu K); the PbO content varies from 6.6 to 12.5 wt.%, or from 0.24 to 0.45 apfu Pb (Table 4.3.2.3). The mineral shows the following overall compositional range: $(Ba_{0.51-0.54}Pb_{0.36-0.45}K_{0.21-0.29}Na_{0.03-0.07})(Ti_{6.22-6.30}Fe_{1.70-1.78})O_{16}$ (Table 4.3.2.3). Recalculation of the microprobe analyses of the Pb-bearing "hollandite" on the basis of 16 atoms of oxygen indicates that most of Fe present in the composition of this mineral occurs in trivalent form, thus suggesting the existence of a solid solution between the two hexatitanate end-members, $BaFe^{3+}_2Ti_6O_{16}$ and $PbFe^{3+}_2Ti_6O_{16}$.

An experimental study shows that the Ba- and Pb-dominant end-members (synthesised at $P$=1atm and $T$=1100°C from the stoichiometric quantities of $PbCO_3$, $BaCO_3$, $TiO_2$ and $Fe_2O_3$ using the ceramic technique) form a continuous solid solution series of the general formula $Pb_{1-x}Ba_xFe^{3+}_2Ti_6O_{16}$ (Reguir & Mitchell, unpublished data). Intermediate members of this series with low-to-moderate Pb contents are tetragonal in symmetry [$I4/m$, $a$ = 10.1119(4) Å, $c$ = 2.9714(2) Å], whereas those with higher Pb contents may be monoclinic.

To our knowledge, prior to the present work, Pb-bearing hollandite-type titanates had not been observed at Murun or elsewhere. However, Pb-bearing manganates, including the end-
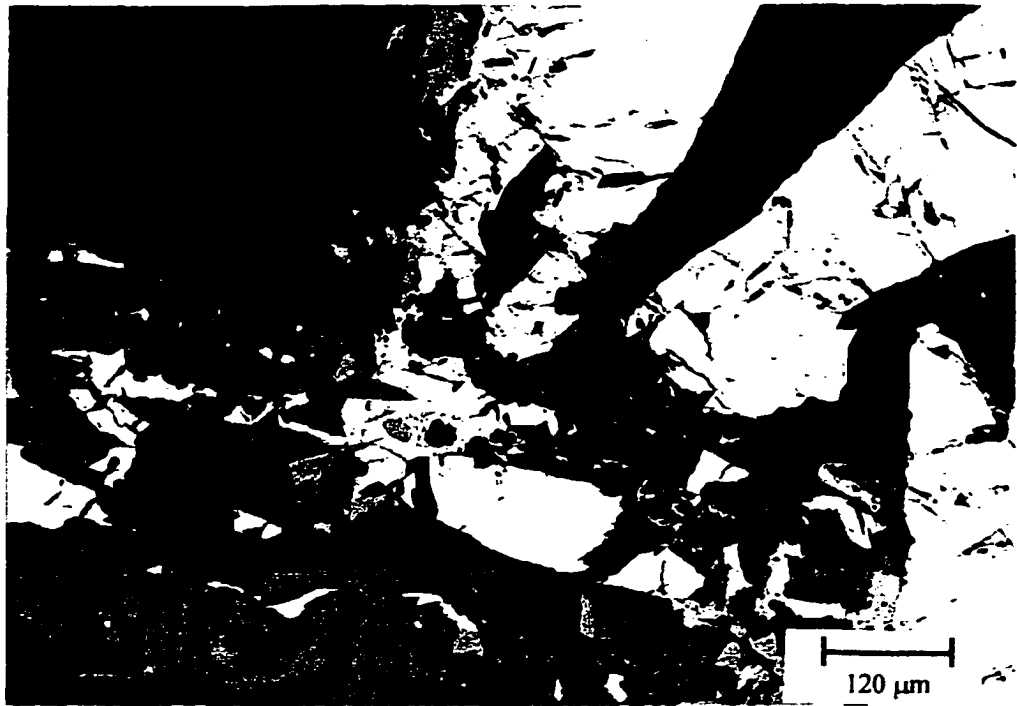
Fig. 4.3.2.1. Pb-free hollandite (indicated by an arrow) developed along fractures in "potassium batisite" (white); associated phases are titanite (light grey) and clinopyroxene (dark grey). BSE image. "Potassium-batisite" syenite (Mu-237).
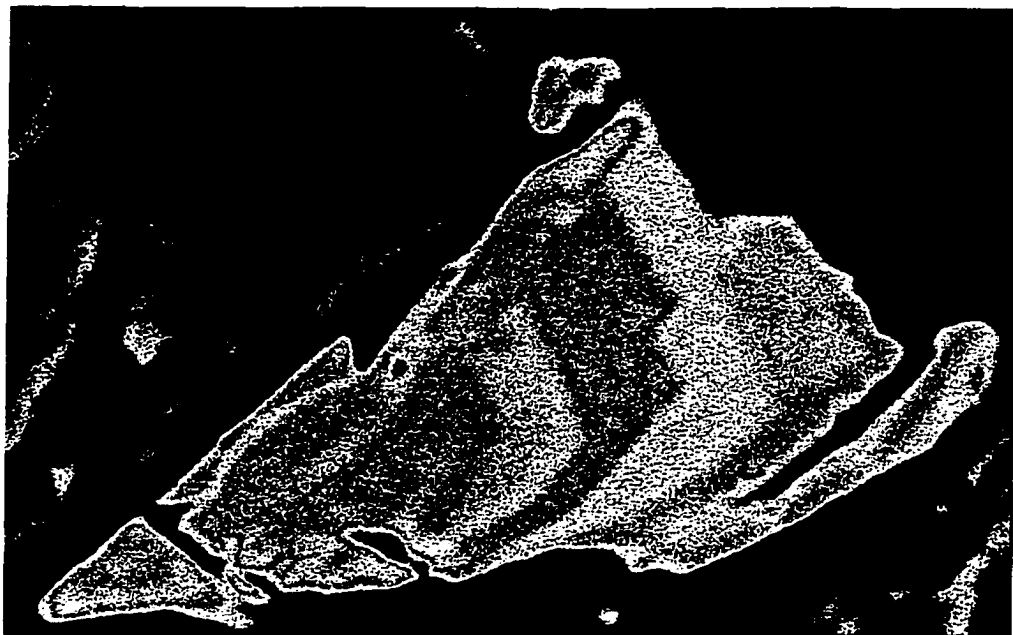


Fig. 4.3.2.2. Zoned grain of Pb-free hollandite. Blue core corresponds to priderite, yellowish-red intermediate part to barian priderite, and peripheral pink zone to henrymeyerite. Green – "potassium batisite". FOV 90 μm. False colour BSE image. "Potassium-batisite" syenite (Mu-237).

168

Table 4.3.2.3. Representative compositions of hollandite-type phases from the "potassium batisite" syenite.

| Wt. % | 1 | 2 | 3 | 4** | 5** | 6 | 7 | 8 | 9 | 10 | 11 | 12 |
|---|---|---|---|---|---|---|---|---|---|---|---|---|
| | low-AZ core | high-AZ rim | high-AZ rim | low-AZ core | intermedi-ate zone | high-AZ rim | rim | | | | | |
| $SiO_2$ | 0.61 | 0.67 | n.d | 0.43 | 0.57 | 0.41 | n.d | n.d | n.d | n.d | 0.19 | 0.49 |
| $TiO_2$ | 79.77 | 71.37 | 68.14 | 76.60 | 73.84 | 63.63 | 60.40 | 60.87 | 60.41 | 61.88 | 60.71 | 61.77 |
| $V_2O_3$ | n.d | n.d | n.d | 0.55 | 0.62 | 1.04 | n.d | n.d | n.d | n.d | n.d | n.d |
| $Fe_2O_3$ | 3.38 | 8.97 | 1.38 | - | - | 6.72 | 13.99 | 13.60 | 13.87 | 12.07 | 15.37 | 16.12 |
| $FeO$ | 4.59 | 2.57 | 8.51 | 7.39 | 7.74 | 5.40 | 2.90 | 3.43 | 3.38 | 4.17 | 1.57 | 0.86 |
| $PbO$ | n.d | n.d | n.d | n.d | n.d | n.d | 9.73 | 11.55 | 12.28 | 12.45 | 8.59 | 6.63 |
| $MnO$ | n.d | n.d | n.d | 0.16 | 0.54 | 0.88 | n.d | n.d | n.d | n.d | n.d | n.d |
| $BaO$ | n.d | 9.72 | 15.77 | 8.32 | 12.33 | 19.67 | 10.02 | 9.48 | 9.75 | 9.52 | 9.49 | 10.01 |
| $Na_2O$ | n.d | 0.30 | 0.61 | n.d | 0.20 | 0.29 | 0.10 | 0.27 | n.d | 0.18 | 0.21 | 0.27 |
| $K_2O$ | 8.01 | 2.23 | 1.35 | 5.76 | 3.90 | 0.34 | 1.64 | 1.41 | 1.44 | 1.21 | 1.35 | 1.27 |
| Total | 96.36 | 95.83 | 95.76 | 99.21 | 99.74 | 98.38 | 98.78 | 100.61 | 101.13 | 101.48 | 97.48 | 97.42 |
| Formulae calculated on the basis of 16 atoms of oxygen | | | | | | | | | | | | |
| Si | 0.063 | 0.074 | - | 0.046 | 0.062 | 0.048 | - | - | - | - | 0.023 | 0.057 |
| Ti | 7.174 | 6.799 | 6.902 | 7.097 | 6.983 | 6.450 | 6.225 | 6.220 | 6.192 | 6.299 | 6.222 | 6.222 |
| $V^{3+}$ | - | - | - | 0.054 | 0.063 | 0.112 | - | - | - | - | - | - |
| $Fe^{3+}$ | 0.304 | 0.855 | 0.140 | - | - | 0.682 | 1.443 | 1.390 | 1.422 | 1.229 | 1.576 | 1.625 |
| $Fe^{2+}$ | 0.459 | 0.272 | 0.958 | 0.761 | 0.814 | 0.608 | 0.332 | 0.390 | 0.386 | 0.472 | 0.179 | 0.096 |
| Mn | - | - | - | 0.017 | 0.058 | 0.100 | - | - | - | - | - | - |
| $\Sigma B$ | 8.000 | 8.000 | 8.000 | 7.975 | 7.980 | 8.000 | 8.000 | 8.000 | 8.000 | 8.000 | 8.000 | 8.000 |
| Pb | - | - | - | - | - | - | 0.359 | 0.422 | 0.451 | 0.454 | 0.315 | 0.239 |
| Ba | - | 0.483 | 0.833 | 0.402 | 0.608 | 1.039 | 0.538 | 0.505 | 0.521 | 0.505 | 0.507 | 0.526 |
| Na | - | 0.074 | 0.159 | - | 0.049 | 0.076 | 0.027 | 0.071 | - | 0.047 | 0.055 | 0.070 |
| K | 1.222 | 0.360 | 0.232 | 0.905 | 0.626 | 0.058 | 0.287 | 0.244 | 0.250 | 0.209 | 0.235 | 0.229 |
| $\Sigma A$ | 1.222 | 0.917 | 1.224 | 1.307 | 1.283 | 1.173 | 1.211 | 1.242 | 1.222 | 1.215 | 1.112 | 1.064 |

n.d = not detected. * $Fe^{3+}/Fe^{2+}$ ratio and analyses totals calculated on the basis of stoichiometry. ** All Fe is given as FeO, stoichiometry suggests that no $Fe_2O_3$ is present. Analyses 1-6: Pb-free hollandite-type phase (1-3 – Mu-186/6; 4-6 – Mu-237); 7-12: Pb-bearing hollandite-type phase (Mu-186/6; 7-10 – one grain, 11-12 – second grain).

169
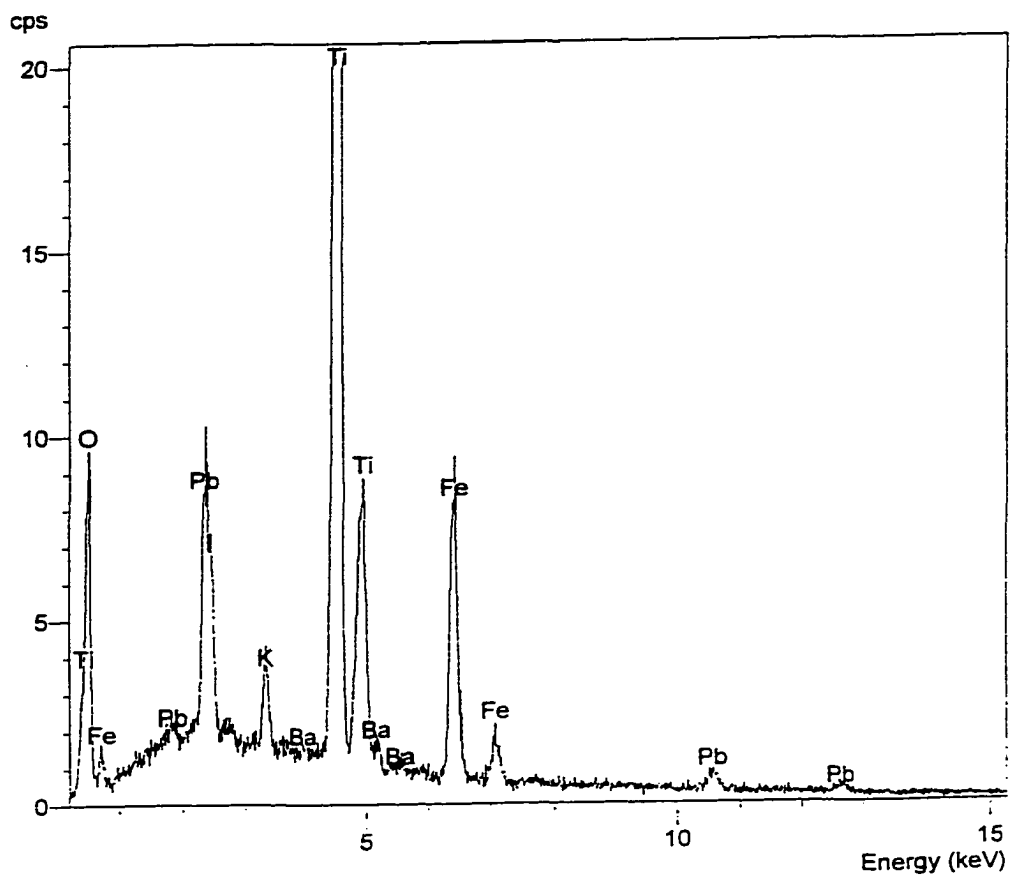
Fig. 4.3.2.3. a) EDS spectrum of the Pb-bearing hollandite.
b) Zoned crystal of Pb-bearing hollandite. Blue –
"potassium batisite". FOV 40 µm. False colour BSE image.
a) and b): "Potassium batisite" syenite (Mu-186/6).

170

member coronadite [$(Pb,Ba)(Mn,V)_8O_{16}$], are relatively common in nature (Bar-Matthews 1987; Nicholson 1986).

*Tausonite* ($SrTiO_3$) is a relatively common accessory mineral in the lamprophyllite-bearing syenite (Mu-184/11). The mineral forms subhedral-to-anhedral rectangular or equant crystals (up to 100 μm across) commonly confined to fractures in lamprophyllite or developed interstitially (Figs. 4.2.11, 4.3.1.15). In BSE, tausonite exhibits a weak irregular zoning with high-$AZ$ zones enriched in $\Sigma REE$ and depleted in Sr. The $\Sigma REE_2O_3$ and SrO contents vary from 11.4 and 36.3 wt.% in the high-$AZ$ zones (respectively) to 2.0 and 46.4 wt.% in the low-$AZ$ zones (Table 4.3.2.4). The mineral shows very little variation in terms of the CaO and $Fe_2O_3$ contents (2.4 – 3.3, and 0.3-0.4 wt.%, respectively). Tausonite from the Murun was described in detail by Vorob'ev *et al.* (1989) and Mitchell & Vladykin (1993). The latter authors reported up to 17.8 wt.% $\Sigma REE_2O_3$ (or 37.4 mol.% of the loparite component) in the composition of tausonite.

*Thorianite* is extremely rare in our samples, and found only in one sample of the "potassium-batisite" syenite (Mu-186/6). The mineral forms anhedral grains (up to 20 μm in size) typically confined to cavities and intergrown with rutile (?). The mineral contains up to 8.6 wt.% $UO_2$ (0.09 *apfu* U) and 1.3 wt.% PbO (0.01 *apfu* Pb).

### 4.3.3 Phosphates

*Apatite-group minerals* are found in most of the samples studied, (except pseudoleucite syenite, "potassium-batisite" syenite and aegirinite). In the lamprophyre, apatite is relatively common, and occurs as anhedral-to-subhedral elongate crystals in the groundmass. Typically, the size of apatite crystals does not exceed 100 μm, but in some samples (*e.g.* Mu-150) reaches 1.5 mm. Apatite is a common accessory mineral in the kalsilite melasyenite (Mu-172), where it forms subhedral prismatic grains up to 0.6 mm in length (Fig. 4.2.7). In the pseudoleucite italite

171

## Table 4.3.2.4. Representative compositions of zoned tausonite from the lamprophyllite-bearing syenite (Mu-184/11).

| Wt.% | 1 | 2 | 3 | 4 | 5 |
|------|------|------|------|------|------|
| | high-$AZ$ zone | | intermediate | low-$AZ$ zone | |
| $TiO_2$ | 43.94 | 44.32 | 44.58 | 44.25 | 44.01 |
| $Fe_2O_3$ | 0.32 | 0.33 | 0.32 | 0.40 | 0.28 |
| $Nb_2O_5$ | n.d | 0.79 | n.d | n.d | n.d |
| $La_2O_3$ | 4.05 | 2.30 | 1.86 | 0.70 | 0.31 |
| $Ce_2O_3$ | 6.42 | 4.85 | 3.20 | 2.44 | 1.70 |
| $Nd_2O_3$ | 0.94 | 0.70 | n.d | n.d | 0.48 |
| $ThO_2$ | 2.74 | 0.68 | 0.79 | 1.01 | 1.54 |
| SrO | 36.34 | 42.58 | 43.95 | 44.62 | 46.42 |
| CaO | 2.40 | 2.58 | 3.30 | 3.30 | 2.76 |
| $Na_2O$ | 2.69 | 1.68 | 1.56 | 1.47 | 1.12 |
| Total | 99.84 | 100.81 | 99.56 | 98.19 | 98.62 |

Formulae calculated on the basis of:

3 atoms of oxygen

| | | | | | |
|------|------|------|------|------|------|
| Ti | 0.989 | 0.984 | 0.995 | 0.998 | 0.997 |
| $Fe^{3+}$ | 0.007 | 0.007 | 0.007 | 0.009 | 0.006 |
| Nb | - | 0.011 | - | - | - |
| La | 0.045 | 0.025 | 0.020 | 0.008 | 0.003 |
| Ce | 0.070 | 0.052 | 0.035 | 0.027 | 0.019 |
| Nd | 0.010 | 0.007 | - | - | 0.005 |
| Th | 0.019 | 0.005 | 0.005 | 0.007 | 0.011 |
| Sr | 0.631 | 0.729 | 0.756 | 0.776 | 0.811 |
| Ca | 0.077 | 0.082 | 0.105 | 0.106 | 0.089 |
| Na | 0.156 | 0.096 | 0.090 | 0.085 | 0.065 |

n.d = not detected; n.a = not analysed.

172

(Mu-235), apatite forms rare subhedral grains in the groundmass. In the eudialyte-bearing syenite, the mineral is rare, and occurs as segregations (ca. 200 μm across) of anhedral crystals developed along fractures in potassium feldspar, and marginally replaced by strontianite (Fig. 4.3.3.1).
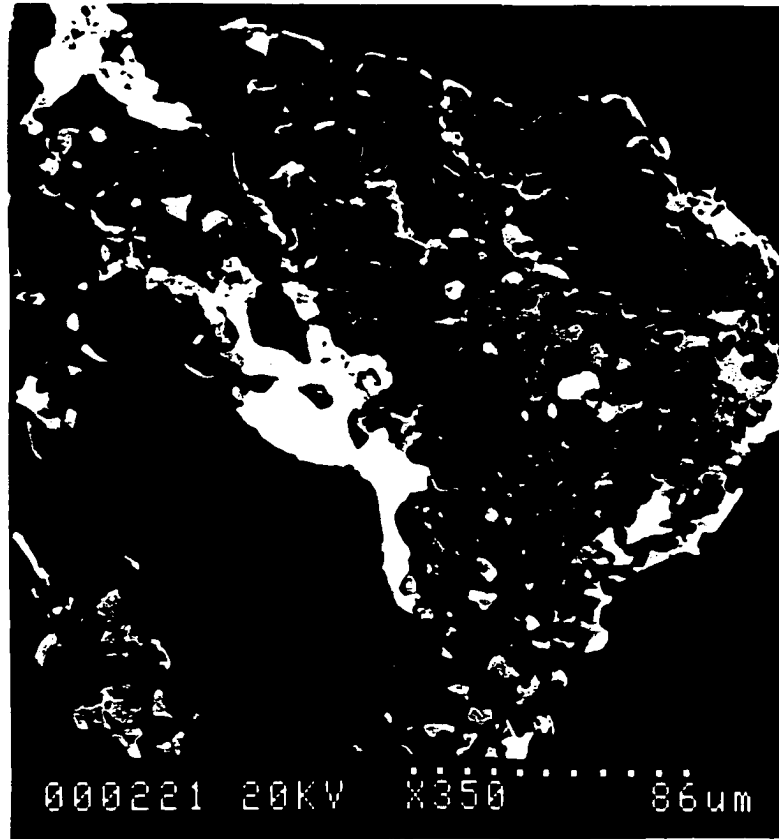


Fig. 4.3.3.1. Sr-rich apatite (grey) with high-$AZ$ parts enriched in SrO content. White – strontianite. Eudialyte-bearing syenite, Mu-196. BSE image.

Apatite is relatively common in the barytolamprophyllite-bearing syenite (Mu-236), where it occurs as anhedral-to-subhedral grains (up to 100 μm in size) containing minute (< 6 μm across) inclusions of galena and an unidentified Pb-Al silicate. Here, apatite is developed along fractures in potassium feldspar and commonly coexists with barytolamprophyllite. In BSE, many of the crystals show irregular or core-to-rim zoning.

173

Table 4.3.3.1. Representative compositions of apatite-group minerals and monazite-(Ce).

| Wt.% | 1 | 2 | 3 | 4 | 5 | 6 | 7 | 8 | 9 | 10 | 11 | 12 | 13 | 14 | 15 | 16 |
|---|---|---|---|---|---|---|---|---|---|---|---|---|---|---|---|---|
| $P_2O_5$ | 41.58 | 41.19 | 41.38 | 37.43 | 41.40 | 41.50 | 36.13 | 34.98 | 34.66 | 36.33 | 34.27 | 33.54 | 41.93 | 41.49 | 30.38 | 29.77 |
| $SiO_2$ | 0.67 | n.d | 0.97 | 1.86 | n.d | n.d | 0.43 | 0.75 | 0.58 | n.d | n.d | n.d | n.d | n.d | n.d | 0.54 |
| $La_2O_3$ | n.d | n.d | n.d | 1.41 | n.d | n.d | 0.23 | 0.21 | 0.11 | n.d | n.d | n.d | n.d | n.d | 20.40 | 19.69 |
| $Ce_2O_3$ | n.d | n.d | n.d | 1.88 | n.d | n.d | 0.79 | 0.64 | 0.71 | n.d | n.d | 0.18 | n.d | n.d | 35.20 | 34.40 |
| $Pr_2O_3$ | n.d | n.d | n.d | n.d | n.d | n.d | n.d | n.d | n.d | n.d | n.d | n.d | n.d | n.d | 3.60 | 2.03 |
| $Nd_2O_3$ | n.d | n.d | n.d | 1.07 | n.d | n.d | 0.21 | 0.40 | 0.18 | n.d | n.d | n.d | n.d | n.d | 8.69 | 9.95 |
| $Sm_2O_3$ | n.d | n.d | n.d | n.d | n.d | n.d | n.d | n.d | n.d | n.d | n.d | n.d | n.d | n.d | 0.47 | 0.70 |
| CaO | 55.17 | 53.16 | 54.45 | 42.61 | 51.90 | 51.90 | 32.90 | 31.42 | 30.18 | 34.35 | 24.19 | 19.96 | 52.76 | 51.54 | 1.24 | 1.11 |
| SrO | 1.42 | 3.80 | 1.35 | 14.00 | 3.74 | 3.92 | 28.71 | 30.05 | 31.94 | 27.41 | 41.88 | 44.87 | 3.17 | 4.25 | n.d | 0.33 |
| $Na_2O$ | 0.21 | n.d | n.d | n.d | 0.36 | n.d | n.d | 0.09 | 0.15 | n.d | n.d | n.d | n.d | n.d | n.d | n.d |
| F | 1.92 | 1.68 | 1.11 | 2.36 | 2.03 | 1.42 | 2.04 | 2.32 | 1.66 | 3.00 | 1.58 | 1.45 | 1.93 | 2.00 | n.d | n.d |
| Cl | n.d | n.d | n.d | n.d | 0.33 | 0.48 | n.d | n.d | n.d | n.d | n.d | n.d | n.d | n.d | n.d | n.d |
| $-O=F_2$ | 0.81 | 0.71 | 0.47 | 0.99 | 0.85 | 0.60 | 0.86 | 0.98 | 0.70 | 1.26 | 0.67 | 0.61 | 0.81 | 0.84 | - | - |
| $-O=Cl_2$ | - | - | - | - | 0.07 | 0.11 | - | - | - | - | - | - | - | - | - | - |
| Total | 100.16 | 99.12 | 98.79 | 101.63 | 98.84 | 98.51 | 100.58 | 99.88 | 99.47 | 99.83 | 101.25 | 99.39 | 98.98 | 98.44 | 99.98 | 99.02* |
| | | | | | | | Formulae calculated on the basis of: | | | | | | | | | |
| | | | | | | | 8 cations | | | | | | | | 2 cations | |
| P | 2.927 | 2.967 | 2.946 | 2.851 | 2.998 | 3.022 | 2.935 | 2.886 | 2.883 | 2.948 | 2.930 | 2.994 | 3.026 | 3.028 | 0.988 | 0.976 |
| Si | 0.056 | - | 0.082 | 0.167 | - | - | 0.041 | 0.073 | 0.057 | - | - | - | - | - | - | 0.021 |
| Σ | 2.983 | 2.967 | 3.028 | 3.018 | 2.998 | 3.022 | 2.976 | 2.959 | 2.940 | 2.948 | 2.930 | 2.994 | 3.026 | 3.028 | 0.988 | 0.997 |
| La | - | - | - | 0.047 | - | - | 0.008 | 0.008 | 0.004 | - | - | - | - | - | 0.290 | 0.282 |
| Ce | - | - | - | 0.062 | - | - | 0.028 | 0.023 | 0.026 | - | - | 0.007 | - | - | 0.496 | 0.490 |
| Pr | - | - | - | - | - | - | - | - | - | - | - | - | - | - | 0.050 | 0.029 |
| Nd | - | - | - | 0.034 | - | - | 0.007 | 0.014 | 0.005 | - | - | - | - | - | 0.119 | 0.139 |
| Sm | - | - | - | - | - | - | - | - | - | - | - | - | - | - | 0.006 | 0.009 |
| Ca | 4.915 | 4.846 | 4.906 | 4.108 | 4.757 | 4.783 | 3.383 | 3.281 | 3.177 | 3.528 | 2.617 | 2.255 | 4.818 | 4.760 | 0.051 | 0.047 |
| Sr | 0.068 | 0.187 | 0.066 | 0.731 | 0.186 | 0.196 | 1.598 | 1.698 | 1.819 | 1.524 | 2.453 | 2.744 | 0.157 | 0.212 | - | 0.007 |
| Na | 0.034 | - | - | - | 0.060 | - | - | 0.017 | 0.029 | - | - | - | - | - | - | - |
| Σ | 5.017 | 5.033 | 4.972 | 4.982 | 5.002 | 4.978 | 5.024 | 5.041 | 5.060 | 5.052 | 5.070 | 5.006 | 4.974 | 4.972 | 1.012 | 1.003 |
| F | 0.505 | 0.452 | 0.295 | 0.672 | 0.549 | 0.386 | 0.619 | 0.715 | 0.516 | 0.909 | 0.505 | 0.484 | 0.520 | 0.545 | - | - |
| Cl | - | - | - | - | 0.048 | 0.070 | - | - | - | - | - | - | - | - | - | - |

n.d = not detected; * Total also includes 0.5 wt.% $ThO_2$ (0.004 apfu Th). Analyses 1-14: apatite-group minerals (1-6: lamprophyre, 1-2 – Mu-231/13; 3-4 – Mu-215; 3: low-AZ zone, 4: high-AZ zone; 5-6 – Mu-3/100, weakly zoned; 7-9: barytolamprophyllite-bearing syenite, Mu-236; 10-12: eudialite-bearing syenite, Mu-196; 10: low-AZ zone, 11 & 12: high-AZ zones; 13-14: pseudoleucite italite, Mu-235; 15-16: monazite-(Ce) (lamprophyre, Mu-232).

174

Representative compositions of apatite-group minerals are given in Table 4.3.3.1. Most of the apatite compositions are very poor in Na and *REE*, with the exception of barytolamprophyllite-bearing syenite (Mu-236), and some lamprophyre samples (*e.g.* Mu-215). In the barytolamprophyllite-bearing syenite, all apatite compositions are slightly enriched in $REE_2O_3$ (up to 1.2 wt.%), whereas in the lamprophyre, high-AZ zones of the crystals contain up to 4.4 wt.% $REE_2O_3$, and low-AZ zones are devoid of *REE*. The apatite compositions obtained in this work essentially belong to the solid solution between the apatite and strontium-apatite $[Ca_5(PO_4)_3(OH,F) - (Sr,Ca)_5(PO_4)_3(OH,F)]$ (Table 4.3.3.1). In the lamprophyre, SrO varies from 1.4 in low-AZ zones to 14.0 wt.% in high-AZ zones (Table 4.3.3.1, analyses 1-6). In weakly zoned apatite from the pseudoleucite italite, SrO content varies from 3.2 to 4.2 wt.% (Table 4.3.3.1, analyses 13-14). The anhedral crystals from the barytolamprophyllite- and eudialyte-bearing syenite are extremely rich in Sr (up to 31.9 and 44.9 wt.% SrO, respectively; Table 4.3.3.1, analyses 7-11); with some compositions corresponding to strontium-apatite (2.74 *apfu* Sr; Table 4.3.3.1, analysis 12).

Sr-rich apatite was previously described from a wide variety of alkaline rocks, including lamproites, nepheline syenites and associated pegmatites (Edgar 1989; Mitchell & Bergman 1991; Konev *et al.* 1996; Chakhmouradian & Mitchell 1999; Mitchell & Chakhmouradian 2000), and carbonatites (see Chapter 3.3.4, and references therein). Strontium-apatite with *ca.* 46 wt.% SrO was found in agpaitic pegmatites of the Inagli and Khibina alkaline complexes (Pekov *et al.* 1995). Apatite from lamproites is typically enriched in Ba, and has lower SrO (< 13 wt.%) contents relative to its counterparts from agpaitic rocks (Edgar 1989; Mitchell & Bergman 1991; Chakhmouradian & Mitchell 1999).

Several elongate grains of *monazite-(Ce)* [ $(Ce,La,Nd,Th)PO_4$] (*ca.* 8 μm in size) were observed in one sample of the lamprophyre (Mu-232). Representative compositions of this mineral are given in Table 4.3.3.1 (analyses 15-16).

175

## 4.3.4 Carbonates

*Ancylite-(Ce)* is found exclusively in sample Mu-190 (aegirinite), where it forms rare anhedral grains (up to 100 μm in size) confined to cavities in calcite. Compositionally, this ancylite shows a wide variation in terms of La, Pr and Nd contents (Table 4.3.4.1). Some of the compositions are enriched in $ThO_2$ (up to 3.6 wt.%).

Table 4.3.4.1. Representative compositions of ancylite-(Ce) from aegirinite (Mu-190).

| | Wt. % | | | | Formulae to 2 cations | | |
| | 1 | 2 | 3 | | 1 | 2 | 3 |
| --- | --- | --- | --- | --- | --- | --- | --- |
| $ThO_2$ | n.d | 3.19 | 3.64 | Th | - | 0.049 | 0.056 |
| $La_2O_3$ | 14.40 | 8.30 | 7.23 | La | 0.328 | 0.207 | 0.180 |
| $Ce_2O_3$ | 25.77 | 25.71 | 25.63 | Ce | 0.583 | 0.638 | 0.633 |
| $Pr_2O_3$ | 1.62 | 2.81 | 3.10 | Pr | 0.036 | 0.069 | 0.076 |
| $Nd_2O_3$ | 5.49 | 9.91 | 10.67 | Nd | 0.121 | 0.240 | 0.257 |
| $Sm_2O_3$ | n.d | n.d | 0.22 | Sm | - | - | 0.005 |
| $Eu_2O_3$ | n.d | 0.94 | 0.15 | Eu | - | 0.022 | 0.003 |
| CaO | 3.99 | 1.85 | 2.18 | Ca | 0.264 | 0.134 | 0.158 |
| SrO | 18.65 | 15.78 | 16.17 | Sr | 0.668 | 0.620 | 0.632 |
| BaO | n.d | 0.75 | n.d | Ba | - | 0.020 | - |
| $CO_2$* | 24.05 | 22.80 | 22.88 | $CO_3$ | 2.000 | 2.000 | 2.000 |
| Total* | 93.97 | 92.04 | 91.87 | | | | |

* calculated on the basis of stoichiometry; n.d - not detected.

*Calcite* is a common alteration product in the majority of the rocks studied. In some of the lamprophyre samples (*e.g.* Mu-215), this mineral also forms subhedral-to-euhedral prismatic grains up to 0.4 mm in size (Fig. 4.3.1.7). *Strontianite* occurs predominantly in the eudialytie-bearing syenite, where it replaces Sr-rich apatite. Coarse (up to 0.2 mm) anhedral grains of *barytocalcite* are developed along fractures in the pseudoleucite italite.

Representative compositions of calcite, strontianite and barytocalcite are given in Table 4.3.4.2. Calcite is typically enriched in SrO (up to 2.2 wt.%), and in some cases, BaO (up to 1.2 wt.%). Calcite from the potassium feldspar-albite-biotite groundmass of sample Mu-232 (lamprophyre) is Sr- and Ba-free, but contains up to 0.7 wt.% FeO and MgO, and 0.5 wt.%

176

Table 4.3.4.2. Representative compositions of calcite, strontianite and barytocalcite.

| Wt. % | 1 | 2 | 3 | 4 | 5 | 6 | 7 |
|---|---|---|---|---|---|---|---|
| CaO | 52.87 | 53.38 | 55.42 | 1.47 | 3.28 | 2.70 | 18.30 |
| SrO | 2.23 | n.d | 0.31 | 66.96 | 63.08 | 64.73 | 2.39 |
| BaO | 1.17 | n.d | n.d | 0.88 | 1.57 | 1.23 | 47.11 |
| FeO | n.d | 0.68 | n.d | n.d | n.d | n.d | n.d |
| MgO | n.d | 0.73 | n.d | n.d | n.d | n.d | n.d |
| MnO | n.d | 0.47 | n.d | n.d | n.d | n.d | n.d |
| $CO_2$* | 42.77 | 43.40 | 43.62 | 29.85 | 29.82 | 29.97 | 28.90 |
| Total* | 99.04 | 98.66 | 99.35 | 99.16 | 97.75 | 98.63 | 96.70 |
| Formulae calculated on the basis of 2 cations | | | | | | | |
| Ca | 0.970 | 0.965 | 0.997 | 0.039 | 0.086 | 0.071 | 0.497 |
| Sr | 0.022 | - | 0.003 | 0.953 | 0.899 | 0.918 | 0.035 |
| Ba | 0.008 | - | - | 0.008 | 0.015 | 0.012 | 0.468 |
| $Fe^{2+}$ | - | 0.010 | - | - | - | - | - |
| Mn | - | 0.007 | - | - | - | - | - |
| Mg | - | 0.018 | - | - | - | - | - |
| $CO_3$ | 1.000 | 1.000 | 1.000 | 1.000 | 1.000 | 1.000 | 1.000 |

n.d - not detected; * calculated on the basis of stoichiometry. Analyses 1-3: *calcite* (1 – Mu-231/13; 2 – Mu-232; 3 – Mu-190); 4-6: *strontianite* (4 – Mu-245; 5-6 – Mu-196); 7: *barytocalcite* (Mu-235).

177

MnO (Table 4.3.4.2, analysis 2). All compositions of strontianite contain appreciable CaO (up to 3.3 wt.%) and BaO (up to 1.6 wt.%). Barytocalcite is typically enriched in SrO content (up to 2.4 wt.%).

### 4.3.5 Sulphates

*Jarosite* [$KFe^{3+}_3(SO_4)_2(OH)_6$] is a common accessory mineral in sample Mu-167/19 (pseudoleucite syenite). In plane polarised light, the mineral appears as honey-yellow to greenish yellow subhedral-to-euhedral rounded or pseudohexagonal crystals (up to 50 μm across) or segregations of such crystals. Jarosite is developed in prismatic or acicular cavities (Fig. 4.3.1.2, 4.3.5.1). The cavities contain anhedral fragments of clinopyroxene strongly altered to muscovite and ferripyrophyllite.
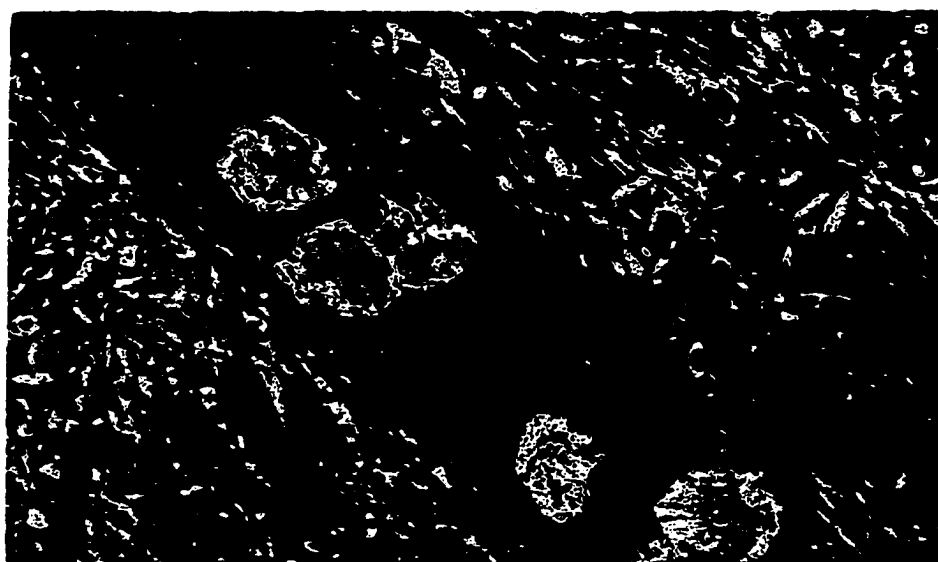


Fig. 4.3.5.1. Round crystals of jarosite (red) and ferripyrophyllite (dark blue) developed in the cavity in potassium feldspar (blue). F.O.V. 100 μm. Mu-167/19. False-colour BSE image.

Jarosite is unusually rich in SrO (up to 1.4 wt.%) and BaO (up to 2.0 wt.%). The overall compositional variation of this mineral can be expressed as ($K_{0.77-0.82}Na_{0.05-0.11}Sr_{0.05-0.07}Ba_{0.04-0.07}$)($Fe^{3+}_{2.62-2.65}Si_{0.11-0.15}Al_{0.10-0.12}Ti_{0.04-0.07}$)($SO_4$)$_{1.82-1.88}$($PO_4$)$_{0.22-0.26}$($OH$)$_6$ (Table 4.3.5.1). Jarosite has not been previously recognised at Murun.

178

Table 4.3.5.1. Representative compositions of jarosite from the pseudoleucite syenite (*Mu-167/19*).

| | Wt. % | | | | Formulae to 6 cations | | |
|---|---|---|---|---|---|---|---|
| | 1 | 2 | 3 | | 1 | 2 | 3 |
| $SiO_2$ | 0.82 | 0.57 | 0.76 | Si | 0.154 | 0.110 | 0.143 |
| $TiO_2$ | 0.54 | 0.58 | 1.08 | Ti | 0.036 | 0.039 | 0.072 |
| $Al_2O_3$ | 1.14 | 0.96 | 1.01 | Al | 0.118 | 0.102 | 0.105 |
| $Fe_2O_3$ | 40.24 | 38.92 | 39.49 | $Fe^{3+}$ | 2.652 | 2.651 | 2.623 |
| SrO | 1.05 | 1.39 | 1.00 | Sr | 0.053 | 0.073 | 0.051 |
| BaO | 1.51 | 2.02 | 1.14 | Ba | 0.052 | 0.072 | 0.039 |
| $K_2O$ | 7.06 | 6.70 | 7.29 | K | 0.789 | 0.773 | 0.821 |
| $Na_2O$ | 0.32 | 0.40 | 0.64 | Na | 0.054 | 0.070 | 0.109 |
| $P_2O_5$ | 2.90 | 3.44 | 2.87 | $PO_4$ | 0.215 | 0.264 | 0.214 |
| $SO_3$ | 28.56 | 27.19 | 27.53 | $SO_4$ | 1.877 | 1.846 | 1.823 |
| Total | 84.14 | 82.17 | 82.81 | | | | |

*Barite* is a common late-stage mineral in most of the samples examined (with the exception of "potassium-batisite" syenite). The mineral is typically confined to fractures and cavities, and also occurs as a part of alteration assemblages developed after earlier-crystallised phases (*e.g.* garnet in psedoleucite syenite Mu-167/19 and pyrrothite in lamprophyre Mu-231/13).

## 4.3.6 Sulphides

In the samples examined, sulphide minerals have not been found in the pseudoleucite italite, kalsilite melasyenite, "potassium-batisite" syenite, and barytolamprophyllite- and lamprophyllite syenite.

*Djerfisherite* [$K_6(Fe,Cu,Ni)_{25}S_{26}Cl$] is found in one sample of the lamprophyre (Mu-231/13). The mineral forms subhedral grains (up to 90 μm across), typically with an altered rim, and is commonly associated with pyrite and chalcopyrite (Fig. 4.3.6.1). Djerfisherite shows a noticeable intergranular variation in terms of its Fe, Cu and Ni contents (Table 4.3.6.1).
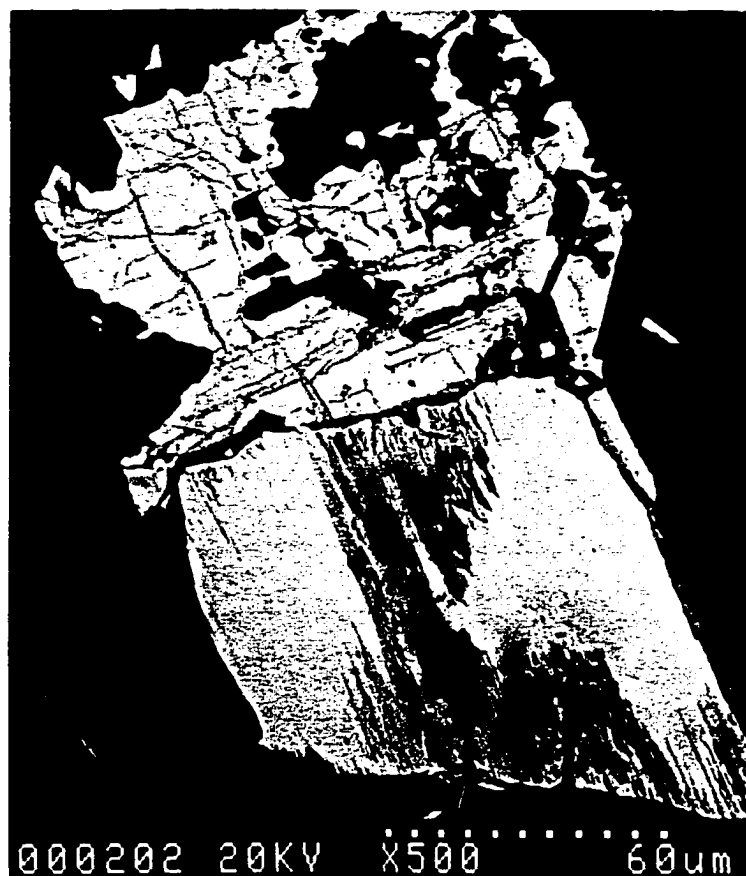
Fig. 4.3.6.1. Djerfisherite (light grey, fractured, top) in association with pyrrhotite (light grey, bottom). BSE image.

Table 4.3.6.1. Representative compositions of djerfisherite from the lamprophylite (*Mu-231/13*).

|  | 1 | 2 | 3 |  | 1 | 2 | 3 |
|---|---|---|---|---|---|---|---|
|  | Wt. % | | | | Formulae to 26 atoms of S | | |
| Fe | 35.21 | 37.17 | 34.33 |  | 16.203 | 16.806 | 16.126 |
| Cu | 19.87 | 18.88 | 19.94 |  | 8.035 | 7.501 | 8.234 |
| Ni | 2.02 | 1.79 | 1.84 |  | 0.881 | 0.769 | 0.820 |
| K | 9.06 | 8.80 | 9.01 |  | 5.954 | 5.681 | 6.042 |
| S | 32.44 | 33.02 | 31.78 |  | 26.000 | 26.000 | 26.000 |
| Cl | 1.24 | 1.45 | 1.26 |  | 0.899 | 1.034 | 0.930 |
| Total | 99.84 | 101.11 | 98.16 | $\Sigma$*(Cu,Fe,Ni)* | *25.119* | *25.076* | *25.180* |

180

*Pyrite* occurs in the majority of the lamprophyre samples (*e.g.* Mu-231/13, -150, -215), in the aegirinite (Mu-190) and some samples of the pseudoleucite syenite (*e.g.* Mu-216). In the lamprophyre, pyrite occurs as anhedral-to-subhedral grains (up to 150 μm in size) in the groundmass, or is developed interstitially. In the aegirinite, pyrite forms anhedral-to-subhedral grains (up to 200 μm in size) commonly developed along fractures and associated with rutile (?), celadonite and calcite. Rare anhedral grains of pyrite (< 50 μm in size) from the pseudoleucite syenite are commonly developed in cavities and along fractures in clinopyroxene.

*Pyrrhotite* is found in the groundmass of one lamprophyre sample (Mu-231/13). The mineral forms rare subhedral grains (*ca.* 100 μm in size) commonly associated with pyrite and djerfisherite, it is strongly altered to a mixture of barite and Fe-sulphates of variable stoichiometry.

*Chalcopyrite* occurs in some samples of the lamprophyre (*e.g.* Mu-215) and pseudoleucite syenite (Mu-216). This mineral forms rare anhedral-to-subhedral grains (up to 20 μm in size) in the groundmass, and is commonly associated with pyrite.

*Galena* is found in the eudialyte-bearing syenite (Mu-196, -245), and some samples of the lamprophyre (Mu-215). The mineral occurs as rare minute (< 30 μm) grains in the groundmass (eudialyte-bearing syenite) or as inclusions in pyrite and chalcopyrite (lamprophyre).

*Sphalerite* occurs in some samples of the pseudoleucite syenite (Mu-216) and eudialyte-bearing synite (Mu-245), where it forms minute (< 40 μm) crystals in the groundmass.

Most of the sulphide minerals are poor in minor elements and typically correspond to the ideal compositions.

181

## 4.4. Discussion and conclusions

Although relatively minor in proportion, the rocks described in this section provide some useful insights into the evolutionary history of the Murun complex. The observed petrographic diversity cannot be explained in terms of a simple differentiation mechanism. For example, compositional trends exhibited by clinopyroxene and mica from different hypabyssal suites (Figs. 4.3.1.3 and 4.3.1.6) clearly indicate that their parental magmas could not be derived from the same source. Very little overlap between individual trends suggests that, in our case, magma mixing was not a significant petrogenetic factor and, by no means, can account for the diversity of hypabyssal rocks observed at Murun. Further, none of the rocks studied contain conspicuous xenocrysts, attesting to generally low degrees of assimilation of the wall-rock material. The data obtained in this work are consistent with the earlier findings of Evdokimov et al. (1989) and Konev et al. (1996) that the Murun complex is a series of discrete successive intrusions, rather than being a colossal differentiated lopolith.

It has been suggested in a number of studies (e.g., Evdokimov and Chakhmouradian 1994, Mitchell and Vladykin 1996) that most of the hypabyssal rock types at Murun could be correlated with a distinct plutonic series. This conclusion is substantiated not only by the spatial association of hypabyssal and plutonic suites, but also by similarities in their modal composition, accessory mineralogy and evolutionary trends of individual minerals. For example, Mitchell and Vladykin (1996) demonstrated that the phlogopite-rich rocks previously identified as lamproites are devoid of the characteristic mineralogical features pertaining to lamproites, and merely represent a lamprophyric facies of the clinopyroxenite-shonkinite suite. The compositional trends of mafic minerals determined in the present study are in good agreement with the data of Mitchell and Vladykin (1996), further supporting the consanguineous nature of lamprophyres, phlogopite clinopyroxenites and shonkinites (including melasyenites). In a broad sense, the lamprophyric rocks from Murun can be classified as minettes; however, the latter term is vague and should be avoided (Mitchell 1994).

The syenitic rocks of types (5) to (7) clearly represent the most evolved magmas, as they contain major proportions of such characteristic "agpaitic" minerals as eudialyte,

182

lamprophyllite, barytolamprophyllite, wadeite and "K-batisite". Present in lesser quantities are tausonite, K-Ba-Pb titanates, strontium-apatite, and unidentified Ba- and Sr-bearing phases. Most of these minerals crystallised early in the evolutionary history (nearly simultaneously with the felsics and prismatic aegirine); hence, their presence reflects enrichment of parental alkaline magmas in Sr, Ba and Zr. A similar mineral assemblage occurs in potassic nepheline-syenite pegmatites associated with the phonolitic rocks in the Crazy Mountains area, Montana (Mitchell and Chakhmouradian 2000), and with the rischorrite-urtite series in the Khibina complex, Kola Peninsula (Yakovenchuk et al., 1999). Therefore, it is reasonable to suggest that the agpaitic rocks studied in this work are genetically related to nepheline syenites and, possibly, phonolites. Alternatively, agpaitic magmas enriched in Sr, Ba and Zr could represent an extreme fractionation product from an alkali-syenitic source. The alkaline syenites comprise the bulk of the Murun complex, being far more common than the nepheline syenites. It is also noteworthy that pegmatites associated with the alkaline syenites contain some of the characteristic "agpaitic" minerals, e.g., wadeite, K-Ba titanates and lamprophyllite.

The relationship of pseudoleucite syenites to other rock types is uncertain. The compositions of clinopyroxene and phlogopite from sample Mu-216 plot significantly off the major evolutionary trends (Figs. 4.3.1.3 and 4.3.1.6). Diopside and aegirine-augite from the garnet-pseudoleucite syenite (Mu-167/19) also are enriched in the $CaFe^{2+}Si_2O_6$ component. Both these samples exhibit a well-defined flow texture, and undoubtedly represent products of magmatic crystallisation. Although the pseudoleucite syenites were affected by late-stage processes (e.g. replacement of primary felsic minerals by sodalite and cancrinite), we do not believe that these processes could be responsible for the "abnormal" compositional characteristics of the mafic minerals (note the fresh appearance of clinopyroxene phenocrysts in sample Mu-216: Fig. 4.2.4). Therefore, the source of these rocks remains problematic; the are most probably related to the plutonic pseudoleucite syenites, kalsilite syenites or synnyrites. Further studies of the geochemistry and mineralogy of the potassic alkaline rocks from Murun are clearly required to resolve this problem.

# REFERENCES

ANDERSEN, T. (1989): Evolution of peralkaline calcite carbonatite magma in the Fen complex, southeast Norway. *Lithos*, **22**, 99-112.

BAR-MATTHEWS, M. (1987): The genesis of uranium in manganese and phosphorite assemblages, Timna Basin, Israel. *Geol. Mag.* **124**(3), 211-229.

BELOVITSKAYA, J.V, PEKOV, I.V. & KABALOV, YU.K. (1998): *RE*-free and *RE*-poor burbankite from pectolite metasomatites: chemical composition and crystal structure refinement. *17th Meet. Int. Mineral. Assoc.*, Toronto, Abstr. Vol., A110.

BORISOV, A.B. (1985): On the time and conditions of formation of the charoite rocks of the different texture. *Zap. Vses. Mineral. Obshchest.* **114**(4), 455-463 (in Russ.).

BORNEMAN-STARYNKEVICH, I.D. (1982): Redefinition of the formula of charoite. *Zap. Vses. Mineral. Obshchest.* **111**(3), 344-345 (in Russ.).

BOULTIF, A. & LOUER, D. (1991): Indexing of powder diffraction patterns for low symmetry lattices by the successive dichotomy method. *J. Appl. Crystallogr.* **24**, 987-993.

BRIGATTI, M.F., MEDICI, L., SACCANI, E. & VACCARO, C. (1996): Crystal chemistry and petrologic significance of $Fe^{3+}$-rich phlogopite from the Tapira carbonatite complex, Brazil. *Am. Min.*, **81**, 913-927.

BÜHN, B., RANKIN, A.H., RADTKE, M., HALLER, M. & KNÖCHEL, A. (1999): Burbankite, a (Sr,REE,Na,Ca)-carbonate in fluid inclusions from carbonatite-derived fluids: Identification and characterization using Laser Raman spectroscopy, SEM-EDX, and synchrotron micro-XRF analysis. *Am. Mineral.*, **84**, 1117-1125.

BUKHTIYAROVA, E.V., SMIRNOV, A.A., INDUTNYI, V.V. & TARAN, M.N. (1992): Nature of mother-of-pearl iridescence of charoite. *Mineral. Zhurn.* **14**(2), 95-99 (in Russ.).

CARLSON, W.D. (1980): The calcite-aragonite equilibrium: effects of Sr substitution and anion orientational disorder. *Am. Mineral.*, **65**, 1252-1262.

CARMICHAEL, IAN S.E. (1967): The mineralogy and petrology of the volcanic rocks from the Leucite Hills, Wyoming. *Contrib. Mineral. Petrol.* **15**, 24-66.

CHAKHMOURADIAN, A.R. & EVDOKIMOV, M.D. (1997): Titanium and zirconium minerals from alkaline-syenitic pegmatites of the Malomurunsky massif, Yakutia. *Proceed. Russian Mineral. Soc.*, **126** (3), 32-42 (in Russ.)

_____ & MITCHELL, R.H. (1999): Primary, agpaitic and deuteric stages in the evolution of accessory Sr, REE, Ba and Nb-Mineralization in nepheline-syenite pegmatites at Pegmatite Peak, Bearpaw Mts., Montana. *Mineral. Petrol.* **67**, 85-110.

_____ & _____ (1998): Lueshite, pyrochlore and monazite-(Ce) from apatite-dolomite carbonatite, Lesnaya Varaka complex, Kola Peninsula, Russia. *Mineral. Mag.*, **62**(6), 769-782.

CHANG, LUKE L.Y. (1965): Subsolidus phase relations in the systems $BaCO_3$-$SrCO_3$, $SrCO_3$-$CaCO_3$, and $BaCO_3$-$CaCO_3$. *J. Geol.* **73**, 346-368.

CHEN, T.T. & CHAO, G.Y. (1974): Burbankite from Mont St. Hilaire, Quebec. *Can. Mineral.*, **12**, 342-345.

CHIRAGOV, M.I., MAMEDOV, CH.S. & BELOV, N.V. (1969): On crystal structure of canasite $Ca_5Na_4K_2[Si_{12}O_{30}](OH,F)_4$. *Dokl. Akad. Nauk SSSR* **185**(3), 672-674 (in Russ.).

_____ & MAMEDOV, CH.S. (1972): Crystal structure of canasite – $K_3Ca_5Na_3[Si_{12}O_{30}](OH,F)_4$. *Sci. Lett. Univ.of Azerbaidjan* **4**, 14-19 (in Russ.).

CHUKHROV, F.V. & SMOL'YANINOVA, N.N. (eds.) (1981): *Minerals, Reference Book,* **3**(3): *Silicates with Chains of $SiO_4$ tetrahedra.* Nauka Press, Moscow, USSR (in Russian).

DAWSON, J.B. (1993): A supposed sölvite from Oldoino Lengai, Tanzania: result of extreme alteration af alkali carbonatite lava. *Mineral. Mag.*, **57**, 93-101.

_____, SMITH, J.V. & STEELE, I.M. (1995): Petrology and mineral chemistry of plutonic igneous xenoliths from the carbonatite volcano, Oldoino Lengai, Tanzania. *J. Petrol.* **36**, 797-826.

DORFMAN, M.D., ROGACHEV, D.Ya., GOROSHCHENKO, Z.I. & USPENSKAYA, E.I. (1959): Canasite – a new mineral. *Trudy Mineralogicheskogo Museya Academii Nauk USSR* **9**, 158-166 (in Russ.).

DOWNS, R.T., BARTELMEHS, K.L., GIBBS, G.V. & BOISEN, M.B. (1993): Interactive software for calculating and displaying X-ray or neutron powder diffractometer patterns of crystalline materials. *Am Mineral* **78**,1104-1107.

DOWTY, E. (1977): ATOMS 4.0.

DUTROW, B. & HENRY, D.J. (1996): Cathodoluminescence of charoite and associated minerals. *Min. Rec.* **27**, 28.

EDGAR, A.D. (1989): Barium- and strontium-enriched apatites in lamproites from West Kimberley, Western Australia. *Am. Mineral.* **74**, 889-895.

EFFENBERGER, H., KLUGER, F., PAULUS, H. & WÖLFEL, E.R. (1985): Crystal structure refinement of burbankite. *Neues Jahrb. Mineral. Monatsh.*, **4**, 161-170.

EVANS, H.T. JR. (1973): The crystal structures of cavansite and pentagonite. *Am. Miner.* **58**, 412-424.

EVDOKIMOV, M.D. (1995): Charoite: A unique mineral from a unique occurrence. *World of Stones.* **7**, 3-11.

_____ & REGUIR, E.P. (1994): Canasite in charoitites of the Murun Alkaline Complex ("Lilac Rock" Deposit). *Zap. Vses. Mineral. Obshchest.* **123**(1), 104-118 (in Russ.).

FAIZIEV, A.R., ISKANDAROV, F.SH & GAFUROV, F.G. (1998): Mineralogical and genetic features of carbonatites from Dunkeldyksky alkaline complex (eastern Pamir). *Zap. Vseross. Mineral. Obshchest.* **127**(3), 54-57 (in Russ.).

GASPAR, J.C., CONCEIÇÃO E SILVA, A.J.G. & DE ARAÚJO, D.P. (1994): Composition of priderite in phlogopitites from the Catalão I carbonatite complex, Brazil. *Mineral. Mag.* **58**, 409-415.

_____ & WYLLIE, P.J. (1982): Barium phlogopite from the Jacupiranga carbonatite, Brazil. *Am. Min.*, **67**, 997-1000.

HAMILTON, D.L. (1961): Nephelines as crystallization temperature indicators. *J. Geol.* **69**, 321-329.

HAWTHORNE, F.C. (1983): The crystal chemistry of the amphiboles. *Can. Min.*, **21**(2), 173-480.

HOGARTH D.D., HARTREE, R., LOOP, J., & SOLBERG, T.N. (1985): Rare-earth element minerals in four carbonatites near Gatineau, Quebec. *Am. Mineral.*, **70**, 1135-1142.

_____, RUSHFORTH, P. & MCCORKELL, R.H. (1988): The Blackburn carbonatites, near Ottawa, Ontario: Dykes with fluidized emplacement. *Can. Mineral.*, **26**, 377-390.

IVANYUK, G. YU. & EVDOKIMOV, M.D. (1991): Pyroxenes of the charoite deposit "Lilac Stone" and some characteristics of their genesis. *Zap. Vseross. Mineral. Obshchest.* **120**(3), 62-74 (in Russ.).

JANECZEK, J. (1996): Nb-, Ta- and Sn-rich titanite and its alteration in pegmatites from Zólkiewka, Poland. *Neues Jahrb. Mineral. Monatsh.* **1996**, 459-469.

JOHNSEN, O., GAULT, R.A., GRICE, J.D. & ERCIT, T.S. (1999): Khomyakovite and manganokhomyakovite, two new members of the eudialyte group from Mont Saint-Hilaire, Quebec, Canada. *Can. Mineral.* **37**(4), 893-899.

_____ & GRICE, J.D. (1999): The crystal chemistry of the eudialyte group. *Can. Mineral.* **37**(4), 865-891.

186

KOGARKO, L.N., KONONOVA, V.A., ORLOVA, M.P. & WOOLEY, A.R. (1995): *Alkaline rocks and carbonatites of the world. 2. Former USSR.* Chapman & Hall, London, UK.

KONEV, A.A., VOROB'EV, E.I., & LASEBNIK, K.A. (1996): The Mineralogy of the Murun Alkaline Massif. *Siber. Branch Russ. Acad. Sci. Press, Novosibirsk* (in Russ.).

_____, VOROB'EV, E.I., PISKUNOVA, L.F., USCHAPOVSKAYA, Z.F., & TIKHONOVA, G.A. (1991): Olekminskite (Sr,Ca,Ba) $CO_3$, a new mineral and a new isomorphous series olekminskite-paralstonite. *Zap. Vseross. Mineral. Obshchest.* **120** (3), 89-96 (in Russ.).

KONONOVA, V.A., PERVOV, V.A., BOGATIKOV, O.A., WOOLLEY, A.R. & SUDDABY, P. (1997): Pseudoleucite and the origin of the highly potassic rocks of the Southern Sakun massif, Aldan shield. *Petrology* **5**(2), 167-182.

KOSTYLEVA-LABUNTSOVA E.E., BORUTSKII B.E., SOKOLOVA M.N., SHLYUKOVA Z.V., DORFMAN M.D., DUDKIN O.B. & KOZYREVA L.V. (1978): *The mineralogy of the Khibina massif.* Vol. 2 (Minerals). Nauka Press, Moscow (in Russ).

KRAEFF, A. POORTER, R.P.E., & SCHUILING, R.D. (1980): Additional information on charoite. *N. Jb. Miner. Mh.* **11**, 498-500.

LASEBNIK, K.A. & LASEBNIK, Yu.D. (1981): Rare silicates – miserite, canasite and fedorite in charoitic rocks. *In* Mineralogy and Geochemistry of Ultramafic and Mafic Rocks of Yakutia. Yakutsk Branch Acad. Sci. USSR, Yakutsk, Russia, 32-50 (in Russ.).

_____ & _____ (1986): Rare minerals of charoitites. *In* Crystallochemistry of Minerals; Materials of XIII IMA Congress (Warna, 19-25.09.1982), Bulgarian Academy of Sciences Press, Sofia, 1986 (Minceva-Stefanova, J. *et al.*, eds.). (in Russ.).

LEAKE, B.E., WOOLLEY, A.R., ARPS, C.E.S., BIRCH, W.D., GILBERT, M.C., GRICE, J.D., HAWTHORNE, F.C., KATO, A., KISCH, H.J., KRIVOVICHEV, V.G., LINTHOUT, K., LAIRD, J., MANDARINO, J.A., MARESH, W.V., NICKEL, E.H., ROCK, N.M.S., SCHUMACHER, J.C., SMITH, D.C., STEPHENSON, N.C.N., UNGARETTI, L., WHITTAKER, E.J.W. & YOUZHI, G. (1997): Nomenclature of amphiboles: report of the subcommittee on amphiboles of the International Mineralogical Association, Commission on New Minerals and Mineral Names. *Can. Min.*, **35**, 219-246.

LEE W.-J. & WYLLIE P.J. (1998): Petrogenesis of carbonatite magmas from mantle to crust, constrained by the system $CaO-(MgO+FeO^*)-(Na_2O+K_2O)-(SiO_2+Al_2O_3+TiO_2)-CO_2$. *J. Petrol.* **39**, 495-517.

LINTHOUT, K. & LUSTENHOUWER, W.J. (1993): Ferrian high sanidine in a lamproite from Cancarix, Spain. *Min. Mag.* **57**, 289-299.

LITVIN, A.L., EGOROVA, L.N., KUL'CHITSKAYA, V.S., MEL'NIKOV, V.S. & SHARKIN, O.P. (1998): Sr-rich burbankite from nepheline syenites of Azov region. *Mineralogicheskii Zurnal*, **20**, 12-18 (in Russ.).

LOWE-MA, C.K. (1993): Refinement of unit-cell parameters by least-squares: comments on an old technique and the development of a new computer program. NAWCWPNS TP8 128.

McCORMICK, G.R. & HEATHCOTE, R.C. (1987): Mineral chemistry and petrogenesis of carbonatite intrusions, Perry and Conway Counties, Arkansas. *Am. Min.*, **72**, 59-66.

_____ & LE BAS, R.C. (1996): Phlogopite crystallization in carbonatitic magmas from Uganda. *Can. Mineral.*, **34**, 469-478.

MITCHELL, R.H. (1995): Accessory rare earth, strontium, barium and zirconium minerals in the Benfontein and Wesselton calcite kimberlites, South Africa. *In* Kimberlites, Related Rocks and Mantle Xenoliths (H.O.A. Mayer & O.H. Leonardos, eds.), Proc. 5th Intern. Kimb. Conf., Brasil, Companhia de Pesquisa de Recursos Minerals, Rio de Janeiro, 115-128.

_____ (1980): Pyroxenes of the Fen alkaline complex, Norway. *Am. Min.*, **65**, 45-54.

_____ & BERGMAN, S.C. (1991): *Petrology of Lamproites*. Plenum Press, New York.

_____ & MEYER, H.O.A. (1989): Niobian K-Ba-V titanates from micaceous kimberlite, Star mine, Orange Free State, South Africa. *Mineral. Mag.* **53**, 451-456.

_____ & Platt, R.G. (1979): Nepheline-bearing rocks from the Poohbah Lake Complex, Ontario: malignites and malignites. *Contrib. Mineral. Petrol.* **69**, 255-264.

_____ & STEELE, I. (1992): Potassian zirconium and titanium silicates and strontian cerian perovskite in lamproites from the Leucite Hills, Wyoming. *Can. Mineral.* **30**, 1153-1159.

_____ & VLADYKIN, N.V. (1993): Rare earth element-bearing tausonite and potassium barium titanates from the Little Murun potassic alkaline complex, Yakutia, Russia. *Mineral. Mag.* **57**, 651-664.

_____ & _____ (1996): Compositional variation of pyroxene and mica from the Little Murun ultrapotassic complex, Aldan Shield, Russia. *Mineral. Mag.* **60**, 907-925.

_____, YAKOVENCHUK, V.N., CHAKHMOURADIAN, A.R., BURNS, P.C. & PAKHOMOVSKY, YA.A. (2000): Henrymeyerite, a new hollandite-type Ba-Fe titanate from the Kovdor Complex, Russia. *Can. Mineral.* **38**, 617-626.

NADEZHINA, T.N, PUSHCHAROVSKII, D.Y., TAROEV, V.K., TAUSON, V.L. & BYCHKOV, A.M. (1993): Crystal structure of the ferrialuminosilicate low sanidine. *Cryst. Rep.*, **38**, 753-755.

NICHOLSON, K. (1986): Mineralogy and geochemistry of manganese and iron veins Anndilly, Banffshire. *Scottish J. Geol.* **22**(2), 213-224.

NIKISHOVA, L.V. & LASEBNIK, Yu.D. (1982): On crystallographic characteristics of charoite. *In* Geology and Natural Resources of Yakutia. Bull. NTI. Yakutsk, 26-29 (in Russ.).

_____, LASEBNIK, K.A. & LASEBNIK, Yu.D. (1985): On the crystal chemical formula of charoite. *In* Crystal Chemistry and Structural Typomorphism of Minerals. Nauka Press, Leningrad, 100-104 (in Russ.).

NIKITIN, A.V& BELOV, N.V. (1962): Crystal structure of batisite $Na_2BaTi_2Si_4O_{14}$ = $Na_2BaTi_2O_2[Si_4O_{12}]$. *Dokl. Akad.Nauk SSSR* **146**, 1401-1403 (in Russ.).

NIKOL'SKAYA, L.V., NOVOZHILOV, A.I. & SAMOILOVICH. M.I. (1976): On the colour nature of the new alkali calcic silikate from the Eastern Zabaikal'e. *Izv. Akad. Nauk SSSR, Ser. Geol.* **10**, 116-120 (in Russ.).

NORRISH, K. (1954): Priderite, a new mineral from the leucite-lamproites of the west Kimberley area, Western Australia. *Mineral. Mag.* **29**, 496-501.

NYFELER, D., ARMBRUSTER, T., & VILLA, I.M. (1998): Si, Al, Fe order-disorder in Fe-bearing K-feldspar from Madagascar and its implications to Ar diffusion. *Schweiz. Mineral. Petrogr. Mitt.*, **78**, 11-20.

ORLANDI, P., PASERO, M., & VEZZALINI, G. (1990): Calcio-ancylite-(Nd), a new carbonate from Baveno, Italy. *Europ. J. Mineral.* **2**, 414-418.

ORLOVA, M.P., BORISOV, A.B. & SHADENKOV, E.M. (1992): Alkali magmatism of Murun areal (*sic.*) (Aldan shield). *Geol. Geophys.* **33**(5), 57-70 (in Russ.).

PANINA, L.I. (1997): Low-titanium lamproites of Aldan (Siberia): the results of investigation of fluid inclusions in minerals. *Geol. Geophys.* **38**(1), 112-122 (in Russ.).

_____ & VLADYKIN, N.V. (1994): Lamproite rocks of the Murun massif and their genesis. *Geol. Geophys.* **35**(12), 100-113 (in Russ.).

PAUTOV, L.A., AGAKHANOV, A., SOKOLOVA, E.V. & KABALOV, YU.K. (1997): Turkestanite $Th(Ca,Na)_2(K_{1-x})Si_8O_{20}·nH_2O$, a new mineral. *Zap. Vseross. Mineral. Obshchest.* **126**(6), 45-55 (in Russ.).

PECORA W.T. & KERR, J.H. (1953): Burbankite and calkinsite, two new carbonate minerals from Montana. *Am. Mineral.*, **38**, 1169-1183.

PEKOV, I.V., CHUKANOV, N.V., ELETSKAYA, O.V., KHOMYAKOV, A.P. & MEN'SHIKOV, YU.P. (1995): Belovite-(Ce): the new data, refined formula, and relationships to other minerals of the apatite group. *Zap. Vseross. Mineral. Obshchest.* **124**(2), 98-110 (in Russ.).

_____, PETERSEN, O.V., & VOLOSHIN, A.V. (1997): Calcio-ancylite-(Ce) from Ilímaussaq and Narssârssuk, Greenland, Kola peninsula and Polar Urals, Russia; ancylite-(Ce) – calcio-ancylite-(Ce) an isomorphous series. *Neues Jahrb. Mineral. Abh.*, **171**(3), 309-322.

PETROV, I., & HAFNER, S.S. (1988): Location of trace $Fe^{3+}$ ions in sanidine. *Am. Min.*, **73**, 97-104.

_____, YUDE, FU, BERSHOV, L.V, HAFNER, S.S. & KROLL, H. (1989): Order-disorder of $Fe^{3+}$ ions over the tetrahedral positions in albite. *Am. Min.*, **74**, 604-609.

PIILONEN, P.C., MCDONALD, A.M. & LALONDE, A.E. (1998): The crystal chemistry of aegirine from Mont Saint-Hilaire, Quebec. *Can. Mineral.* **36**, 779-791.

PLATT, R.G. (1994): Perovskite, loparite and Ba-Fe hollandite from the Schryburt Lake carbonatite complex, northwestern Ontario, Canada. *Mineral. Mag.* **58**, 49-57.

_____ & WOOLLEY, A.R. (1990): The carbonatites and fenites of Chipman Lake, Ontario. *Can. Mineral.*, **28**, 241-250.

PRIDER, R.T. (1965): Noonkanbahite, a potassic batisite from the lamproites of Western Australia. *Mineral. Mag.* **34**, 403-405.

REGUIR, E.P., CHAKHMOURADIAN, A.R., & EVDOKIMOV, M.D. (1999): The mineralogy of a unique baratovite- and miserite-bearing quartz-albite-aegirine rock from the Dara-i-Pioz complex, northern Tajikistan. *Can. Mineral.*, **37**, 1369-1384.

_____ & MITCHELL, R.H. (2000): The mineralogy of carbonatites and related potassic syenites from the Rocky Boy stock, Bearpaw Mountains, north-central Montana. *In*: GeoCanada 2000 Conference CD (extended abstracts), file 374.pdf.

ROGOV, YU.G., ROGOVA, V.P., VORONKOV, A.A., & MOLEVA, V.A (1965): Tinaksite $NaK_2Ca_2TISI_7O_{19}(OH)$ – new mineral. *Dokl. Akad Nauk SSSR*, **162** (3), 658-661 (in Russ.).

ROGOVA, V.P., ROGOV, Yu.G., DRITS, V.A. & KUZNETSOVA, N.N. (1978): Charoite – a new mineral and a new gemstone. *Zap. Vses. Mineral. Obshchest.* **107**(1), 94-100 (in Russ.).

ROZHDESTVENSKAYA, I.V., NIKISHOVA, L.V., BANNOVA, I.I. & LAZEBNIK, YU.D. (1988): Canasite: refinement and characteristics of the crystal structure and structural typomorphism. *Mineral. Zhurn.* **10**(4), 31-44 (in Russ.).

SAMSONOVA, N.S. & DONAKOV, V.I. (1968): Kalsilite from Murun alkaline massif (Eastern Siberia). *Zap. Vses. Mineral. Obshchest.* **87**(3), 291-300 (in Russ.).

SCHMAHL, W.W & TILLMANNS, E. (1987): Isomorphic substitutions, straight Si-O-Si geometry, and disorder of tetrahedral tilting in batisite, $(Na,K)(K,Na)Na(Ti,Fe,Nb,Zr)Si_4O_{14}$. *N. Jahrb. Mineral. Monatsh.* **1987 (3)**, 107-118.

SKOSYREVA, M.V., BAGDASAROV, YU.A., VLASOVA, V. & ZHUKLISTOV, A.P. (1988): Typical features of micas from an East European Platform carbonatite deposit (Kursk Magnetic Anomaly region). *Geochem. Int.*, **25**, 24-34.

SCOTT, J.D. (1976): Crystal structure of miserite, a Zoltai type 5 structure. *Can. Min.* **14(4)**, 515-528.

SETO, K. (1923): Chemical study of some feldspars. *Sci. Rep. Tôhoku Univ.*, Ser. 3(1), 219-231.

SINCLAIR, W. & MCLAUGHLIN, G.M. (1982): Structure refinement of priderite. *Acta Crystallogr.* **B38**, 245-246.

TILLEY, C.E. (1954): Nepheline-alkali feldspar paragenesis. *Am. J. Sci.* **252**, 65-75.

VILADKAR, S.G. & WIMMENAUER, W. (1986): Mineralogy and geochemistry of the Newania carbonatite-fenite complex, Rajasthan, India. *Neues Jahrb. Mineral. Abh.*, **156**, 1-21.

VISSER, J. & SHIRLEY, R. (1998): Automatic powder indexing by zone indexing. Documentation and data formulas for ITO12.

VLADYKIN, N.V. (1997): Geochemistry and genesis of lamproites from the Aldan Shield. *Geol. Geophys.* **38(1)**, 123-135 (in Russ.).

_____, SIMONOV, V.A. & SOKOLOV, S.V. (1994): Fluid regime and crystallization temperatures of minerals of charoitic rocks. *Termobarogeokhim. Mineraloobraz. Protsessov* 3, 76-82 (in Russ.).

_____& TZARUK, I.I. (1999): Geological setting, chemistry and genesis of benstonite carbonatites from the Murun complex. *Carbonatites of Kola Peninsula*, St.-Petersburg, Vol. Abstr., 49-50. (in Russ.).

VOROB'EV, E.I. & MALYSHONOK, YU.V. (1985): First finding of Mesozoic carbonatites on Aldan shield. *In* Geologia i poleznye iskopaemye Vostochnoi Sibiri, Novosibirsk, Nauka, 116-122 (in Russ.).

_____, MALYSHONOK, YU.V. & ALEKSEEV, YU.A. (1983): On genesis of charoite. *In* Problems of Crystal Chemistry and Genesis of Minerals. Nauka Press, Leningrad, 72-91 (in Russ.).

WALL, F., LE BAS, M.J., & SRIVASTAVA, R.K. (1993): Calcite and carbocernaite exsolution and cotectic textures in a Sr, *REE*-rich carbonatite dyke from Rajasthan, India. *Min. Mag.*, **57**, 495-513.

191

WERNER, P.-E., ERIKSSON, L. & WESTDAHL, M. (1985): TREOR, a semi-exhaustive trial-and-error powder indexing program for all symmetries. *J. Appl. Crystallogr.* **18**, 367-370.

WONES, D.R. & APPLEMAN, D.E. (1961): X-ray crystallography and optical properties of synthetic monoclinic $KFeSi_3O_8$ iron-sanidine. *USGS Prof. Paper*, 424-C, C-309.

_____ & _____ (1963): Properties of synthetic triclinic $KFeSi_3O_8$ iron-microcline, with some observations on the iron-microcline ↔ iron-sanidine transition. *J. Petrol.*, **4**, 131-137.

WOOLLEY, A.R., BARR, M.W.C., DIN, V.K., JONES, G.C., WALL, F. & WILLIAMS, C.T. (1991): Extrusive carbonatites from the Uyaynah Area, United Arab Emirates. *J. Petrol.*, **32**, 1143-1167.

YAKOVENCHUK, V.N., MENSHIKOV, YU.P., PAKHOMOVSKY, YA.A., & IVANYUK, G.YU. (1997): Ancylite-(La) $Sr(La, Ce)(CO_3)_2$ (OH) $H_2O$ — a new carbonate from hydrothermal vein at the Kukisvumchorr Mountain (Khibiny Massif) and its comparison with ancylite-(Ce). *Zap. Vser. Mineral. Obschest.*, **126**(1), 96-109 (in Russ.).

YOUNG, B.N., PARSONS, I. & THREADGOULD, R. (1994): Carbonatite near the Loch Borralan intrusion, Assynt. *J. Geol. Soc. London*, **151**, 945-954.

ZAITSEV, A.N., YAKOVENCHUK, V., CHAO, G.Y., GAULT, R.A., SUBBOTIN, V.V., PAKHOMOVSKY, Y.A. & BOGDANOVA, A.N. (1996): Kukharenkoite-(Ce), $Ba_2Ce(CO_3)_3F$, a new mineral from Kola peninsula, Russia, and Québec, Canada. *Europ. J. Mineral.* **8**, 1327-1336.

_____, WALL, F., & LE BAS, M. J. (1998): *REE*-Sr-Ba minerals from the Khibina carbonatites, Kola Peninsula, Russia: their mineralogy, paragenesis and evolution. *Mineral. Mag.*, **62**(2), 225-250.

## APPENDIX A.

### Analytical techniques.

The composition and BSE images of minerals were obtained using a Hitachi 570 scanning electron microscope equipped with a LINK ISIS analytical system incorporating a Super ATW Light Element Detector or a JEOL JSM-5900LV scanning electron microscope. Raw EDS spectra were acquired for 100-200 seconds (live time) with an accelerating voltage of 20 kV and a beam current of 0.86 or 0.55 nA. The spectra were processed with the LINK ISIS-SEMQUANT software, with full ZAF corrections applied. The following lines (and well-characterised natural and synthetic standards) were used: P$K$ & F$K\alpha$ (fluorapatite), Cl$K$ (sylvine), Ba$L$ (benitoite), Al$K$ (corundum), Fe$K$ & Ti$K$ (ilmenite), Na$K\alpha$ (jadeite), Mn$K$ (manganoan fayalite), K$K$ (orthoclase), Mg$K$ (periclase), Ca$K$, Si$K$ (wollastonite), Sr$L$ (synthetic SrTiO$_3$), S$K$ (chalcopyrite), La$L$, Ce$L$, Pr$L$, Nd$L$ & Nb$L$ (loparite), Y$L$ (synthetic YF$_3$), Eu$L$ (synthetic EuF$_3$), Cr$K$, Gd$L$, Hf$M$, Pb$M$, Sm$L$, Sn$L$, Ta$M$, Th$M$, Zr$L$, U$M$ and V$K$ (pure metals).

XRD powder patterns of charoite (Cu K$\alpha$ radiation) were obtained at Lakehead University with a Philips 3710 diffractometer (Ni monohromator, $\lambda$=CuK$\alpha$, 2$\theta$ range: 5-145°; step size: 0.02°; time per step: 1s), and at Queen's University with a STOE Stadi diffractometer (Ge monochromator, $\lambda$=CuK$\alpha$, 2$\theta$ range: 2-120°; step size: 0.02°; time per step: 43s).

TEM examination of the charoite samples was done at the Brockhouse Institute for Materials Research (McMaster University, Ontario) using a JEOL 2010F field-emission STEM operated at 200 kV.

193